Photoelectron spectroscopy of some atmospherically important species and heavy metal compounds

A thesis submitted to the University of Southampton
for the degree of
Doctor of Philosphy

Levi James Beeching

Department of Chemistry
University of Southampton

· August 2002 ·

UNIVERSITY OF SOUTHAMPTON

ABSTRACT

FACULTY OF SCIENCE
DEPARTMENT OF CHEMISTRY

Doctor of Philosphy

PHOTOELECTRON SPECTROSCOPY OF SOME ATMOSPHERICALLY IMPORTANT SPECIES AND HEAVY METAL COMPOUNDS

by Levi James Beeching

UV photoelectron spectroscopy studies of the reactive intermediates $O_2(a^1\Delta_g)$, OH and O has been performed using using two different synchrotron sources. Autoionizing resonances have been observed and assigned to members of series of Rydberg states converging towards higher ionic limits. Vibrational resolution has been obtained for $O_2(a^1\Delta_g)$ and OH, and rotational resolution has been achieved for OH. Measurements of angular distributions of photoelectrons allowed insight into the photoionization dynamics to be obtained.

The UV photoelectron spectra of UBr_4 and $ThBr_4$ have been recorded in the gas-phase and complete ionic state assignment (including spin orbit splittings) has been achieved with the aid of relativistic density functional calculations. Matrix isolation infrared spectra have been recorded for UBr_4 and $ThBr_4$ and the results obtained are consistent with a tetrahedral geometry for these compounds.

2-Azidoethanol and 2-Azidoethylacetate have been studied by a variety of spectroscopic techniques, and their thermal decompositions have been studied by matrix isolation infrared spectroscopy and real-time ultraviolet photoelectron spectroscopy. This has allowed their mechanisms for decomposition to be proposed.

The HeI photoelectron spectrum of F_2O has been recorded with a better resolution than previously reported. New vibrational structure has been observed for the first time. The order and positions of the lowest four states of F_2O^+ have been established by near state-of-the-art *ab initio* calculations and vibrational envelopes have been simulated employing both harmonic and anharmonic methods. Geometrical parameters were obtained for the $F_2O^+(\tilde{X}^2B_1)$ and $F_2O^+(^2A_2)$ cationic states for the first time using the iterative Franck-Condon analysis (IFCA) procedure. Vibrational analysis of the second and third, heavily overlapped, photoelectron bands in the HeI photoelectron spectrum of F_2O, was achieved based on a simulation of the experimental spectrum.

Memorandum

This thesis is an account of original research performed by the author in the Department of Chemistry of the University of Southampton, between October 1998 and October 2001. Where findings of other work have been used, due reference has been given.

Contents

List of Figures

List of Tables

Acknowledgments

I acknowledge Leybold and BAT for financial support.

I have benefitted from fruitful collaboration with many people on the varied aspects of the different projects. I would like to acknowledge all who were involved in making this a success and I shall briefly outline the major contributors.

Firstly I would like to acknowledge the role of my supervisor, Prof. John Dyke, who has provided unstinting encouragement and support throughout. Similarly, I would like to thank Dr. Alan Morris my advisor and also experimental technical expert.

I would also like to thank the rest of the research group, past and present, particularly, Dr. Ed Lee, who contributed greatly to the theoretical calculations, Dr. J. S. Ogden, for his matrix isolation work, Nicole Hooper, a co-worker on azide pyrolysis and Dr. Stuart Gamblin, Dr. Alberto Defanis and Lucia Zuin, all of whose tireless efforts made the synchrotron studies possible.

Further thanks must also be extended to the staff at both ELETTRA and Daresbury Laboratories for their support during periods of beam-time at the synchrotron sources, in particular Prof. John West and Dr. Nicolas Zema.

Finally I acknowledge the contribution of Dr. M. L. Costa's group at the Faculdade de Ciencias e Tecnologia, Universidade Nova de Lisboa to the azide pyrolysis studies.

Chapter 1

Introduction

1.1 Photoelectron spectroscopy

Photoelectron spectroscopy (PES) has its roots in the 19th century when in 1887 the photoelectric effect was discovered by Hertz [1]. Hertz found that the irradiation of a solid alkali metal with suitably energetic, ultraviolet radiation would produce the ejection of electrons from the metal. This effect was explained theoretically by Einstein in 1905 [2] with the equation

$$h\nu = \frac{1}{2}m_e v^2 + I \tag{1.1}$$

where $h\nu$ is the energy of the incident photon, $\frac{1}{2}m_e v^2$ is the kinetic energy of the ejected photoelectron and I is the work function of the metal. It was not until fifty years after this early work that photoelectron spectroscopy was used to probe the electronic structure of solids. Siegbahn analyzed the energies of the electrons produced from a solid sample when irradiated with X-rays [3] and called the method Electron Spectroscopy for Chemical Analysis (ESCA). Similar techniques were developed using vacuum UV radiation to ionize free molecules in the gas phase, for example, by Turner [4] [5], Price [6] and Vilesov. [7]

Photoelectron spectroscopy (PES) extends the concept of the photoelectric effect to both solid state or gas phase samples. In PES, both the probability of producing a photoelectron (the cross-section) and also the kinetic energy of the photoelectrons produced is recorded.

PES may be broadly divided into two areas:

- X-ray photoelectron spectroscopy (XPS sometimes referred to as ESCA)
- Ultraviolet photoelectron spectroscopy (UPS, UV-PES)

XPS uses X-rays that are energetic enough to remove both core and valence electrons, whereas UV radiation is only sufficient to eject valence electrons. The

experimental resolution in gas phase UV-PES is usually much greater than that achieved with XPS and is therefore of greater interest to the chemist as it directly supplies information on those electrons involved in **chemical bonding**. It is the technique used throughout this thesis.

If ionization of a molecule with an incident photon is considered, as in equation 1.2

$$M^+ + e^- \leftarrow M + h\nu \tag{1.2}$$

then conservation of energy gives equation1.3

$$E(e^-) = h\nu - E(M^+) + E(M), \tag{1.3}$$

where $E(e^-)$ is the kinetic energy carried by the photoelectron that is determined by the energy of the incident photon, $h\nu$, the energy of the initial neutral molecule, $E(M)$, and energy of the final state of the ion $E(M^+)$. Considering the difference in energy between the initial state M, and final state M^+, and ignoring any change in kinetic energy between M and M^+ gives equation 1.4. The approximation that the photoelectron carries away all the excess kinetic energy is reasonable as the electron is always much lighter than the resultant molecular ion; it should be noted that the *mass of a single proton* $\simeq 1800 \times$ *mass of an electron.*

$$E(e^-) = h\nu - I_e - \Delta E_{vib} - \Delta E_{rot} \tag{1.4}$$

In this equation I_e is the ionization energy of the molecule and ΔE_{vib} and ΔE_{rot} represent the change in vibrational and rotational energy on ionization. A photoelectron spectrum is a plot of the yield of electrons as a function of their ionization energies (I_e). Ionization energies may be directly measured from a photoelectron spectrum by simple subtraction of the electron kinetic energies from the known energy of the incident radiation, if ΔE_{vib} and ΔE_{vrot} are known (see equation1.4). Usually the resolution of conventional spectrometers (typically around 25meV, 200cm^{-1})is insufficient to resolve rotational structure except for exceptional cases like H_2 [8], H_2O [9] and H_2S [10] where rotational structure may be resolved. In a conventional photoelectron spectrum the vibrational structure observed supplies information on the **ionic state** because only the ground vibrational state of M is sufficiently populated at normal ambient temperatures.

Gas phase photoelectron spectroscopy of neutral molecules has been an invaluable tool to study many gases and volatile compounds. Over the last half- century a vast number of studies have been carried out on stable atoms and molecules which are able to be produced at sufficient partial pressures in the gas phase.

These are documented in a large number of publications and a good overview can be found in books by Kimura [11], Turner [5], Eland [12] and Rabalais [13].

As photoelectron spectroscopy has become more developed it has been possible to study a greater range of more experimentally challenging compounds, *e.g.* compounds with a low vapor pressure at room temperature, or short-lived gas phase species. These are the focus of the research of the Southampton photoelectron spectroscopy group.

An extension of conventional photoelectron spectroscopy is constant ionic state (CIS) spectroscopy, where the relative cross-section for ionization to a specific ionic vibronic state is measured as a function of photon energy, using a tunable photon source *e.g.* a synchrotron; this is described in Chapter 3 and 5, section 5.2.

1.2 Overview of reactive intermediates studied by PES and information to be obtained from such studies

Some of the most important chemical species that control many chemical systems in the natural environment (*e.g.* in atmospheric chemistry) and man made processes (*e.g.* in combustion chemistry) are short-lived. These reactive intermediates may be present in low partial pressures relative to that of stable molecules, yet may make major contributions to controlling the major reaction pathways. The often low partial pressures and short life times makes reactive intermediates inherently difficult to study. However, if they can be produced in sufficient partial pressures, in the gas phase, then photoelectron spectroscopy is a powerful tool to investigate their electronic structure and reactivity. A large number of free radicals have been studied using discrete line source photon sources and some using synchrotron radiation (see Chapter 3). Most radicals and reactive intermediates have been studied with He(I) radiation at 21.22eV. A large number of photoelectron spectra of short-lived molecules are collected in a monograph by Kimura [14] and there are several comprehensive reviews on the subject by the Southampton photoelectron spectroscopy group [15] [16] and others [17]. The study of the photoelectron spectroscopy of radicals is important as it can supply a wealth of information on their structure, bond strengths and thermochemistry. The measurement of ionization energies enables the calculation of heats of formation of radicals, when allied with available thermochemical data (heats of formation) on neutral molecules and ions. In brief, the adiabatic ionization energy

and the electron affinity of a reactive intermediate provide a link to several thermochemical cycles [18] that allow bond dissociation energies to be determined. For example, if the heat of formation of the neutral molecule has been accurately determined by other studies, then an accurate heat of formation of the positive ion is obtained by combining the heat of formation of the neutral with the adiabatic ionization energy determined by PES. The derived heats of formation can be used to determine bond dissociation energies that in turn can prove useful in models of atmospherically important reactions and combustion. Good examples of the relationship between heats of formation, ionization energies (from PES) and appearance potentials (from mass spectrometry) can be found in a paper by Chen [18]. Furthermore, photoelectron spectroscopy provides extra detail, due to the ionic vibrational structure resolved in a photoelectron band. The vibrational separations can be used to determine vibrational constants, while the shape of the vibrational envelope provides an insight into the change in bond length on ionization, and may also reveal resonant processes.

Studies of the photoelectron spectroscopy of reactive intermediates using synchrotron radiation by the Southampton group has focussed on atmospherically important diatomic species, notably SO [19], CS [20], OH [21], OD [21] and $O_2(a^1\Delta_g)$ [22] [23]. As synchrotron radiation is polarized and continuously tunable (see Chapter 3), extra information about the photoionization process can be gained by the study of the angular distribution of photoelectrons [24](see section 2.4) and the variation of the photoionization cross-section with respect to the energy of the incident radiation (see section 2.2).

1.3 Photon sources

Two distinct types of photon source were used in this work,

1. a helium discharge lamp,

2. a synchrotron radiation source.

The capillary discharge helium lamp is an unpolarized, discrete line source, which can be readily constructed. Almost all of the usable output photon intensity, produced by a high-voltage discharge in helium, consists of the HeIα line at a photon energy of 21.218eV (58.4nmm). This type of source is adequate for conventional photoelectron spectroscopy but is of little use for angle-resolved (see section 2.4) or constant ionic state (CIS) studies.

Synchrotron radiation sources can be highly polarized, be of high brilliance and be continuously tunable. They are, therefore, ideal for angle-resolved and CIS studies of reactive intermediates. Unfortunately synchrotrons are few in number and in great demand, so their availablility is limited. More information on both types of source is given in the chapter covering synchrotron radiation (Chapter 3) and the experimental chapter (Chapter 5).

1.4 Resonant effects and Rydberg states

In a VUV photoelectron spectrum resolution is usually sufficient to resolve vibrational structure, so for direct ionization, as shown in Figure 1.1, equation 1.2 can be written as equation 1.5.

$$M^+(v^+) + e^- \leftarrow M(v'') + h\nu, \tag{1.5}$$

The relative intensity of each vibrational component within a photoelectron band is dependent on the overlap of the wavefunctions of the initial neutral state, $M(v'')$, and the final ionic state, $M^+(v^+)$. The relative intensity of each vibrational component is proportional to the **square** of the overlap integral between the initial and final states (see equation 1.6)

$$I_{v^+ \leftarrow v''} \propto \left| \int_0^{+\infty} \Psi_{M^+,v^+}(R)\Psi_{M,v''}(R)dR \right|^2, \tag{1.6}$$

where, for a given v^+ and v'', this integral is known as the Franck-Condon Factor (FCF). In the case above, only direct photoionization is considered. This is adequate for most instances in photoelectron spectroscopy , where HeIα(21.22eV) radiation is used. In practice HeIα(21.22eV) radiation is too great in energy to excite a valence electron and form an excited neutral state (necessary for indirect, resonant ionization) and therefore only direct ionization is possible with this photon source. Use of lower energy incident radiation may often give rise to indirect ionization via a neutral, excited state, as shown in Figure 1.2, which is a resonant effect. If a molecular ionization via an excited state, as in equation 1.7 is considered,

$$M^+(v^+) + e^- \leftarrow M^*(v') \leftarrow M(v'') + h\nu, \tag{1.7}$$

then the relative intensities of the vibrational components in a photoelectron band are now a product of the FCFs for the two separate steps. Therefore equation 1.6 becomes the equation 1.8, where the relative intensity of a vibrational component

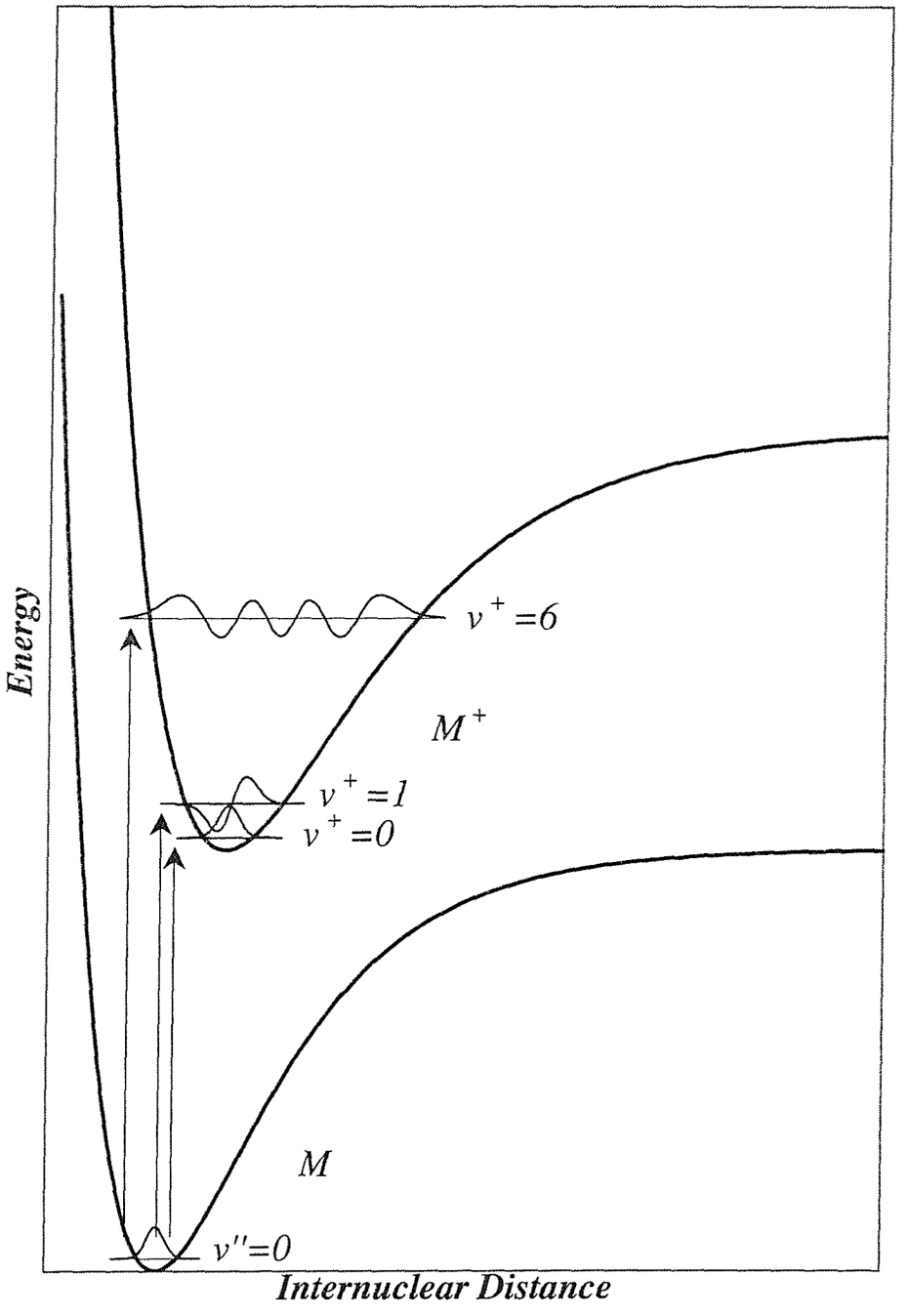

Figure 1.1: Schematic representation of direct Ionization.

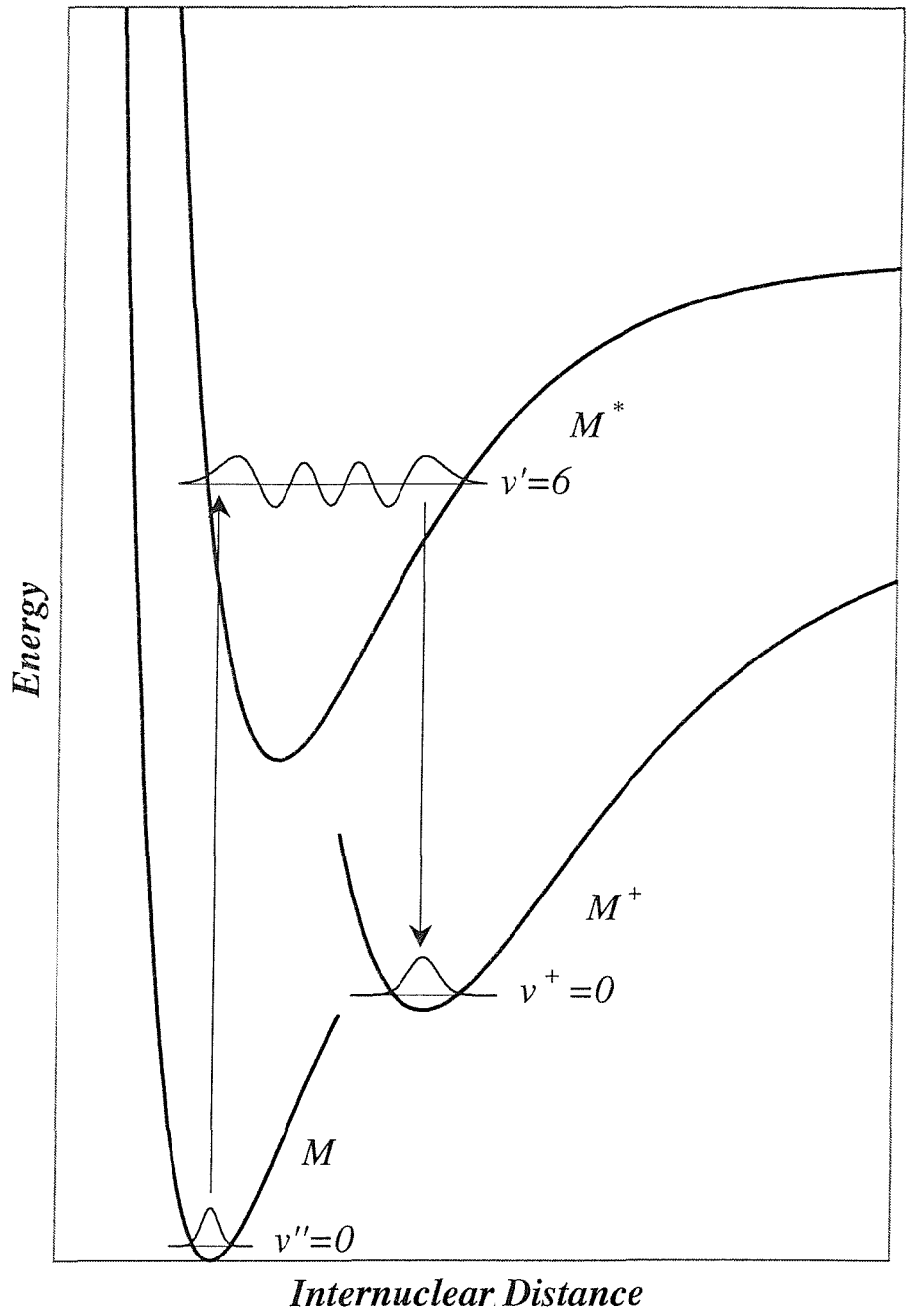

Figure 1.2: Schematic representation of autoionization via a Rydberg state.

in the photoelectron band is proportional to the product the square of each of overlap integrals.

$$I_{v^+\leftarrow v'\leftarrow v''} \propto \left| \int_0^{+\infty} \Psi_{M^+,v^+}(R)\Psi_{M^*,v'}(R)dR \right|^2 \times \left| \int_0^{+\infty} \Psi_{M^*,v'}(R)\Psi_{M,v''}(R)dR \right|^2 \tag{1.8}$$

If an incident photon energy is close to the energy of a resonance then the vibrational envelope in a photoelectron spectrum may change dramatically. The extra contribution to vibrational component intensities from indirect (resonant) processes often leads to an extension of the vibrational profile of a photoelectron band so that many higher vibrational components may be observed in the ionic state. One of the best examples of this is the difference between the photoelectron spectrum of oxygen using HeIα(21.22eV) and NeIα(16.85eV, 73.6nm) radiation. The first band in the HeIα spectrum (corresponding to the ionization, $O_2^+(X^2\Pi_g) \leftarrow O_2(X^3\Sigma_g^-)$) is greatly extended in the NeIα spectrum [12] due to an autoionizing resonance at the energy of the strong neon line at 73.6nm (16.85eV).

The excited neutral states accessible on VUV irradiation are usually Rydberg in character. A Rydberg state is a state in which the outermost occupied orbital is constructed from atomic orbitals of higher principal quantum number than those used to construct the valence shell. For example in O_2 the valence orbitals are σ and π orbitals constructed from O_2 2s and 2p orbitals; therefore the first Rydberg orbital would have a principal quantum number, $n = 3$. The excitation energy ($E_{n,l}$) for a transition from the ground state to a Rydberg state can be written as in equation 1.9 [24],

$$E_{n,l} = I_e - \frac{R}{(n-\delta)^2}, \tag{1.9}$$

where I_e is the ionization energy (*i.e.* limit of the Rydberg series), R is the Rydberg constant ($13.61\,eV$), n is the principal quantum number and δ is called the quantum defect. If the state is Rydberg in character then the Rydberg electron spends little time in the proximity of the ionic core of the molecule and behaves in a hydrogenic fashion. In fact excitation energies to hydrogen atomic states fit equation 1.9 with $\delta = 0$. It is therefore sensible to describe a Rydberg state by using a combination of the state of the ionic core (not including the Rydberg electron) and the hydrogenic orbital occupied by the Rydberg electron, *e.g.* $O_2(D^2\Delta_g, 5p\pi)$ (see Chapter 6). One of the principal uses of Rydberg series is for the accurate calculation of ionization energies, as each series converges to an ionic limit. It is straightforward to determine an accurate ionization energy by performing an extrapolation that is fitted to equation 1.9. The size of the

quantum defect (δ) is representative of the penetration of the Rydberg orbital into the ionic core. δ is related to the radial distribution of the Rydberg orbital and therefore to its angular momentum (l). It has been found that for a large number of molecules the quantum defect is closely correlated to the angular momenta of the Rydberg electron, *i.e.* for s, p and d Rydberg orbitals of first row atoms, δ is about 1.0, 0.5 and 0.1 respectively.

Rydberg states and resonant ionization are particularly pertinent to CIS spectra, where the photoionization cross-section is measured as a function of incident photon energy. In practice, Rydberg series may be observed as sharp changes in the photoionization cross section when the photon energy matches that of a resonance above the first or higher ionization energies. Direct and indirect ionization is discussed further in Chapter 2 and CIS spectra are discussed in Chapter 5.

1.5 Aims of the project

The aims of this project were to use the technique of photoelectron spectroscopy to investigate the electronic structure of selected small molecules.

- The first aim was to use angle-resolved photoelectron spectroscopy with synchrotron radiation to investigate photoionization of the reactive intermediates $O_2(a^1\Delta_g)$, OH and O atoms, that are important in the upper atmosphere

- It was proposed to study these short-lived species using CIS, to investigate Rydberg series (see section 1.5) that alter the cross-section for the photoionization process as the incident photon energy is varied, above the first or higher ionization energies.

- The next aim was to extend previous work within the Southampton PES group on the actinide tetrahalide compounds, ThF_4, $ThCl_4$, UF_4 and UCl_4 [25]. The aim was to investigate the electronic structure of UBr_4 and $ThBr_4$with high-temperature UV-photoelectron spectroscopy and with the assistance of relativistic density functional calculations using the ADF code (see Chapter 4), to assign the observed spectral structure including the large spin-orbit splittings.

- It was proposed to use photoelectron spectroscopy as a tool for investigating the high-temperature pyrolysis products and decomposition pathways of azido-acetic acid ethyl ester ($N_3CH_2CO_2Et$) and 2-azido-ethanol ($N_3CH_2CH_2OH$).

- The final aim was to investigate the photoelectron spectroscopy of oxygen difluoride (F_2O), by obtaining spectra of better quality than previously recorded [26] [27]. These experimental studies were to be supported by calculations that combined *ab initio* calculations with Franck-Condon calculations to simulate photoelectron band envelopes.

1.6 Structure of the thesis

The thesis is structured in the following way.

Immediately after the Introduction, three chapters follow that contain most of the theoretical background to the work. This comprises of chapters covering; the fundamental principles related to photoionization (Chapter 2), a detailed description of the properties of synchrotron radiation (Chapter 3), and the theoretical methods used in photoelectron spectroscopy (Chapter 4).

These are followed by a chapter covering all the details of the experiments carried out in this work (Chapter 5). This includes a description of the two different spectrometers used, a description of the different photon sources used and a description of how data was actually acquired for the different types of spectra obtained (PES or CIS).

The next chapters contain the results from each of the individual studies. This comprises of six separate chapters, each concentrating on a specific type of molecular species.

The final chapter contains a summary of the work, a section outlining what objectives were achieved and some suggestions for further work. It outlines possibilities for future developments that could build on the work contained in this thesis.

Bibliography

[1] H. Hertz, Annalen der Physik **31**, 983 (1887).

[2] A. Einstein, Annalen der Physik **17**, 132 (1905).

[3] K. Siegbahn and K. Edvarson, Nucl. Phys. **1**, 137 (1956).

[4] M. I. Al-Joboury and D. W. Turner, J. Chem. Phys. **37**, 3007 (1962).

[5] D. W. Turner, *Molecular Photoelectron Spectroscopy* (Wiley-Interscience, London, UK, 1971).

[6] W. C. Price, A. E. Potts, and D. G. Streets, in *Electron Spectroscopy*, edited by D. A. Shirley (North Holland, Amsterdam, 1972).

[7] F. I. Vilesov, B. L. Kurbatov, and A. N. Terenin, Dokl. Akad. Nauk. SSSR **138**, 1329 (1961).

[8] L. Asbrink, Chem. Phys. Lett. **7**, 549 (1970).

[9] L. Asbrink and J. W. Rabalais, Chem. Phys. Lett. **12**, 182 (1971).

[10] R. N. Dixon, G. Duxbury, M. Horani, and J. Rostas, Mol. Phys. **22**, 977 (1972).

[11] K. Kimura, S. Katsumata, Y. Achiba, T. Yamzaki, and S. Iwata, *Handbook of HeI Photoelectron Spectra of Fundamental Organic Molecules* (Halsted Press, New York, 1981).

[12] J. H. D. Eland, *Photoelectron Spectroscopy* (Butterworths, London, UK, 1974).

[13] J. W. Rabalais, *Photoelectron Spectroscopy* (Wiley and Sons, London, UK, 1977).

[14] K. Kimura, *Photoelectron Spectroscopy of Small Molecules* (Japan Scientific Societies Press/Halstead Press, Tokyo/New York, 1974).

[15] J. M. Dyke, N. Jonathan, and A. Morris, in *Electron Spectroscopy*, edited by C. R. Brundle and A. D. Baker (Academic Press, New York, 1979), Vol. 3, p. 189.

[16] J. M. Dyke, N. Jonathan, and A. Morris, in *Electron Spectroscopy*, edited by G. R. Brundle and A. D. Baker (Academic Press, New York, 1979), Vol. 3, p. 189.

[17] C. Y. Ng, T. Baer, and I. Powis, *Unimolecular and Bimolecular Reaction Dynamics* (John Wiley and Sons Ltd, UK, 1994).

[18] J. A. Blush, H. Clauberg, D. W. Kohn, D. W. Minsek, Z. Xu, and P. Chen, Accounts of Chemical Research **25**, 385 (1992), english Review SEP ACCOUNT CHEM RES.

[19] J. M. Dyke, D. Haggerston, A. Morris, S. Stranges, J. B. West, T. G. Wright, and A. E. Wright, J. Chem. Phys. **106**, 821 (1997).

[20] J. M. Dyke, S. D. Gamblin, D. Haggerston, A. Morris, S. Stranges, J. B. West, T. G. Wright, and A. E. Wright, J. Chem. Phys. **108**, 6258 (1998).

[21] J. D. Barr, A. De Fanis, J. M. Dyke, S. D. Gamblin, N. Hooper, A. Morris, S. Stranges, J. B. West, and T. G. Wright, J. Chem. Phys. **110**, 345 (1999).

[22] J. D. Barr, A. De Fanis, J. M. Dyke, S. D. Gamblin, A. Morris, S. Stranges, J. B. West, T. G. Wright, and A. E. Wright, J. Chem. Phys. **109**, 2737 (1998).

[23] L. Beeching, A. De Fanis, J. M. Dyke, S. D. Gamblin, N. H. Hooper, A. Morris, and J. B. West, J. Chem. Phys. **112**, 1707 (2000).

[24] J. Berkowitz, *Photoabsoption, Potoionization and Photoelectron Spectroscopy* (Academic Press, New york, US, 1979).

[25] J. M. Dyke, N. K. Fayad, A. Morris, and I. R. Trickle, J. Chem. Phys. **72**, 3822 (1980).

[26] A. B. Cornford, D. C. Frost, F. G. Herring, and C. A. McDowell, J. Chem. Phys. **55**, 2820 (1971).

[27] C. R. Brundle, M. B. Robin, N. A. Kuebler, and H. Basch, Journal of the American Chemical Society **94**, 1451 (1972).

Chapter 2

Fundamental principles related to photoionization

2.1 Direct ionization

Direct ionization in UV-PES (as considered in section 1.4) is a process in which an electron may be ejected from a molecule on interaction with a sufficiently energetic photon, without progressing via an intermediate excited state (see equation 1.5). A direct ionization may be represented as in Figure 1.1. Photoionization is a rapid process with respect to the timescale of a molecular vibration, so the molecular framework is effectively frozen during an ionization. This means that, with respect to the classical picture, only **vertical** transitions on a potential energy diagram are permitted. In the ground state of the neutral molecule, at room temperature, only the $v'' = 0$ state is populated, because the $v'' = 0 \leftrightarrow 1$ separation is usually large with respect to $k_B T$. Ionization is permitted to **any** vibrational state in the ion as long as there is some overlap of the initial and final vibrational wavefunctions. The relative intensity of each vibrational component within a photoelectron band is dependent on the Franck-Condon Factor (FCF), which is proportional to the **square** of the overlap integral between the initial and final vibrational states (see equation1.6). This overlap integral is greatly affected by the change in equilibrium bond length between the ground neutral state and that of the ion. If a molecule undergoes photoionisation, with an electron being removed from non-bonding orbital, it will undergo little change in the equilibrium bond length. With no change in the bond length, the most probable transition is from the vibrational ground state of the neutral to the vibrational ground state of the ion, *i.e.* $M^+(v^+ = 0) + e^- \leftarrow M(v'' = 0) + h\nu$. The probability of a transition to all other vibrational levels of the ion, in these cases, will be virtually zero, as positive and negative contributions to the overlap integral cancel. Therefore, only

a single vibrational component will be observed in the photoelectron spectrum for this band. Conversely, if a transition is considered in which a large change in equilibrium bond length is observed, the greatest Franck-Condon Factor will be seen for ionizations to $M^+(v^+ > 0)$. A progression of vibrational components will be observed in the photoelectron spectrum (the vibrational envelope) [1].

2.2 Autoionization via Rydberg states

Autoionization may occur in PES when a super excited state (above at least one of the ionization limits) is formed by the resonant absorption of a photon as in equation 2.1 (see figure 1.2).

$$M^*(v') \leftarrow M(v'') + h\nu \tag{2.1}$$

$$M^+(v^+) + e^- \leftarrow M^*(v') \tag{2.2}$$

The superexcited states are Rydberg states and they can decay in different ways:

1. By dissociation of the molecule, producing no free electrons.

2. By vibrational autoionization, *i.e.* the excess vibrational energy of the ionic core is transferred to the kinetic energy of the Rydberg electron causing its ejection. In this case only very low kinetic energy electrons are produced which are difficult to observe in conventional photoelectron spectra.

3. By electronic ionization, *i.e.* the conversion of the excess electronic energy available into the kinetic energy of an ejected electron (equation 2.2). This is a concerted process involving two electrons. The outer Rydberg electron falls back into a valence orbital hole, while a different valence electron is ejected. The result is the formation of an ionic state, that is lower in energy than the Rydberg state, and the production of an electron with a kinetic energy equal to that which would have been produced by direct ionization of the neutral molecule to the same final ionic state. [1]

An important point to note about the three schemes outlined above is that dissociation and vibrational ionization will **reduce** any photoelectron signal observed at that particular photon energy which gives rise to resonance to the Rydberg state. Conversely, electronic autoionization may greatly **increase** a photoelectron signal observed at a resonant photon energy for a transition to the **same** final ionic state. This means that transitions via Rydberg states may be observed

as changes in overall cross-section for a particular photoionization process (resonances). This can be achieved if the intensity of photoelectrons observed for the ionization is measured as a function of the incident photon energy, as in a constant ionic state (CIS) spectrum.

These different decay channels are always in competition and this can be investigated by looking at the ionization efficiency (I_{eff}) as expressed in equation 2.3.

$$I_{eff} = \frac{\sigma_{ion}}{\sigma_{abs}}, \tag{2.3}$$

In this equation, σ_{ion} is the photoionization cross section and σ_{abs} is the total absorption cross-section. At HeI photon energies the ionization efficiency usually approaches unity, away from threshold. However, for small molecules there may be sharp fluctuations in the ionization efficiency, in the photon energy region of a resonance. This can be seen in a recent study by Hatano on photoabsorption and the dynamics of the decay of excited states, by measurement of the absolute cross sections of photoabsorption, photoionization and neutral dissociation processes along with absolute photoionization quantum yields for a number of small molecules. [2]

In general the main contributions to photoelectron spectra arise from direct ionization. However the expected photoelectron band envelopes may be affected by contributions from autoionizing resonances. The relative intensities of the contributions to the vibrational structure in a band with contributions from an autoionizing resonance are governed by a product of the Franck-Condon factors from the two separate steps shown in equations 2.1 and 2.2. The FCFs for the production of the Rydberg state are similar to those for the production of the ionic state on which it is built. This is due to the small influence of the Rydberg electron on the electronic structure, as it spends little time in close proximity to its ionic core. The FCFs for the autoionization process depend only on the overlap integral of the vibrational wavefunctions of the Rydberg state and the final ionic state. For the overall process for ionization via a Rydberg state, the relative intensity of each vibrational component, within a photoelectron band, is proportional to the product of the two Franck-Condon factors (see equation 1.8).

In a photoelectron spectrum, recorded at a photon energy near a resonance, the total observed relative intensity of each vibrational component contains contributions from both the direct and indirect processes. These will depend on three terms:

1. The FCF for the direct process from equation 1.6 (F_{dir}):

$$F_{dir} = \left| \int_0^{+\infty} \Psi_{M^+,v^+}(R)\Psi_{M,v''}(R)dR \right|^2 \quad . \quad (2.4)$$

2. The FCF for the indirect process from equation 1.8 (F_{ind}):

$$F_{ind} = \left| \int_0^{+\infty} \Psi_{M^+,v^+}(R)\Psi_{M^*,v'}(R)dR \right|^2 \times \left| \int_0^{+\infty} \Psi_{M^*,v'}(R)\Psi_{M,v''}(R)dR \right|^2 \quad (2.5)$$

3. The term representing the quantum-mechanical interference between the direct pathway and the autoionization route $F_{dir}F_{ind}$.

The relative intensities of each vibrational component now depend on the three terms outlined above, [1]

$$I_{v^+\leftarrow v'',v^+\leftarrow v'\leftarrow v''} \propto F_{dir} + F_{ind}C + F_{dir}F_{ind}C' \quad (2.6)$$

where C and C' are factors depending on the proximity of the pgoton energy to the resonance, *e.g.* well away from a resonance C and C' equal zero.

2.3 Polarization of the radiation source

2.3.1 General

Polarization of radiation is one of its most fundamental properties, along with intensity, wavelength and coherence. The understanding of polarized radiation has its roots in the 17^{th} century, when Erasmus Bartholinus observed double refraction in calspar (1669). Later, around 1690, Huygens furthered the investigation of polarization by extinguishing the polarized light arising from light passing through a calcite crystal, by passing this through a second crystal that was rotated with respect to the first. It was Isaac Newton who explained the phenomena by postulating that the light had "sides", contrary to the popular idea at this time that if light had wave nature then it would be similar to that of sound (*i.e.* longitudinal). The transverse nature of light and its different polarizations can be best explained by the Polarization Ellipse [3]. If light is considered to be a propagating electromagnetic wave composed of perpendicular electric and magnetic vectors as in figure 2.1 [4], then it is the electric component which is of importance, as it strongly interacts with matter. The amplitude of the electric component of a wave, propagating in the z-direction, at any point is given by the

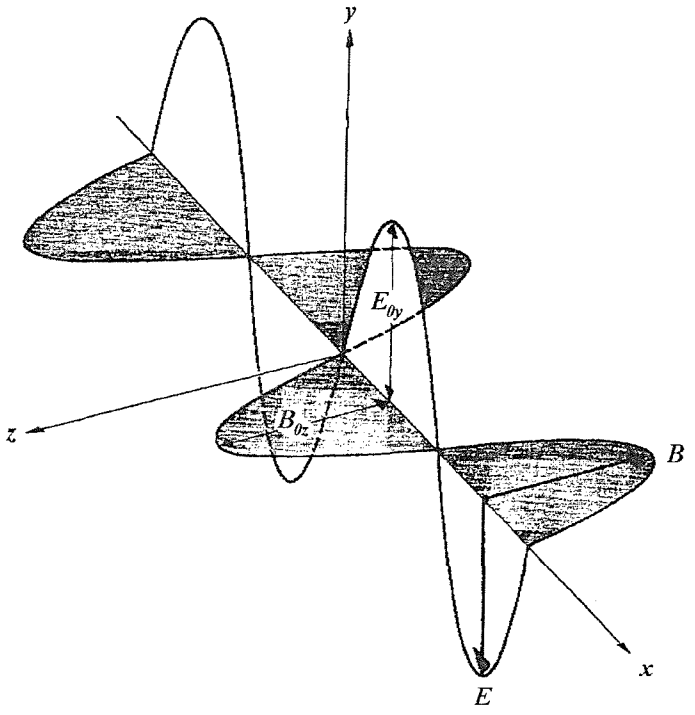

Figure 2.1: Schematic representation of a propagating electromagnetic wave with orthogonal E- and B-fields.

two transverse components (x and y) in the wave equations 2.7 and 2.8,

$$E_x(z,t) = \hat{i}E_{0x}\cos(\tau + \delta_x) \tag{2.7}$$

$$E_y(z,t) = \hat{j}E_{0y}\cos(\tau + \delta_y), \tag{2.8}$$

where the propagator $\tau = \omega t - \kappa z$, $\hat{i}$ and $\hat{j}$ are the unit vectors, E_{0x} and E_{0y} are the respective maximum amplitudes, and δ_x and δ_y are the respective phases. As the wave propagates, the resultant vector of the two components describe a locus of points which form an ellipse, when viewed along the z-axis. In the general case the resultant vector $E(z,t)$ for elliptically polarized light has a constantly changing magnitude and direction as given by the vector sum of the x and y components,

$$E(z,t) = E_x(z,t) + E_y(z,t). \tag{2.9}$$

Two extremes of elliptical polarization may be considered as special cases.

2.3.2 Linear polarization

If the resulting ellipse is completely flat, *i.e.* has no width, and is a "line" then this represents the **linearly polarized** case. This arises when:

1. $E_x(z,t) = 0$, *i.e.* there is no horizontal component, therefore the radiation is vertically polarized.

2. $E_y(z,t) = 0$, *i.e.* there is no vertical component, therefore the radiation is horizontally polarized.

3. $\delta_y = \delta_x$ or the difference is a multiple of 2π, then the two component vectors are in phase, then equation 2.9 becomes

$$E = (\hat{i}E_{0x} + \hat{j}E_{0y})\cos(\tau + \delta) \tag{2.10}$$

and the resultant wave has a constant amplitude and is tilted at a constant angle in the xy-plane.

2.3.3 Circular polarization

If the polarization ellipse is in fact a perfect circle then the radiation is said to be circularly polarized. This can only occur when the two perpendicular components are equal in amplitude (*i.e.* $E_{0x} = E_{0y} = E_0$) and they are out of phase by $\pm\pi/2$ (*i.e.* $\delta_y - \delta_x = -\pi/2 + 2m\pi$, where m is an integer). This implies equations 2.7 and 2.8 may be rewritten as:

$$E_x(z,t) = \hat{i}E_{0x}\cos(\tau) \tag{2.11}$$

$$E_y(z,t) = \hat{j}E_{0y}\sin(\tau), \tag{2.12}$$

Consequently

$$E = E_0[\hat{i}\cos(\tau) + \hat{j}\sin(\tau)] \tag{2.13}$$

The form of equation 2.13 shows that the magnitude of E remains constant, but the direction of the vector in the xy-plane varies continuously as the wave propagates. The locus of points formed is now a circular spiral. It is noted that circular polarization is a chiral property and the radiation may be left- or right-circularly polarized. [4]

2.3.4 Degree of polarization

It is useful to be able to describe polarized radiation using a set of simple parameters. It was discovered by Stokes in 1852 that any possible state of polarization of light could be completely described by four observable quantities. One is required to define the total intensity of the radiation while the other three could be used

to completely describe the nature of the polarization. The Stokes polarization parameters are, [3, 5]

$$S_0 = E_{0x}^2 + E_{0y}^2 \tag{2.14}$$

$$S_1 = E_{0x}^2 - E_{0y}^2 \tag{2.15}$$

$$S_2 = 2E_{0x}E_{0y}\cos\delta \tag{2.16}$$

$$S_3 = 2E_{0x}E_{0y}\sin\delta \tag{2.17}$$

where $\delta = \delta_y - \delta_x$. It should also be noted that:

$$S_0^2 = S_1^2 + S_2^2 + S_3^2. \tag{2.18}$$

Each of the Stokes parameters is a measure of a particular type of polarization, each of which may be measured independently.

- S_0 represents the total intensity of the light.
- S_1 represents the degree of linear polarization. $S_1 = 1$ for horizontal polarization, $S_1 = -1$ for vertical polarization and $S_1 = 0$ for circular polarization.
- S_2 represents the degree of +45 or -45 degree polarization.
- S_3 represents the degree of left or right circular polarization. [3]

In this work, due to the geometry of the experiment, it is the second Stokes parameter that is of significance. The degree of **linear** polarization of the radiation, is used in the calculation of the angular distribution of photoelectrons.

2.4 Angular distribution of photoelectrons

The foundation of the behavior of the angular distribution of photoelectrons was laid in 1948 by Yang who proved the theorem.

> '*If only incoming waves of orbital angular momentum L contribute appreciably to the reaction, the angular distribution of the outgoing particles in the centre-of-mass system is an even polynomial of* $\cos\theta$ *with maximum exponent not higher than* $2L$.' [6]

Yang also considered the relativistic case where odd powers of $\cos\theta$ arise in the polynomial for the angular distribution of the outgoing particle, but their coefficients are negligibly small for systems involving light atoms. For electric dipole

interactions, such as photoionization, $L = 1$ and only terms involving $(\cos\theta)^0$ and $(\cos\theta)^2$ are permitted. Therefore the equation describing the angular distribution of photoelectrons, produced by linearly polarized radiation $I(\theta)$, is of the form,

$$I(\theta) = A + Bcos^2\theta, \tag{2.19}$$

where A and B are constants and θ is measured from the direction of the electric vector. The angular distribution can be characterized by a single parameter β where,

$$\beta = \frac{2B}{3A + B}. \tag{2.20}$$

and β is defined by,

$$I(\theta) \propto P_0 + \beta P_2(cos\theta), \tag{2.21}$$

where $P_{0,2}$ are Legendre polynomials ($P_0 = 1$ and $P_2(cos\theta) = 3/2\cos^2\theta - 1/2$). This means that the photoelectron differential cross section is,

$$\frac{d\sigma}{d\Omega} = \frac{\sigma}{4\pi}\{1 + \beta P_2\cos(\theta)\}, \tag{2.22}$$

where σ is the total cross section. Substituting P_2 and including the degree of linear (horizontal) polarization for elliptically polarized light gives,

$$\frac{d\sigma}{d\Omega} = \frac{\sigma}{4\pi}\{1 + \frac{\beta}{4}[3S_1\cos(2\theta) + 1]\} \tag{2.23}$$

The β parameter may be calculated as described by Cooper and Zare, from equation 2.24, which was derived by Bethe [7,8]. β for dipole photoemission from the nl subshell of a closed shell system is,

$$\beta = \frac{l(l-1)D_{l-1}^2 + (l+1)(l+2)D_{l+1}^2 - 6l(l+1)D_{l+1}D_{l-1}\cos(\delta_{l+1} - \delta_{l-1})}{(2l+1)\left[lD_{l-1}^2 + (l+1)D_{l+1}^2\right]}, \tag{2.24}$$

where δ_l is the respective phase shift of the l^{th} partial wave, and $D_{l\pm1}$ is the dipole radial matrix element,

$$D_{l\pm1} \equiv \int_o^\infty R_{nl}(r) r R_{\epsilon l\pm1}(r) r^2 dr, \tag{2.25}$$

between the radial part of the initial bound orbital, $R_{nl}(r)$, and of the degenerate channels of the outgoing photoelectron, $R_{\epsilon l\pm1}(r)$, with angular momenta $l \pm 1$. [9–11]

It is relatively straightforward to show using equation 2.24 that the β-values for the following atomic ionizations will be as in Table 2.1. [9,11]

The Cooper-Zare formula (equation 2.24) is usually only useful for photoionization from **atomic** orbitals. However it will be seen later that in some cases it

Ionization	β-value
$s \rightarrow p$	2
$p \rightarrow s$	0
$p \rightarrow d$	1
$d \rightarrow p$	0.2
$d \rightarrow f$	0.8

Table 2.1: Beta-values

is valid to approximate a molecular orbital to a single atomic orbital, for analysis in angle-resolved photoelectron spectroscopy .

Bibliography

[1] J. H. D. Eland, *Photoelectron Spectroscopy* (Butterworths, London, UK, 1974).

[2] Y. Hatano, J. Electron Spectosc. Relat. Phenom. **119**, 107 (2001).

[3] E. Collett, *Polarized Light, Fundamentals and Applications* (Marcel Dekker Inc., 270 Madison Avenue, New York, New York, 10016, 1993).

[4] E. Hecht, *Optics, World student series*, 2nd ed. (Addison-Wesley Publishing Company, Inc., US, 1987).

[5] V. Schmidt, *Electron Spectrometry of Atoms using Synchrotron Radiation.* (Cambridge University Press, Cambridge, UK, 1997).

[6] C. N. Yang, Phys. Rev. Lett. **74**, 764 (1948).

[7] J. Cooper and R. N. Zare, J. Chem. Phys. **48**, 942 (1968).

[8] H. A. Bethe, *Handbuch der Physik* (Springer-Verlag, Berlin, 1933), Vol. 24.

[9] J. Berkowitz, *Photoabsoption, Potoionization and Photoelectron Spectroscopy* (Academic Press, New york, US, 1979).

[10] A. DeFanis, Ph.D. thesis, Department of Physics and Astronomy, University of Southampton, 2000.

[11] J. B. West, in *Vacuum ultraviolet photoionization and photodissociation of moleculs ions and clusters*, edited by C. Y. Ng (World Scientific, London, 1991), Chap. 8, p. 369.

Chapter 3

Synchrotron radiation

3.1 Introduction

Synchrotron radiation (SR) is emitted by electrons travelling at high velocity in high energy accelerators, storage rings, or synchrotrons.The radiation is characteristically intense, highly polarized and emitted over a broad continuous ("white") spectrum.

The earliest experimental evidence of synchrotron radiation was seen by Blewett in 1946, at the General Electric Research Laboratory, when he suggested that the energy loss of electrons in a betatron, seen as a contraction of their orbits, was due to emitted SR. Direct observation of SR was not possible due to the betatron being compeletely enclosed, by coating of the "doughnut" and radiation shielding [1]. Later in the same laboratory, a 70MeV Synchrotron was completed that was transparent, and on the 24 April 1974, Floyd Haber first observed visible synchrotron radiation by peering around the radiation shielding with the aid of a mirror [2]. This "intense arc" was quickly established as what is now called **synchrotron radiation** by its high polarization.This observation was correctly explained and published by Elder in the same year. [3, 4]

Since its discovery, initially manifesting itself as a problematic energy loss in accelerators, synchrotrons have established themselves as powerful sources of intense polarized radiation. They advance research as versatile photon sources, providing radiation from the far infrared to hard X-rays for a diverse range of experiments at many facilities worldwide (see table 3.1). [5]

Synchrotron radiation is usually produced in a storage ring that consists of a number of straight sections and bending magnets, to deflect the electrons. Useful radiation is produced at each of the bending magnets and/or from insertion devices placed on the straight sections. For example the SRS at Daresbury laboratories has 16 bending magnets joined by straight sections. All the basic parts

Country	SR Facility / Storage Ring
Asia	
India	INDUS-I, INDUS-II
Japan	NIJI-II, NIJI-IV, TERAS NIJI-III (Product of a Compact Synchrotron Radiation Ring) HiSOR (Japanese Page) Photon Factory (PF), TRISTAN Accumulation Ring (AR) UVSOR Facility (Japanese Page) SPring-8 NewSUBARU Nano-Hana KSR Saga Synchrotron Light Research Center (Japanese page) Rits SR VSX Light Source
Korea	Pohang Light Source (PLS)
P. R. China	Beijing Electron-Positron Collider (BEPC) Shanghai Synchrotron Radiation Facility (SSRF) National Synchrotron Radiation Laboratory (NSRL)
R. of China (Taiwan)	Taiwan Light Source (TLS)
Singapore	Helios II
Thailand	Siam Photon Source (SPS)
Europe	
Denmark	ASTRID, ASTRID-II
France	European Synchrotron Radiation Facility (ESRF) DCI, Super ACO Source Optimisée de Lumiére d'Energie Intermédiaire de LURE (SOLEIL)
Germany	BESSY, BESSY-II DORIS-III, PETRA-II Dortmunder Elektronen Testspeicherring Anlage (DELTA) Ångströmquelle Karlsruhe (ANKA) Electron Stretcher Accelerator (ELSA)
Italy	ELETTRA, European Round Table DAFNE (Phi-Factory)
Russia	Sibir-1, Sibir-2 VEPP-3, VEPP-4M
Spain	LLS Project
Sweden	MAX-I, MAX-II
Switzerland	Swiss Light Source (SLS)
United Kingdom	Synchrotron Radiation Source (SRS), DIAMOND (proposed)
North America	
Canada	Canadian Light Source (CLS)
USA	Advanced Photon Source (APS) Cornell Electron Storage Ring (CESR) Duke FEL (Free Electron Laser) Laboratory (DFELL) Center for Advanced Microstructures and Devices (CAMD) Advanced Light Source (ALS) Synchrotron Ultraviolet Radiation Facility (SURF-II, SURF-III) X-Ray Ring, VUV Ring North Carolina Storage Rings for Technology and Advanced Research (NC-STAR) Stanford Positron Electron Asymmetric Ring (SPEAR), SPEAR3 Aladdin
South America	
Brazil	LNLS synchrotron light source

Table 3.1: Worldwide Synchrotron Facilities (data from Spring8 website: www.spring8.or.jp)

of a synchrotron are shown in the schematic of the National Synchrotron Light Source (NSLS) at Brookhaven, shown in Figure 3.1 [4]. At the NSLS the electrons are initially accelerated in a linear accelerator (linac) up to 50-100MeV, followed by acceleration in a slow cycling synchrotron to 700MeV before being injected into the main storage ring. In the storage ring the cycling electrons are accelerated to 2.5GeV producing intense synchrotron radiation, mainly in the X-ray region.

3.2 Theory

The theory for SR can be traced back to the turn of the 19^{th} century when Lienard [6] and Schott [7–9] showed that an electron in a circular orbit (*i.e.* with acceleration perpendicular to its flight) should be a strong source of radiation. These ideas were developed into an early theory for synchrotron radiation by Ivanenko and Pomeranchuk [10], and a little later by Schwinger [11, 12]. This work was popularized by Blewett who suggested the production of SR was a mechanism for energy loss of electrons in high energy accelerators, as mentioned in section 3.1. The behaviour and properties of synchrotron radiation can be explained by applying classical electrodynamics to the circular orbits of electrons travelling at relativistic velocities [5, 13]. A brief summary is presented here of the most important relationships.

3.2.1 Radiated power

The total power radiated (P) by a relativistic electron can be written as:

$$P = \frac{2}{3}\frac{e^2 c}{R^2}\frac{E^4}{(m_0 c^2)^4}, \tag{3.1}$$

where e is the charge on the electron, R is the radius of the electron orbit, E is the kinetic energy of the electron, and m_0 is its rest mass. The expression is general for any charged particle, but the $1/m_0^4$ term means that for proton accelerators, SR is negligable.

The total power radiated by a number of circulating electrons with total current $I(A)$ can be written as:

$$P_{tot}(kW) = 26.6E^3(GeV) \cdot B(T) \cdot I(A), \tag{3.2}$$

where $B(T)$ is the strength of the magnetic field used to deflect the electrons in Tesla.

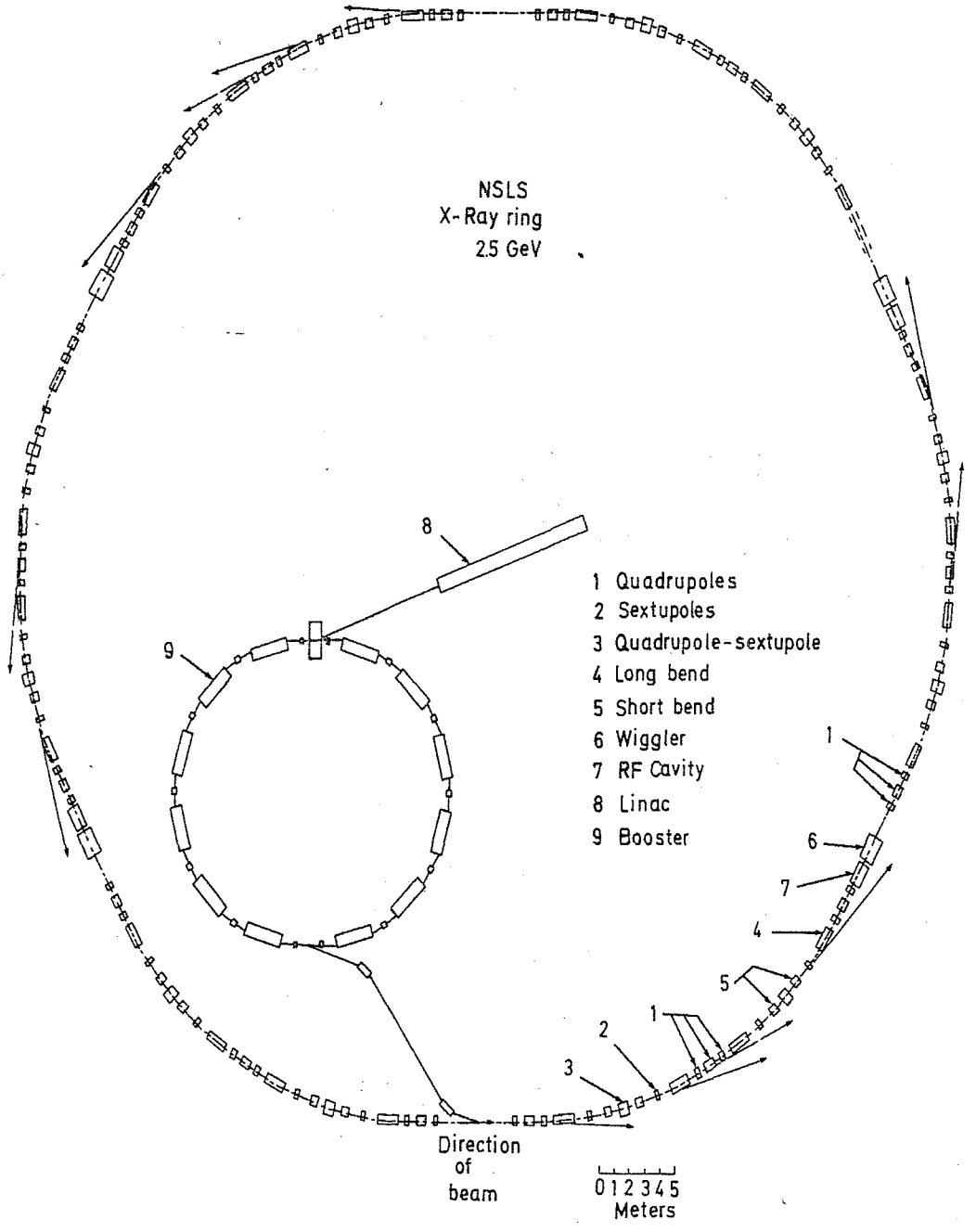

Figure 3.1: Plan view of the Brookhaven storage ring, NSLS, showing the major components. [4]

3.2.2 Wavelength distribution

For the radiation to be useful for spectroscopy, it is not the total power that is important, but its intensity at the particular wavelength of interest. The spectral intensity varies slowly over a broad range, and then drops off exponentially at wavelengths shorter than the critical wavelength (λ_c), where λ_c is given by:

$$\lambda_c(\text{Å}) = 5.58\frac{R(m)}{E^3(GeV)} = \frac{18.64}{B(T)\cdot E^2(GeV)}. \tag{3.3}$$

The distribution of intensity over all wavelengths for a particular critical wavelength (λ_c) is given by:

$$P(\lambda) = \frac{3^{5/2}}{16\pi^2}\frac{e^2c}{R^3}\left(\frac{E}{mc^2}\right)^7\left(\frac{\lambda_c}{\lambda}\right)^3\int_{\lambda_c/\lambda}^{\infty} K_{5/3}(\eta)d\eta, \tag{3.4}$$

where $K_{5/3}(\eta)$ is a modified Bessel function of the second kind. Equation 3.4 shows that the wavelength distribution is a universal function of λ_c/λ and in practice the peak of the intensity of the energy distribution (λ_{max}) is given by:

$$\lambda_{max} \simeq 0.4\lambda_c \tag{3.5}$$

The distribution of intensity may therefore be easily calculated for any synchrotron. Figure 3.2 shows an example distribution curve for the synchrotron ELETTRA (at Trieste, Italy).

3.2.3 Geometry of emission

For a low velocity ($\nu/c \ll 1$) electron in a circular orbit, experiencing radial acceleration, the radiation pattern is toroidal as shown in Figure 3.3. The zero nodes are perpendicular the electron's orbit in the radial direction. This picture becomes greatly distorted for particles travelling at relativistic velocities ($\nu/c \simeq 1$). In a synchrotron, with electrons travelling with near-light velocities, the relativistic effects cause the toroid to be squeezed forward, in the direction of motion of the electron. The zero nodes of the radiation pattern are now swung forward in the orbital plane to an angle $\theta = \sin^{-1}[1-(\nu/c)^2]$ from the direction of motion, as shown in Figure 3.4. [14] This behaviour has the effect of ensuring that virtually all of the intensity of synchrotron radiation produced from a storage ring will be concentrated in the plane of the ring, tangential from the bending magnets. The properties of the spectral and angular distribution of synchrotron radiation were explained by Tomboulian and Hartman in 1956. [14] They expressed quantitively

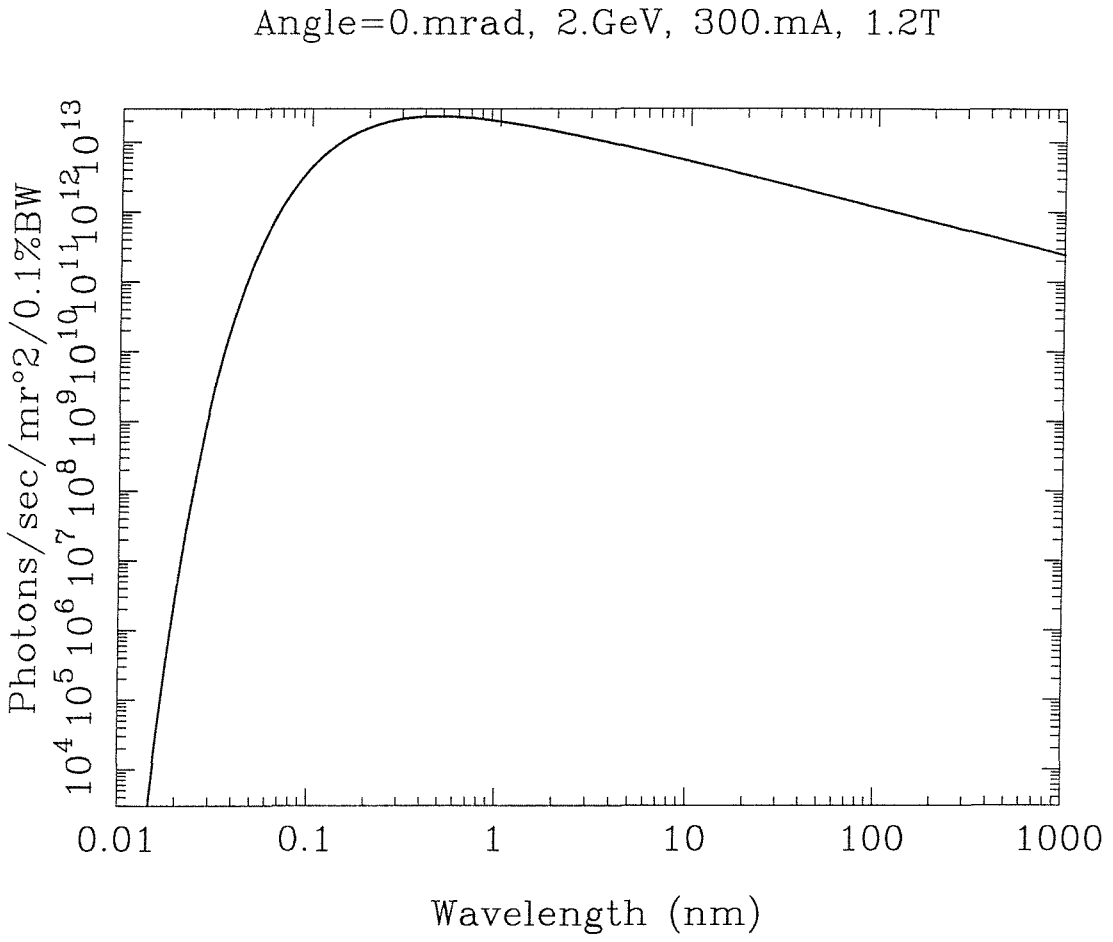

Figure 3.2: Example distribution of intensity of radiation from a bending magnet over a wide spectral range for ELETTRA. Data is courtesy of The Center for X-Ray Optics (CXRO) website at the Lawrence Berkeley National Laboratory (LBNL, www-cxro.lbl.gov).

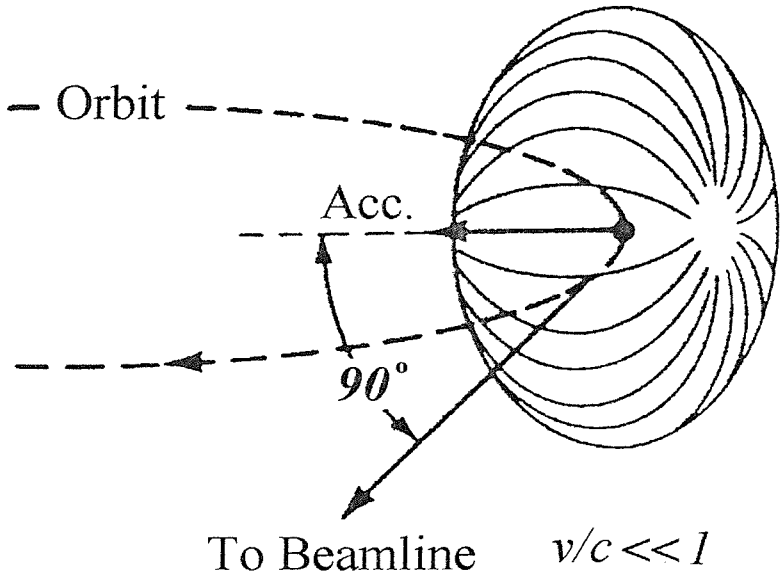

Figure 3.3: The radiation pattern for an electron moving in a circular orbit at low energies. [14]

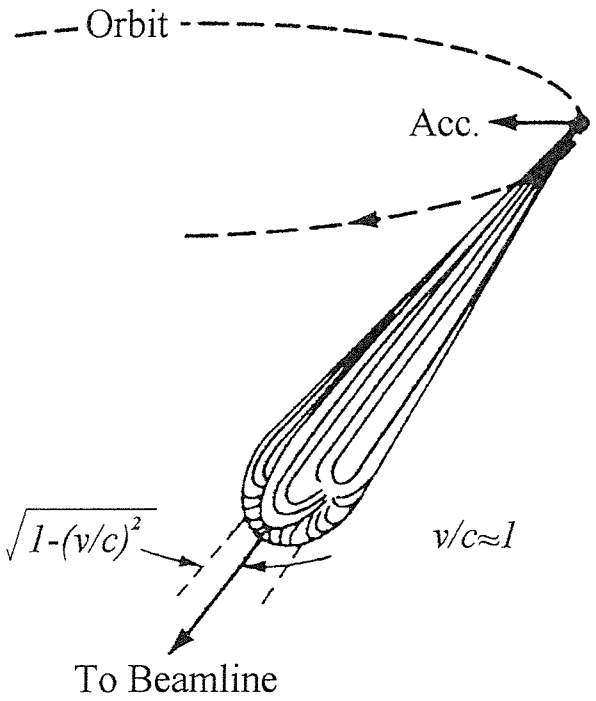

Figure 3.4: The radiation pattern for an electron moving in a circular orbit at relativistic energies. [14]

the angular distibution of the radiated power, per unit angle, per unit wavelength as:

$$P(\psi,\lambda) = \frac{3}{4\pi^2}\frac{e^2}{R}\left(\frac{\lambda_c}{\lambda}\right)^2\left(\frac{2\pi c}{\lambda^2}\right)\left(\frac{E}{m_0c^2}\right)^2\left[1+\left(\frac{E\psi}{m_0c^2}\right)^2\right]^2 \times\left[K^2_{2/3}(\xi)+\frac{(E\psi/m_0c^2)^2}{1+(E\psi/m_0c^2)^2}K^2_{1/3}(\xi)\right], \tag{3.6}$$

where ψ is the angle with respect to the plane of the orbit of an electron. $K_{n/3}(\xi)$ are modified Bessel functions, where:

$$\xi = \frac{\lambda_c}{2\lambda}\left[1+\left(\frac{E\psi}{m_0c^2}\right)^2\right]^{3/2}. \tag{3.7}$$

The practical outcome of these relationships is that for a synchrotron operating in the GeV region, the emission angle is less than 1mrad (0.1mrad at 4Gev) [5, 15].

3.2.4 Polarization of the source

The radiation produced by a synchrotron is highly polarized. If the degree of linear polarization is considered as a function of wavelength and angle of emission from the orbit plane, then the polarization $P(\lambda,\psi)$ may be expressed as:

$$P(\lambda,\psi) = \frac{K^2_{2/3}(\xi)-[(\gamma\psi)^2/(1+(\gamma\psi)^2)]K^2_{1/3}(\xi)}{K^2_{2/3}(\xi)+[(\gamma\psi)^2/(1+(\gamma\psi)^2)]K^2_{1/3}(\xi)}, \tag{3.8}$$

where $\gamma = E/m_0c^2$ (it should be noted that *emission angle* $\approx 1/\gamma$). In fact in the plane of the orbit ($\psi = 0$), equation 3.8 shows that the radiation is completely plane polarized ($P = S_1 = 1$) with the electric vector in the orbit plane. Out of the orbit plane, the radiation becomes elliptically polarized and then circularly polarized within a few mrads [5]. Despite the high degree of polarization at $\psi = 0$, it is often found that after passing through subsequent optical devices, such as mirrors and monochromators, the polarization may be greatly reduced.

3.3 Insertion devices

So far only radiation from bending magnets has been discussed, which is continuous over a large range of wavelengths as expressed by equation 3.4. For most spectroscopic needs, at any moment, only one very narrow bandwidth of the radiation is required. This means that most of the radiated power is wasted. It is far better if the distribution of the output radiation can be confined to a narrow

range of wavelengths in the region of interest. This may be achieved by the use of **insertion devices** such as **wigglers** and **undulators** placed on the straight sections of a storage ring, in between the bending magnets as can be see in Figure 3.1.

3.3.1 Wigglers and undulators

Wigglers and undulators are insertion devices that periodically deflect the electrons away from their normal pseudo-circular orbit and then back again, so that there is no overall displacement. The electrons appears to wiggle, or undulate about their normal path. The radius of curvature of each of the individual oscillations can be much smaller than that of a bending magnet, due to the use of high local magnetic fields, thus shifting the characteristic energy of the radiation to higher energies. Each wiggler may be considered to consist of N periods of length λ_0, so that the overall length L is:

$$L = N\lambda_0. \tag{3.9}$$

The radiation produced at each oscillation can contribute individually or coherently to the useful radiation extracted down a beamline. A characteristic parameter to determine the interaction between the individual oscillations is the deflection parameter K, given by:

$$K = \frac{eB_0\lambda_0}{2\pi m_0 c} = \alpha\gamma \simeq 0.1 B_0\lambda_0, \tag{3.10}$$

where B_0 is the peak field in Tesla, λ_0 is in mm and α is the maximum deflection angle of the electrons' path.

- If $K \gg 1$ then the radiation from each wiggle contribute separately and the device is a **wiggler**.
- If $K \leq 1$ then the radiation from each undulation contribute coherently and the device is an **undulator**.

In a wiggler the additive nature of the incoherent radiation for each wiggle means that the photon intensity varies with N. In a undulator the radiation from the same electron emitted at each subsequent undulation will interfere coherently and the photon intensity will vary as the number of undulations squared (N^2). However the electromagnetic waves from different electrons will be incoherent and the photon intensity will remain proportional to the ring current. For useful constructive interference at a particular wavelength proper temporal and spatial

alignment of the electron with the undulator is required. By comparing the path and time differences for an electron traversing between two undulations and the photons emitted at an angle θ from the unperturbed path, it is possible to derive an expression for the observed harmonics:

$$\lambda_n = \frac{\lambda_0}{2n\gamma^2}\left(1 + \frac{K^2}{2} + \gamma^2\theta^2\right), \tag{3.11}$$

where λ_n is the wavelength of the n^{th} harmonic. [5] The position of harmonics can be easily shifted by altering the strength of the magnetic fields within the undulator. In the case where permanent magnets are used, this is achieved by physically altering the distance between the magnets. If static electromagnets are used then the working current can simply be altered to achieve the same effect. The resultant wavelength selection and control over the harmonics means that high fluxes of radiation may be produced in the region where it is needed. The radiation from an undulator also has better collimation and polarization than that extracted from a normal bending magnet. Radiation from an undulator can therefore be of very high **brilliance**, where **brilliance** (or **brightness**, a good measure of the effective use of a source) is given by: [5, 16]

$$Brilliance = \frac{spectral\ flux\ into\ 0.1\%\ \Delta\epsilon/\epsilon\ per\ 100mA\ ring\ current[phot\ s^{-1}]}{source area \times solid\ angle[mm^2 mrad^2]} \tag{3.12}$$

The brilliance of radiation from an undulator can easily be three orders of magnitude greater than that produced by a bending magnet.

Undulators may also possess two perpendicular sets of magnets capable of deflecting the electron beam both in the horizontal, plane of orbit, and the perpendicular, vertical direction. These two sets of poles working together can force the electrons to trace a helical path. This will result in the production of elliptically polarized radiation (circularly polarized if the horizontal and vertical deflections are equal).

In summary, the flexibility an undulator can provide for polarization combined with the massive gains in brilliance makes it the best choice for many applications.

Further information on synchrotron radiation and extra details on wigglers may be found in books by Koch [5], Kunz [4] and Schmidt [15] and in several review papers by Farge [17] and Winick [18–20].

In this work the use of synchrotron radiation was imperative, as high polarization was required to successfully complete angular distribution studies, and high brilliance was essential, due to the weak signals observed for radicals, which could only be produced at low partial pressures.

Bibliography

[1] J. P. Blewett, Phys. Rev. **69**, 87 (1946).

[2] G. C. Baldwin, Physics Today **28**, 9 (1975).

[3] F. R. Elder, A. M. Gurewitsch, R. V. Langmuir, and H. C. Pollock, Phys. Rev **71**, 829 (1947).

[4] C. Kunz, *Synchrotron Radiation, Techniques and Applications*, Vol. 10 of *Topics in Current Physics* (Springer-Verlag, Berlin, Heidelberg, New York, 1979).

[5] E. E. Koch, *Handbook on Synchrotron Radiation* (North Holland Publishing Company, Nederlands, 1983), Vol. 1A.

[6] A. Lienard, L'Eclairage Electr. **16**, 5 (1898).

[7] G. A. Schott, Annalen der Physik **24**, 641 (1907).

[8] G. A. Schott, Phil. Mag. **13**, 189 (1907).

[9] G. A. Schott, *Electromagnetic Radiation* (Cambridge University Press, Cambridge, UK, 1912).

[10] D. D. Ivanenko and I. Pommeranchuk, Phy. Rev. **65**, 343 (1944).

[11] J. Schwinger, Phys. Rev. **70**, 798 (1946).

[12] J. Schwinger, Phys. Rev. **75**, 1912 (1949).

[13] J. D. Jackson, *Classical Electrodynamics*, 2nd ed. (Wiley, New York, 1975).

[14] D. H. Tomboulian and P. L. Hartman, Phys. Rev. **102**, 1423 (1956).

[15] V. Schmidt, *Electron Spectrometry of Atoms using Synchrotron Radiation.* (Cambridge University Press, Cambridge, UK, 1997).

[16] A. DeFanis, Ph.D. thesis, Department of Physics and Astronomy, University of Southampton, 2000.

[17] Y. Farge, Appl. Opt. **19**, 4021 (1980).

[18] H. Winick, G. Brown, K. Halbach, and J. Harris, Journal of the Optical Society of America **71**, 1579 (1981).

[19] H. Winick, G. Brown, K. Halbach, and J. Harris, Physics Today **34**, 50 (1981).

[20] G. Brown, K. Halbach, J. Harris, and H. Winick, Nuclear Instruments & Methods in Physics Research **208**, 65 (1983).

Chapter 4

Theoretical methods used in photoelectron spectroscopy

4.1 Introduction

Molecular photoelectron spectroscopy (PES) yields information on ionization energies, relative photoionization cross-sections, geometry changes on ionization and ionic state vibrational constants. If a molecular system can be accurately modelled, then a clearer understanding of its electronic structure is often gained. Molecular electronic structure calculations can be used to establish spectral assignments and, more importantly, can be used in a predictive way to compute the electronic structure of reactive molecules not previously studied by PES.

4.2 Koopmans' theorem [1]

Koopmans' theorem states that for a closed shell molecule the vertical ionization energy (I_j^K) for ionization from an occupied molecular orbital is equal to the negative of the orbital energy (ϵ_j) where the orbital energy is obtained from an *ab initio* calculation at the Hartree-Fock limit. This theorem can be written as in equation 4.1. [2]

$$I_j^K = -\epsilon_j \tag{4.1}$$

This is an approximation, but is useful as it means that a photoelectron spectrum will be a direct observation of occupied molecular orbitals in a closed-shell molecule. However Koopmans' theorem neglects any reorganization of the electrons on ionization and also any change in electron correlation between the molecule and the ion. This may lead to errors in assignment and the ordering of ionic states. A Koopmans' theorem VIE (I_j^K) may be related to the true VIE

(I_j) as shown in equation 4.2.

$$I_j = I_j^K - R + C, \tag{4.2}$$

where R is a reorganization energy term and C is a correlation energy correction term (both of which are usually positive). In many cases Koopmans' theorem performs well as R and C tend to largely cancel each other out, but generally $R > C$ leading to I_j^K values being slightly too large.

A better approach is to compute the vertical ionization energy as the **difference** in total energy between the initial neutral molecule and the final ionic state, as in equation 4.3:

$$I_e = E(M^+) - E(M) \tag{4.3}$$

This approach, known as the ΔSCF method, incorporates the electron reorganization on ionization, but still neglects any change in electron correlation on ionization. To compare ΔSCF vertical ionization energies with those from experiment, it is necessary to calculate the total energy of the initial state (usually the ground state) and then subtract this from the total energy of the resultant ion. The main problem is how to calculate the required molecular and ionic wavefunctions and the molecular orbital and total energies. These major points are covered in the rest of this chapter, starting from the basis functions used to build the atomic and molecular orbitals.

4.3 Basis sets [3]

In molecular orbital theory each molecular orbital ϕ_i may be expressed as a linear combination of "atomic" orbitals (or basis functions) χ_p as shown in equation 4.4. [2, 4]

$$\phi_i = \sum_p c_{ip}\chi_p \tag{4.4}$$

In practice, the functions χ_p are chosen at the start of a calculation, but the coefficients c_{ip} are varied to minimize the total energy of the system. The choice of the basis functions is of critical importance in a molecular orbital calculation, as it ultimately limits the accuracy and the time taken to perform the calculation. An obvious choice for the basis functions is to use atomic orbitals of known form for the χ_p. The solutions of the Schrödinger equation for hydrogen-like atoms yields the orbitals:

$$\chi_{nlm_l}(r, \theta, \phi) = R_{nl}(r)Y_{lm_l}(\theta, \phi), \tag{4.5}$$

where n, m and m_l are quantum numbers, R_{nl} is the radial part and $Y_{lm_l}(\theta, \phi)$ is the angular part of the wavefunction. The angular part is simply a spherical harmonic and the radial part is:

$$R_{nl}(r) = -\left(\frac{2Z}{na}\right)\left\{\frac{(n-l-1)!}{2n[(n+l)!]^3}\right\}\rho^l L_{n+l}^{2l+2}(\rho)e^{-\rho/2}, \tag{4.6}$$

where $\rho = (2Z/na)r$, $a = 4\pi\varepsilon_0\hbar^2/\mu e^2$, the reduced mass $\mu \simeq m_e$, $a \simeq a_0$ (the Bohr radius), and L are the associated Laguerre functions. [2, 4]

These atomic orbitals can be approximated by using **Slater type orbitals** (STOs) with the form of equation 4.7. [4]

$$\chi_{nlm_l}^{STO}(r, \theta, \phi) = Nr^{n^*-1}e^{-\zeta r}Y_{lm_l}(\theta, \phi), \tag{4.7}$$

where N is a normalization constant, $\zeta = Z^*/a_0 n^*$, n^* is the effective principal quantum number, and Z^* is the effective atomic number, taking into account shielding effects. In a molecular orbital calculation using a minimal basis set, each formally occupied atomic orbital is represented by just **one** STO *i.e.* one exponent zeta (ζ). If two different STOs are used to approximate each formally occupied atomic orbital, a Double-Zeta (DZ) basis set, then the accuracy of the calculation is improved due to the larger basis set better approximating the real orbitals. This may be extended further to Triple-Zeta (TZ) and Quadruple-Zeta (QZ). It is also common to add so-called polarization (P) functions that are formally unoccupied diffuse orbitals that allow for mobility of charge around a molecule. If polarization functions are used then the basis set label will have a P added. For example, a DZ+P (or DZP) basis set for a carbon atom ($1s^2 2s^2 2p^2$) would consist of two ζ-functions for each occupied s-orbital, six ζ-functions for the three p-orbitals and five ζ-functions representing the formally empty 3d-orbitals for the polarization [4]. This type of basis set was used for the DFT calculations described in Chapter 9.

Slater type functions are physically realistic, good representations of exact atomic wavefunctions. However they are not ideal for many molecular orbital calculations as the two electron integrals which are needed in the calculation, cannot be evaluated analytically. Numerical integration is time consuming and is not practicable for high level calculations. To circumvent this problem Gaussian type functions are often used as an alternative to STOs. The general form of a GTO is given in equation 4.8. [4]

$$\chi_{nlm_l}^{GTO}(r, \theta, \phi) = N'p(\alpha)e^{-\alpha r^2}Y_{lm_l}(\theta, \phi), \tag{4.8}$$

where N' is a normalization constant, $p(\alpha)$ is a polynomial in α, and α is the **Gaussian orbital exponent**. The key difference between STOs and GTOs is

the exponential term. STOs contain the exponential $e^{-\zeta r^2}$, rather than the $e^{-\alpha r}$ of the Gaussian type functions. This means that in an MO calculation using GTOs, the evaluation of the two electron integrals can be achieved analytically and therefore quickly. However, Gaussian type functions do not reproduce the true form of atomic orbitals as closely as STOs. This is overcome by using more Gaussian-type functions in the place of each STO. Initially a large number of individual GTOs were used in molecular orbital calculations, but this approach was superseded by **contraction** of Gaussian type functions [3]. Using this approach each basis function is represented by a linear combination of a set of Gaussian type functions to accurately approximate atomic-like orbitals, as shown in equation 4.9.

$$\chi_{nlm_l}^{CGTO}(r,\theta,\phi) = N'' \left[\sum_{i=1}^{L} d_i p_i(\alpha_i) e^{-\alpha_i r^2} \right] \times Y_{lm_l}(\theta,\phi), \tag{4.9}$$

where L is the number of GTOs used in each contracted Gaussian type orbital (CGTO) and d_i are the contraction coefficients. The contraction coefficients are fixed throughout a molecular orbital calculation and define the form of the CGTO in the basis set. [4]

It is common to use contracted Gaussian type functions that are fitted to Slater type functions. In this case the functions will approximate the true electronic wavefunctions, yet have integrals that can be easily evaluated analytically. This type of function dominates the *ab initio* field and are used as building blocks for many extensively used basis sets [3, 4]. Basis sets based on GTOs were used in *ab initio* calculations in this work (see Chapters 10 and 11).

In summary there are a number of different contraction schemes whose composition and nomenclature are given below.

4.3.1 STO-nG basis set

This is one of the simplest and computationally inexpensive minimal basis sets. In this case each formally occupied atomic orbital is represented by a single Slater type orbital that has been approximated by n primitive gausssians in a contracted guassian type orbital (as described in section 4.3).

4.3.2 Split valence basis set

The split valence basis sets are designed to give greater accuracy than that of the minimal basis sets by improving the accuracy and flexibility of the orbitals most involved in chemical bonding. In a split valence basis set, the inner shells are usually single-zeta (one basis function per atomic orbital), while the more

influential valence orbitals are double- or triple-zeta or better. The term **split valence** derives from the difference in number of functions used to represent the core and valence orbitals. The split valence basis sets are designated as shown below. The digit (or digits) preceding the dash(-) correspond to the the inner

$$\underset{\text{inner}}{3} - \underset{\text{valence}}{21} \quad \underset{\text{Gaussian}}{G}$$

orbitals and those succeeding the dash(-) correspond to the valence region. The simplest split valence basis set is given in the above example as 3-21G. The initial 3 means that the inner shell functions are single-zeta, consisting of one function made from three primitive Guassians. The **number** of digits following the dash determines whether the valence orbitals are double-zeta (2 digits), triple-zeta (3 digits), quadruple (4 digits) etc. In the case of 3-21G, the first of the double-zeta valence functions is a contraction of two primitive Gaussians whereas the second consists of only a single Gaussian function. To clarify the designation table 4.1 outlines the basis functions used for the 6-311G split valence basis set for a nitrogen atom.

4.3.3 Polarization and diffuse fuctions

A basis set may be improved by adding more and more exponential ($e^{-\zeta r}$) functions, to obtain triple-, quadruple- and quintuple-zeta functions. This requires more and more computational resources and leads to ill-balanced basis sets. Instead it is often desirable to add functions corresponding to orbitals that are not formally occupied. These extra functions fall into two broad categoies:

1. **Polarization Functions.** Functions of higher angular momentum (greater l) than the highest occupied orbital. These functions increase the flexibility

Atomic orbital	-Zeta	No. of primitive Guassian functions	Orbital type
1s	single	6	inner
2s	triple	3	valence
2s'	triple	1	valence
2s"	triple	1	valence
$2p_x$,$2p_y$,$2p_z$	triple	3	valence
$2p'_x$,$2p'_y$,$2p'_z$	triple	1	valence
$2p''_x$,$2p''_y$,$2p''_z$	triple	1	valence

Table 4.1: 6-311G Basis set for a nitrogen atom. [5]

Atom	cc-pVDZ	cc-pVTZ	cc-pVQZ	cc-pV5Z
H	2s, 1p	3s, 2p, 1d	4s, 3p, 2d, 1f	5s, 4p, 3d, 2f, 1g
1st row	3s, 2p, 1d	4s, 3p, 2d, 1f	5s, 4p, 3d, 2f, 1g	6s, 5p, 4d, 3f, 2g, 1h
2nd row	4s, 3p, 1d	5s, 4p, 2d, 1f	6s, 5p, 3d, 2f, 1g	7s, 6p, 4d, 3f, 2g, 1h

Table 4.2: Dunning's correlation consistent basis sets for the first three rows of the periodic table. [6–10]

of the orbitals and allow the electron density of a molecule to be distorted. Addition of polarization functions means therefore that a molecule will become more polarizable. The simplest example is the hydrogen atom. If only a 1s function is used in the basis set, the electron density distribution within the atom can only be spherically symmetric; however the addition of p, d, or f-type functions will allow some distortion of the orbitals. Polarization functions are usually indicated by asterisks (*) placed at the end of the basis set. A single asterisk (*) denotes that a single set of d-type functions have been added to the heavy atoms and a double asterisk (**) denotes that one set of p-type functions has in addition been added to all the hydrogens. Polarizaton functions may also be explictly described by a list of the functions used in parentheses following the basis set, *e.g.* 6-31G(2d,2p).

Polarization functions are so commonly used to achieve chemical accuracy that they are an integral part of modern basis sets. The correlation-consistent (cc) basis sets of Dunning [6–10], contain polarization functions. These basis sets are the polarized-Valence Double-Zeta (cc-pVDT) or Triple/Quadruple/Quintuple-zeta (cc-pVT/Q/5Z) type. These types of basis sets are used in both the studies of F_2O and the azide pyrolysis studies. For clarification, the types of function used or each basis set are given in table 4.2

2. **Diffuse Functions.** Diffuse functions are functions of low angular momentum, but have exponents such that they can extend far from the nuclear centre *i.e.* they are diffuse. Diffuse functions are good at modelling systems with weak interactions. The addition of diffuse functions to a basis set is denoted by a plus sign (+). A single-plus (+) is used if diffuse functions are only added to heavy atoms, and a double-plus (++) is used if diffuse functions are applied to all atoms in a system. If correlation-consistent basis sets are used then the prefix *aug* is alternatively used to denote the addition of diffuse functions to the basis set.

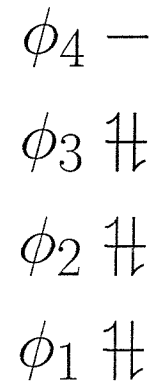

Figure 4.1: Schematic of molecular orbitals used in the Hartree-Fock method.

It should be noted that the final choice of basis set depends on many factors including the size of the system, the types of atoms, symmetry, cumpuational resources available and what information is required for a molecule. As a result, often several basis sets may be applied to the same system and their results compared.

4.4 The Hartree-Fock SCF method

In the Hartree-Fock method, for a closed shell system the electrons are assigned in pairs to a set of molecular orbitals as in Figure 4.1, and can be represented by the single determinantal wavefunction ($\triangle_n$)in equation 4.10:

$$\triangle_n = (\phi_1\bar{\phi}_1\phi_2\bar{\phi}_2 \ldots \phi_{n/2}\bar{\phi}_{n/2}), \tag{4.10}$$

where n is the number of electrons, ϕ_i represents an α-spin electron in orbital ϕ_i, whereas a bar above ϕ_i, $\bar{\phi}_i$, denotes a β-spin electron in orbital ϕ_i. [2, 4, 11]

Each molecular orbital is expressed in terms of the basis set as described in section 4.3, giving a great deal of flexibility. In order to find the best single determinantal wavefunction for the molecule, the Variation Principle is applied and the total energy of the system is minimized by optimizing the parameters (c_{ip}) in equation 4.4. The total energy of the system (E_n) is given by equation 4.11. [2]

$$E_n = 2\sum_r I_r + \sum_r \sum_s (2J_{rs} - K_{rs}), \tag{4.11}$$

where the first sum represents the sum of the one-electron energies I_r and the double sum represents the two electron integrals summed over the occupied orbitals. J_{rs} are the **coulomb integrals** and K_{rs} are the **exchange integrals** for

interactions between electrons in orbitals r and s as shown in equations 4.12 and 4.13. [2, 12, 13]

$$J_{rs} = \int\int \phi_r^*(1)\phi_s^*(2)\frac{1}{r_{12}}\phi_r(1)\phi_s(2)dv(1)dv(2) \tag{4.12}$$

$$K_{rs} = \int\int \phi_r^*(1)\phi_s^*(1)\frac{1}{r_{12}}\phi_r(2)\phi_s(2)dv(1)dv(2) \tag{4.13}$$

The minimization of the total energy is achieved using an iterative procedure whose basic steps are outlined below.

- Firstly a suitable basis set for the molecule must be chosen and I_{pq} and $(pq|rs)$ integrals are evaluated where:

$$I_{pq} = \int \chi_p^*(1)H_N(1)\chi_q(1)dv(1) \tag{4.14}$$

$$(pq|rs) = \int\int \chi_p^*(1)\chi_r^*(2)\frac{1}{r_{12}}\chi_q(1)\chi_s(2)dv(1)dv(2) \tag{4.15}$$

  These integrals are used later.

- Then an initial estimate is made of the coefficients c_{ip} for each molecular orbital in the LCAO approach.

- The **Fock** (F_{pq}) and **overlap** (S_{pq}) matrices are then computed, where:

$$F_{pq} = \int \chi_p^* F \chi_q dv \tag{4.16}$$

$$S_{pq} = \int \chi_p^* \chi_q dv \tag{4.17}$$

- The **Fock** (F_{pq}) and **overlap** (S_{pq}) matrices are then used to solve equation 4.18 to yield a set of energies ε_i:

$$|F_{pq} - S_{pq}\varepsilon_i| = 0 \tag{4.18}$$

- A new set of coefficients are then calculated from the secular equations shown in equation 4.19.

$$\sum_p c_{ip}(F_{pq} - S_{pq}\varepsilon_i) = 0 \tag{4.19}$$

- The new coefficients are then used in the first step of the iterative procedure. The iteration continues until some predetermined threshold is reached, which is defined as a minimum change in the overall total energy of the system (E_n) for one cycle.

This method, the Roothaan-Hartree-Fock method, is useful but not perfect, as it cannot generate the exact solution to the Schrödinger equation. Errors arise due to the use of a finite basis set and an incorrect correlation of the electronic motion within the system. The correlation error, in the Hartree-Fock method, arises from the initial determinantial wavefunction being represented as a product of one-electron orbitals. Therefore, electron-electron interaction is treated by allowing each electron to only have an interaction with a time-averaged charge of the other electrons. For an exact solution, instantaneous interactions between all the electrons would have to be evaluated.

The correlation energy is usually defined as the difference in energy between that calculated from the HF-SCF method and that of an exact non-relativistic solution of the Schrödinger equation.

The examples in this section are restricted to closed shell molecules. However these methods may be extended to cover open shell molecules [14]. The secular equations and total energy expressions are more complex, but the overall approach remains the same. Greater details can be found in publications by Parr, Szabo, Roothaan and McWeeny. [4, 11–14]

4.5 Density functional theory (DFT)

An alternative approach to describing the electronic structure of molecules is density functional theory (DFT). DFT differs from the *ab initio* approach in that the theory is based on the electron density distribution $\rho(r)$ rather than the many electron wavefunction $\Psi(1, 2, 3, \ldots)$ [15]. The electron density distribution depends on the probability of finding an electron in a given volume of space as shown in equation 4.20.

$$\rho(r) = n \int_{-\infty}^{\infty} \int_{-\infty}^{\infty} \ldots \int_{-\infty}^{\infty} \Psi^*(1, 2, \ldots, n)\Psi(1, 2, \ldots, n) dr_1 dr_2 \ldots dr_n, \qquad (4.20)$$

where n is the number of electrons in the system.

DFT has quickly established itself as an attractive alternative to Hartree-Fock theory for systems other than simple small molecules as it scales more favorably with system size. In this thesis DFT was applied to heavy metal compounds with many electrons that would be too time consuming to treat with meaningful accuracy using the more traditional *ab initio* methods.

DFT is based on the Hohenberg-Kohn theorems presented in the 1964 paper, "Inhomogeneous Electron Gas" by these authors [16]. These were built on by Kohn and Sham to generate density functional methods [15, 17].

The first Hohenberg-Kohn theorem states that the specification of the ground state electron density, ρ, determines the external potential, V_{ext} uniquely, to within an additive constant. ρ also determines the number of electrons, N, in an N-electron system by integration and therefore it determines the full Hamiltonian H and all properties determined by H [15]. It follows that the ground state energy may be derived as a functional of the ground state density, ρ, as in equation 4.21 [16]. The second Hohenberg-Kohn theorem applies a variational principle to the total energy with respect to the density and states that $E[\rho]$ is at a minimum and equivalent to the true energy of the ground state of the system if ρ is the true ground state density, [16, 18], where $E[\rho]$ is:-

$$E[\rho] = F[\rho] + \int \rho V_{ext} dr, \tag{4.21}$$

where $F[\rho]$ is an inter-electronic functional of ρ that can be separated into its main contributions. These contributions are a kinetic energy term, $T[\rho]$, and an electron-electron interaction term, E_{ee} as shown in equation 4.22.

$$E[\rho] = T[\rho] + E_{ee}[\rho] + \int \rho V_{ext} dr \tag{4.22}$$

In the Kohn-Sham approach, employed in DFT calculations, the kinetic energy term is replaced by the kinetic energy of a system of **non-interacting** particles and the interaction term, E_{ee}, is separated into a familiar electrostatic (Coulomb)interaction, $E_{Coul}[\rho]$, and the exchange and correlation energy, $E_{XC}[\rho]$, as shown in equation 4.23.

$$E[\rho] = T_s[\rho] + E_{Coul}[\rho] + E_{XC}[\rho] + \int \rho V_{ext} dr, \tag{4.23}$$

where $E_{XC}[\rho]$ is formally defined to maintain the equivalence of equations 4.22 and 4.23, such that:

$$E_{XC}[\rho] = T[\rho] - T_s[\rho] + E_{ee}[\rho] - E_{Coul}[\rho] \tag{4.24}$$

To obtain secular equations, equation 4.23 is minimized with respect to the density ρ that is found from the solutions of the Euler-Lagrange equations associated with the stationarity of $E[\rho]$, as shown in equation 4.25.

$$\begin{aligned} \mu &= \frac{\partial T_s[\rho]}{\partial \rho} + \frac{\partial E_{Coul}[\rho]}{\partial \rho} + \frac{\partial E_X C[\rho]}{\partial \rho} + V_{ext} \\ &= \frac{\partial T_s[\rho]}{\partial \rho} + V_{Coul} + V_{XC} + V_{ext} \end{aligned} \tag{4.25}$$

Equation 4.25 is the same as that for a system of non-interacting electrons being subjected to an external potential, V_{eff}, given by equation 4.26.

$$V_{eff}[\rho] = V_{Coul} + V_{XC} + V_{ext} \tag{4.26}$$

The ground state density required can be found by solving a new set of self-consistent equations as shown in equations 4.27 and 4.28.

$$\left[-\frac{1}{2}\nabla^2 + V_{eff}\right]\phi_i = \epsilon_i\phi_i \tag{4.27}$$

$$\rho = \sum_i^N |\phi_i|^2 \tag{4.28}$$

Equations 4.26, 4.27 and 4.28 represent one form of a set of Kohn-Sham equations. In these equations ϕ_i are the Kohn-Sham orbitals. If these are solved self-consistently, then the exact ground state density, and the exact solution to the Schrödinger equation will be obtained. It should be noted that up to this point **no** approximations have been made. However the form of $E_{XC}[\rho]$ is not known and approximations must now be made. Finding a suitable form for the remaining unknown functional $E_{XC}[\rho]$ is at the heart of DFT.

The simplest and very useful approximation for the form of the unknown exchange-correlational functional is the local density approximation (LDA) where the exchange-correlational functional is defined by equation 4.29.

$$E_{XC}^{LDA}[\rho] \equiv \int \rho(r)\epsilon_{XC}(\rho(r))dr, \tag{4.29}$$

where $\epsilon_{XC}(\rho)$ is the exchange-correlation energy for a uniform interacting electron gas which is known with a high degree of accuracy. The functional $\epsilon_{XC}(\rho)$ is usually expressed as the sum of an exchange term , $\epsilon_X(\rho)$, and a correlation term, $\epsilon_C(\rho)$, (hence the name exchange-correlation functional) as shown in equation 4.30.

$$\epsilon_{XC}(\rho) = \epsilon_X(\rho) + \epsilon_C(\rho) \tag{4.30}$$

Early methods used pure exchange formulae, without a correlation part. The most popular being the X-alpha (X_α) method where [5],

$$E_X^{LDA}[\rho] = -\frac{3}{2}\left(\frac{3}{4\pi}\right)^{1/2}\int \rho^{4/3}(r)dr. \tag{4.31}$$

These were followed by methods that incorporated allowance for correlation effects, such as that of Vosko, Wilk and Nusair (VWN) [19].

The next level of improvement to the approximation of the exchange-correlation functional is the generalized gradient approximation (GGA) [20] which better represents the gradients of the electron density in molecular systems. The GGA exchange-correlation energy term is shown in equation 4.32.

$$E_{XC}^{GGA}[\rho] = \int f\left(\rho(r), |\nabla\rho(r)|\right) dr, \tag{4.32}$$

where $f\left(\rho, |\nabla\rho|\right)$ is a suitable chosen function of its two variables. One of the most popular gradient corrected formulae for the exchange part is that of Becke developed in 1988, denoted B88, as shown in equation 4.33:

$$E_X^{B88}[\rho] = E_X^{LDA}[\rho] - b \int \frac{\rho^{4/3}(r)x^2}{1 + 6b\sinh^{-1}x} dr, \tag{4.33}$$

where b=0.0042 a.u. and x incorporates the gradient of the electron density as shown in equation 4.34,

$$x = \rho^{-4/3}|\nabla\rho|. \tag{4.34}$$

This could be combined with a correlation correction such as that of Lee, Yang and Parr (LYP) [21–23] or Perdew and Wang (PW91) [24]. It is common to define the DFT method used in a calculation by combining the acronyms of the exchange and correlation functionals used. In this work, for the actinide tetrahalides studied (see Chapter 9), the **B**ecke gradient correction [25] was applied to the exchange part and the **L**ee-**Y**ang-**P**arr [21–23] correlation correction was used. This method is simply described as **BLYP**. Other suitable forms of the GGA functionals are described with some illustrative applications, by Kohn, Becke, and Parr [15].

Once a suitable method has been used to perform a density functional calculation, for a chosen molecule, then for the information to be useful, calculated values must be compared with measured quantities from experiment. This, for example, may be structural data, vibrational frequencies, electronic transitions, ionization energies or heats of formation.

4.6 Calculation of ionization energies

In the field of molecular photoelectron spectroscopy , the calculation of **ionization energies** is of prime importance as this is the quantity actually measured by experiment. The simplest and most approximate method is to use the negative of the orbital energies as in Koopmans' theorem, mentioned in section 4.2. Koopmans' theorem is usually inadequate for Hartree-Fock calculations and is not

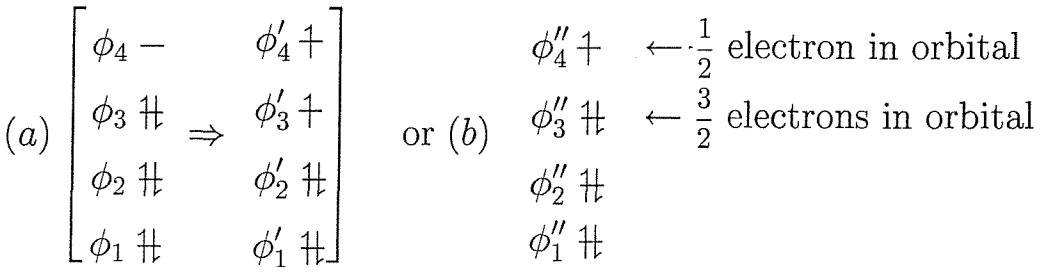

Figure 4.2: Schematic example of molecular orbitals used in (a)a ΔSCF calculation and (b) the transition state method.

theoretically justified for DFT calculations. Better alternatives are to use the **ΔSCF** method, which can be performed via Hartree-Fock or DFT calculations, or the **transition state** method which is unique to DFT.

In the ΔSCF method two separate Hartree-Fock or DFT calculations must be undertaken. The total energy for both the initial neutral state and the final ionic state must be calculated and their difference is taken to be the ionization energy as previously shown in equation 4.3. The calculation therefore includes orbital relaxation effects (R), but does not incorporate changes in the correlation energy (C) on ionization.

Due to the formulation of DFT, there is a more efficient way of obtaining vertical ionization energies from a **single** calculation, that uses the **transition state method** [26,27]. This method may be used to calculate excitation energies, electron affinities and ionization energies.

In general, the transition state method states that the energy of a transition, for example an excitation, can be calculated from the difference in the energies of the molecular orbitals calculated for a 'transition state' in which half an electron is in the initial orbital and half is in the final orbital. This is demonstrated in the example shown in Figure 4.2. For a ΔSCF calculation both the total energies of the initial ground state and the final excited state are calculated and the excitation energy is taken to be the difference between their total energies. An accurate approximation to this value is found by simply taking the difference in energy between the two fractionally occupied orbitals ϕ''_3 and ϕ''_4 obtained from a single converged DFT calculation.

A further simplification occurs if ionization is considered, as this is energetically equivalent to an electron being excited to an orbital of energy equal to zero. Therefore, if a converged DFT calculation is made for an ion ($charge = +\frac{1}{2}$) with fractionally occupancy, then the ionization energy, is simply the negative of the

energy of the orbital from which half an electron has been removed.

This means that if DFT is employed, then the most efficient way to calculate vertical ionization energies is to use the transition state method as less computation time is required.

4.7 Further methods used in this thesis

The *ab initio* Hartree-Fock approach is unsuitable for the study of heavy metal compounds, due to the large computational resources required for atoms with so many electrons. However, DFT scales more favorably with system size than the *ab initio* method and was therefore employed for calculations on the actinide tetrahalides as described in Chapter 9.

In the cases of F_2O studied in Chapter 11 and the azides studied in Chapter 10, a range of techniques and methods were employed to achieve the most accurate and reliable electronic structure calculations.

4.7.1 Geometry optimization

In order to carry out calculations to determine the electronic properties of molecules, it is imperative to know accurately the equilibrium geometry of the molecular framework. This may come directly from experiment (*e.g.* gas phase electron diffraction, microwave, infrared or high-resolution electronic spectroscopy) or may come from a geometry optimization calculation. The purpose of a geometry optimization calculation is to find the minimum energy geometry *i.e.* the equilibrium geometry the molecule would adopt if it was isolated. This is achieved by starting from a trial geometry and systematically varying geometric parameters (bond lengths and bond angles) until the total energy of the molecule is minimized. This is usually an iterative process where one parameter is varied and then the energy of the molecule recalculated. The molecule is said to be geometry optimized when the geometry with the lowest energy has been found.

4.7.2 Vibrational frequencies and wavefunctions

In order to usefully compare computed values with those obtained from a PES experiment with vibrational resolution, it is necessary to compute both molecular and ionic vibrational frequencies. To calculate molecular vibrational frequencies, the Born-Oppenheimer approximation is used to separate the electronic (Ψ_e) and

nuclear (Ψ_n) wavefunctions as shown in equation 4.35.

$$\Psi = \Psi_e \Psi_n = \Psi_e \Psi_{vib} \Psi_{rot} \Psi_{trans} \tag{4.35}$$

where the nuclear wavefunction is further separated into a vibrational (Ψ_{vib}), rotational (Ψ_{rot}) and translational (Ψ_{trans}) part. With the nuclear motion separated, it may be described. Either an harmonic or a more accurate anharmonic approach may be used as detailed below:

1. In the harmonic case, for a diatomic molecule, the potential energy of the system (V) is given by equation 4.36.

$$V = \frac{k}{2}x^2, \tag{4.36}$$

where k is the force constant and x is the displacement from the equilibrium position. This is a good approximation in the region close to the equilibrium position for a molecular potential surface. Equation 4.36 can be extended to all the potential energy components between nuclei in a polyatomic molecule. This is shown for a system with N nuclei in equation 4.37.

$$V = \sum_{i=1}^{3N} \sum_{j=1}^{3N} \frac{k_{ij}}{2} q_i q_j, \tag{4.37}$$

where k_{ij} are the harmonic force constants and q_i and q_j are the mass-weighted nuclear displacement coordinates. The force constants are found from the second derivative of the electronic energy (the Hessian matrix) as shown in equation 4.38

$$k_{ij} = \left(\frac{\partial^2 E_e}{\partial q_i \partial q_j} \right) \tag{4.38}$$

If the eigenvalue equation is solved for the Hessian, then the force constants may be calculated from equation 4.38. The required harmonic vibrational frequencies may be derived by classical mechanics or the solution of the vibrational Schrödinger equation for the harmonic potential shown in equation 4.39.

$$-\frac{\hbar^2}{2} \sum_i \frac{\partial^2 \Psi}{\partial q_i^2} + \frac{1}{2} \sum_i \sum_j k_{ij} q_i q_j \Psi = E\Psi \tag{4.39}$$

This harmonic treatment requires only the second derivatives of the potential surface, available from an *ab initio* calculation of the geometry optimized molecule, and therefore the harmonic frequencies can be obtained from relatively fast calculations. For many, relatively rigid molecules, the

harmonic approximation is sufficient as vibrational displacements are small and the molecular potential is fitted well by a simple parabola close to the equilibrium position.

2. For small systems of a few atoms, it is possible, though expensive, to perform an anharmonic analysis of the potential energy functions to improve accuracy and better represent the real anharmonicity of the vibrations of a molecule. To calculate the fundamental frequencies and the anharmonic corrections, the **shape** of the potential energy functions (PEFs) must be found about the stationary point on the surface. This is achieved by calculating the potential at a number of systematic displacements from the stationary point. These single energy points are then fitted by a polynomial of suitable co-ordinates. The example given in equation 4.40 is for the symmetric vibrational modes of a C_{2v} molecule.

$$\begin{aligned} V &= \sum_{ij} C_{ij}(S_1)^i(S_2)^j + V_{eqm}, \\ \text{where } S_1 &= (\Delta r_1 + \Delta r_2)\sqrt{2}, \\ S_2 &= \Delta\theta + \alpha\Delta\theta^2 + \beta\Delta\theta^3, \end{aligned} \tag{4.40}$$

$\Delta r_{1,2}$ and $\Delta\theta$ are the changes in bond lengths and the bond angle respectively ($\Delta r_1 = \Delta r_2$ for a symmetric stretch in a $C_{2v)}$ molecule). S_1 is a function of the changes in bond length and S_2 is the pure bending co-ordinate suggested by Carter and Handy [28]. The parameters α and β are related as in equation 4.41, if the energy gradient is restricted to zero when the molecule is linear.

$$\alpha = -\frac{[1 + 3\beta(\pi - \theta_{eqm})^2]}{2(\pi - \theta_{eqm})} \tag{4.41}$$

The PEF can be fitted to the single energy points by optimizing the variable parameters using a non-linear least square fit procedure, such as NL2SOL [29] that was employed in the F_2O study in Chapter 11. Once the multidimensional PEF has been obtained then it can be used in a variational calculation to calculate the anharmonic vibrational wavefunctions.

The anharmonic vibrational wavefunction of the mth vibrational state is expressed as in equation 4.42.

$$|m\rangle = \sum c_{m,\mathbf{v}}\phi(\nu_1)\phi(\nu_2)\phi(\nu_3), \tag{4.42}$$

where $c_{m,\mathbf{v}}$ are the expansion coefficients, in which the subscript $\mathbf{v}$ denotes ν_2, ν_1 and ν_3. $\phi(\nu_i)$ are the νth order harmonic oscillator functions of the

normal mode i. The expansion coefficients are obtained from the diagonalization of the Watson's Hamiltonian (for a non-linear molecule) [30, 31].

Whether the harmonic or anharmonic treatment has been applied to a system, further Franck-Condon-Factor calculations must be undertaken to simulate the vibrational envelopes observed in experimental molecular photoelectron spectroscopy.

4.7.3 Franck-Condon-Factor (FCF) Calculations

FCF calculations have been employed in this work to simulate bands observed in vibrationally resolved photoelectron spectra. It was seen in Chapter 1 that the FCF for a photoionization process is proportional to the square of the overlap of the initial ($|m\rangle$) and final ($|n\rangle$)vibrational wavefunctions, as in equation 4.43. [32]

$$FCF(m,n) = \langle m|n\rangle^2 \tag{4.43}$$

In order to readily evaluate the overlap of the wavefunctions they must be expressed in the same co-ordinate system. This is a problem for polyatomic molecules as the normal modes of the two states are usually not the same. This means that the vibrational wavefunctions calculated (to the highest possible accuracy), as described in section 4.7.2, are based on different co-ordinate systems. This is overcome by using a co-ordinate transformation known as the Duschinsky rotation [33] to transfer between the different geometries. For the harmonic case, it is straightforward to calculate the FCFs from equation 4.43 taking into account the Duschinksky effect.

For calculation of the FCFs in the anharmonic case, as for F_2O in Chapter 11, the anharmonic vibrational wavefunctions were expressed as a linear combinations of the normal harmonic modes of the molecule (see equation 4.42). The FCF for the anharmonic case may be found using in equation 4.44 [32].

$$\langle m|n\rangle^2 = \left(\sum_{\mathbf{v}',\mathbf{v}''} c_{m,\mathbf{v}'} c_{n,\mathbf{v}''} \langle \nu_1', \nu_2', \nu_3' | \nu_1'', \nu_2'', \nu_3'' \rangle \right)^2 , \tag{4.44}$$

where $c_{m,\mathbf{v}'}$ and $c_{n,\mathbf{v}''}$ are the expansion coefficients of the linear combinations used for the initial and final state wavefunctions, and $\langle \nu_1', \nu_2', \nu_3' | \nu_1'', \nu_2'', \nu_3'' \rangle$ is the overlap integral of the corresponding harmonic integrals. The anharmonic case only differs from the harmonic case in that in order to calculate the overlap of the initial and final wavefunctions the sum of the overlap of the **component** harmonic modes must be calculated. The anharmonic wavefunctions are expressed

as linear combinations of harmonic functions in the normal co-ordinates of the system they are based upon. Therefore a co-ordinate transformation is required as for the harmonic case. The overlap inntegral can be evaluated using a model that includes the Duschinsky rotation matrix [34]. This method calculates FCFs, incorporating anharmonicity and the Duschinsky rotation [32].

4.7.4 Post Hartree-Fock Methods

It has been shown previously in this chapter, that despite the usefulness of the Hartree-Fock method, it is limited in that it does not include the proper correlation of the electrons in a system. No matter how large a basis set is used, there will always be a difference in the calculated HF energy (E_{HF}) of a system and its exact non-relativistic energy (E_{Exact}). This correlation energy (E_{Corr}) is defined at the Hartree-Fock limit, *i.e.* with an infinite basis set, to be:

$$E_{Corr} = E_{Exact} - E_{HF} \tag{4.45}$$

It should be noted that E_{Corr} will be negative as proper correlation of the motion of the electrons will lead to an extra lowering of energy of the system. [4, 5]

To combat the problem of electron correlation, methods have been developed to allow for its effects and therefore improve the accuracy of the theoretical treatment. The first method to be considered here is **configuration interaction** (CI). CI incorporates the interaction of excited wave functions with the ground state wave function. This gives additional functional freedom for the total CI wave function to adjust and a more optimal energy can be found than from a single determinantal Hartree-Fock approach. The single determinantal wavefunction as used in the Hartree-Fock method was given in equation 4.10 and can be written for a wavefunction with N spin orbitals as in equation 4.46.

$$\Phi_0 = |1, 2 \ldots i \ldots j \ldots N\rangle, \tag{4.46}$$

where all orbitals are occupied up to N. A singly excited state may be produced by removing one electron from one of the occupied orbitals, i or j and placing it in an unoccupied orbial r or s. The determinantal wavefunction for the singly excited state can be written as in 4.47.

$$\Phi_i^r = |1, 2 \ldots i \ldots N, r\rangle \tag{4.47}$$

A doubly excited state is formed by removing electrons from both i and j and putting them in r and s.

$$\Phi_{ij}^{rs} = |1, 2 \ldots N, r, s\rangle. \tag{4.48}$$

These ideas are easily extended to incorporate triply, quadruply and quintuply excited wavefunctions.

A CI wavefunction is a linear combination of the ground state wavefunction and corresponding singly and multiply excited state wavefunctions as shown in equation 4.49.

$$\Psi_{CI} = \sum_{i=0}^{\infty} C_i \Phi_i, \tag{4.49}$$

where i represents the number of substitutions in the excited state wavefunction and *lim* is the upper limit of the summmation. Equation 4.49 can be rewritten as in equation 4.50.

$$\Psi_{CI} = C_0\Phi_0 + \sum_{i}^{occupied} \sum_{r}^{virtual} C_i^r \Phi_i^r + \sum_{ij}^{occupied} \sum_{rs}^{virtual} C_{ij}^{rs} \Phi_{ij}^{rs} + \cdots \tag{4.50}$$

Equations 4.49 and 4.50 represent the **complete CI wavefunction**, if all excitations are considered to an infinite number of orbitals, and the expansion can exactly represent the non-relativistic wavefunction. The optimum CI coefficients ($C_{ij\ldots}^{rs\cdots}$) are obtained by application of the Variational Principle to minimize the energy calculated from the CI wavefunction.

$$E_{CI} = \langle \Psi_{CI} | H | \Psi_{CI} \rangle \tag{4.51}$$

Obviously for a calculation to be completed in a finite time, a finite basis must be used. If all possible excitations are included in a calculation for the specified basis set being used, then this is a **full CI** method. The CI method can be extended by including excitations from more than one reference determinantal wavefunction (Ψ_0). This is called multi-reference-CI (MRCI) and is particularly useful for open-shell states which cannot be described satisfactorily by a single determinantal wavefunction. MRCI inevitably demands more computational time.

Although a full configuration interaction calculation is the most complete CI calculation that can be performed, it is only practicable for a few small molecules. As a result a number of methods for including electron correlation have been developed.

1. **Limited CI**: The expression for the wavefunction given in equation 4.50, can be truncated so as to only incorporate a given level of excitation. Limited CI wavefunctions are described by the types of excitations that they include:

- CIS, includes only single excitations,
- CISD, also includes double excitations,
- CISDT, also includes triple excitations,
- CISDTQ, also includes quadruple excitations.....

Including more excitations lowers the total energy of the system, but demands more computational time. A serious problem with limited CI is that, while it is variational, it is not size consistent, *i.e.* the product of the individual wavefunctions of the separated fragments of a system will have more terms than a single wavefunction describing the whole system that is truncated at the same level.

2. **Møller-Plesset (MP) perturbation method** [35]: This is a simple many-body perturbation method for estimating the correlation energy [2, 4, 5]. This method is size consistent, but non-variational. In perturbation theory the system under investigation is treated as a pertubation of a model system whose exact solutions are known. The Schrödinger equation for the model system is given in equation 4.52.

$$H^{(0)}\Psi^{(0)} = E^{(0)}\Psi(0) \tag{4.52}$$

The Schrödinger equation for the real system is given in equation 4.53, with the Hamiltonian expressed as a perturbation of the model system, as in equation 4.54.

$$H\Psi = E\Psi. \tag{4.53}$$

$$H = H^{(0)} + \lambda V, \tag{4.54}$$

where V is the potential function corresponding to the difference between the real and model systems, and λ is the perturbation parameter (usually small). As a model system is used that closely approximates the true system, the perturbation should be small, *i.e.* $\Psi \approx \Psi^{(0)}$ and $E \approx E^{(0)}$. This can be expressed exactly, as in equations 4.55 and 4.56.

$$\Psi = \Psi^{(0)} + \lambda\Psi^{(1)} + \lambda^2\Psi^{(2)} + \cdots \tag{4.55}$$

$$E = E^{(0)} + \lambda E^{(1)} + \lambda^2 E^{(2)} + \cdots, \tag{4.56}$$

where $\Psi^{(k)}$ are the perturbed wavefunctions, which are chosen to be orthogonal to $\Psi^{(0)}$. By insertion of equations 4.55 and 4.56 into equation 4.53

equation 4.57 is obtained.

$$\begin{aligned} H^{(0)}\Psi^{(0)} + \lambda[V\Psi^{(0)} + H^{(0)}\Psi^{(1)}] + \lambda^2[V\Psi^{(1)} + H^{(0)}\Psi^{(2)}] + \cdots \\ = E^{(0)}\Psi^{(0)} + \lambda[E^{(1)}\Psi^{(0)} + E^{(0)}\Psi^{(1)}] \\ + \lambda^2[E^{(2)}\Psi^{(0)} + E^{(1)}\Psi^{(1)} + E^{(0)}\Psi^{(2)}] + \cdots \end{aligned} \tag{4.57}$$

This is satisfied for an arbitrary value of λ only if the coefficients for each λ^n are equal, as shown in equations 4.58.

$$\begin{aligned} H^{(0)}\Psi^{(0)} &= E^{(0)}\Psi^{(0)} \\ V\Psi^{(0)} + H^{(0)}\Psi^{(1)} &= E^{(1)}\Psi^{(0)} + E^{(0)}\Psi^{(1)} \\ V\Psi^{(1)} + H^{(0)}\Psi^{(2)} &= E^{(2)}\Psi^{(0)} + E^{(1)}\Psi^{(1)}E^{(0)}\Psi^{(2)} \\ &\vdots \\ V\Psi^{(k-1)} + H^{(0)}\Psi^{(k)} &= \sum_{i=0}^{k} E^{(k-1)}\Psi^{(i)} \end{aligned} \tag{4.58}$$

The order of perturbation depends on which powers of λ are included in the expansion. Zero order perturbation theory (PT) would include the model system alone, first order PT would yield $\Psi^{(1)}$ and $E^{(1)}$, second order PT also gives $\Psi^{(2)}$ and $E^{(2)}$, *etc.* [2, 4, 5]. In the Møller Plesset perturbation method [35] the Hartree-Fock solution is used as the model unperturbed system. This means that the perturbation V is the difference between the Hamiltonian operator for the exact solution (H) and the zero order operator from the HF solution ($H^{(0)}$).

$$V = H - H^{(0)} = \sum_{i}^{n} \sum_{<\ j}^{n} \frac{e^2}{r_{ij}} - \sum_{i} V_1^{eff}(i), \tag{4.59}$$

where n is the number of electrons and $V_1^{eff}(i)$ is the effective one electron potential [5]. The Møller-Plesset (or many-body perturbation theory) approach is abbreviated as MPn (or MBPT(n)) with n equal to the order of the many-body perturbation.

Due to the formulation of the MP perturbation approach, the MP1 level corresponds to the Hartree-Fock result. The MP2 method accounts for approximately 80-90% of the correlation and is therefore roughly comparable with a CISD calculation and requires not much more computation than a Hartree-Fock-Roothaan calculation. Perturbation calculations are size consistent at all levels, but they are not variational methods.

3. **Coupled Cluster (CC) theory** : This is based on a cunning reformulation of the expression for the CI wavefunction to separate out the different types of excitations and is founded on the early work of Cízek and Paldus [36–38]. If equation 4.49 is rewritten as in equation 4.60.

$$\Psi = e^{T}\Phi_0 \tag{4.60}$$

where T produces all possible types of excitation (*i.e.* singles(T_1), doubles (T_3), triples (T_3), *etc*) as in 4.61.

$$T = 1 + T_1 + T_2 + T_3 + \cdots \tag{4.61}$$

The exponential in equation 4.60 can be rewritten as a power series as in equation 4.62.

$$\begin{aligned}\Psi &= \left(1 + T + \frac{1}{2}T^2 + \frac{1}{3!}T^3 + \frac{1}{4!}T^4 + \cdots\right)\Phi_0 \\ &= \left(1 + T_1 + T_2 + \frac{1}{2}T_1^2 + T_3 + T_1T_2 + \frac{1}{3!}T_1^3 + T_4 + \frac{1}{2}T_2^2\right. \\ &\quad \left. + \frac{1}{2}T_2T_1^2 + T_1T_3 + \frac{1}{4!}T_1^4 + \cdots\right)\Phi_0\end{aligned} \tag{4.62}$$

In this equation, the powers of the operators denotes repeated operation, an example of which is shown in equation 4.63.

$$T_2^2 = T_2(T_2\Phi_0) \tag{4.63}$$

This would denote all double excitations, of doubly excited states of the reference wavefunction (mostly quadruple excitations). This means that the excitations are grouped in the coupled cluster formulation as powers of their base operator T_n (where $n = 1, 2, 3, 4\ldots$). Coupled cluster calculations have a level determined by which T_n operators are included in the expansion given in equation 4.62. If just T_2 are included then this is CCD, if T_1 and T_2 are both included this is CCSD and if T_1, T_2 and T_3 are all included then this is CCSDT. It is noted that if T_2 is included, then not only double excitations are considered, but quadruples, sextuples *etc.* are also included. The strength of coupled cluster theory lies in the way the operators are used **repeatedly** to generated high-substitution excitations. The T_2 operator is again considered in equations 4.64 and 4.65.

$$T_2\Phi_0 = \sum_{ij}\sum_{rs} C_{ij}^{rs}\Phi_{ij}^{rs} \tag{4.64}$$

$$T_2^2\Phi_0 = \sum_{ij}\sum_{kl}\sum_{rs}\sum_{tu} C_{ij}^{rs}C_{kl}^{tu}\Phi_{ijkl}^{rstu} \tag{4.65}$$

The coefficients for the quadruple excitations in equation 4.65 are simple products of previously calculated coefficients for the double excitations. This means that, due to the clever formulation, highly multiply excited states are included with little computational cost.

Coupled cluster theory is not perfect as the Variation Theorem cannot be applied to the infinite power series in equation 4.62. The series must be truncated, causing loss of size consistency, or the variation method avoided. The alternative is to solve the resulting large set of non-linear equations iteratively, which is practicable for many molecules at the CCSD level. It is chemically desirable to also include the triple excitations at the CCSDT level, but this is almost impossible for all but the smallest systems due to the N^8 scaling with system size (N). An important popular method, that includes the triple excitations, is CCSD(T) in which the linear coefficients of the triple excitations are deduced from terms involving a single excitation and a double excitation ($T_1 T_2 \Phi_0$). This is one of the best methods available and is used extensively. It was used in this work as part of the study of F_2O (Chapter 11).

4. **Quadratic Configuration Interaction (QCI)**: This is a method developed by Pople and co-workers as a size consistent version of the limited CI approach and is somewhat similar to coupled-cluster theory [39]. If the same operators are considered as discussed for coupled-cluster theory then the quadratic CI method that includes single and double excitations (QCISD) will incorporate the terms, T_1, T_2, T_1T_2 and T_2^2. The extra quadratic terms are added in quadratic CI to maintain size consistency [5,39]. As with coupled cluster theory inclusion of triple excitations in QCISDT may greatly improve the accuracy of the correlation energy, but for most systems this massively increases the computational time required. As with coupled-cluster theory some methods have been developed to include a portion of the triple excitations (*e.g.* QCISD(T)) [6,39].

5. **Multiconfigurational self-consistent field method (MCSCF)** [40–45]: Most of the previous methods have been based on calculating the correlation energy using a single reference determinant, Φ_0. However these include mainly dynamic correlation effects (excitations contributing to the wavefunction) and are unsatisfactory for systems which cannot be adequately described by a single determinant, *e.g.* open-shell systems [5]. For these cases a multiconfigurational approach must be used, in which a set

of carefully chosen determinants are used in place of a single determinant. The determinants are generated by selecting the most relevant occupied and virtual orbitals (the active space) and performing a SCF calculation followed by a full CI calculation, while all other obitals are treated as full or completely vacant. An MCSCF calculation, therefore, involves an SCF calculation with a full CI treatment of a defined subset of orbitals [6]. This method is usually denoted as complete active space SCF (CASSCF).

The multideterminantal approach is capable of calculating virtually all the correlation energy. However, the limit on computational resources makes it difficult to include a comprehensive enough active space for larger molecules.

For any computational problem, it is unlikely that there is a perfect single approach. Often a combination of methods must be used to support each other. A number of considerations must be taken into account before any successful theoretical work can be undertaken:

- **Information required**: Any calculation should be aimed at elucidating a particular problem. It is important to know what chemical properties need to be modelled. Usually calculation values need to be compared with experimental data, to test the calculational methods and to be useful.
- **Resources**: The computational resources available will be critical to the level of calculation that may be performed.
- **System type**: The number of atoms in a system and their weight will limit the level of calculation possible.
- **Method**: Selection of the best method(s) to achieve chemical accuracy will vary from molecule to molecule.
- **Basis set**: All calculations can only be as good as the basis sets used to construct the molecular orbitals.

The process is usually an exercise in compromise. It is impossible to use the best largest basis sets available along with the most sophisticated high level calculations for anything but the smallest systems. As a result both basis set and level of calculation are given as part of the results of any theoretical study.

4.8 Conclusion

The methods and calculation details within this chapter are drawn on in later chapters where they are used to understand and interpret experimental spectroscopic data. Specifcally, the *ab initio* FCF methods were used in the work on F_2O in Chapter 11. The assignment of pyrolysis products of some azide compounds was augmented by calculations using the Møller Plesset perterbation method, in Chapter 10. Finally, density functional theory calculations were instrumental in the assignment and understanding of the photoelectron spectra of the actinide tetrahalides studied in Chapter 9.

Bibliography

[1] T. Koopmans, Physica **1**, 104 (1933).

[2] P. W. Atkins, *Molecular quantum mechanics* (Oxford University Press, Walton street, Oxford, OX2 6DP, 1983).

[3] E. R. Davidson and D. Feller, Chem. Rev. **86**, 681 (1986).

[4] A. Szabo and N. S. Ostlund, *Modern quantum chemistry: Introduction to advanced electronic structure theory* (Macmillan Publishing Co., Inc., London, 1982).

[5] T. Veszprémi and M. Fehér, *Quantum Chemistry* (Kluwer Academic/Plenum Publishing, Dordrecht, New York, Norwell, 1976).

[6] M. J. Frisch, Æ. Frisch, and J. B. Foresman, *Gaussian 94 User's Reference* (Gaussian Inc., Pittsburgh, PA15106 U. S. A., 1994).

[7] T. H. Dunning, Journal of Chemical Physics **90**, 1007 (1989).

[8] R. A. Kendall, T. H. Dunning, and R. J. Harrison, Journal of Chemical Physics **96**, 6796 (1992).

[9] D. E. Woon and T. H. Dunning, Journal of Chemical Physics **98**, 1358 (1993).

[10] D. E. Woon and T. H. Dunning, Journal of Chemical Physics **100**, 2975 (1994).

[11] R. McWeeny and B. T. Sutcliffe, *Methods of molecular quantum mechanics* (Academic press-, London and New York, 1976).

[12] R. G. Parr, *The quantum theoery of molecular electronic structure* (W. A. Benjamin, Inc., New York, 1964).

[13] C. C. J. Roothaan, Rev. Mod. Phys. **23**, 69 (1951).

[14] C. C. J. Roothaan, Rev. Mod. Phys. **32**, 179 (1960).

[15] W. Kohn, A. D. Becke, and R. G. Parr, J. Chem. Phys. **100**, 12974 (1996).

[16] P. Hohenberg and W. Kohn, Phys. Rev. **136**, B846 (1964).

[17] W. Kohn and L. J. Sham, Phys. Rev. **140**, A1133 (1965).

[18] O. Warschkov, Ph.D. thesis, Department of Chemistry, University of Southampton, Highfield, Southampton, SO17 1BJ, 1999.

[19] S. H. Vosko, L. Wilk, and M. Nusair, Can. J. Phys. **58**, 1200 (1980).

[20] J. P. Perdew and Wang Yue, Phys. Rev. B **33**, 8800 (1986).

[21] C. Lee, W. Yang, and R. G. Parr, Phys. Rev. B **37**, 785 (1988).

[22] B. G. Johnson, P. M. W. Gill, and J. A. Pople, J. Chem. Phys. **98**, 5612 (1993).

[23] T. V. Russo, R. L. Martin, and P. J. Hay, J. Chem. Phys. **101**, 7729 (1994).

[24] J. P. Perdew *etal.*, Phys. Rev. B **46**, 6671 (1992).

[25] A. D. Becke, Phys. Rev. **38**, 3098 (1988).

[26] J. C. Slater, Adv. Quantum Chem. **6**, 1 (1972).

[27] N. H. F. Beebe, Chemical Physics Letters **19**, 290 (1973).

[28] S. Carter and N. C. Handy, J. Chem. Phys. **87**, 4294 (1987).

[29] J. E. Dennis, Jnr, D. M. Gay, and R. E. Walsh, ACM Transactions on Mathematical Software **7**, 348 (1981).

[30] J. K. G. Watson, Mol. Phys. **15**, 479 (1968).

[31] J. K. G. Watson, Mol. Phys. **19**, 465 (1970).

[32] D. K. W. Mok, E. P. F. Lee, F.-T. Chau, D.-C. Wang, and J. M. Dyke, J. Chem. Phys. **113**, 5791 (2000).

[33] F. Duschinsky, Acta Physicochim. URSS **7**, 55 (1937).

[34] P. Chen, in *Photoelectron spectroscopy of reactive intermediates*, edited by C. Y. Ng, T. Baer, and I. Powis (Wiley, New York, 1994), pp. 371–425.

[35] C. Møller and M. S. Plesset, Phys. Rev. **46**, 618 (1934).

[36] J. Cízek, J. Chem. Phys. **45**, 4256 (1966).

[37] J. Cízek, J. Chem. Phys. **14**, 35 (1969).

[38] J. Cízek and J. Paldus, J. Chem. Phys. **5**, 359 (1971).

[39] J. A. Pople, M. Head-Gordon, and K. Raghavachari, J. Chem. Phys. **87**, 5968 (1987).

[40] D. Hegarty and M. A. Robb, Mol. Phys. **38**, 1795 (1979).

[41] R. H. E. Eade and M. A. Robb, Chem. Phys. Lett. **83**, 362 (1982).

[42] H. B. Schlegel and M. A. Robb, Chem. Phys. Lett. **93**, 43 (1982).

[43] M. Frisch, I. N. Ragazos, M. A. Robb, and H. B. Schlegel, Chemical Physics Letters **189**, 524 (1992).

[44] N. Yamamoto, T. Vreven, M. A. Robb, M. J. Frisch, and H. B. Schlegel, Chemical Physics Letters **250**, 373 (1996).

[45] M. Klene, M. A. Robb, M. J. Frisch, and P. Celani, Journal of Chemical Physics **113**, 5653 (2000).

Chapter 5

Experimental details

5.1 Introduction

In this work two separate photoelectron spectrometers were used.

- **The synchrotron spectrometer**: This is a photoelectron spectrometer with added angle-resolution capabilities. This was designed specifically for the study of reactive intermediates using synchrotron radiation.
- **The high-temperature spectrometer**: This is a photoelectron spectrometer, that incorporates a high-temperature induction furnace. This can be used for high-temperature evaporations or pyrolysis studies.

Both spectrometers were designed and built within the Southampton PES Group, and were specifically designed to enable the measurement of the photoelectron spectra of reactive intermediates and cope with the problems this entails (*i.e.* generation, handling and pumping of reactive gases). The spectrometers are robust and can be readily taken apart and cleaned. Most of the inner surfaces are coated with colloidal graphite (dag) to prevent local charging effects and protect the surfaces from chemical attack.

5.2 Photon sources

Two distinctly different types of photon source were used in this work. The first was an inert gas discharge lamp. This type of photon source was used for all of the high-temperature studies, and also for all testing and development carried out with the synchrotron spectrometer. The second type of photon source was a synchrotron radiation source, previously described in Chapter 3.

5.2.1 Inert gas discharge lamp

This type of photon source is the most commonly used in gas-phase ultraviolet photoelectron spectroscopy [1]. The photons are produced by the high voltage discharge of an inert gas flowing through a small cavity maintained at low pressure (≈0.1 Torr). Helium is the most useful and widely used discharge gas and was used in all experiments in this work. A range of alternative gases and different styles of lamps have been described by Eland [2]. The photons produced travel into the ionization chamber of the spectrometer via a differentially pumped quartz glass capillary. Windows are not used, due to the lack of suitably robust materials that are transparent to VUV-wavelength radiation.

97% of the usable output photon intensity, produced by a high-voltage discharge in helium, consists of the HeIα line at a photon energy of 21.218eV (58.4nm). The HeIα line is produced by the He $1s2p...^1P \rightarrow 1s^2...^1S$ emission. The next most intense component is the HeIβ line at a photon energy of 23.085eV (53.7nm), produced by the He $1s3p...^1P \rightarrow 1s^2...^1S$ emission [2].

This type of photon source is ideal for photoelectron spectroscopy, as it can be easily constructed and produces almost pure monochromatic radiation, with a narrow bandwidth, at a reasonable flux (typically $\approx 10^{11} - 10^{12}$ photons/sec). However, the photons are unpolarized and non-tunable and therefore of little use for angle-resolved (see section 2.4) or constant-ionic-state (CIS) studies.

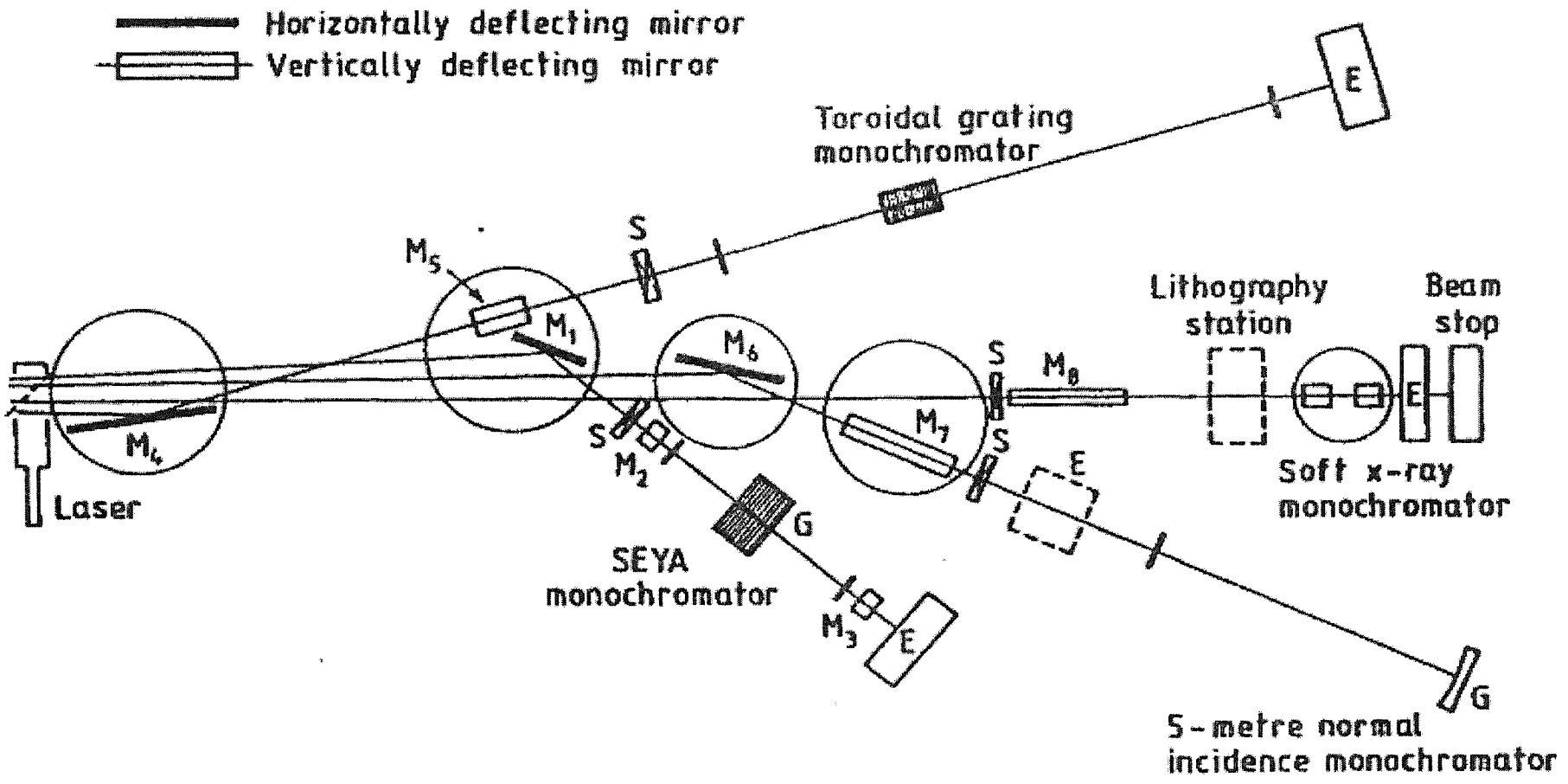

Figure 5.1: Layout of BL3, not to scale. M_n=Mirror, E=experimental chamber, G=diffraction grating.

5.2.2 Beamline 3.3 at the SRS (Daresbury)

The angle-resolved and constant-ionic-state (CIS) studies of reactive intermediates performed by the Southampton PES Group were initially carried out on the VUV-XUV beamline (BL3.3) at the synchrotron Radiation Source (SRS), Daresbury Laboratories, Cheshire, UK. BL3.3 is one of four beamlines fed from Line 3. Line 3 accepts synchrotron radiation on a tangent, from bending magnet Number 3 of the main storage ring of the SRS. The solid angle of acceptance is approximately 28 mrad×5 mrad (FWHM) in the horizontal and vertical planes. The radiation beam in line 3 is split into four components, by three mirrors as shown in Figure 5.1. The undeviated portion of the radiation is used for the soft X-ray beam-line (BL 3.4), while the three other components go to beam-line 3.1 (Seya-Namioka Monochromator), beam-line 3.2 (MacPherson normal incidence monochromator) and beam-line 3.3 (Toroidal Grating Monochromator (TGM)). During the course of this thesis, experiments have been undertaken on BL3.3, although BL3.2 has been previously used by the Southampton PES group.

Station 3.3 has usable photon flux in the 10 eV to 120 eV region produced from two interchangeable Toroidal Grating Monochromators (TGMs) with an achievable resolution 1000. The beam-line is also a good source of circularly polarized radiation at the higher energies. The TGM itself utilises 3 optical elements, a horizontally focusing mirror, a vertically focusing mirror and the interchangeable toroidal gratings as shown in Figure 5.2. There are entrance and exit slits (and other interchangeable masks) that can be used to select part of the photon beam. Reducing the size of the apertures will reduce the bandwidth of the radiation and improve the polarization, but this will also severely reduce the amount of photon flux. A differentially pumped Pyrex capillary of 1 mm internal diameter was used to transfer the radiation from the end of the beam-line to the Southampton synchrotron spectrometer.

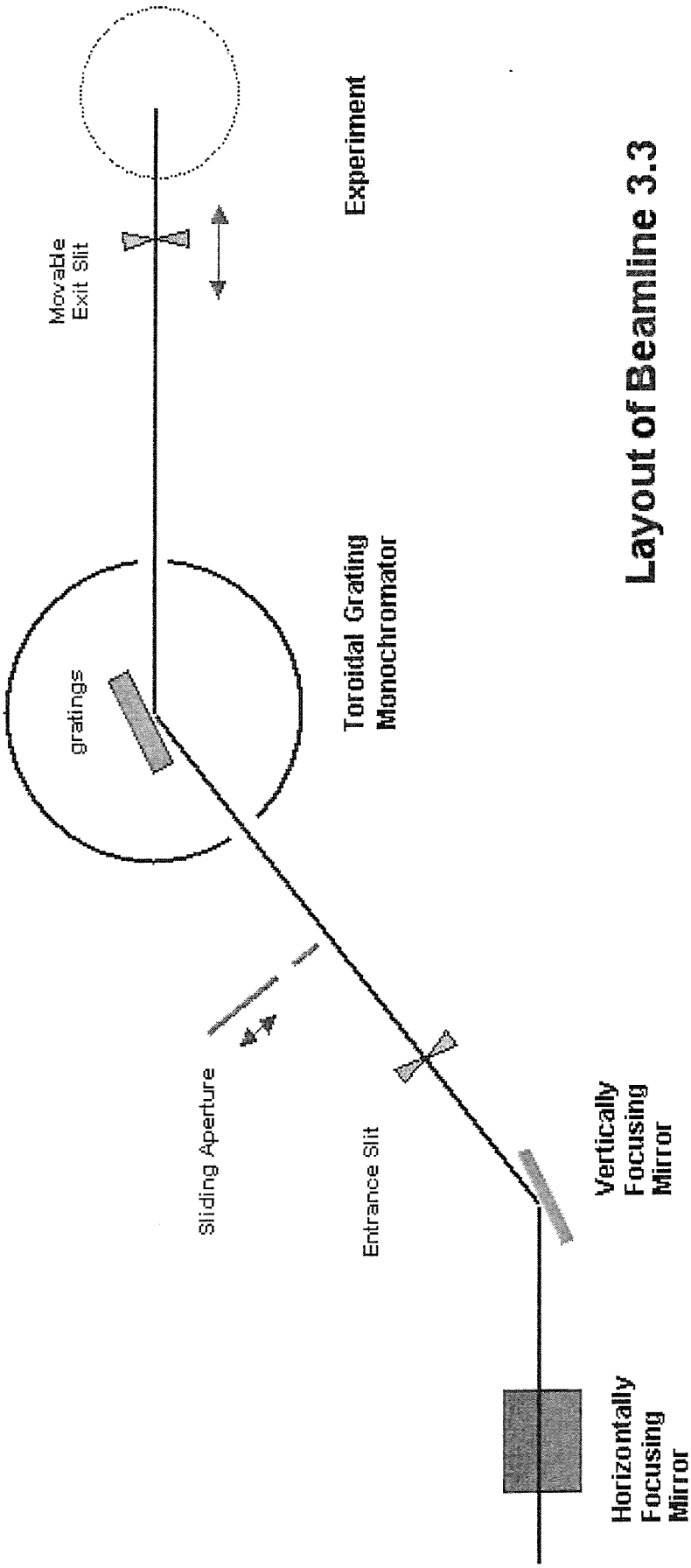

Figure 5.2: Layout of BL3.3. Not to scale.

Element	Base material	Coating	Focusing properties	Included Angle
Horizontal focusing mirror	Silicon Carbide	Platinum	2:1 Horizontal demagnification	170°
Vertical focusing mirror	Fused Silica	Platinum	4:1 Vertical demagnification	155°
LEG (Grating)	Fused Silica	Platinum	Toroidal Focusing	155°
HEG (Grating)	Fused Silica	Platinum	Toroidal Focusing	155°

Table 5.1: Mirror and grating parameters for BL3.3

The monochromator consists of two interchangeable gratings ruled with 710 and 2400 lines/mm. The details of the individual mirrors and gratings available are given in Tables 5.1 and 5.2. The energy range and peak energy are typical values found under normal operating conditions. The gratings have the shape of a section of a torus with meridional and sagittal radii of curvature 15 m and 60 cm [3]. In this work, only the Low Energy Grating (LEG) was used, as this gave the best flux in the energy region of interest. The typical output of the low energy grating is shown in Figure 5.3. The wavelength output of the monochromator is dependent on the angle of the incident radiation (α) and on the angle of diffraction (β). The source (bending magnet) and the final target (BL3.3) are fixed so that $\alpha - \beta = 155\,^{\circ}$. The different wavelengths are dispersed according to equation 5.1 [4].

$$nN\lambda = \sin\alpha + \sin\beta, \tag{5.1}$$

where n is the order of diffraction, N is the number of grooves per unit length in the grating, and λ is the wavelength diffracted at the angle β. Usually first order radiation ($n = 1$) is used, as this is the most intense component. α and β are altered by rotating the toroidal grating about its pole, which is perpendicular to the entrance and exit arms of the monochromator. In this way it is possible to scan through a range of wavelengths, as required. Zero order radiation is obtained when $\alpha = \beta$, which is useful for alignment and testing procedures, as this contains all wavelengths and is therefore seen as visible bluish-white light.

Another important property of synchrotron radiation is its high degree of polarization (see Chapter 3). The pure plane polarized radiation ($S_1 = 1$) produced by the bending magnet is adversely affected by the beamline optics and

Grating	Line Density	Energy Range	Peak Energy
LEG	710 l/mm	15 eV to 45 eV	24 eV
HEG	2400 l/mm	40 eV to 150 eV	90 eV

Table 5.2: Comparison of the High and Low Energy Gratings for BL3.3

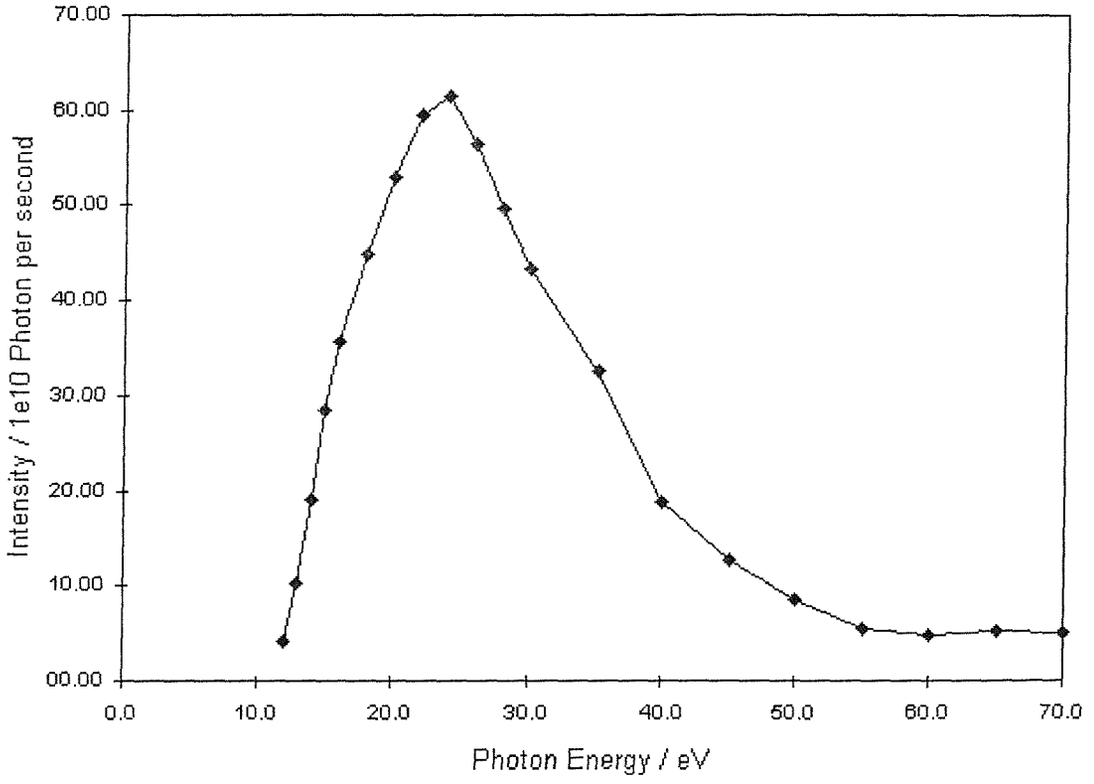

Figure 5.3: Output of the Low Energy Grating (LEG) on BL3.3 (SRS, Daresbury), over a range of photon energies, at 50 meV bandwidth. Units for the photon flux scale are 10^{10} photon/sec per 100 mA of ring current. [5]

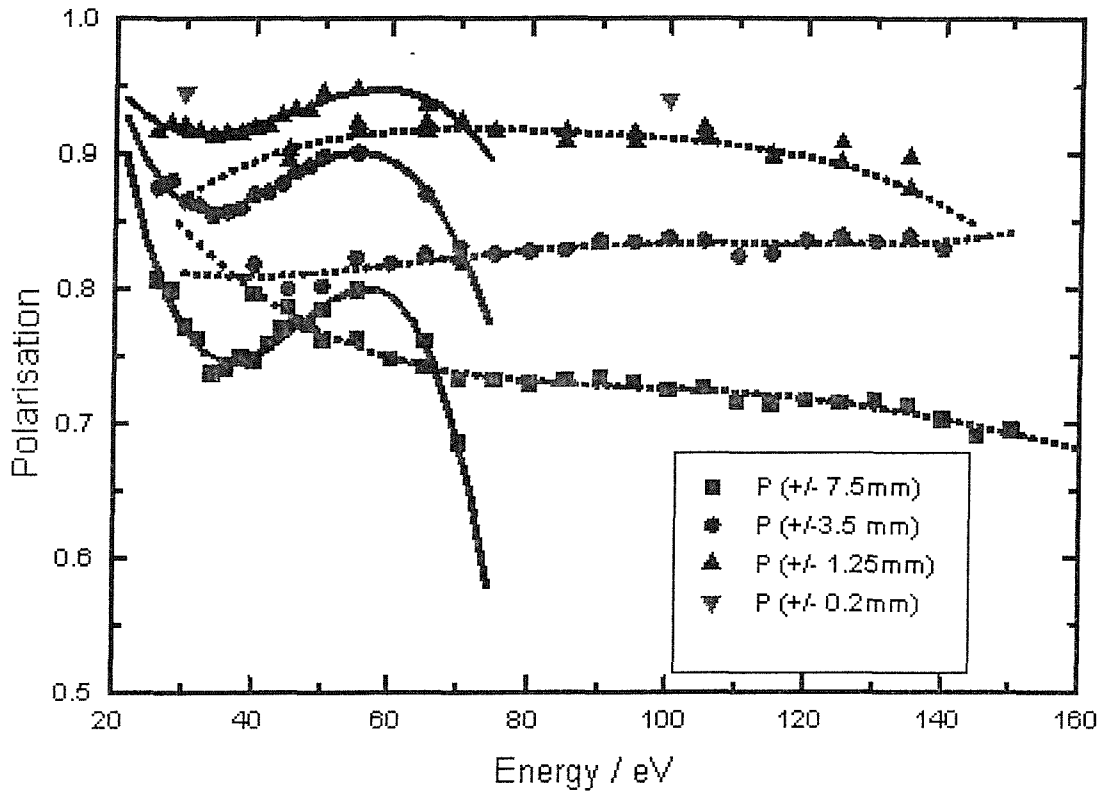

Figure 5.4: Polarization of output of the Low Energy Grating (LEG) on BL3.3 (SRS, Daresbury), over a range of photon energies with, using the various polarization masks [5].

inevitably some polarization is lost. The polarization of the radiation output from the monochromator is shown in Figure 5.4. It is seen that for photon energies around 21 eV, linear polarizations of greater than 90% can be acheived, but with loss of a large proportion (90%) of the flux. This high degree of polarization is critical for angle-resolved PES studies such as the angle-resolved study of $O_2(a^1\Delta_g)$ described in Chapter 6.

5.2.3 Circularly polarized beamline (BL4.2) at ELETTRA

The Elettra synchrotron facility in Trieste (Italy) is a 2.0 GeV, third generation source, primarily aimed at the production of X-rays. A third generation synchrotron source is one that has been specifically designed to incorporate insertion devices (see section 3.3) on the straight section of the ring. In this work the so-called, circularly polarized beamline (BL4.2) was used, and this has an elliptical wiggler (EEW) as its source [6]. The wiggler has two sets of perpendicular

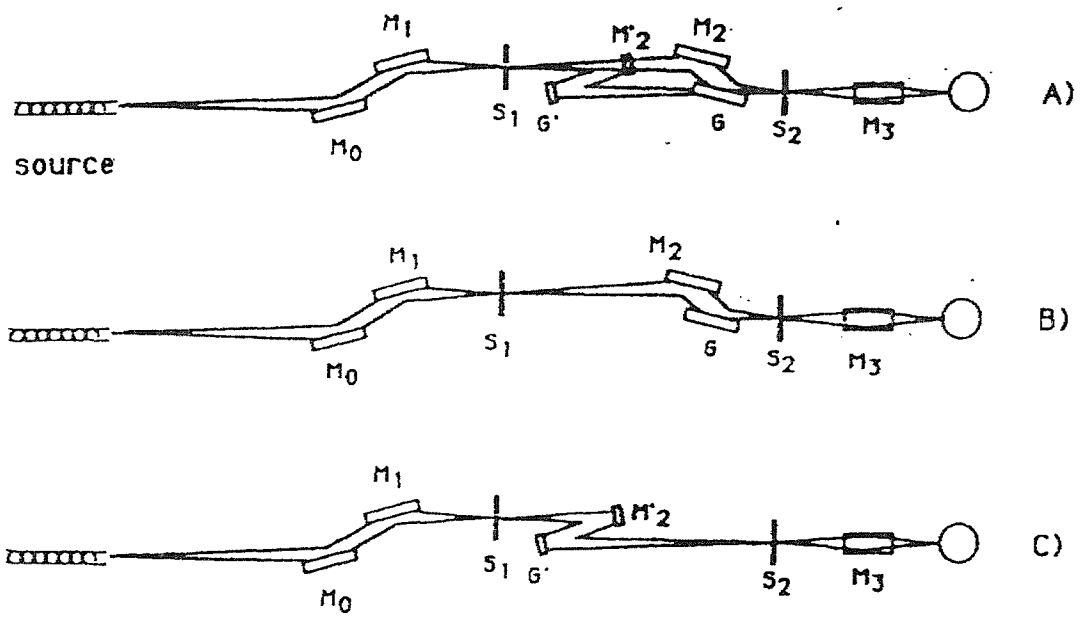

Figure 5.5: Schematic of BL4.2 at Elettra.(A)General layout; (B)grazing incidince configuration; (C) normal incidence configuration (used in this work). M_x, S_y and $G^{(')}$ denote mirrors, slits and gratings, respectively. [8].

magnets. The vertical field in the EEW is generated by permanent magnetic poles and the horizontal field is generated by arrays of electromagnets. The strength of the magnetic fields can be varied by physically changing the separation of the permanent magnets, about the electron orbit, and by altering the current flowing in the electromagnets. The acceptance angle of the radiation from the EEW is 2 mm by 1 mm, in the horizontal and vertical planes, respectively. This is a compromise between the use of the total flux available and the loss of polarization away from the central photon axis [7]. This means that BL4.2 is a very flexible source, able to generate a high flux of electrons (10^{12} photons/sec) at a broad range of energies (5-1200 eV), with almost any polarization desired. If the electromagnets in the EEW are switched of then pure plane polarized radiation is produced.

BL4.2 possesses two independent monochromators that cover the energy ranges 5 to 35 eV and 30 to 1200 eV respectively. The low energy range is covered by a normal incident monochromator, while the higher photon energies are produced by a grazing incident monochromator. A general layout of the beamline, operating in the two different modes, is shown in Figure 5.5. For VUV PES the low energy range is of interest, and so the normal incidence mode was used in this work. The details of the individual optical elements are given in Table 5.3.

Optical Element	Shape	R(m)	ρ(m)
M_0	Flat		
M_1	Toroidal	200	0.6
M_2	Flat		
M_2'	Cylindrical		2.3
G_1 (1050 l/mm)	Spherical	42.8	
G_2 (1050 l/mm)	Spherical	33.7	
G_3 (1050 l/mm)	Spherical	22.7	
G_4 (1050 l/mm)	Spherical	17.8	
G_1' (2400 l/mm)	Spherical	2.9	
G_2' (2400 l/mm)	Spherical	2.9	
M_3	Toroidal	46	0.09

Table 5.3: Parameters of the optical elements of BL4.2 at Elettra. R and ρ are the curvature radii in the tangential and sagittal planes, respectively

In the normal incidence mode the theoretical resolving power was calculated to be $\approx$13000 [8], but in this work it was experimentally found to be $\approx$8000.

BL4.2 (Elettra) proved to be superior to BL3.3 (Daresbury) in all aspects. Under normal working conditions there was a gain of at least one order of magnitude in resolution, two orders of magnitude in flux, and better polarization relative to BL3.3 (Daresbury). This is best demonstrated by the work on oxygen atoms described in Chapter 7.

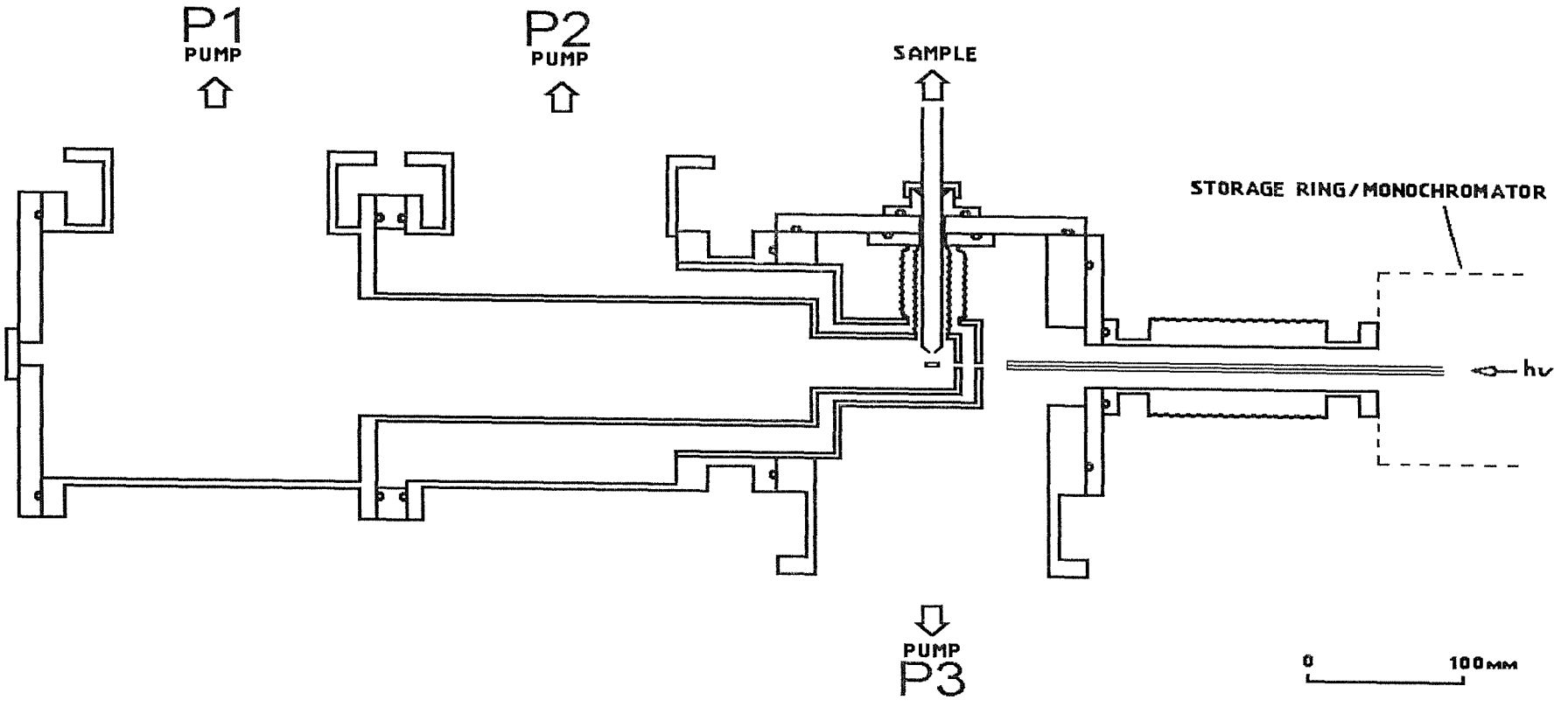

Figure 5.6: Vertical cross-section of the synchrotron spectrometer, along the photon axis. [9].

5.3 The synchrotron spectrometer

5.3.1 Introduction

The synchrotron spectrometer used in this work was designed specifically for studying reactive intermediates with synchrotron radiation. Angle resolved studies could be performed with this instrument [9]. The spectrometer has been transported to the SRS and to Elettra for studies on reactive species. Schematics of the spectrometer are given in Figures 5.6 and 5.7.

5.3.2 The Vacuum system

Photoelectron spectroscopy of reactive species requires a high vacuum environment and a high gas throughput. To enable the coupling of the spectrometer to a synchrotron source, the differential pumping must be such that the outer region of the ionization chamber, that is connected to a beamline, via a small bore capillary, is maintained at high vacuum around 10^{-6} mbar. To achieve the pressures required, the spectrometer must efficiently pump away the sample gas. The pumping system is designed so that a high partial pressure of sample gas can be maintained in the central ionization region (around 10^{-3} mbar), while low pressures are maintained in the rest of the spectrometer;

- to ensure unperturbed motion of the photoelectrons,
- to prevent contamination of the inner sufaces of the spectrometer,
- to protect the electron detector system,
- and to protect the beamline.

Contamination is an acute problem in the study of reactive species and radicals, as they are usually chemically aggressive themselves, and the conditions and reactions used to produce them are also invariably contaminating. The pumping system can be seen clearly in Figures 5.6 and 5.7. The specification of the individual tubomolecular pumps used are given in Table 5.4, each of which is backed by oil sealed rotary pumps. The sample gas is admitted though the top of the spectrometer through a 12mm bore glass inlet tube (See section 5.3.7), into the ionization region. This region is surrounded by two differentially pumped boxes. These are separately pumped by turbo pumps **P1** and **P2** as shown in Figure 5.6. Most of the gas load is taken by **P1**. Both **P1** and **P2** are fitted with purge valves, that slowly admit dry nitrogen, to protect the pumps' bearings from corrosive

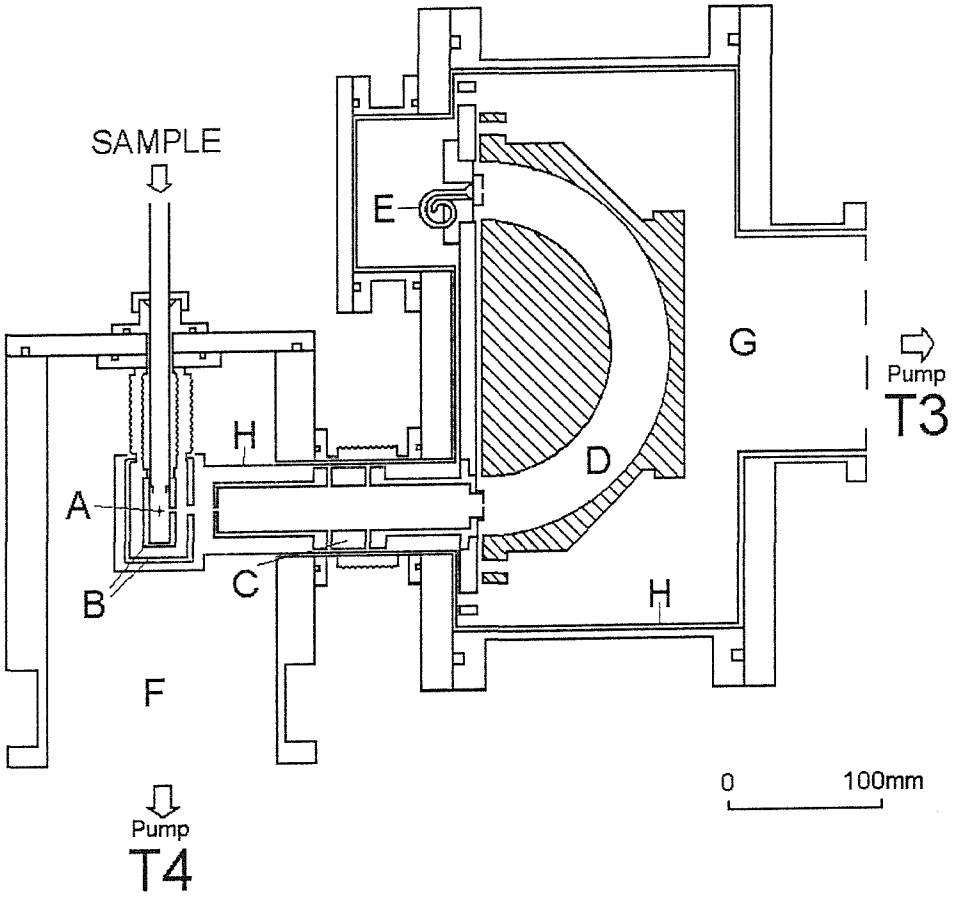

Figure 5.7: Vertical cross-section of the synchrotron spectrometer, perpendicular to the photon axis. A=photon axis/ionization region, B=containment boxes, C=electron lens, D=analyzer, E=detector, F=ionization chamber, G=analyzer chamber and H=mu-metal shielding. [9].

Pump	Pumping Speed	Type
P1	400 l/sec	Leybold Turbovac 361C
P2	400 l/sec	Leybold Turbovac 361C
P3	1000 l/sec	Leybold Turbovac 1000
P4	600 l/sec	Leybold Turbovac 600

Table 5.4: Specification of the turbomolecular pumps of the synchrotron spectrometer

gases and to extend their operational lifetime. The surrounding region provides another stage of differential pumping between the central containment boxes and the beamline, and also pumps the electron lens. This region is pumped by turbo pump **P3**. The analyzer chamber is connected to the ionization chamber only by a narrow slit, and is separately pumped by turbo pump **P4**. This minimizes contamination of the analyzer and protects the high voltage detector.

5.3.3 The shielding

Successful recording of photoelectron spectra is dependent on the energy analysis of photoelectrons by the hemispherical analyzer (See section 5.3.5). It is imperative that the photoelectrons are not perturbed by external electric or magnetic fields. Electric fields, in this case, do not pose a problem as the bulk of the spectrometer is made from non-magnetic metals (*i.e.* aluminium) that screen external electric fields. Magnetic fields are screened by surrounding the important elements of the spectrometer with a metal of very high magnetic permeability. In this case the containment boxes, electron lens, analyzer and detector are surrounded by two continuous, 1mm thick layers of μ-metal shielding (H, Figure 5.7). The μ-metal layers constrain any magnetic fields within themselves rather than allowing them to pass through. Due to the pumping constraints, there must be some holes in this shielding, but these are kept as small and as few possible to minimize field penetration.

5.3.4 Electron lens

The spectrometer is operated at a constant-pass-energy mode (*i.e.* the pass energy of the analyzer is fixed, usually to E_{pass}=5 eV). A spectrum is recorded by sweeping the acceleration imparted on the photoelectrons in a three element zoom lens [10], by altering the voltage on the lens' final element. The lens consists of three electrically isolated, co-axial, cylindrical elements. The initial element is grounded ($V_1 = 0$) so that as electrons pass through this section the photo-

electrons retain the kinetic energy from ionization (E_1). The final element has an accelerating potential (V_3), such that at any moment, for electrons that reach the the detector, $V_3 = (E_{pass} - E_1)/e$. The central element serves to focus the electrons onto the entrance slit of the analyzer and is set to a focus voltage (V_2), so that within this element the electrons have energy, E_2. The focus voltage is determined empirically by optimizing the photoelectron signal at the detector, for a range of kinetic energy of electrons. The resulting sets of voltages are used to determine a **focus curve** which is expressed as E_2/E_1 vs. E_{pass}/E_1 [10]. The parameters determined for the focus curve are input into the control software, which sets the appropriate voltages during an experiment.

5.3.5 Hemispherical analyzer

The analyzer is a 100mm mean radius (R_0), 180° hemispherical sector analyzer. The inner hemisphere and outer hemisphere have radii of 80 mm (R_{inner}) and 120 mm (R_{outer}) respectively. For a given pass energy E_{pass}, the potentials of the analyzer are set so that electrons of this energy will travel in a circular orbit and reach the detector. If $V_0 = E_{pass}/e$, then the potential difference between the two hemispheres, V, is given by equation 5.2 [11].

$$V = V_0 \left(\frac{R_{outer}}{R_{inner}} - \frac{R_{inner}}{R_{outer}} \right) \tag{5.2}$$

The **relative** potential on the inner and outer hemispheres (V_{inner}, V_{outer}) is given by equations 5.3 and 5.4.

$$V_{inner} = V_0 \left(3 - 2\frac{R_0}{R_{inner}} \right) \tag{5.3}$$

$$V_{outer} = V_0 \left(3 - 2\frac{R_0}{R_{outer}} \right) \tag{5.4}$$

$$\tag{5.5}$$

For proper alignment of the fields in the analyzer and electrostatic lens, the central path of the analyzer (mean radius= R_0) must have an **absolute** potential equal to that of V_3 (refer to section 5.3.4). This is achieved by using a battery box, with an appropriate voltage divider circuit, to produce the three voltages, V_{inner}, V_0 and V_{outer}. The V_0 output is then coupled to the third element of the electron lens (V_3). The result is that the inner and outer hemispheres maintain their potential difference but now their potentials are such that they lie appropriately either side of V_3.

The analyzer geometry and slit widths contribute a significant amount to the overall resolution of the spectrometer. This contribution to the full-width-at-half-maximum of a photoelectron band (ΔE_{FWHM}) is determined by the width of the entrance slits (ΔS_{ent}) and exit slits (ΔS_{exit}; $\Delta S = \Delta S_{ent} = \Delta S_{exit}$), the mean radius of the hemispheres and the pass energy, as given by equation 5.6 [12].

$$\Delta E_{FWHM} = 0.56 \times \frac{\Delta S}{R_0} E_{pass} \tag{5.6}$$

Therefore, the resolution of synchrotron spectrometer working at a pass energy of 5 ev is given by;

$$\Delta E_{FWHM} = 0.56 \times \frac{1\text{mm}}{100\text{mm}} 5\text{eV} = 28\text{meV}. \tag{5.7}$$

This is the ideal resolution, but in reality the geometry and the surfaces are not perfect and contamination may cause local charging effects. As a result of this, the typical working resolution is at least 40 meV.

5.3.6 Electron detection and control system

Electrons that successfully complete the journey from the ionization region, through the electrostatic lens and around the hemispherical analyzer are detected by a single channel electron multiplier (channeltron). The channeltron has a gain of around 10^5, and so for every single photon incident on the detector there is an output pulse of 1.6×10^{-14} coulombs. Each small pulse is amplified by a preamplifier circuit that is situated outside the spectrometer, as close as possible to the channeltron, to minimize noise on the weak signals. These pulses are then passed to an Ortec 590A amplifier which converts them into standard TTL pulses. The pulses can then be visibly monitored on a ratemeter and passed to a CAMAC module counter (Hytec 350A), which is monitored with a PC.

All data acquisition and control is by way of the PC controlled CAMAC crate with supporting NIM modules and power supplies. The potentials required for the electron optics for focussing (V_2) and acceleration (V_3) are supplied by Kepco APH500 and BOP100 power supplies respectively. Both of these are controlled by a pair of digital-to-analogue converters (DACS), Hytec650 and Hytec620, housed within the CAMAC crate. The PC and tailored software calculates all the necessary voltages and parameters for a scan, which are then passed to the CAMAC crate. The CAMAC crate then simultaneously scans the voltages and counts the frequency of photoelectrons for each point in a scan, and streams the data back to the PC. The combined use of PC and CAMAC module makes the system

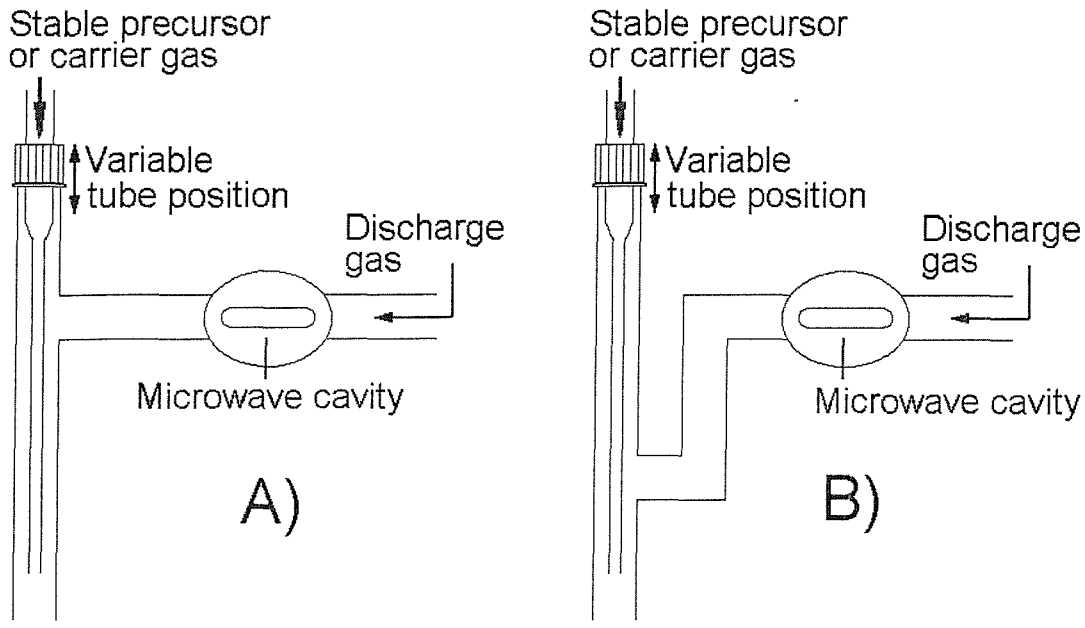

Figure 5.8: Schematic of the inlet systems used. (A)Normal inlet tube, (B)Dog-leg inlet tube.

very efficient and dead time is less than 1%. The software also integrates with the control system for the monochromator at Daresbury, facilitating CIS scans. Alternative software using the LabView environment has been developed for use at Elettra.

5.3.7 Microwave discharge and inlet system

Some of the species studied in this work were short-lived species, with lifetimes of the order of milliseconds or less under the conditions used, *i.e.* $O_2(a^1\Delta_g)$, OH and oxygen atoms. To study these using VUV-PES it was necessary to generate them *in situ*, close to the ionization region and then pump them away very rapidly.

$O_2(a^1\Delta_g)$ and oxygen atoms were generated by flowing oxygen through a microwave discharge (2.45 GHz) in a 12 mm bore, glass inlet tube as shown in Figure 5.8. $O_2(a^1\Delta_g)$ is the major molecular excited state produced, along with a negligible amount of $O_2(b^1\Sigma_g^+)$ and a substantial amount of atomic oxygen [$O(X^3P)$] [13]. The inner surfaces of the tubes were coated with a layer of boric acid to inhibit deactivation or recombination reactions at the walls of the inlet tube. The normal inlet tube (Figure 5.8 [A]) could be used to generate good yields of oxygen atoms. However these T-shaped tubes were found to be unsuitable for most CIS studies as electrons and ions may reach the ionization region from the discharge. This could cause a high background signal to be

observed when sampling low kinetic energy photoelectrons. The dog-leg tube (Figure 5.8 [B]), was used for most studies in this work, as the three 90°bends prevent charged species, produced in the microwave discharge, from reaching the ionization region of the spectrometer. For the production of $O_2(a^1\Delta_g)$, the extra bends also encourage recombination of oxygen atoms, lowering the relatively intense O atom signal. A small amount of argon was also added as a carrier gas to improve the yield of $O_2(a^1\Delta_g)$.

A fast atom-molecule reaction was used to produce the OH radical using a dog-leg tube (Figure 5.8 [B]). Hydrogen atoms were produced by dissociating H_2 in the microwave discharge, with a small partial pressure of added helium to maintain the discharge. The hydrogen atoms were subsequently reacted with NO_2 admitted via the central, inner inlet tube. The 1mm bore inner inlet tube can be seen in Figure 5.8 positioned down the centre of the inlet system. The distance between where the reaction occurs and the point of photoionization can be varied by moving the central tube up and down. This allows the effective time between mixing and photoionization to be optimized, for a maximum photoelectron signal of the OH rdical. These reactions are as given in equations 5.8 and 5.9.

$$H_2 \xrightarrow[discharge]{\mu-wave} H + H \tag{5.8}$$

$$H + NO_2 \xrightarrow[atom-molecule]{fast} OH + NO \tag{5.9}$$

The rate constant for the reaction in equation 5.9 is
$1.1 \times 10^{-10}\text{cm}^3\text{molecule}^{-1}\text{sec}^{-1}$, at room temperature [14]. Optimizing the reaction conditions is critical for this fast reaction, as the OH radical undergoes rapid secondary reactions as shown in equations 5.10 and 5.11.

$$OH + OH \longrightarrow H_2O + O \tag{5.10}$$

$$O + O + M \xrightarrow[reaction]{3rd-body} O_2 + M \tag{5.11}$$

These reactions not only reduce the partial pressure of OH, but also give rise overlapping bands in the photoelectron spectrum from water.

5.3.8 Rotation Mechanism

In order to be able to study the angular distribution of electrons for a photoionization process (section 2.4), it is necessary to use a polarized radiation source (section 2.3) and to monitor the photoelectron intensity with respect to the angle of detection from the polarization axis. It is not possible to rotate the polarization axis of a synchrotron source, so the angle of detection of photoelectrons must

be rotated with respect to the fixed, horizontal polarization axis. Traditionally, to do this, a small analyzer and detector system would be used that rotates about the photon axis, within a large vacuum chamber. However preparative conditions and pumping requirements for the prodction of short-lived molecules precluded this approach. It was necessary for the entire vacuum system, including the turbomolecular pumps to be rotated, as shown in Figure 5.9 [9]. It can be seen from Figure 5.9 that the whole spectrometer may be rotated in the plane perpendicular to the photon axis, through a range of 0° to 75°. At 0°, photoelectrons ejected parallel to the major polarization axis are detected and also the photoelectron intensity can be monitored at any angle from the major polarization axis, up to 75°.

The rotation is driven by an electric stepper-motor that rotates the screw drive mechanism, which in turn raises and lowers the analyzer side of the spectrometer. The front of the spectrometer, which must be coupled to a beamline, has a differentially pumped rotary feedthrough, to preserve the integrity of the vacuum on rotation of the spectrometer.

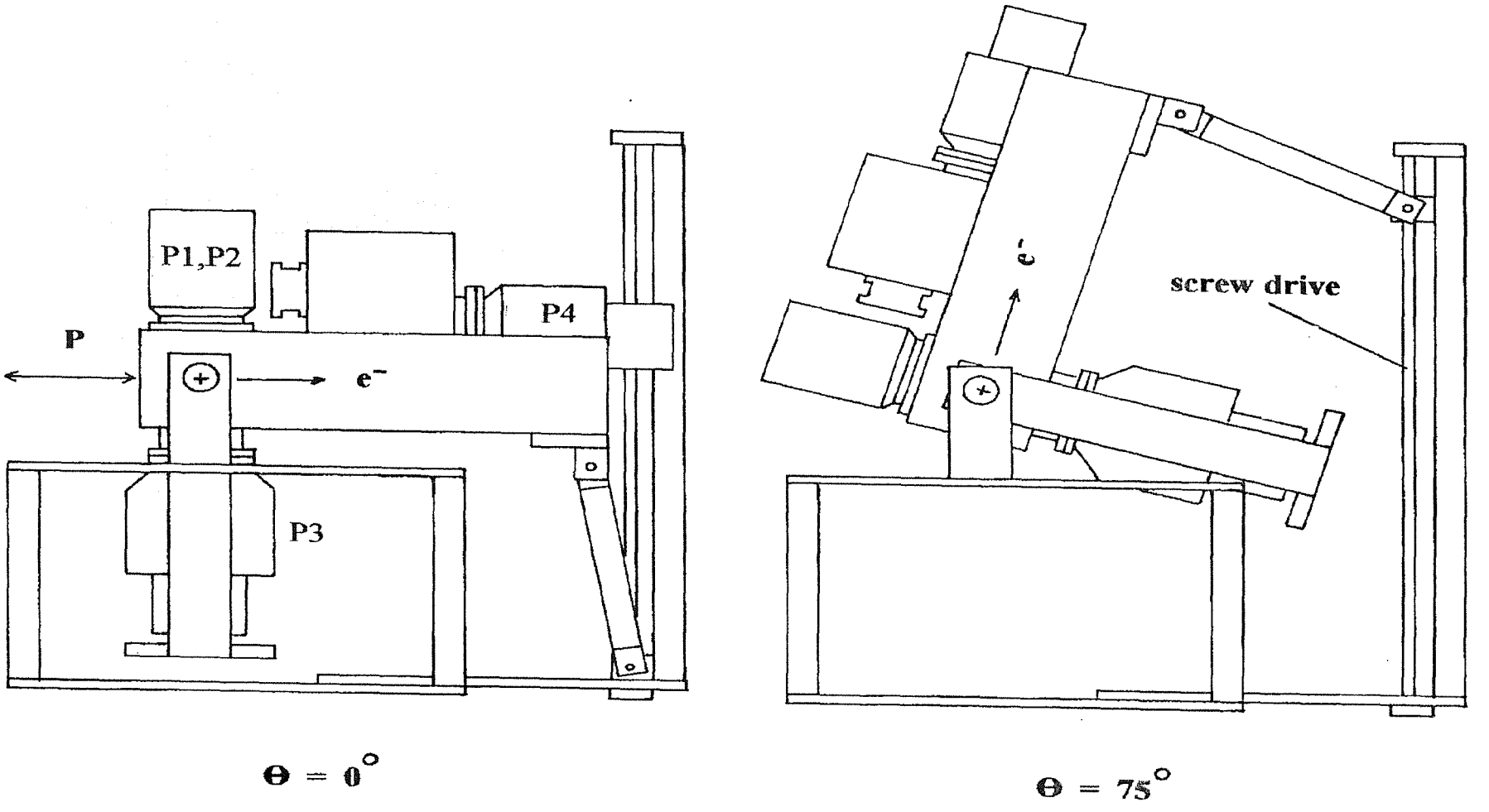

Figure 5.9: Schematic of the rotation mechanism. The spectrometer is depicted at the two extremes of rotation, 0° and 75°. P1-P4 are the four turbomolecular pump, and P indicates the plane of polarization of radiation, from either of the synchrotron sources.

5.4 High-temperature photoelectron spectrometer

The high-temperature spectrometer used in this work is a photoelectron spectrometer, designed to study short-lived molecules, that has been adapted for high-temperature work [15–17]. This spectrometer is similar to the synchrotron spectrometer, but uses a helium discharge lamp as a photon source (as described in section 5.2.1). The main components of the high-temperature spectrometer and its differences from the previously described synchrotron spectrometer are outlined below.

5.4.1 The Vacuum system

A schematic of the spectrometer showing the main pumps is shown in Figure 5.10. As with the synchrotron spectrometer, the design uses separate ionization and analyzer chambers, to prevent contamination of the analyzer and to protect the detector. The analyzer and ionization chambers are separately pumped by six-inch, oil diffusion pumps with a pumping speed of 1300 l/sec. Both diffusion pumps are each backed by suitable oil-sealed rotary pumps. The front diffusion pump is fitted with a liquid nitrogen trap, to prevent any back-streaming of oil or moisture into the sensitive ionization region. A separate rotary pump is used to differentially pump the discharge lamp to minimize the amount of helium diffusing into the ionization chamber. The base pressure of the spectrometer with no gas load is routinely 6×10^{-6} mbar. During the acquisition of photoelectron spectra, the pressure in the ionization chamber can be as high as 10^{-4} mbar, while the pressure in the analyser chamber remains well below 10^{-5} mbar.

5.4.2 Magnetic shielding

As with the synchrotron spectrometer, care must be taken to shield the spectrometer from the Earth's magnetic field and any stray fields from nearby electronic equipment. The spectrometer is fabricated from non-magnetic materials and is surrounded by three mutually perpendicular sets of Helmholtz coils (instead of μ-metal shielding) [19]. The current flowing in each of the three pairs of coils can be adjusted independently to produce magnetic fields that neutralize any local fields including the Earth's magnetic field. This is achieved by an iterative process of adjusting the current in each pair of coils, and monitoring a real photoelectron signal (usually the argon doublet). The result of this is that the ionization and analyzer chambers lie within a field free region.

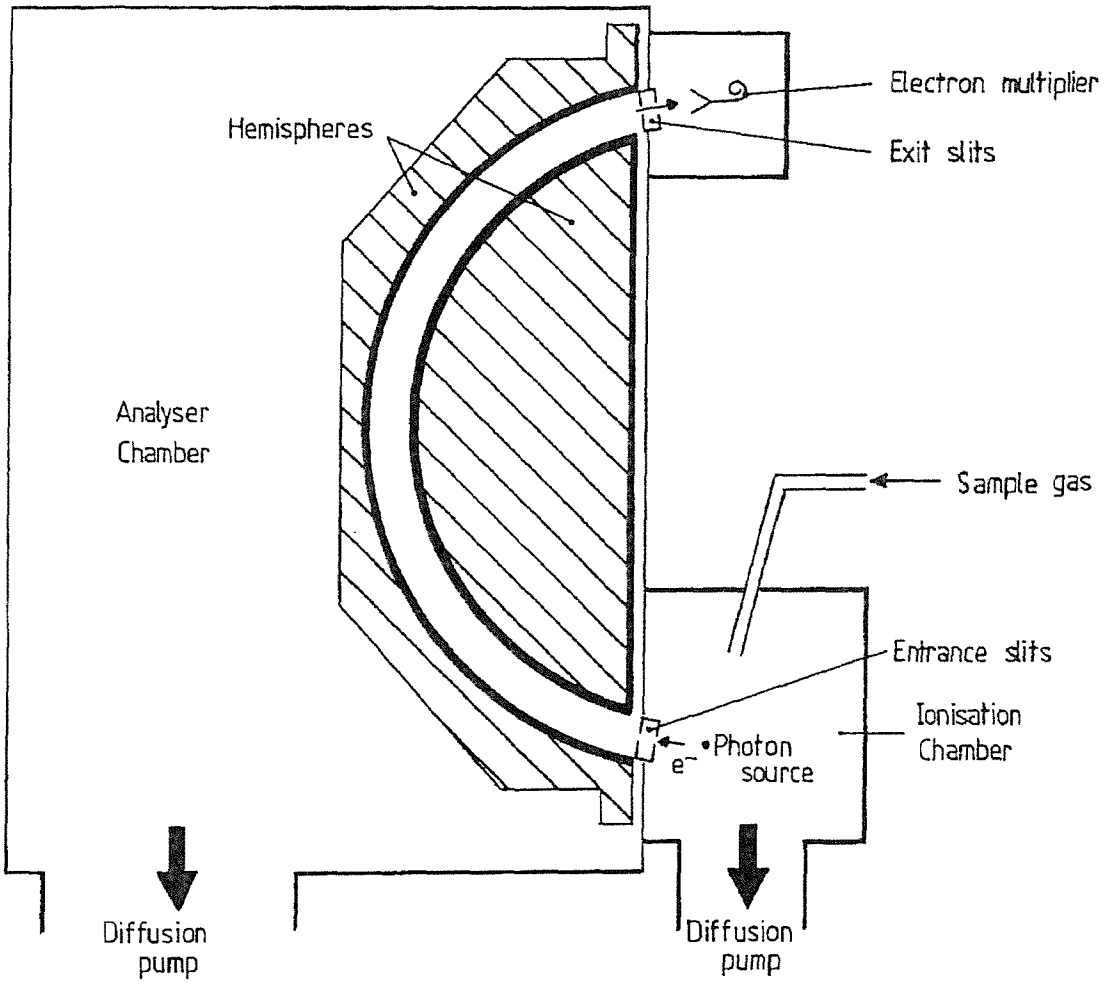

Figure 5.10: Schematic of the high-temperature spectrometer. The cross-section is perpendicular to the photon axis with the helium discharge lamp mounted on the far side. [18]

5.4.3 Hemispherical analyzer

The electron energy analyzer is a hemispherical deflection analyzer, similar to that described in section 5.3.5. In this case the hemispherical analyzer has a mean radius of 200 mm and angle of 150°. The reduced angle removes the need for electron optics to focus the photoelectrons from the point of ionization to the entrance to the analyzer and allows the positioning of slits between the points of production and detection. To satisfy the double-focussing condition the ionization point, the detector and the centre of the hemispheres all lie in a single plane. The photoelectrons are produced in only a very small volume, due to the collimation of the photon source, and are therefore effectively already focussed at this point. The use of a 150° analyzer allows the extra room needed to generate the photoelectrons at the geometrically ideal point for double-focussing. If, as in the case for the synchrotron spectrometer, a full 180° analyzer is employed, then the photoelectrons must be extracted and then refocussed.

The simplicity of the analyzer makes the spectrometer robust and easy to disassemble for cleaning purposes. This is important particularly when working with corrosive samples, or with low volatility compounds. However, without an electron lens there is no means to accelerate or retard photoelectrons and this precludes working in a constant pass energy mode. Altering the pass energy during the acquisition of a photoelectron spectrum will affect both the transmission and resolution of the spectrometer (as described in section 5.3.5), and this needs to be taken into account when spectra are analyzed. In practice, to acquire a photoelectron spectrum, the potential difference between the hemispheres is swept linearly. This means that the energy of the electrons focussed onto the detector also changes linearly. The transmission is proportional to the pass energy of the analyzer and the instrumental contribution to the resolution also increases as the pass energy increases [20].

5.4.4 Electron detection and control system

The detector of the high-temperature photoelectron spectrometer is a single channel electron multiplier (channeltron), identical to that described in section 5.3.6. As for the synchrotron spectrometer, the photoelectron signal is immediately preamplified before being passed to an amplifier and discriminator. The photoelectron intensity is displayed on an Ortec ratemeter which acts as a frequency-to-analogue converter, providing input into a PC. To record a photoelectron spectrum, the voltages on the inner and outer hemispheres of the analyzer are swept

by a ramp generator, thus altering the pass energy, while the photoelectron intensity is continuously recorded.

5.4.5 The high-temperature furnace

The high-temperature spectrometer is fitted with a high-temperature induction heater. This was used, in this work, for both evaporation experiments (Chapter 9) pyrolysis experiments (Chapter 10).

Other than induction heating, suitable heating methods available are resistive heating and laser heating. Laser heating of solids has seen some limited use for PES, but tends to produce erratic partial pressures of the sample [21,22]. Resistive heating has been used extensively in PES and can be used for temperatures up to 1800°K [23]. In this work it was found to be problematic to use resistive heaters above ≈1300°K as the electromagnetic fields they generate begin to affect the resolution of the spectrometer, even when non-inductively wound heating elements were used.

Within the Southampton PES group a radio frequency (RF) induction heating system was developed that can be mounted directly onto a photoelectron spectrometer, and vaporize samples up to 2500°K [17]. A schematic of the high-temperature induction heater assembly mounted onto the high-temperature spectrometer is shown in Figure 5.11.

RF induction heating works by using the rapidly fluctuating magnetic field produced by RF current flowing in an induction coil, to induce currents in a susceptor. The susceptor is a conductor placed within the induction coil and is heated due to its resistance to the eddy currents induced within it. The heat energy produced in the susceptor (H) is related to its resistance (R) and the induced currents (I) as shown in equation 5.12.

$$H \propto I^2 R, \tag{5.12}$$

where R is the resistance of the susceptor as given by equation 5.13

$$R = \rho \times \frac{length}{cross - section}, \tag{5.13}$$

where ρ is the resistivity of the susceptor. The induced current (I) is proportional to the rate of change of the magnetic field. From the above equations it is evident that to efficiently heat a susceptor, a high frequency current must be used coupled with a susceptor of reasonable resistivity. In this work a home built 1 MHz RF generator was used [17] that was designed by A. Morris. Various susceptor

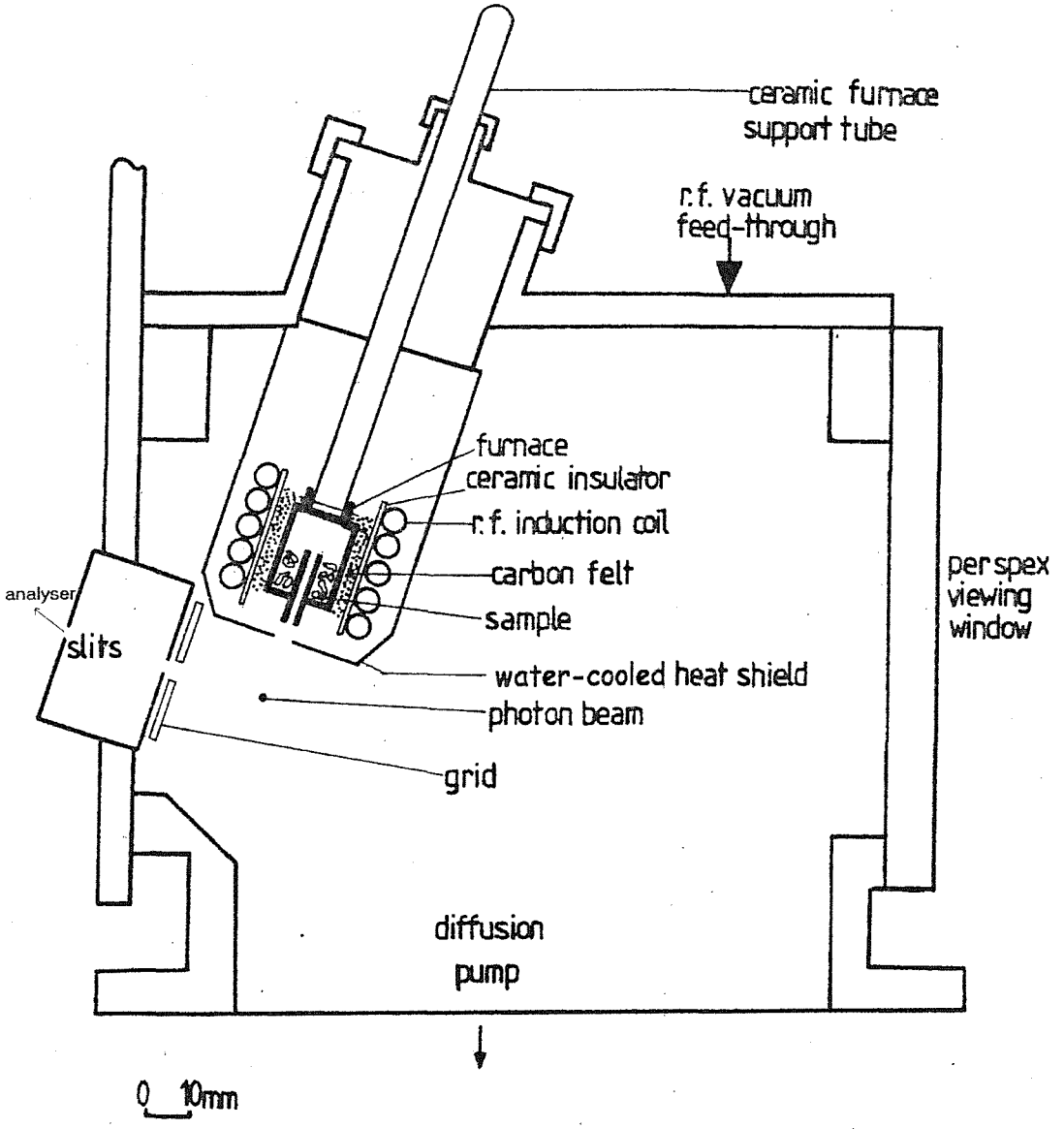

Figure 5.11: Schematic of the RF-furnace mounted onto the high-temperature spectrometer used in this work.

materials were used including graphite and tantalum depending on the nature of the proposed experiment.

A further consideration when using RF heating is the **skin effect**. This arises because the induced current is induced in the surface of a susceptor, penetrating to a skin depth (d) given by equation 5.14 [24].

$$d = \left(\frac{1}{2\pi}\right)\left(\frac{\rho \times 10^9}{\mu f}\right), \tag{5.14}$$

where d is in cm, ρ is in Ωcm, μ is the relative magnetic permeability of the susceptor and f is the frequency of the RF supply [25]. The skin effect means that all the heat will be produced in the surface layer of the susceptor and subsequently conducted to the rest of its bulk. This was taken into account in the design of the susceptor furnaces used in this work and they were fabricated so that the thickness of the walls of a hollow, cylindrical susceptor were approximately equal to the skin depth. This results in rapid, efficient and even heating of the susceptor furnace, containing within its walls a sample to be vaporized (as in Figure 5.11). Figure 5.11 also shows some other important aspects of the heating system:

- The susceptor furnace is mounted on the end of a hollow alumina rod (ceramic furnace support tube) through which a carrier gas or calibrant may be passed. Vaporized sample is collimated via a capillary to give a good partial pressure around the photon beam.
- The susceptor furnace is thermally insulated by a layer of carbon felt surrounding it.
- The carbon felt and the RF induction coils are separated by a ceramic insulator to prevent electrical shorting.
- The induction coils are 1/4" copper pipe, wound into a helix and kept cold by cold water flowing through them.
- The RF heating assembly is surrounded by a water-cooled heat shield, that prevents any radiative heating of spectrometer components.

This design allows the heating of solid or vapour samples up to 2500°K in very close proximity to the photoionization region while all of the surrounding spectrometer remains cool.

To prevent electrical interference from the RF induction heater with the detection electronics, the RF supply is switched on an off at 50 Hz. Photoelectron signal is only collected while the RF current is **off**. Operating in this mode does

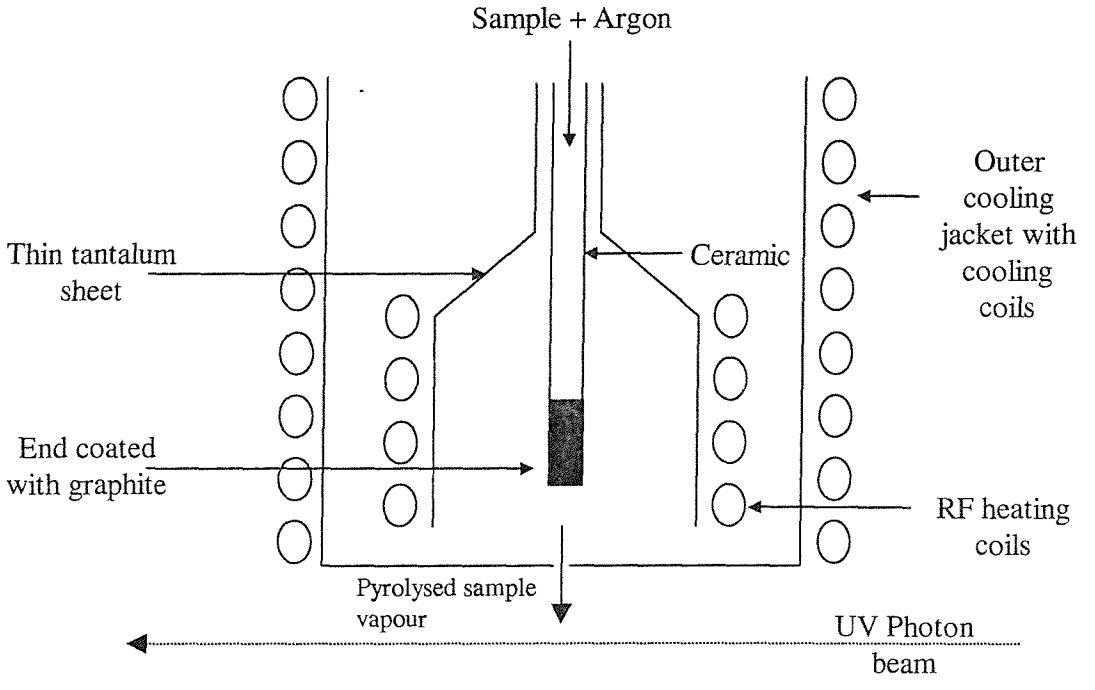

Figure 5.12: Schematic of inductive/radiative heating system used for pyrolysis experiments

not affect the resolution or transmission of the spectrometer, but unfortunately ≈60% of signal intensity is lost. [26]

In this work, directly inductively heated, graphite furnaces were used for the studies involving the involatile actinide tetrahalides (Chapter 9), as this type is the most efficient for working at high temperatures (>1300°K for samples that do not react with graphite). For the pyrolysis studies of the azides (Chapter 10), graphite furnaces were unsuitable as at the temperatures used as they are reactive with the sample compounds, and are not solid at room temperature. The azides were liquids, and had sufficient vapor pressure to be kept outside the spectrometer and admitted via the alumina support tube into the centre of the RF induction heater. The outside of the alumina tube was coated with graphite in the induction region and was radiatively heated by a tantalum susceptor as shown in Figure 5.12. The tantalum sheet susceptor is efficiently, inductively heated and then radiatively heats the alumina tube. With this set-up, the sample passes through the heated region and is pyrolyzed shortly before it reaches the region where it is photoionized. By varying the temperature of the heated region, it is possible to observe photoelectron bands from both short-lived and longer-lived products and understand pyrolysis mechanisms (See Chapter 10).

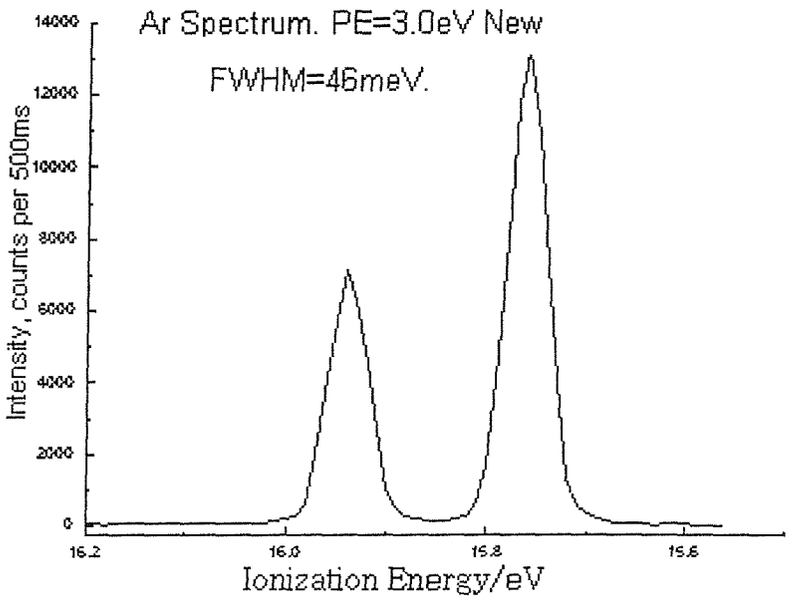

Figure 5.13: Example HeI (21.22eV) photoelectron spectrum of argon.

5.5 Types of spectra

5.5.1 Photoelectron spectra

In an ordinary photoelectron spectrum, the photoelectron intensity is measured as a function of the ionization energy [2]. In reality the photoelectron intensity is actually recorded by sampling the different kinetic energies of photoelectrons produced when a monochromatic source of radiation is incident on a sample. The ionization energy is then calculated by simple subtraction. An example of a HeI photoelectron spectrum of argon is given in Figure 5.13. This is the traditional type of spectrum used in photoelectron spectroscopy (for many more examples see ref. [27]).

5.5.2 Constant ionic state spectra

A constant ionic state (CIS) spectrum measures the relative cross-section of a certain ionization process as a function of photon energy. This requires a tunable photon source, such as a synchrotron (Chapter 3). In a CIS spectrum the photon energy is scanned at the same time as the particular ionization energy that is being sampled, so as to maintain a constant ionic state, i.e. the energy separation between the initial molecular state and final ion state does not change.

To run a CIS spectrum of a molecule, it is usual to first acquire a conventional PES spectrum from which an accurate ionization energy for the particular ionic

Species studied	Photon source	Spectrometer	Chapter
$O_2(a^1\Delta_g)$	synchrotron, SRS	synchrotron spectrometer	6
O atoms	synchrotron, Elettra	synchrotron spectrometer	7
OH	synchrotron, Elettra	synchrotron spectrometer	8
UBr_4 and $ThBr_4$	helium lamp	High-temp. spectrometer	9
azides	helium lamp	High-temp. spectrometer	10
F_2O	helium lamp	High-temp. spectrometer	11

Table 5.5: Summary of experimental details

state and vibrational component of interest can be determined. A CIS scan can then be taken by looking at the dependence of the ionization efficiency on photon energy, for the specified ionization.

A CIS spectrum may show sharp features due to resonant ionization via an autoionizing Rydberg state, usually increasing the overall ionization efficiency (see Section 2.2). An example CIS spectrum is given in Figure 5.14 from a previous study on $O_2(a^1\Delta_g)$ [28].

This chapter has outlined the experimental methods used in this thesis and their main features, and a brief summary of the main components for all the experiments is given in Table 5.5.

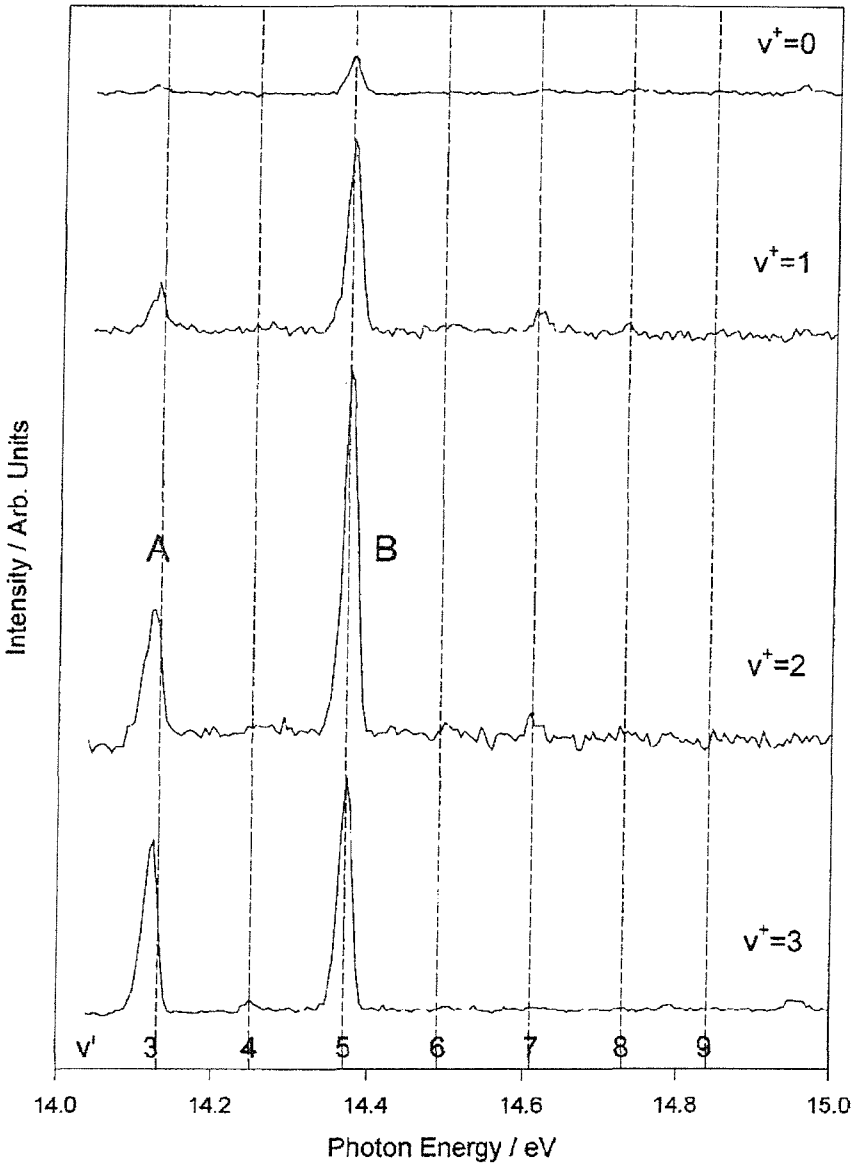

Figure 5.14: Example CIS spectra recorded for $O_2^+(X^2\Pi_g\, v^+) \leftarrow O_2(a^1\Delta_g\, v'' = 0)$for $v^+ = 0, 1, 2, 3$. [28].

Bibliography

[1] J. A. R. Samson, *Techniques of Vacuum Ultraviolet Spectroscopy* (Wiley, New York, 1967).

[2] J. H. D. Eland, *Photoelectron Spectroscopy* (Butterworths, London, UK, 1974).

[3] A. DeFanis, Ph.D. thesis, Department of Physics and Astronomy, University of Southampton, 2000.

[4] H. G. Beutler, Journal of the Optical Society of America **35**, 111 (1945).

[5] SRS Station 3.3, User Guide and Manual, Toroidal Grating Monochromator, SRS. Daresbury Laboratories.

[6] R. P. Walker and B. Diviacco, Rev. Sci. Instrum. **63**, 332 (1992).

[7] ELETTRA,Trieste, Italy, Conceptual Design Report, 1989, internal publication.

[8] A. Derossi, F. Lama, M. Piacentini, T. Prosperi, and N. Zema, Rev. Sci. Instrum. **66**, 1718 (1995).

[9] J. M. Dyke, S. D. Gamblin, A. Morris, T. G. Wright, A. E. Wright, and J. B. West, J. Electron Spect. Relat. Phenom. **97**, 5 (1998).

[10] E. Harting and F. H. Read, *Electrostatic lenses* (Elsevier, Amsterdam, 1976).

[11] C. E. Kuyatt and J. A. Simpson, Rev. Sci. Instrum. **38**, 103 (1967).

[12] A. Poulin and D. Roy, J. Phys. E. **11**, 35 (1978).

[13] N. Jonathan, M. Okuda, K. J. Ross, and D. J. Smith, J. Chem. Soc., Far. Trans.II **70**, 1810 (1974).

[14] P. P. Bernard and M. A. A. Clyne, J. Chem. Soc., Far. Trans.II **73**, 394 (1977).

[15] J. M. Dyke, N. Jonathan, and A. Morris, in *Electron Spectroscopy*, edited by C. R. Brundle and A. D. Baker (Academic Press, New York, 1979), Vol. 3, p. 189.

[16] J. M. Dyke, N. Jonathan, and A. Morris, Int. Rev. Phys. Chem. **2**, 3 (1982).

[17] D. Bulgin, J. M. Dyke, F. Goodfellow, N. Jonathan, E. P. F. Lee, and A.Morris, J. Electron Spect. Relat. Phenom. **12**, 67 (1977).

[18] M. P. Hastings, Ph.D. thesis, Department of Chemistry, University of Southampton, 1986.

[19] J. W. Rabalais, *Photoelectron Spectroscopy* (Wiley and Sons, London, UK, 1977).

[20] J. L. Gardner and J. A. R. Samson, J. Elect. Spec. Relat. Phenom. **8**, 469 (1976).

[21] T. D. Goodman, L. C. Cusachs J. D. Allen, and G. K. Schweitzer, J. Elect. Spec. Relat. Phenom. **3**, 289 (1974).

[22] D. G. Streets and J. Berkowitz, J. Elect. Spec. Relat. Phenom. **9**, 269 (1976).

[23] J. Berkowitz, *Electron Spectroscopy, Techniques and Applications* (Academic Press, London, 1979).

[24] C. A. Adams, J. C. Hodge, and M. H. Mackusick, Elec. Eng. **53**, 194 (1934).

[25] D. Haggerston, Ph.D. thesis, Department of Chemistry, University of Southampton, 1995.

[26] J. M. Dyke, A. Morris, G. D. Josland, M. P. Hastings, and P. D. Francis, High Temperature Science **22**, 95 (1986).

[27] K. Kimura, *Photoelectron Spectroscopy of Small Molecules* (Japan Scientific Societies Press/Halstead Press, Tokyo/New York, 1974).

[28] J. D. Barr, A. De Fanis, J. M. Dyke, S. D. Gamblin, A. Morris, S. Stranges, J. B. West, T. G. Wright, and A. E. Wright, J. Chem. Phys. **109**, 2737 (1998).

Chapter 6

Angle-resolved photoelectron spectroscopy of $O_2(a^1\Delta_g)$ with synchrotron radiation

6.1 Introduction

This chapter presents work on the angular resolved photoelectron spectroscopy of $O_2(a^1\Delta_g)$ carried out at the SRS at Daresbury Laboratories. This continues the Southampton PES group's work on short-lived, atmospherically important, diatomic species, studied with synchrotron radiation, notably SO [1], CS [2], OH [3], OD [3] and specifically $O_2(a^1\Delta_g)$ [4]. The work described here may also be found in a recently published paper [5].

The interaction of VUV radiation with oxygen has received considerable attention, due to its importance in the photochemistry of the upper atmosphere. $O_2(a^1\Delta_g)$ and $O(^1D)$ are produced from photodissociation of ozone in the troposphere. Photoionization of $O_2(a^1\Delta_g)$ has been suggested as an important source of ions in the D region of the atmosphere. This could help to explain both the relatively high O_2^+ partial pressure and the high total ion densities at these altitudes (<70 km) [6]. Spectroscopic investigations on oxygen have been mainly directed at its ground state, $X^3\Sigma_g^-$. Hence, less is known about photoionization of O_2 from its metastable state $a^1\Delta_g$.

The ground electronic configuration of molecular oxygen is;

$$1\sigma_g^2\,1\sigma_u^2\,2\sigma_g^2\,2\sigma_u^2\,3\sigma_g^2\,1\pi_u^4\,1\pi_g^2, \tag{6.1}$$

which gives rise to the $O_2(X^3\Sigma_g^-)$, $O_2(a^1\Delta_g)$ and $O_2(b^1\Sigma_g^+)$ states. The HeI ($h\nu$=21.22 eV) photoelectron spectrum of ground state oxygen ($O_2(X^3\Sigma_g^-)$) has been well characterized since the early PES work of Turner and May [7,8], and Edqvist [9]. The HeI photoelectron spectrum of the first excited state, $O_2(a^1\Delta_g)$,

Ionization	Ionic state	AIE from $X^3\Sigma_g^-$/eV	AIE from $a^1\Delta_g$/eV
$1\pi_g$	$X^2\Pi_g$	12.08	11.10
$1\pi_u$	$a^4\Pi_u$	16.10	-
$1\pi_u$	$A^2\Pi_u$	17.04	16.06
$3\sigma_g$	$b^4\Sigma_g^-$	18.17	-
$1\pi_u$	$C^2\Phi_u$	-	17.51
$3\sigma_g$	$D^2\Delta_g$	-	18.81
$3\sigma_g$	$B^2\Sigma_g^-$	20.30	-

Table 6.1: AIEs and symmetries of the states of O_2^+ accessible from dipole photoionization of $O_2(X^3\Sigma_g^-)$ and $O_2(a^1\Delta_g)$ with a photon energy of $21.22eV$. [12]

has also been studied in detail [10,11]. The difference in energy of the $O_2(X^3\Sigma_g^-)$ and $O_2(a^1\Delta_g)$ states is 0.98 eV. A summary of the adiabatic ionization energies (AIEs) from the ground and first excited state of O_2, taken from HeI photoelectron spectra is given in Table 6.1.

The selection rules for dipole photoionization mean that different states are acccessible on ionization from the two neutral states of O_2 and this can be seen in Table 6.1.

A sixth band of unknown symmetry has been discovered by Baltzer *et al.*, in a high resolution HeI PES study of $O_2(X^3\Sigma_g^-)$ [13]. This band was at an AIE of 20.35 eV, interspaced between the vibrational progression of the $B^2\Sigma_g^-$ band. The new band is very weak and it most likely corresponds to a formally forbidden ionization that becomes allowed by configuration interaction.

Rydberg series (see section 1.4) converging to the ionic states of oxygen have been widely studied by VUV photoabsorption spectroscopy, dispersed emission spectroscopy and high resolution photoionization mass spectrometry. A paper by Lindholm summarized the known Rydberg series (up to 1968) converging to the $X^2\Pi_g$, $a^4\Pi_u$, $A^2\Pi_u$, $b^4\Sigma_g^-$, $D^2\Delta_g$, $B^2\Sigma_g^-$ and $c^4\Sigma_u^-$ states of O_2^+ [14]. This was later augmented by Yoshino and Tanaka [15] who added extra information on the Rydberg series converging to the $b^4\Sigma_g^-$ and $B^2\Sigma_g^-$ states of O_2^+. A high resolution photoionization mass spectrometry study by Dehmer and Chupka, of $O_2(X^3\Sigma_g^-)$, reported Rydberg series converging to the $a^4\Pi_u$, $b^4\Sigma_g^-$, $B^2\Sigma_g^-$ and $c^4\Sigma_u^-$ states of O_2^+ [16]. Studies of the photoionization efficiency curves for isotopically substituted $O_2(X^3\Sigma_g^-)$ by Nishitani and co-workers also found Rydberg series converging to the $a^4\Pi_u$, $A^2\Pi_u$, $b^4\Sigma_g^-$ and $B^2\Sigma_g^-$ ionic states of O_2 [17].

The absorption spectrum of $O_2(a^1\Delta_g)$ in the VUV region has been investigated by Katayama, Huffman and co-workers [18–20]. A vibrationally resolved band at $\approx$14.0 eV was assigned to $(C^2\Phi_u,\ 3s\sigma_g)p^1\Phi_u v' \leftarrow a^1\Delta_g v'' = 0$ excita-

tions. Some vibrational components of this band were rotationally resolved and more intense than others; this effect was attributed to a vibrationally dependent competition between autoionization and predissociation of the excited state [5].

The early absorption studies were restricted to the use of the poor continuous VUV radiation produced by rare discharge lamps [21]. The availability of synchrotron radiation has enabled PES to be used, to understand better, photoionization processes. This intense continuous photon source has been exploited by measuring CIS spectra for selected vibronic components of the ion. Measuring the intensity of the ionization with respect to photon energy, allows the study of contributions of the different autoionization channels (via Rydberg states) for each of the different vibrational components of the ion.

Prior to the work by the Southampton PES group on $O_2(a^1\Delta_g)$ [4], previous CIS studies only looked at photoionization of ground state molecular oxygen, $O_2(X^3\Sigma_g^-)$. CIS spectra for the $X^2\Pi_g$, $b^4\Sigma_g^-$ and $B^2\Sigma_g^-$ states of $O_2(X^3\Sigma_g^-)$ in the photon energy region 18.5-25.0 eV, were measured by Cafolla *et al.* in 1989 [22]. In this energy range Rydberg states converging to the $B^2\Sigma_g^-$ and $c^4\Sigma_u^-$ ionic states were found, and also a shape resonance centered at an energy of 21.5, was observed eV [22].

CIS spectra were measured for the first PE band of $O_2(X^3\Sigma_g^-)$ in the 14.75-15.05 eV region by Čubrić *et al.* in 1996 [23]. In this energy region, autoionizing Rydberg states of a $^3\Pi_u$ series converging to the second ionic limit were found.

The work reported here directly follows on from the only previous CIS study of $O_2(a^1\Delta_g)$, undertaken by the Southampton PES group. In the $O_2^+(X^2\Pi_g\, v^+ = 0-3) \leftarrow O_2(a^1\Delta_g\, v'' = 0)$ constant ionic state spectra (CIS) [4], resonances in the region between 14.0 and 15.0 eV were found at energies corresponding to the $O_2^*(^1\Phi_u v') \leftarrow O_2(^1\Delta_g v'' = 0)$ excitations observed by Katayama [19]. The vibrational patterns in this region showed relative intensities very different from those expected from the results of Franck-Condon-Factor (FCF) calculations carried out assuming no predissociation in the excited resonant state. Further analysis [4] confirmed and clarified the earlier hypothesis of competition between autoionization and predissociation [5]. Excited states that autoionize via Rydberg states were also found in the CIS spectra, in the photon energy range 18.0-19.0 eV, for the $O_2^+(X^2\Pi_g\, v^+ = 0-3) \leftarrow O_2(a^1\Delta_g\, v'' = 0)$ band. It was thought that two overlapping vibrational progressions were observed, with the first member of the lower energy progression at an energy of 18.46 eV. The only state of O_2^+ accessible on ionization from neutral $O_2(a^1\Delta_g)$ above 18.0 eV is the $D^2\Delta_g$ state (AIE=18.81 eV); therefore the resonant Rydberg state associated with the observed 18.46 eV

series was tentatively assigned as $(D^2\Delta_g\, 7p\pi)$ [4,12].

6.2 Angle resolved PES of O_2

Linearly polarized, synchrotron radiation, allows angle resolved PE measurements to be recorded. The angular distribution of photoelectrons has long been an important topic in PE spectroscopy. It has been known since 1948 [24] that for electric dipole photoionization of a randomly oriented sample with elliptically polarized radiation, the angular distribution of photoelectrons in the plane perpendicular to the incoming radiation, can be expressed as previously given section 2.4 (equation 2.23).

$$\frac{d\sigma}{d\theta} = \frac{\sigma}{4\pi}\left\{1 + \frac{\beta}{4}\left[3S_1\cos(2\theta) + 1\right]\right\}, \tag{6.2}$$

where S_1 is the degree of linear polarization, θ is the angle between the direction of the photoelectron and the axis of major linear polarization, σ is the integrated cross section and β is the asymmetry parameter.

In equation 6.2, the dynamical and geometrical information is separated: all the dynamical information is included in β. The asymmetry parameter can be expressed in terms of matrix elements of the dipole operator with the bound molecular orbital and the free electron wave function, both for photoionization of atoms (as in equation 2.24) [25], or diatomic molecules [26,27]. From equation 2.24, it is seen that the asymmetry parameter β depends on the relative **strengths** and the **phase difference** of the degenerate channels of ejected photoelectrons with different angular momenta. Photoelectron channels with different angular momenta gain strength when the photoionization occurs via an intermediate highly-excited state, as in autoionization. This means that the β parameter is also dependent on the nature of the intermediate state. The higher angular momentum components of the photoelectron become stronger at resonant energies. This is due to the angular momentum of the electron trapped, in a Rydberg orbital, coupling with the angular momentum of the final state (ion plus free electron) during the lifetime of the autoionizing state. Therefore, channels with higher value of l can be increased in strength, when the electron is emitted [12].

Measurements of the asymmetry parameter (β) and its energy dependence can reveal additional information over that derived from the integrated cross section σ measured as a function of photon energy, because of its different dependence on quantities describing the dynamics of the photoionization process. This is why there has always been great interest in angular distribution stud-

ies of small molecules. It appears that, despite the fundamental importance of radicals and other reactive species in chemistry, angle resolved PE experiments on molecules have so far only focused on stable species. This chapter reports results on the angular distribution of photoelectrons for the processes $O_2^+(X^2\Pi_g\, v^+) \leftarrow O_2(a^1\Delta_g\, v'' = 0) + h\nu$ at the photon energy of 21.22 eV and in the ranges 13.8-15.2 eV and 18.0-19.2 eV [5].

6.3 Experimental

The experiment was carried out on beam-line 3.3 at the synchrotron radiation source located at Daresbury Laboratory (as described in section 5.2.2). The synchrotron spectrometer described in section 5.3 was used for these studies. Experimentally measured angular distributions have been corrected for instrumental effects by measuring the intensity of isotropic ($\beta = 0$) PE bands: $Ar^+(^2P) \leftarrow Ar(^1S)$ at $h\nu = 16.53$ eV [28, 29], and $N_2^+(A^2\Pi_u v^+ = 0) \leftarrow N_2(^1\Sigma_g^+ v = 0)$ at $h\nu = 19.30$ eV [30] at different angles. The results of this angular calibration have been cross checked by measuring the angular distribution of photoelectrons from Ar and He at some photon energies, where they have known β values [28, 29] (β is always 2 for He). This last test confirmed that the instrumental correction on the measured angular distribution was the same at different electron kinetic energies in the range investigated. This angular calibration is made more challenging because the complete spectrometer is rotated, making maintainence of the alignment of the rotation axis with the photon beam difficult; in fact, the biggest contribution to the uncertainty reported for the present work is due to the reproducibility of the angular calibration. The resolution in a typical PES spectrum was 40 meV, and about 20 meV in a typical CIS spectrum. $O_2(a^1\Delta_g)$ was produced by passing oxygen through a microwave discharge (2.45 GHz) in a glass inlet tube, as described in section 5.3.7. The synchrotron photon energy was calibrated by recording CIS spectra for the $O^+(^4S) \leftarrow O(^3P)$ and $Ar^+(^2P) \leftarrow Ar(^1S)$ photoionization processes in the photon energy regions 13.5-19.0 eV and 26.5-29.0 eV, and comparing the positions of the resonances with those known in the literature [31,32]. The degree of linear polarization of the radiation was unknown for the energies of interest. It was measured using Xe as a calibrant, for which β-parameters are known [30], and it was found to be 0.90±0.02. The asymmetry parameters for $O_2(a^1\Delta_g)$ (and also $O_2(X^3\Sigma_g^-)$ and O atoms) were measured at a selected photon energy, or over a photon energy range, by recording PE and CIS spectra at two different angles (0°and 75°) with respect to the main polarization

axis of the photon source; at each photon energy the β-parameter was calculated from the experimental intensity ratio at these angles using Equation 6.2.

6.4 Results and discussion

The results presented here are divided into the following sections:

1. Angle resolved photoelectron spectra of the discharge products of O_2 recorded at the non-resonant photon energy of 21.22 eV. This photon energy was chosen so that the spectra would be directly comparable with HeI spectra recorded with a traditional helium discharge lamp.

2. Angle resolved photoelectron spectra recorded at the photon energies of 14.11 and 14.37 eV. These energies correspond to the $O_2^*(p^1\Phi_u\, v' = 3, 5) \leftarrow O_2(a^1\Delta_g\, v'' = 0)$ resonances [19].

3. CIS spectra and asymmetry parameters for the $v^+ = 0 - 3$ components of the $O_2^+(X^2\Pi_g\, v^+) \leftarrow O_2(a^1\Delta_g\, v'' = 0)$band measured in the photon energy ranges 13.8-15.2 eV, where the above resonances occur.

4. CIS spectra and asymmetry parameters for the $v^+ = 0 - 3$ components of the $O_2^+(X^2\Pi_g\, v^+) \leftarrow O_2(a^1\Delta_g\, v'' = 0)$band measured in the photon energy range 18.0-19.2 eV, where from the work of reference [4] autoionizing resonances are known to exist.

6.4.1 Photoelectron spectra at hν= 21.22 eV

Photoelectron spectra of the discharge products of O_2 recorded at the photon energy of 21.22 eV at $\theta = 0°$ and $\theta = 75°$ are shown in the lower panel of Figure 6.1. The two spectra have been plotted on the same vertical scale (counts normalized by photon flux), as is the case for all other plots, and the change in intensity at the two different angles is therefore directly observable from the figure. It can be clearly seen that for each of the v^+ components in the $O_2^+(X^2\Pi_g\, v^+) \leftarrow O_2(a^1\Delta_g\, v'' = 0)$ band, the asymmetry parameter is close to zero as these components have the same intensities at the two angles. The result is quite different for the $O_2^+(X^2\Pi_g\, v^+) \leftarrow O_2(X^3\Sigma_g^-\, v'' = 0)$ band. When moving from $\theta = 0°$ to $\theta = 75°$, it shows a different vibrational pattern and the change in intensity is different for the different vibrational components. In these spectra the $O^+(^4S) \leftarrow O(^3P)$ band at 13.61 eV ionization energy is also present and shows a clear difference in intensity between $\theta = 0°$ and $\theta = 75°$.

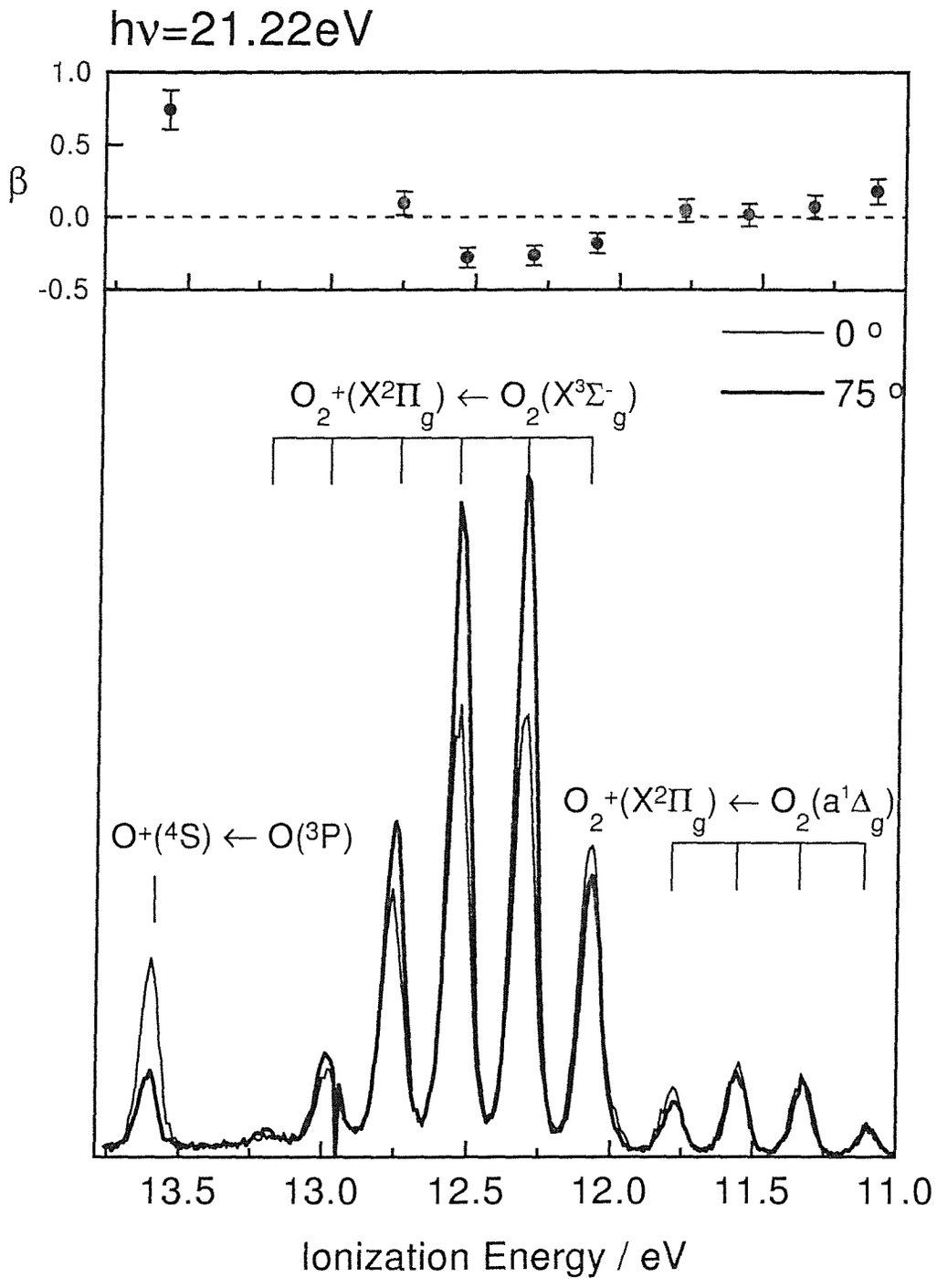

Figure 6.1: Upper panel: β-parameters for the photoelectron bands shown. Lower panel: photoelectron spectra of discharged O_2 at $h\nu$=21.22 eV at $\theta = 0°$and 75°

Band	v^+	β, This work	β, Previous work
$O_2^+(X^2\Pi_g\, v^+) \leftarrow O_2(a^1\Delta_g\, v''=0)$	0	0.05	
	1	0.01	-
	2	0.07	-
	3	0.18	-
$O_2^+(X^2\Pi_g\, v^+) \leftarrow O_2(X^3\Sigma_g^-\, v''=0)$	0	0.09	-0.18(05) [33]
	1	-0.28	-0.28(05) [33]
	2	-0.27	-0.30(05) [33]
	3	-0.18	-
$O^+(^4S) \leftarrow O(^3P)$		0.74	0.60(05) [34]

Table 6.2: β-parameters obtained from the PE spectrum of discharged O_2 at the non-resonant photon energy of 21.22 eV.

The asymmetry parameters calculated from the photoelectron spectra in the lower panel of Figure 6.1, using equation 6.2, are plotted in the upper panel of the same figure. The actual results are listed in Table 6.2. The error in the β-parameters is ± 0.10, and is dominated by the reproducibility of the geometrical alignment of the spectrometer with respect to the photon source, which affects the efficiency of the analyzer. The estimated error in the β-parameter for O atoms is notably larger due to extra contributions from the unstable partial pressure of this species.

The β values listed in Table 6.2 can be compared with previously published results. The results for the $O_2^+(X^2\Pi_g\, v^+) \leftarrow O_2(X^3\Sigma_g^-\, v''=0)$ band are in very good agreement with those of Codling *et al.* [33] who obtained -0.18 $\pm$ 0.05, -0.28 $\pm$ 0.05 and -0.30 $\pm$ 0.10. The β value for $O^+(^4S) \leftarrow O(^3P)$ (0.74 $\pm$ 0.10) is close to that of van der Meulen et al. [34] who obtained 0.60$\pm$0.05. The values of β for $O_2^+(X^2\Pi_g\, v^+) \leftarrow O_2(a^1\Delta_g\, v''=0)$ were measured in this work for the first time, so no comparison with previous results is possible.

6.4.2 Photoelectron spectra at photon energies of 14.11 and 14.37 eV

The photoelectron spectra of discharged oxygen recorded at the photon energies of 14.11 and 14.37 eV at $\theta = 0°$and $\theta = 75°$are shown in the lower panels of Figures 6.2 and 6.3 respectively. These two photon energies correspond to the $O_2^*(p^1\Phi_u\, v'=3,\, 5) \leftarrow O_2(a^1\Delta_g\, v''=0)$ resonances. At these two energies ionization to the $O_2^+(X^2\Pi_g\, v^+) \leftarrow O_2(a^1\Delta_g\, v''=0)$ band is resonantly enhanced, and

Band	v^+	$\beta(h\nu = 14.11eV)$	$\beta(h\nu = 14.37eV)$
$O_2^+(X^2\Pi_g\, v^+) \leftarrow O_2(a^1\Delta_g\, v'' = 0)$	0	-0.26	-0.24
	1	-0.42	-0.35
	2	-0.52	-0.39
	3	-0.44	-0.43
$O_2^+(X^2\Pi_g\, v^+) \leftarrow O_2(X^3\Sigma_g^-\, v'' = 0)$	0	-0.23	-0.37
	1	-0.50	-0.71
	2	-0.65	-0.83
	3	-0.64	-0.59
	4	-0.15	-0.11
	5	-0.17	-
	6	-0.08	-
$O^+(^4S) \leftarrow O(^3P)$		-0.36	-

Table 6.3: β-parameters obtained from the PE spectrum of discharged O_2 at the resonant photon energies of 14.11 and 14.37 eV.

this is evident when comparing with Figures 6.2 and 6.3 with Figure 6.1. No enhancement of the $O_2^+(X^2\Pi_g\, v^+) \leftarrow O_2(X^3\Sigma_g^-\, v'' = 0)$ band occurs as it is not separated from an intermediate Rydberg state by the correct energy difference and the $O_2^*(p^1\Phi\, v' = 3,\, 5) \leftarrow O_2(X^3\Sigma_g^-\, v'' = 0)$ transitions are formally spin and $\Delta\Lambda$ forbidden.

As for the photoelectron spectra at recorded at 21.22 eV, the values of β at the photon energies of 14.11 and 14.37 are plotted in the upper panels of Figures 6.2 and 6.3 respectively. The actual values of β for each of the vibrational components of each photoelectron band are listed in Table 6.3.

Measurements of β for the $O_2^+(X^2\Pi_g\, v^+) \leftarrow O_2(X^3\Sigma_g^-\, v'' = 0)$ band at these energies have not been reported before the present work. Previous measurements were restricted to the photon energy regions 16.8-18.5 eV [35] and 20.65-21.60 eV [33].

From the spectra recorded at the photon energy 14.11 eV (Figure 6.2), it can be seen that the change in intensity with angle of the $O_2^+(X^2\Pi_g\, v^+) \leftarrow O_2(a^1\Delta_g\, v'' = 0)$ PE band is negligible for the $v^+ = 0$ component, whereas it is very similar for the $v^+ = 1 - 3$ components and corresponds to negative values of β (see Table 6.3). The O atom signal is enhanced by the chance presence of a resonance at this photon energy ($O^*(^3P) \leftarrow O(^3P)$) [31] and it overlaps with the $O_2^+(^2\Pi_g, v^+ = 7) \leftarrow O_2(^3\Sigma_g^-, v = 0)$ component. However from the PE spectrum recorded at 14.11 eV with the microwave discharge turned off (see Figure 6.4), it

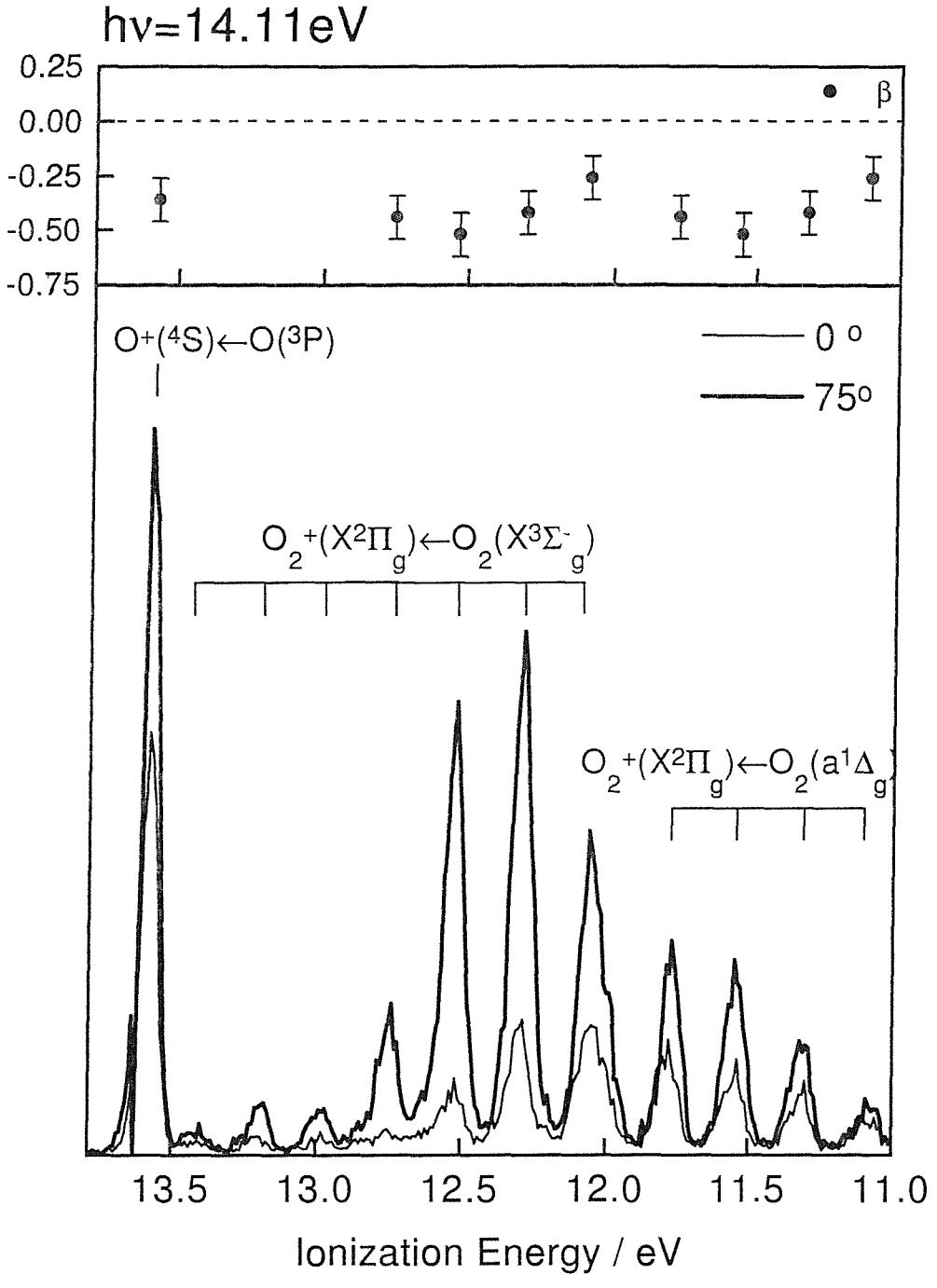

Figure 6.2: Upper panel: β-parameters for the photoelectron bands shown. Lower panel: photoelectron spectra of discharged O_2 at $h\nu$=14.11 eV at θ=0°and 75°.

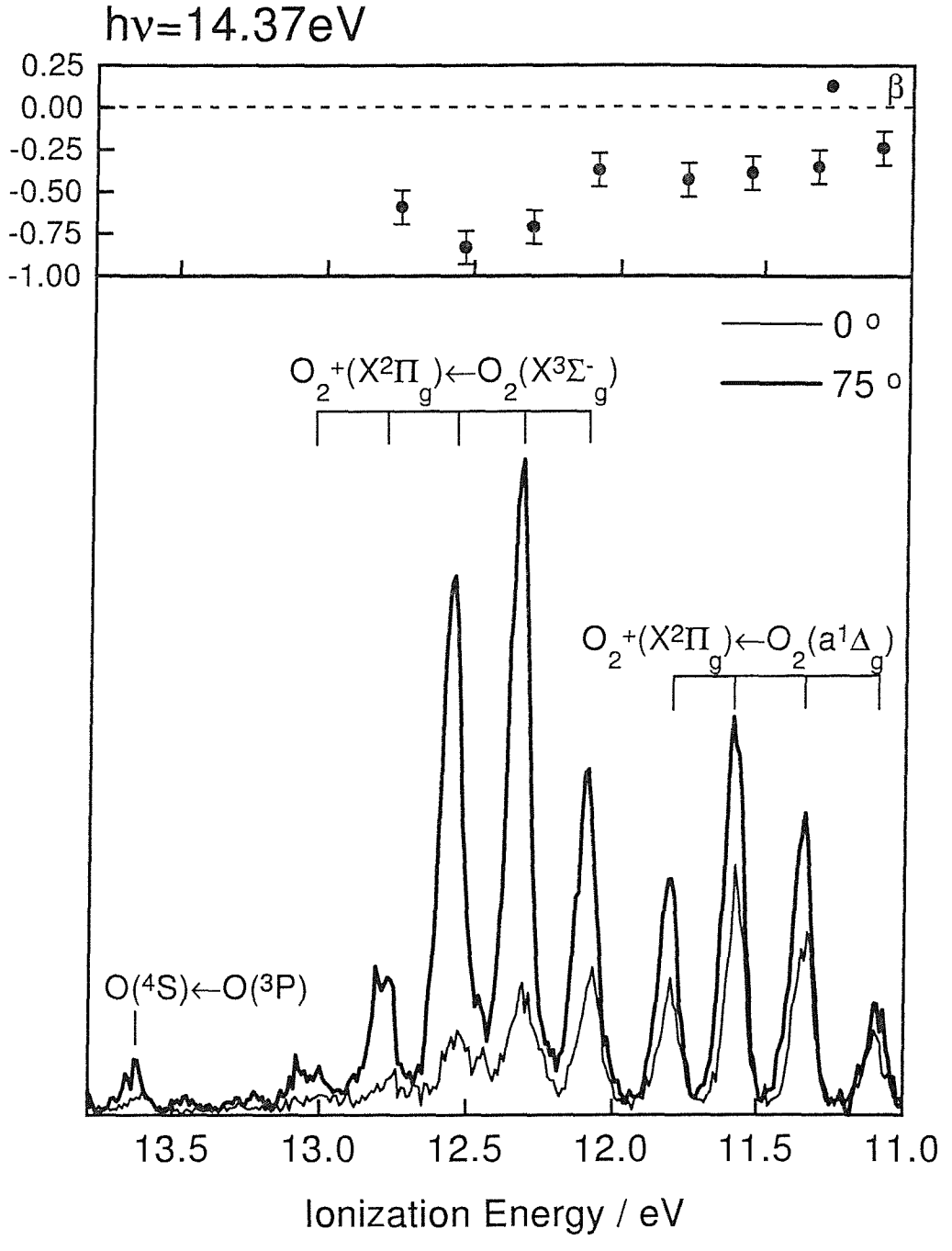

Figure 6.3: Upper panel: β-parameters for the photoelectron bands shown. Lower panel: photoelectron spectra of discharged O_2 at $h\nu$=14.37 eV at θ=0°and 75°.

can be clearly seen that this O_2 component has very little intensity. If the small O_2 contribution to the intensity of the band at 13.61 eV is neglected, then the β value for O atoms is obtained as -0.36 $\pm$ 0.10.

The spectra recorded at a photon energy of 14.37 eV (Figure 6.3) show similar results in terms of angular distribution to those at 14.11 eV. The relative change in intensities in the $O_2^+(X^2\Pi_g\, v^+) \leftarrow O_2(a^1\Delta_g\, v'' = 0)$ band is very small for the $v^+ = 0$ component, and for the $v^+ = 1 - 3$ members it is very similar to that observed at 14.11 eV.

In these resonant photoelectron spectra, the $O_2^+(X^2\Pi_g\, v^+) \leftarrow O_2(a^1\Delta_g\, v'' = 0)$ band shows an extended vibrational progression and for the higher vibrational components serious overlap with the $O_2^+(X^2\Pi_g\, v^+) \leftarrow O_2(X^3\Sigma_g^-\, v'' = 0)$ band occurs [4]. Because of this, it has not been possible to obtain the β-parameters for any of the components of the $O_2^+(X^2\Pi_g\, v^+) \leftarrow O_2(a^1\Delta_g\, v'' = 0)$ band, higher than $v^+ = 3$, from these spectra. Nevertheless by recording PE spectra under similar conditions with the microwave discharge turned off, angle resolved PE spectra for O_2 in its ground state could be obtained.

Figures 6.4 show PE spectra of $O_2(X^3\Sigma_g^-)$recorded at $h\nu$=14.11 eV and 14.37 eV. The change in intensity of the vibrational components between the two angles is quite dramatic and shows negative values of β for every component. The change in intensity is also different for different vibrational components, giving rise to significantly different values of β, indicating a breakdown of the Born-Oppenheimer approximation for the photoionization process. A v^+ dependence of β for the $O_2^+(X^2\Pi_g\, v^+) \leftarrow O_2(X^3\Sigma_g^-\, v'' = 0)$ band was also found by Codling *et al.* [33] in the photon energy range $20.65-21.60\, eV$, where Rydberg states converging to the $O_2^+(c^4\Sigma_g^-)$ limit are present [12]. The β values for the $O_2^+(X^2\Pi_g\, v^+) \leftarrow O_2(X^3\Sigma_g^-\, v'' = 0)$ band obtained at photon energies 14.11 and 14.37 eV are plotted in the upper panels of Figures 6.2 and 6.3, and are also listed in Table 6.3.

It is interesting that for the lowest four components of this band, the β values are on average more negative than for the higher vibrational members. This would suggest different dynamics between the low and the high v^+ levels for the photoionization process. In fact, this is not unexpected as it is already known that the higher components are virtually absent in an off resonant spectrum, and they are predominantly produced by autoionization. In view of this, it would have been highly interesting to obtain the asymmetry parameter for the higher members of the $O_2^+(X^2\Pi_g\, v^+) \leftarrow O_2(a^1\Delta_g\, v'' = 0)$ band as they are present only in on-resonant PE spectra. However this did not prove possible with the data

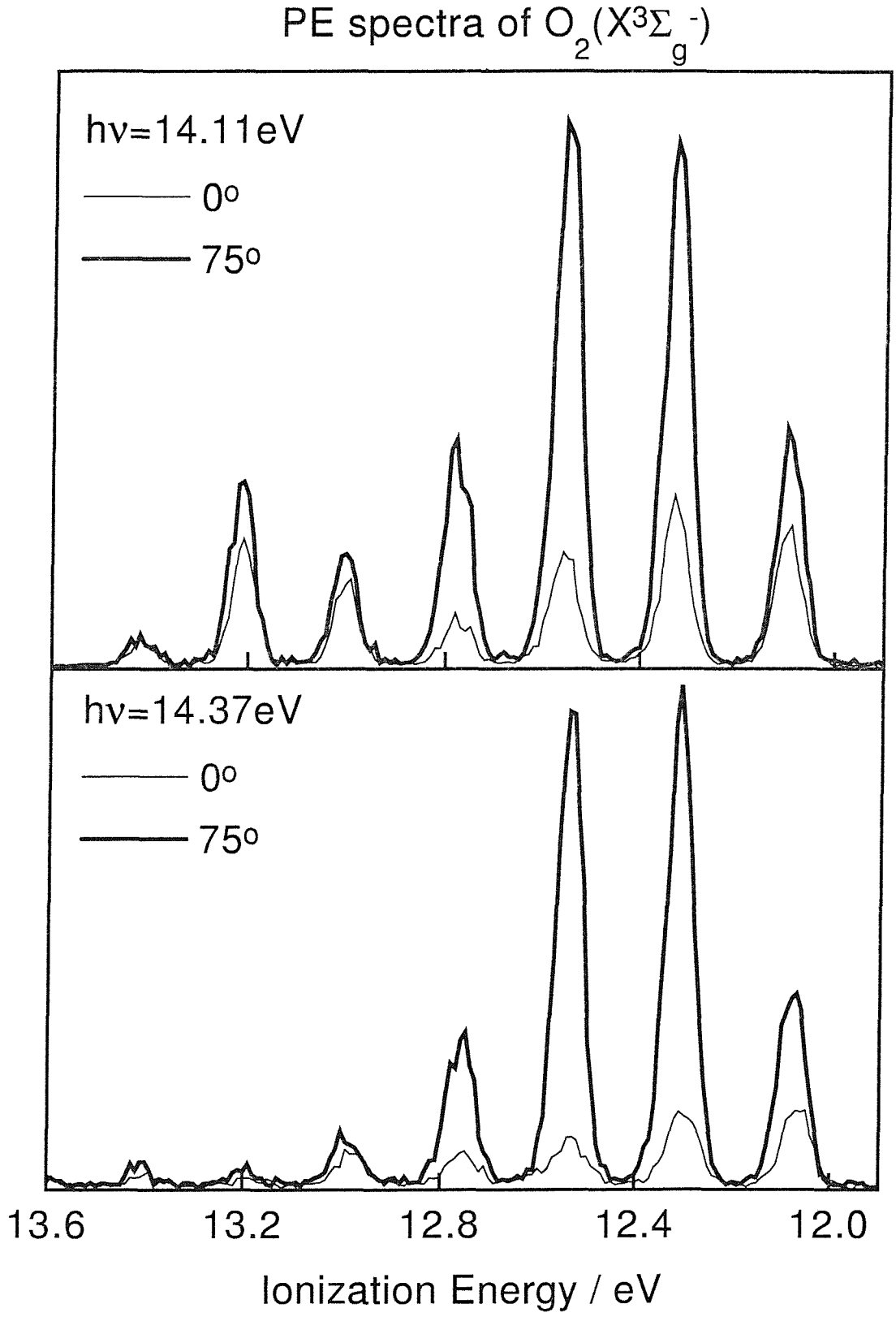

Figure 6.4: Photoelectron spectra of O_2 at photon energies of 14.11 eV (upper panel) and 14.37 eV (lower panel) with the microwave discharge turned off at $\theta = 0°$ and 75°.

obtained.

The v^+ dependence of β well away from resonant energies is normally a manifestation of either the breakdown of the Born-Oppenheimer approximation or the presence of a shape resonance [16]. Both of these effects are very difficult to identify with conventional (non-angle resolved) PES, and this underlines the importance of using angle resolved PES on small molecules.

6.4.3 β-parameters for the $O_2^+(X^2\Pi_g\, v^+) \leftarrow O_2(a^1\Delta_g\, v'' = 0)$ band in the photon energy range 13.8-15.2 eV

The change of the β-parameter as a continuous function of photon energy can be more interesting than its value at selected photon energies. It has been shown both theoretically [36] and experimentally [33], [35], [37], that measurements of β as a function of photon energy can show structure corresponding to autoionizing resonances. The asymmetry parameter depends on the phase shift of the photoelectron waves (see equation 2.24) as well as their relative cross-sections. As a result a plot of β as a function of photon energy can reveal the presence of resonances which are barely visible in CIS spectra. Also, for the same reason, lineshapes in β plots can be different from those in CIS spectra.

CIS spectra for the $v^+ = 0 - 3$ components of the $O_2^+(X^2\Pi_g\, v^+) \leftarrow O_2(a^1\Delta_g\, v'' = 0)$ band, in the photon energy range $13.8 - 15.2$ eV, are shown in Figure 6.5. These spectra, obtained using beam-line 3.3 (SRS), compared favorably with those previously recorded by the Southampton PES group on beam-line 3.2 (SRS), where the degree of linear polarization is much worse [4]. The CIS spectra show that strong resonances are present for the $v' = 3$ and 5 components of $O_2^*(p^1\Phi_u\, v')$ at excitation energies of 14.11 and 14.37 eV respectively, whilst no band is present in the position of the $v' = 4$ resonance at an energy of 14.24 eV. The reason for this effect is that the $v' = 4$ level undergoes more rapid predissociation than the $v' = 3$ and 5 levels. The $O_2^*(p^1\Phi_u\, v' = 3, 5)$ states decay by autoionization, giving rise to strong signals in the CIS spectra [4, 12].

The β-parameters for $O_2^+(X^2\Pi_g\, v^+ = 0 - 3) \leftarrow O_2(a^1\Delta_g\, v'' = 0)$ in the photon energy range 13.8 - 15.2 eV are plotted in Figure 6.6. The most interesting feature of these spectra is that β shows positive peaks at energies corresponding to the autoionizing resonances $O_2^*(p^1\Phi_u\, v') \leftarrow O_2(a^1\Delta_g\, v'' = 0)$. The β plots strongly reflect the structure observed in the CIS spectra in Figure 6.5. The lack of a **strong** peak at 14.24 eV in the *beta* plot shown in Figure 6.6 confirms the explanation that the $v' = 4$ component undergoes more efficient predissociation than the $v' = 3, 5$ components. However, a small band is seen at 14.24 eV, the

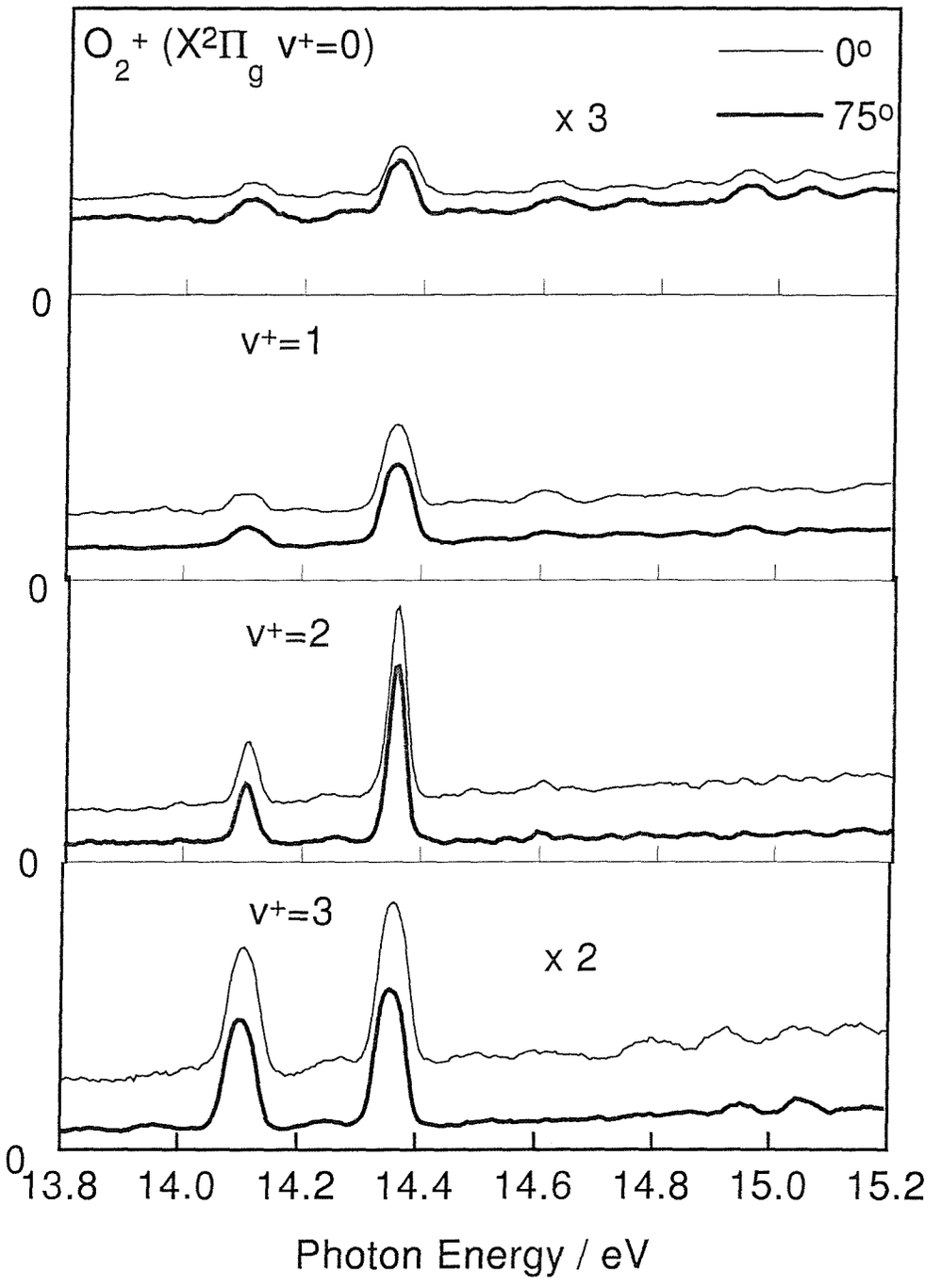

Figure 6.5: CIS spectra for the $O_2^+(X^2\Pi_g\, v^+) \leftarrow O_2(a^1\Delta_g\, v'' = 0)$ band in the region of the $O_2^*(p^1\Phi_u\, v') \leftarrow O_2(a^1\Delta_g\, v'' = 0)$ resonances at two angles of observation: $\theta = 0°$ and 75°.

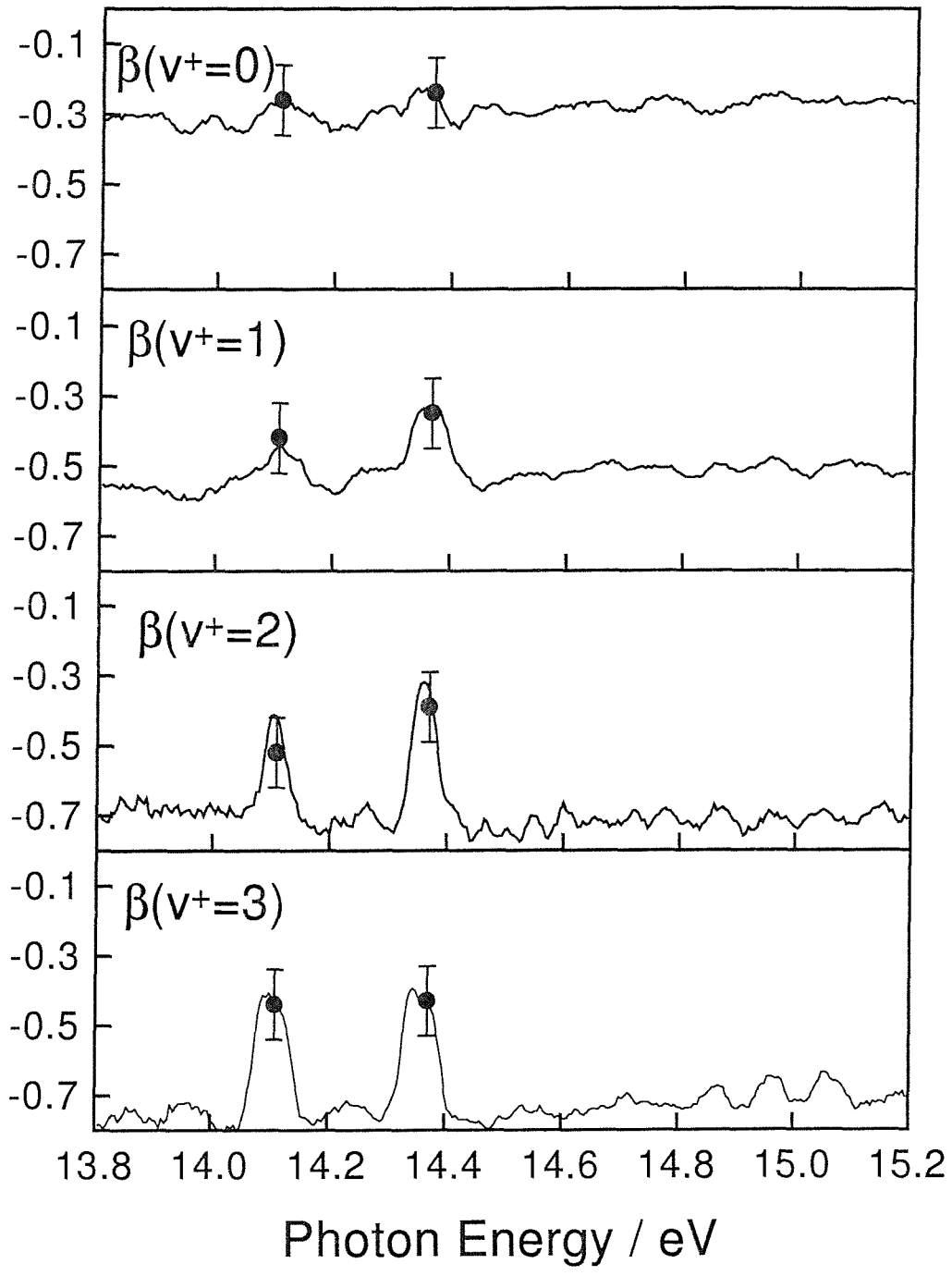

Figure 6.6: β-parameters for the $O_2^+(X^2\Pi_g\, v^+) \leftarrow O_2(a^1\Delta_g\, v'' = 0)$ band in the region of the $O_2^*(p^1\Phi_u\, v') \leftarrow O_2(a^1\Delta_g\, v'' = 0)$ resonances. The continuous lines are calculated from the CIS spectra at two angles, and the circles with error bars come from the PE spectra recorded at the resonant energies.

$v' = 4$ position, in the β plots for $v^+ = 2, 3$ supporting the presence of the $O_2^*(p^1\Phi_u\, v' = 4) \leftarrow O_2(a^1\Delta_g\, v'' = 0)$ resonance reduced in size by predissociation of the excited state. Examination of the β-parameter as a function of incident photon energy avoids the problem of a band appearing weak at a fixed angle due to angular effects. For example if CIS spectra are recorded only at $\theta = 0°$, with respect to the major polarization axis, then bands with a negative β-parameter would appear misleadingly small.

It is desirable to explain why the β-parameter changes to less negative values at energies corresponding to the $O_2^*(p^1\Phi_u\, v') \leftarrow O_2(a^1\Delta_g\, v'' = 0)$ excitations from the β values recorded off-resonance. According to electric dipole selection rules, in the $O_2^+(X^2\Pi_g) + e^- \leftarrow O_2(a^1\Delta_g) + h\nu$ direct photoionization process, the photoelectron can have σ_u, π_u and δ_u character. For the analysis of the behavior of β in terms of the symmetry character of the photoelectron, it is of a useful approximation to change to atomic symmetry and to use the united atom picture. In a united atom picture, the π_g orbital becomes a d orbital, so the prominent components of the outgoing photoelectron wave are expected to be $l = 1(p)$ or $l = 3(f)$. From equation 2.24 it can be seen that a pure atomic $d \rightarrow f$ ionization is expected to have $\beta = 0.8$ and a pure $d \rightarrow p$ ionization is expected to have $\beta = 0.2$ [38]. This result can be compared with the selection rules that govern autoionization from the intermediate $O_2^*(p^1\Phi_u)$ excited state. Autoionization cannot change the overall symmetry of the system, so the ion plus the free electron must also have $^1\Phi_u$ symmetry. Since the final ionic state formed by the ionization is $^2\Pi_g$, the photoelectron channel must have δ_u or γ_u symmetry, which cannot be derived with an $l = 1(p)$ free electron wave. Therefore, it is expected that the relative f contribution (and that of higher odd l values) to the outgoing photoelectron wave increases at resonant energies, as the p contribution can only arise from direct ionization and not by autoionization. This explanation is based on the fact that the resonant state has $^1\Phi_u$ symmetry. If it was for example $^1\Pi_u$, considerations of this kind would have still been possible, but both the p and f channels would receive autoionization contributions.

It is expected, therefore, that changing the photon energy from an off-resonant to an on-resonant position, the ratio of the photoionization cross-sections $\sigma_f : \sigma_p$ will increase. The phase shift between the photoelectron waves, $\Delta = \delta_f - \delta_p$, will also change between resonant and nonresonant photon energies. Unfortunately, however, neither Δ nor the ratio $\sigma_f : \sigma_p$, at resonant and nonresonant photon energies, can be quantified from the present measurements. The change in the β-parameters with photon energy is clearly seen in Figure 6.6, where the on-

resonance values become far less negative. In terms of the angular momentum transfer mechanism described by Dill [36], this means that parity unfavoured transitions, for which $\beta = -1$, are less prominent at the resonance position. It is tempting to apply such an analysis here, but unfortunately the number of open channels is large and no definitive conclusion can be reached. In general, parity unfavored transitions occur in regions where the outgoing electron exchanges momentum with the ion core (*e.g.* where there is strong spin-orbit interaction or in resonance regions), so the behavior seen here is counter-intuitive. This effect has, however, been observed before, for example by Parr *et al.* [39] for the CO_2 molecule, and reflects the fact that the background continuum contains both parity favored and unfavored channels, compared to the resonance region where in the $O_2(a^1\Delta_g)$ case considered here, there appears to be a bias towards parity favoured transitions. In a simplistic picture this would be consistent with the presence of partial waves of higher angular momentum, in agreement with the symmetry considerations above, but this ignores the fact that the β-parameter is sensitive to the relative phases of the outgoing partial waves. These phases are likely to vary rapidly in the resonance region, further complicating the analysis. In the interpretation of angular distribution data in resonance regions, it would be very valuable for a realistic calculation to be undertaken in order to gain an understanding of the physical processes which lie behind this phenomenon. [5]

6.4.4 β-parameters for the $O_2^+(X^2\Pi_g\, v^+) \leftarrow O_2(a^1\Delta_g\, v'' = 0)$ band in the photon energy range 18.0-19.2 eV

In order to understand better the observed overlapping vibrational progressions in the CIS spectra (mentioned in section 6.1 [4]), in the 18.0-19.2 eV energy region for $O_2^+(X^2\Pi_g\, v^+) \leftarrow O_2(a^1\Delta_g\, v'' = 0)$, CIS spectra for the $v^+ = 1 - 3$ components were recorded at the two angles $\theta = 0°$ and $\theta = 75°$ in the photon energy range 18.0-19.2 eV. Unfortunately, as was found previously, the $v^+ = 0$ component proved to be too weak to allow reliable spectra to be recorded [4]. The CIS spectra for the ionic $v^+ = 3$ vibrational component recorded at two angles is shown in Figure 6.7.

The structure observed in Figure 6.7 could not be analyzed in terms of two vibrational series; it could only be analyzed using three vibrational series. The need for three series in this region can be seen most clearly in the $v^+ = 3$ spectra in Figure 6.7 in the components labeled M, M', and M". On changing from 0°to 75°, the maximum of the main component (composed of M and M") moves to lower photon energy and the component M' decreases in intensity. The three vibrational

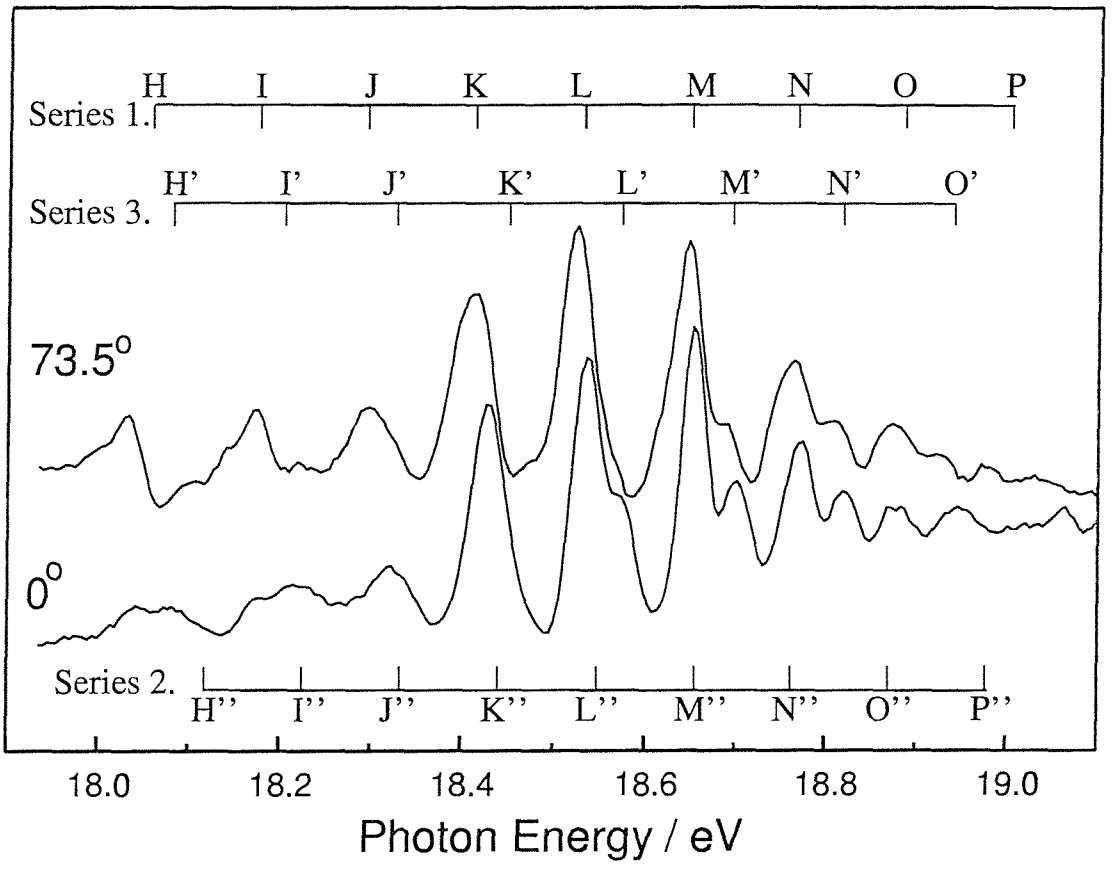

Figure 6.7: CIS spectra for the $O_2^+(X^2\Pi_g\, v^+ = 3) \leftarrow O_2(a^1\Delta_g\, v'' = 0)$ band in the photon energy range 18.0-19.2 eV. The photoelectron intensity has been normalized by the light flux.

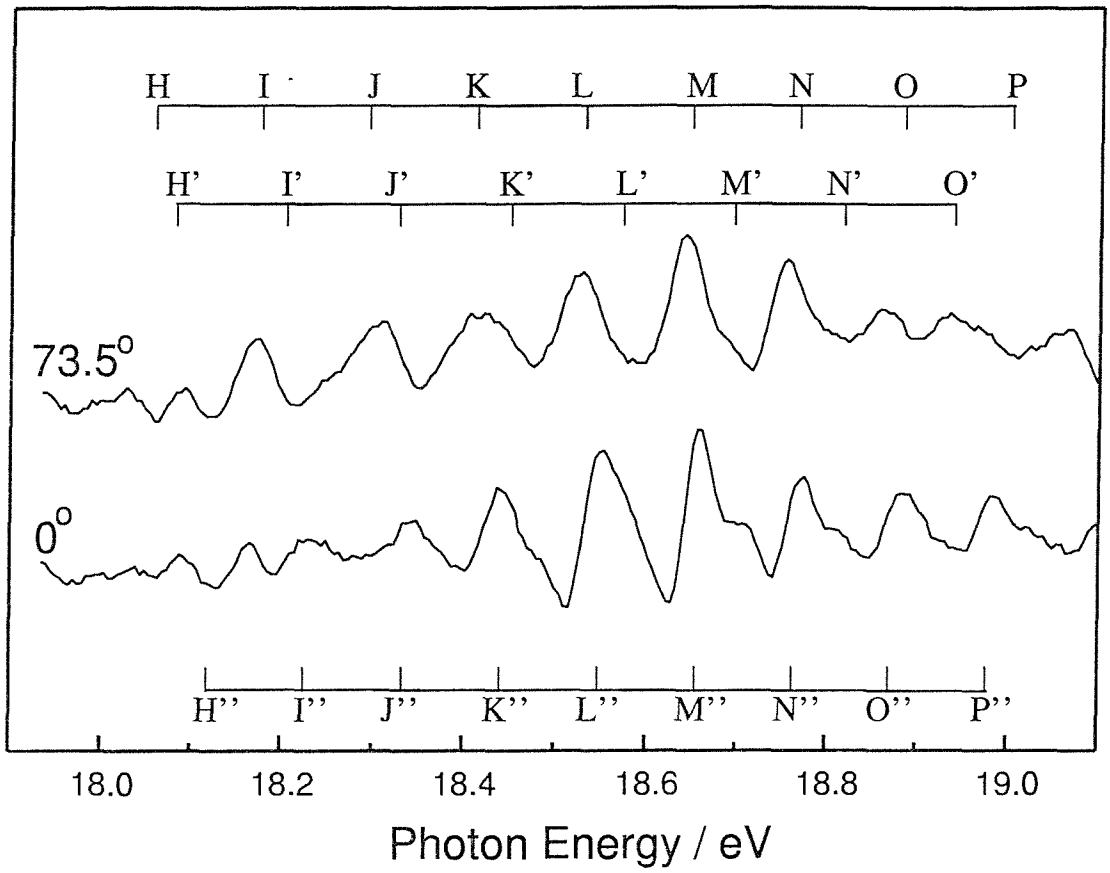

Figure 6.8: CIS spectra for the $O_2^+(X^2\Pi_g\, v^+ = 1)$ $\leftarrow O_2(a^1\Delta_g\, v'' = 0)$ band in the photon energy range 18.0 – 19.2 eV. The photoelectron intensity has been normalized by the light flux.

series needed to account for the observed structure had mean vibrational spacings of (950±30), (870±30), and (990±30)cm^{-1}. These values compare favorably with the value of the vibrational constant, ω_e , of 995 cm^{-1} in the $O_2^+(^2\Delta_g)$ state.

Figure 6.8 shows CIS spectra recorded for the $O_2^+(X^2\Pi_g\, v^+ = 1)$ $\leftarrow O_2(a^1\Delta_g\, v'' = 0)$ component at the two angles with the three series marked on. In these spectra, the three series start at energies of 18.06, 18.12, and 18.08 eV, well before the component observed in the earlier work at 18.46 eV [4] and labeled K in Figure 6.7. In view of the presence of components observed at lower energy than 18.46 eV, the previous interpretation can now be revisited. Assuming features H, H', and H" at 18.06, 18.12, and 18.08 eV to be the first members of vibrational progressions, the effective quantum number of the associated Rydberg states (see section 1.4) based on a $D^2\Delta_g$ core would be 4.26, 4.44, and 4.32, suggesting a $(D^2\Delta_g, 5p\pi)(^1\Phi_u and ^1\Pi_u)$ excited state assignment for the series beginning at H and H" and a $(D^2\Delta_g, 5p\sigma)(^1\Delta_u)$ assignment for the series beginning at H'. [14,40]

β-parameter plots were obtained in the photon energy range 18.0-19.2 eV for

the $O_2^+(X^2\Pi_g\, v^+ = 1,2,3) \leftarrow O_2(a^1\Delta_g\, v'' = 0)$ processes and these are shown in Figure 6.9. Again the β-parameter plots are similar to the CIS spectra. The presence of at least two vibrational progressions can be seen in the $v^+ = 1$ and 2 graphs, and the $v^+ = 3$ plot shows evidence of the three overlapping vibrational series seen in Figures 6.7 and 6.8. On the basis of the present angle resolved measurements, these series can be assigned with more confidence than in the earlier work [4]. These results, combined with those of the earlier study [4], mean that excitation to $(D^2\Delta_g, 3p)$, $(D^2\Delta_g, 4p)$ and $(D^2\Delta_g, 5p)$ Rydberg states from $O_2(a^1\Delta_g)$ have now been observed.

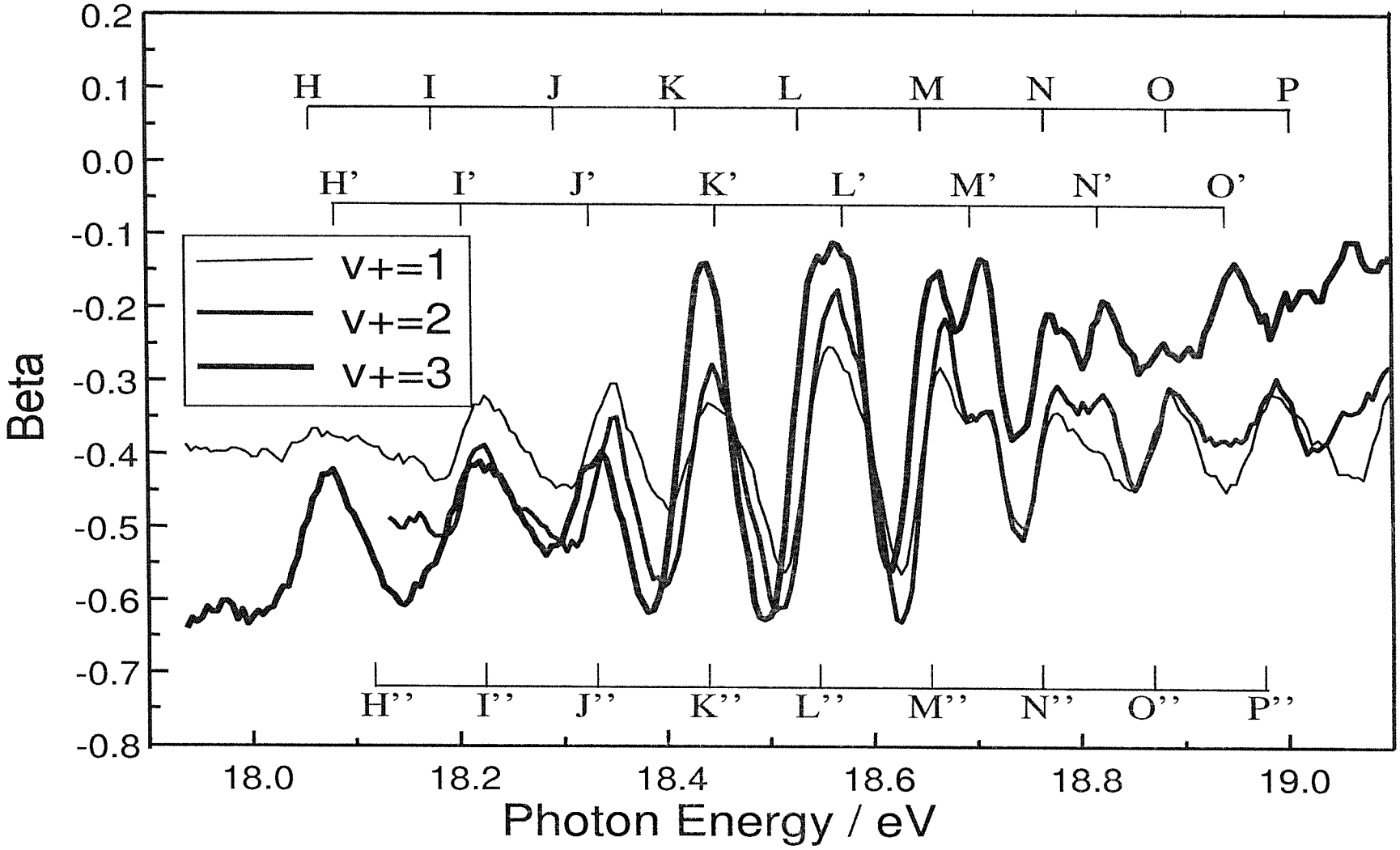

Figure 6.9: β-parameter plot for the $O_2^+(X^2\Pi_g\, v^+ = 1,2,3) \leftarrow O_2(a^1\Delta_g\, v'' = 0)$ band in the photon energy range 18.0-19.2 eV.

6.5 Conclusions

Angle resolved photoelectron spectra and constant-ionic-state spectra have been recorded for $O_2(a^1\Delta_g)$ in the photon energy regions 13.8-15.2 and 18.0-19.2 eV. In the photon energy region 13.8-15.2 eV, autoionization resonances in the CIS spectra have been observed corresponding to the excitations $O_2^*(p^1\Phi_u\, v') \leftarrow O_2(a^1\Delta_g\, v'' = 0)$ and angle resolved measurements have allowed new information on the photoionization dynamics in this photon energy region to be obtained. In the higher photon energy region, 18.0-19.2 eV, angle resolved measurements extend information gained in PES and CIS experiments and allow identification of three absorption series to excitation to three singlet Rydberg states of O_2 from $O_2(a^1\Delta_g)$. This chapter has illustrated the extra information that can be obtained from angle resolved studies short-lived molecules which have previously been studied by the PES and CIS methods. The work in this chapter proved the viability of angular resolution studies of short-lived molecules with the PES spectrometer constructed for synchrotron studies of short-lived species. This work lead to further studies on O atoms (Chapter 7) and OH (Chapter 8) at the Elettra synchrotron (Trieste); species for which PES and CIS measurements have previously been made at the SRS (Daresbury).

Bibliography

[1] J. M. Dyke, D. Haggerston, A. Morris, S. Stranges, J. B. West, T. G. Wright, and A. E. Wright, J. Chem. Phys. **106**, 821 (1997).

[2] J. M. Dyke, S. D. Gamblin, D. Haggerston, A. Morris, S. Stranges, J. B. West, T. G. Wright, and A. E. Wright, J. Chem. Phys. **108**, 6258 (1998).

[3] J. D. Barr, A. De Fanis, J. M. Dyke, S. D. Gamblin, N. Hooper, A. Morris, S. Stranges, J. B. West, and T. G. Wright, J. Chem. Phys. **110**, 345 (1999).

[4] J. D. Barr, A. De Fanis, J. M. Dyke, S. D. Gamblin, A. Morris, S. Stranges, J. B. West, T. G. Wright, and A. E. Wright, J. Chem. Phys. **109**, 2737 (1998).

[5] L. Beeching, A. De Fanis, J. M. Dyke, S. D. Gamblin, N. H. Hooper, A. Morris, and J. B. West, J. Chem. Phys. **112**, 1707 (2000).

[6] R.P. Wayne, *Chemistry of Atmosphere* (Clarendon Press, Oxford, 1969).

[7] D. W. Turner and D. P. May, J. Chem. Phys. **45**, 471 (1966).

[8] D. W. Turner, Proceedings of the Royal Society of London **307**, 15 (1968).

[9] O. Edqvist, E. Lindholm, L. E. Selin, and L. Åsbrink, Physica Scripta **1**, 25 (1970).

[10] N. Jonathan, M. Okuda, K. J. Ross, and D. J. Smith, J. Chem. Soc., Far. Trans.II **70**, 1810 (1974).

[11] H van Lonkhuyzen and C. A. de Lange, J. Elect. Spec. Relat. Phenom. **27**, 255 (1982).

[12] A. DeFanis, Ph.D. thesis, Department of Physics and Astronomy, University of Southampton, 2000.

[13] P. Baltzer, B. Wannberg, L. Karlsson, M.C. Göthe, and M Larsson, Phys. Rev. A **45**, 4374 (1992).

[14] E. Lindholm, Arkiv för Physik **40**, 117 (1968).

[15] K. Yoshino and Y. Tanaka, J. Chem. Phys. **48**, 4859 (1968).

[16] P. M. Dehmer and W. A. Chupka, J. Chem. Phys. **62**, 4525 (1975).

[17] E. Nishitani and I. Tanaka, J. Chem. Phys. **81**, 3429 (1984).

[18] R. E. Huffman, J. C. Larrabee, and Y Tanaka, J. Chem. Phys. **46**, 2213 (1967).

[19] D. H. Katayama, R. E. Huffman, and Y Tanaka, J. Chem. Phys. **62**, 2939 (1975).

[20] D. H. Katayama, S Ogawa, M Ogawa, and Y Tanaka, J. Chem. Phys. **67**, 2132 (1977).

[21] J. A. R. Samson, *Techniques of Vacuum Ultraviolet Spectroscopy* (Wiley, New York, 1967).

[22] A. A. Cafolla, T. Reddish, A. A. Wills, and J. Comer, J. of Phys. B **23**, 1433 (1989).

[23] D. Čubrić, P. Hammond, A. A. Wills, and J. Comer, J. of Phys. B **29**, 4151 (1996).

[24] C. N. Yang, Phys. Rev. Lett. **74**, 764 (1948).

[25] J. Cooper and R. N. Zare, J. Chem. Phys. **48**, 942 (1968).

[26] A. D. Buckingham, B. J. Orr, and J. M. Sichel, Philos. Trans. R. Soc. London **268**, 147 (1970).

[27] J. C. Tully, R.S. Berry, and B.J. Dalton, Phys. Rev. Lett. **176**, 95 (1968).

[28] D. M. P. Holland, A. C. Parr, D. L. Ederer, and J. B. West, Nucl. Instrum. Methods **195**, 331 (1982).

[29] R. G. Houlgate, J. B. West, K. Codling, and G. V. Marr, J. Elect. Spec. Relat. Phenom. **9**, 205 (1976).

[30] R. M. Holmes and G. V. Marr, J. Phys. B. **13**, 945 (1981).

[31] C. E. Moore, *Atomic Energy Levels*, Vol. 1 of *Circular of the national bureau of standards 467* (US Govt. Printing Office, Washington, DC, 1949).

[32] R. P. Madden, D. L. Ederer, and K. Codling, Phys. Rev. **117**, 136 (1969).

[33] K. Codling, A.C. Parr, D.L. Ederer, R. Stockbauer, J. B. West, B.E. Cole, and J.L. Dehmer, J. of Phys. B **14**, 657 (1981).

[34] P. van der Meulen, M. O. Krause, and C. A. de Lange, Phys. Rev. A. **43**, 5997 (1981).

[35] A.C. Parr, G.V. Marr, J.L. Dehmer, and J. B. West, J. of Phys. B **31**, 5161 (1998).

[36] D. Dill, Phys. Rev. A. **7**, 1973 (1976).

[37] G.V. Marr, J.M. Morton, R.M. Holmes, and D.G. McCoy, J. of Phys. B **12**, 43 (1979).

[38] J. B. West, in *Vacuum ultraviolet photoionization and photodissociation of moleculs ions and clusters*, edited by C. Y. Ng (World Scientific, London, 1991), Chap. 8, p. 369.

[39] A. C. Parr, P. M. Dehmer, J. L. Dehmer, K. Ueda, J. B. West, M. R. F. Siggel, and M. A. Hayes, Journal of Chemical Physics **100**, 8768 (1994).

[40] C. Y. R. Wu, Journal of Quantum Spectroscopy and Radiation Transfer **A37**, 1 (1987).

Chapter 7

Oxygen atoms, $O(X^3P)$

7.1 Introduction

The work described in this chapter is part of on-going investigations into the photoelectron spectroscopy of radicals by the Southampton PES group carried out at the ELETTRA synchrotron radiation source (see section 5.2.3). The work is closely related to the synchrotron studies of $O_2(a^1\Delta_g)$(Chapter 6) and OH (Chapter 8) and forms the basis of a recent paper [1].

In the earth's ionosphere, atomic oxygen is the dominant neutral species above 150 km for average solar conditions. The solar spectrum between 9.5 eV and 45.9 eV consists of numerous lines, arising from emissions from multiply ionized atoms, superimposed on a broad continuum [2].

In the ionosphere, photoionization of atomic oxygen by solar radiation is the major source of photoelectrons. The electrons produced can travel a considerable distance along geomagnetic field lines before losing their energy. It is therefore important to know the photoionization cross-section of atomic oxygen, as well as the relative contributions from autoionization and direct ionization, as a function of photon energy in order that the photoelectron flux in the upper atmosphere and its energy distribution can be estimated [3, 4].

The first HeI photoelectron spectrum of atomic oxygen was obtained by Jonathan *et al.* [5,6]. Subsequently, the branching ratios for the production of the $O^+(^4S$,^2D and $^2P)$ states arising from the $(2p)^{-1}$ ionization of $O(^3P)$, as well as the angular distribution parameters for these ionizations, were measured at the HeI, HeII and NeI photon energies [7–9]. Calculations have also been made of the photoionization cross-sections and angular distribution parameters of atomic oxygen into these three ionic channels, as a function of photon energy [10, 11].

The partial photoionization cross-sections for these ionizations have been measured by Hussein *et al.* [12] from 17.1 to 21.4 eV using synchrotron radiation. The

absolute values for the $O(^3P)$ photoionization cross-section have been measured from threshold (13.6 eV) to 103.0 eV, using monochromatized radiation from a helium continuum discharge lamp, by Samson and Pareek [13]. The absolute value for the photoionization cross-section for the $O^+(^4S)\leftarrow O(^3P)$ ionization was determined at the HeI photon energy by de Lange *et al.* [14].

Later, using synchrotron radiation, Prumper *et al.* [15] measured angular distribution parameters for ionization to all three ionic states at the photon energies of 24, 30, 35, 40, 45, and 70eV, and Van der Meulen *et al.* [16] measured the relative partial photoionization cross-sections and angular distribution parameters for the $O^+(^4S, ^2D)\leftarrow O(^3P)$ ionizations from threshold at 13.6 eV to 30.0 eV. This was the first study of atomic oxygen in which the angular distribution parameter, β, was measured across autoionization resonances [16]. The angular distribution parameters for these autoionizations from 13.6 to 50.0 eV have been calculated by Tayal [11], using the R-matrix method with configuration interaction include in the wavefunction for both the initial $O(^3P)$ and the final continuum states.

Further absorption and emission studies of atomic oxygen have also been made, in the energy region 13.6-19.0 eV above the ground state [17, 18]. Also in this photon energy region, photoionization investigations have been made of $O(^3P)$, using a mass spectrometer as the ion detector and a helium discharge with a vacuum ultraviolet monochromator as the tunable photon source [19, 20].

The purpose of this present work was to measure relative partial photoionization cross-sections and angular distribution parameters for the $O^+(^4S)\leftarrow O(^3P)$ and $O^+(^2D)\leftarrow O(^3P)$ ionizations, in the photon energy range 13.6-19.0 eV. Initially these experiments were performed to compare the Daresbury synchrotron source (a second generation source, see section 5.2.2) with the ELETTRA synchrotron source (a third generation source, see section 5.2.3). This was done to establish the characteristics of the ELETTRA source when used to study reactive intermediates and to quantify the improvement in intensity and resolution that can be obtained at ELETTRA when studying short-lived species. The constant-ionic-state (CIS) spectra obtained were of higher resolution than previous CIS measurements and this allowed detailed comparison to be made of the relative photoionization cross-sections and angular distribution parameters, recorded as a function of photon energy, with previous experiments and calculations.

7.2 Experimental

The bulk the experiments reported in this chapter have been undertaken on the circularly polarized (VUV) beam-line 4.2R at the ELETTRA Synchrotron Source, Trieste. The beamline is described in detail in Chapter 5 section 5.2.3. From the synchrotron source, the radiation passes to the spectrometer via a normal incidence monochromator, which covers the photon energy range 5-35 eV [21, 22]. The synchrotron spectrometer described in section 5.3 was used for these studies. Experiments could be performed either of the conventional photoelectron spectroscopy (PES), or of the constant-ionic-state (CIS) type (see section 5.5). Measurements were normally performed in the constant-ionic-state mode (CIS) in which both the photon energy and the photoelectron energy are scanned synchronously to ensure that the intensity of a chosen photoelectron feature with a constant ionization energy is always measured.

Oxygen atoms were produced by passing a flowing mixture of molecular oxygen with argon as a carrier, through a microwave discharge (2.45GHz) in a glass inlet tube, coated with boric acid (as described in section 5.3.7).

The photon energy was calibrated by recording the CIS spectrum of the $O^+(^4S)\leftarrow O^*\leftarrow O(^3P)$ process in the photon energy region 14.0-18.5 eV, and comparing the positions with known $O^*\leftarrow O$ transition energies above the first ionization energy [19]. Intensities of the CIS spectra were normalized by the photon flux and by the transmission function of the spectrometer. The photon flux was estimated as a function of photon energy from the current measured on an aluminium photodiode placed on the opposite side of the spectrometer ionization chamber from the photon source. The transmission function for electrons of different initial electron kinetic energies was determined by measuring the intensity of the helium photoelectron band at different photon energies and correcting with the known cross-section at each photon energy [23].

The radiation from the BL4.2 was set to plane polarization ($P = S_1 = 1$). As a result, the asymmetry parameter. β, could be measured for oxygen atoms at selected photon energies and over a photon energy range, by recording CIS spectra at two different angles (0°and 60°), at each photon energy; the β parameter could then be calculated from equation 7.1 (derived from equation 2.23).

$$\beta = \frac{8(R-1)}{R+8}, \tag{7.1}$$

where $R = I_0/I_{60}$ *i.e.* the ratio of the normalized experimental intensities at the two angles.

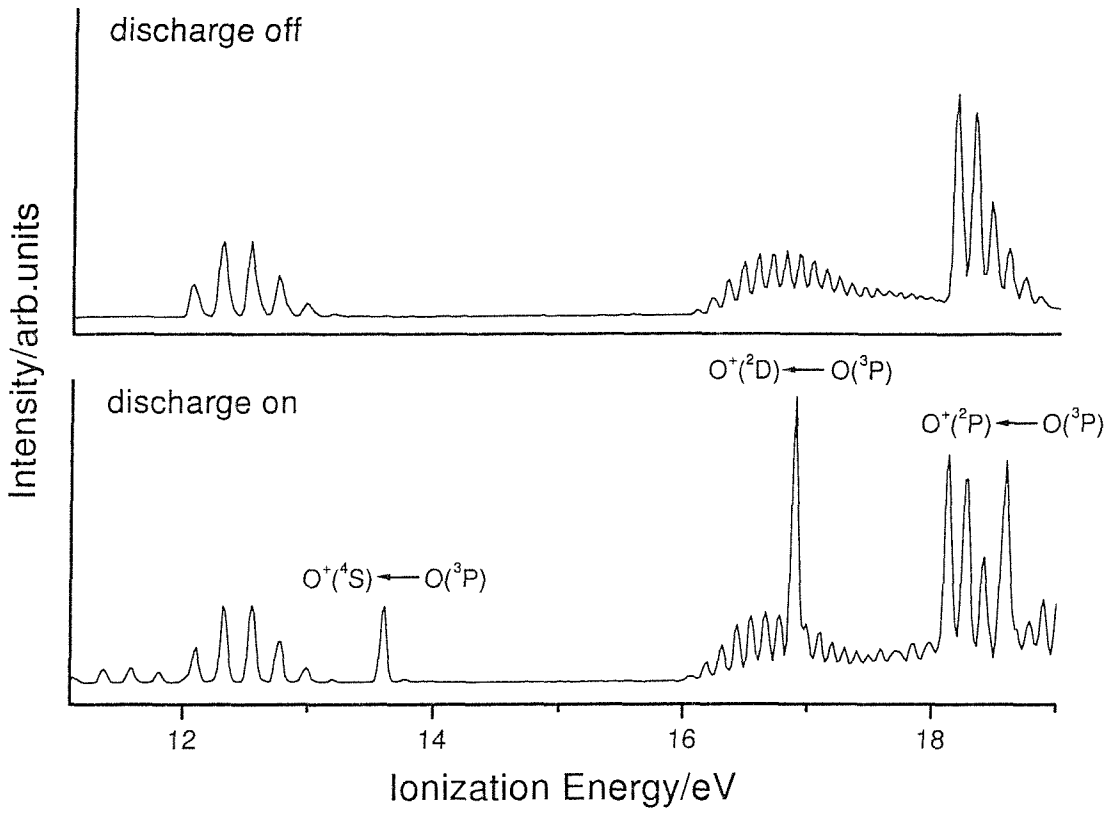

Figure 7.1: Photoelectron spectra, recorded at a synchrotron photon energy of 21.22 eV, for a flowing mixture of oxygen and argon with the microwave discharge on and off

Photoelectron spectra recorded at a synchrotron photon energy of 21.22eV, for a flowing gas-mixture of oxygen and argon with the microwave discharge on and off, are shown in Figure 7.1. These spectra were recorded at a detection angle (θ) with respect to the direction of polarization of the radiation of 60°. As can be seen from the discharge-on spectrum, sharp bands can be seen at 13.62, 16.94 and 18.63 eV, corresponding to the $O^+(^4S)\leftarrow O(^3P)$, $O^+(^2D)\leftarrow O(^3P)$, and $O^+(^2P)\leftarrow O(^3P)$ ionizations respectively. The other features seen in the spectra arise from molecular ionizations of $O_2(X^3\Sigma_g^-)$ and $O_2(a^1\Delta_g)$ (also seen in Chapter 6).

CIS spectra could be successfully recorded for the $O^+(^4S)\leftarrow O(^3P)$, $O^+(^2D)\leftarrow O(^3P)$ ionizations but this was not possible for the $O^+(^2P)\leftarrow O(^3P)$ band, as it was too heavily overlapped by molecular features. The bandwidth of the radiation from the monochromator, which in a CIS scan is the only factor contributing to the overall resolution, was normally set to 3 meV. The step-size in the CIS scans was 1 meV.

The earlier experiments were performed on beamline 3.2 at the SRS (Dares-

bury, see section 5.2.2) also using the synchrotron spectrometer (see section 5.3). This beamline uses a 5 metre normal incidence monochromator. The transmitted radiation from the monochromator had a typical width of 15 meV and the step-size used in the CIS scans was 5 meV.

7.3 Results and Discussion

The first stage in these studies was to make a comparison between the Daresbury beamline 3.2 (BL3.2) and the Elettra beamline (BL4.2R). These two beamlines were used as these are the beamlines most suited to photoionization studies of reactive intermediates in the vacuum ultraviolet region, at Daresbury and Elettra respectively.

It was found by that for photoelectron count-rates of atomic oxygen and other reactive species at the similar gas pressures, production conditions and synchrotron ring currents, an intensity improvement of 75-125 could be achieved using the third generation source at ELETTRA (for PE spectra of similar photoelectron resolution). Measurements of the photon flux by monitoring the current from an aluminium photodiode in the ionization chamber, opposite the photon source, at a photon energy of 21.22 eV, showed an intensity improvement of ~75 on BL4.2 (ELETTRA). At Daresbury on BL3.2, at a ring current of 200mA at 15meV photon width, a current of 0.1nA was measured. At Elettra on BL4.2R at a ring current of 200mA, at 4meV photon width, a current of 7.5nA was measured.

The improvement in spectral resolution can be demonstrated by comparing CIS spectra recorded for oxygen atoms, as shown in Figures 7.2(a) and 7.2(b). Both spectra were recorded at θ=0° with respect to the major polarization axis of the photon source. The spectra show structure arising from two separate processes. In the photon energy region 13.6-16.9eV structure is observed in the CIS spectra for the process $O^+(^4S)\leftarrow O^*\leftarrow O(^3P)$ and for the process $O^+(^2D)\leftarrow O^*\leftarrow O(^3P)$ in the photon energy region 16.9-18.5eV. It is convenient to record spectra in these regions as the first ionization energy , $O^+(^4S)\leftarrow O(^3P)$, is 13.62 eV and the second ionization energy, $O^+(^2D)\leftarrow O(^3P)$, is 16.94 eV. Rydberg states are observed in Figure 7.2 between 13.6 and 16.9 eV which are parts of series which converge to the second and third ionization limits (O^+,^2D and O^+,^2P), that autoionize to $O^+(^4S)$ (full assignment of this structure will be given later).

An expanded section of the photon energy range in Figures 7.2(a) and 7.2(b)

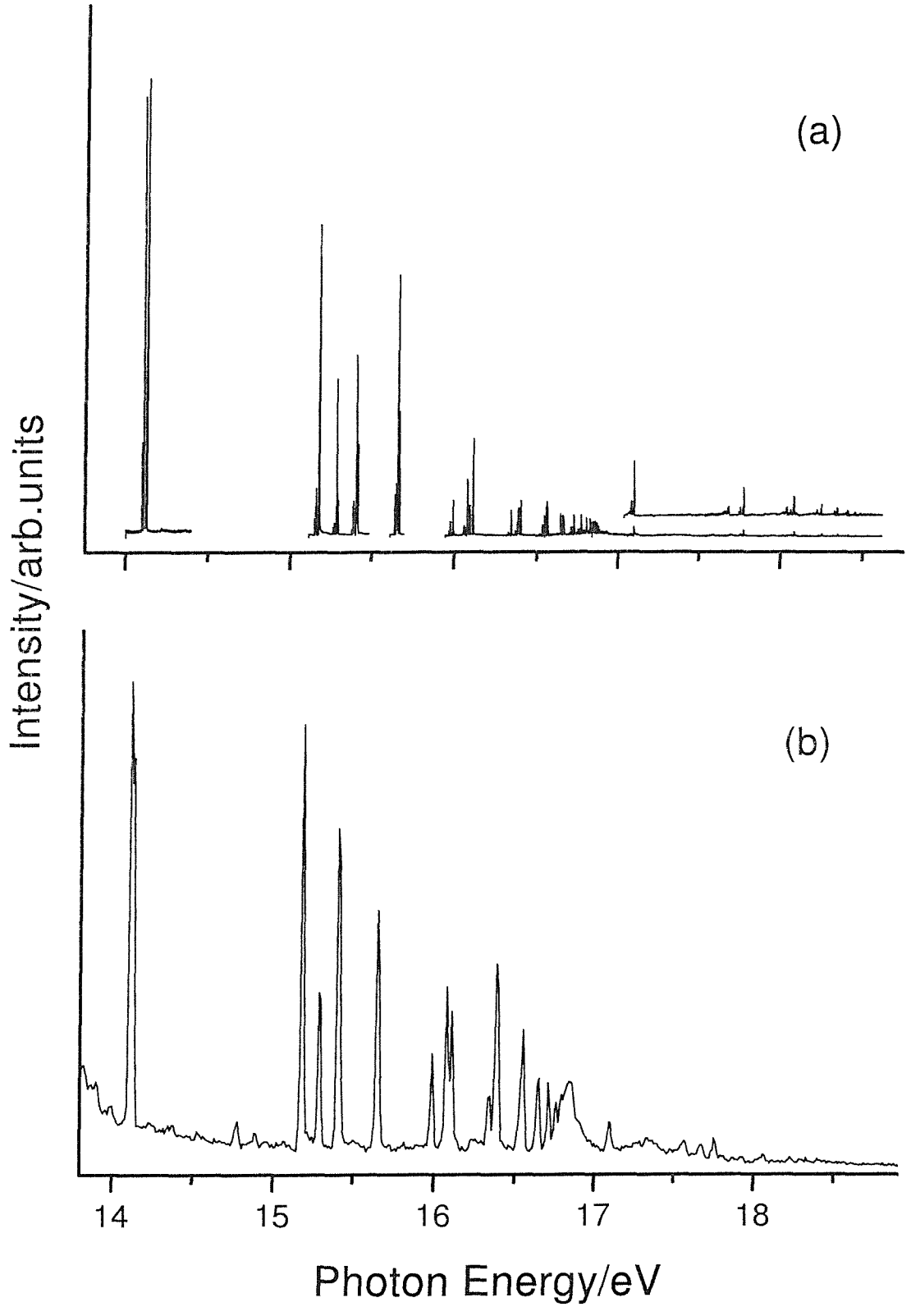

Figure 7.2: Constant-ionic-state (CIS) spectra of atomic oxygen recorded at θ=0°, (a) at ELETTRA on BL4.2R, and (b) at Daresbury on BL3.2

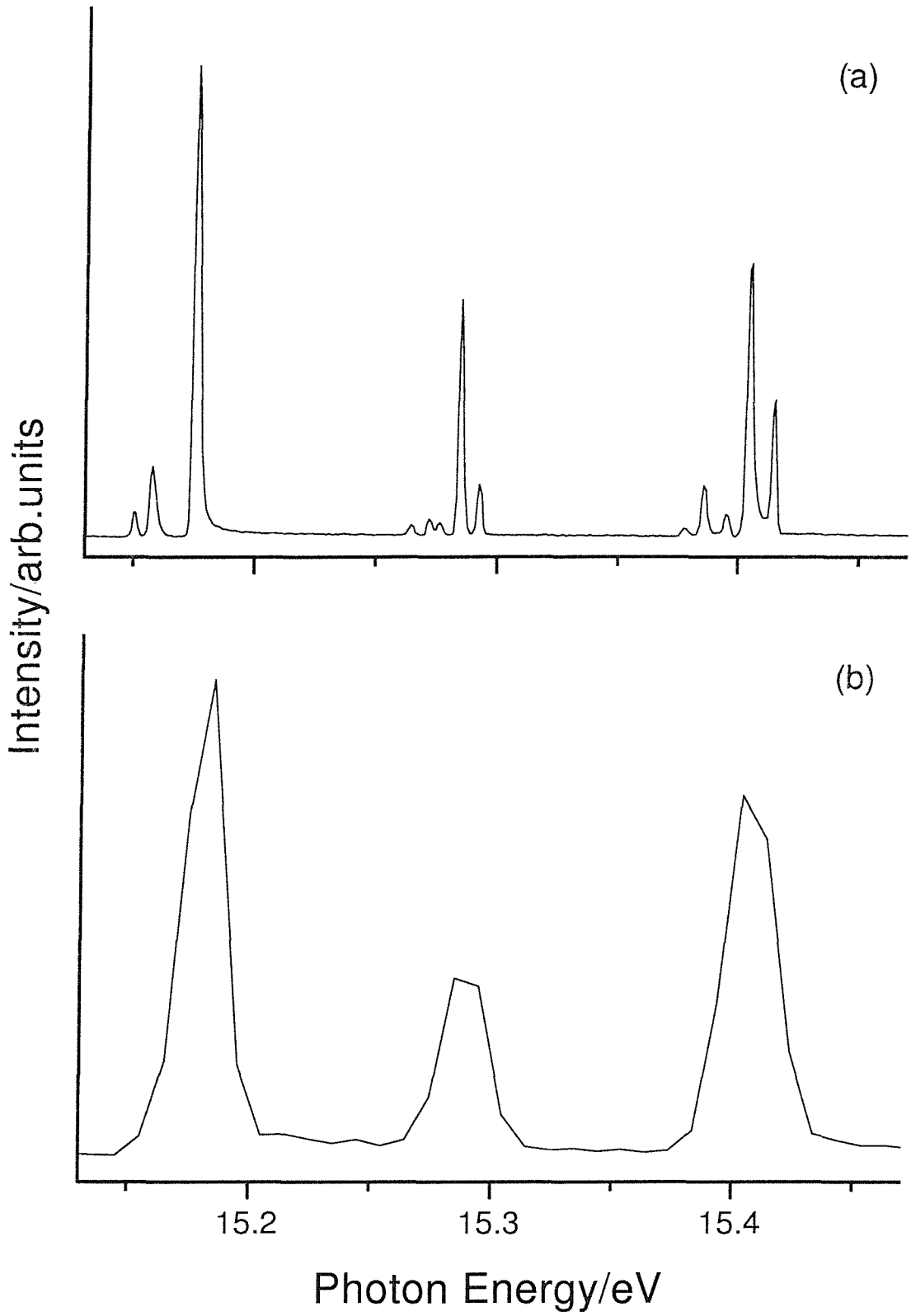

Figure 7.3: The 15.1-15.5 eV photon energy regions of Figures 7.2(a) and 7.2(b), expanded to show a comparison of resolution in CIS spectra recorded with the ELETTRA (BL4.2R) and Daresbury (BL3.2) synchrotron sources.

(15.15-15.45 eV) is shown in Figures 7.3(a) and 7.3(b), clearly showing the marked improvement in resolution. The band-width in 7.3(a) is 2.5 meV whereas that in Figure 7.3(b) is 20 meV, demonstrating the obvious improvement in resolution on the ELETTRA beamline 4.2R compared to the Daresbury beamline 3.2.

The full O atom CIS spectrum with the first, second and third ionization limits marked in is shown in Figure 7.4. This was recorded at θ=0° and consists of the $O^+(^4S)\leftarrow O^*\leftarrow O(^3P)$ CIS spectrum between 13.6 and 16.9 eV and the $O^+(^2D)\leftarrow O^*\leftarrow O(^3P)$ CIS spectrum between 16.9 and 18.6 eV photon energy. These bands can be readily assigned to known $O^*\leftarrow O(^3P_{J''})$ transitions by comparison with known O* term values [19, 24]. The assignments are shown in Figure 7.4, where transitions have been denoted as (J'',J'). Inspection of this figure shows that in the photon energy region 15.0-16.9 eV, all the transitions can be assigned to excitation to Rydberg states which are members of series which converge to the second ionization energy, apart from a group of bands associated with excitation to a $2s^12p^5\ ^3P$ state. The observed Rydberg states correspond to $1s^22s^22p^3ns$ and $1s^22s^22p^3nd$ configurations accessed from the $1s^22s^22p^4\ ^3P$ state. Transitions from J''=1 and J''=2 components of the ^3P state can readily be identified. The bands in the 14.0-14.2 eV region are the most intense bands in the spectrum. They arise from a $2p\ ^3P\rightarrow 3s''\ ^3P$ excitation and components arising from transitions from J''=0, 1 and 2 can be identified in this spectral region (see Figure 7.5).

In the photon energy region 13.6-16.9 eV, the bands associated with $s'\ ^3D$ and d'^3S excited states are allowed on the basis of L-S selection rules for the two steps shown below

$$O^+(^4S) + e^- \leftarrow O^* \leftarrow O(^3P) + h\nu$$

i.e. for the first (resonance) step

$$\Delta S = 0,\ \Delta L = 0,\ \Delta J = 0,\ \pm 1,\ J = 0 \nleftrightarrow J = 0,\ \textit{even} \leftrightarrow \textit{odd parity}$$

and for the second (autoionization) step

$$\Delta S = 0,\ \Delta L = 0,\ \Delta J = 0,\ \textit{no change in parity.}$$

In the case of an s'^3D O* state, $O^+(^4S)$ will be produced with a d free electron, and for a d'^3S O* state, $O^+(^4S)$ will be produced with an s free electron. For the bands at ≈14.1 eV (corresponding to excitation to a $3s''^3P$ state), the bands in the 15.6-15.7 eV region (corresponding to excitation to a $2s^12p^5\ ^3P$ state), and the d'^3P states in the 13.9-16.9 eV region, even though they can be accessed by an allowed transition from the ^3P initial state, the parity selection rule forbids

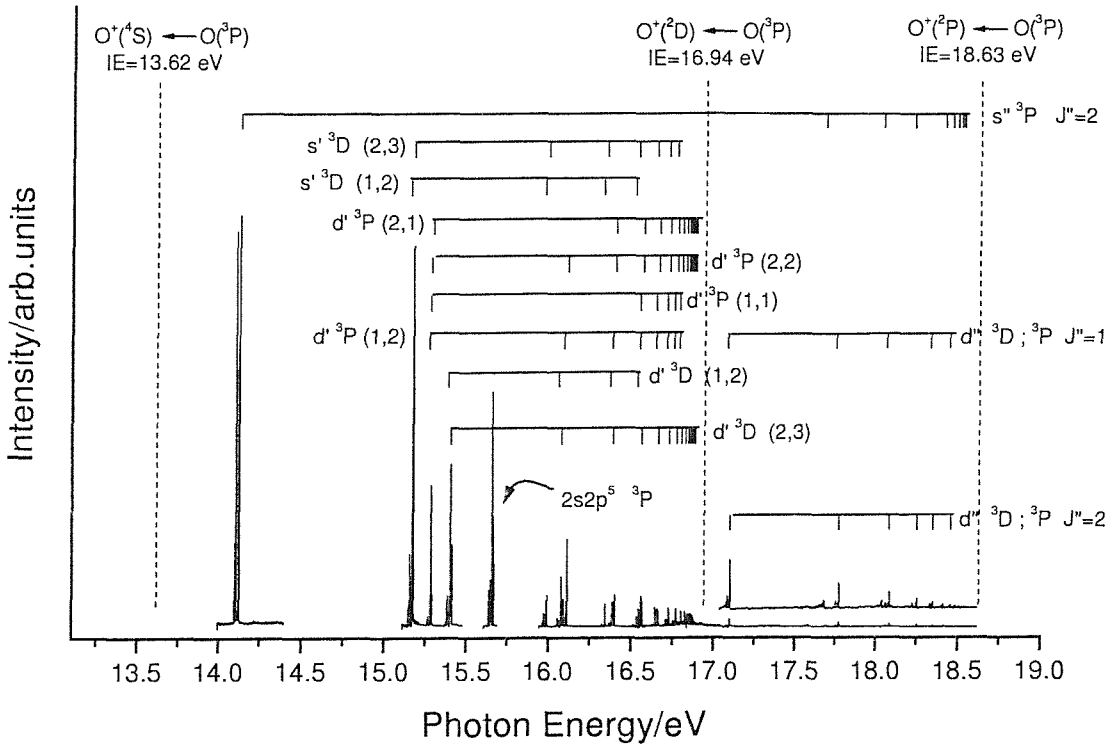

Figure 7.4: O atom CIS spectra recorded at θ=0°, with the first, second and third ionization limits marked on. This spectrum is made up of the $O^+(^4S) \leftarrow O^* \leftarrow O(^3P)$ CIS spectrum (main structure between 13.6 and 16.9 eV photon energy) and the $O^+(^2D) \leftarrow O^* \leftarrow O(^3P)$ CIS spectrum in the 16.9-18.6eV photon energy region. $O^* \leftarrow O$ transitions are labelled as (J'', J'). To simplify the labelling on this diagram, labelling of bands associated with ^3S O^* states between 13.9 and 16.9 eV has been omitted.

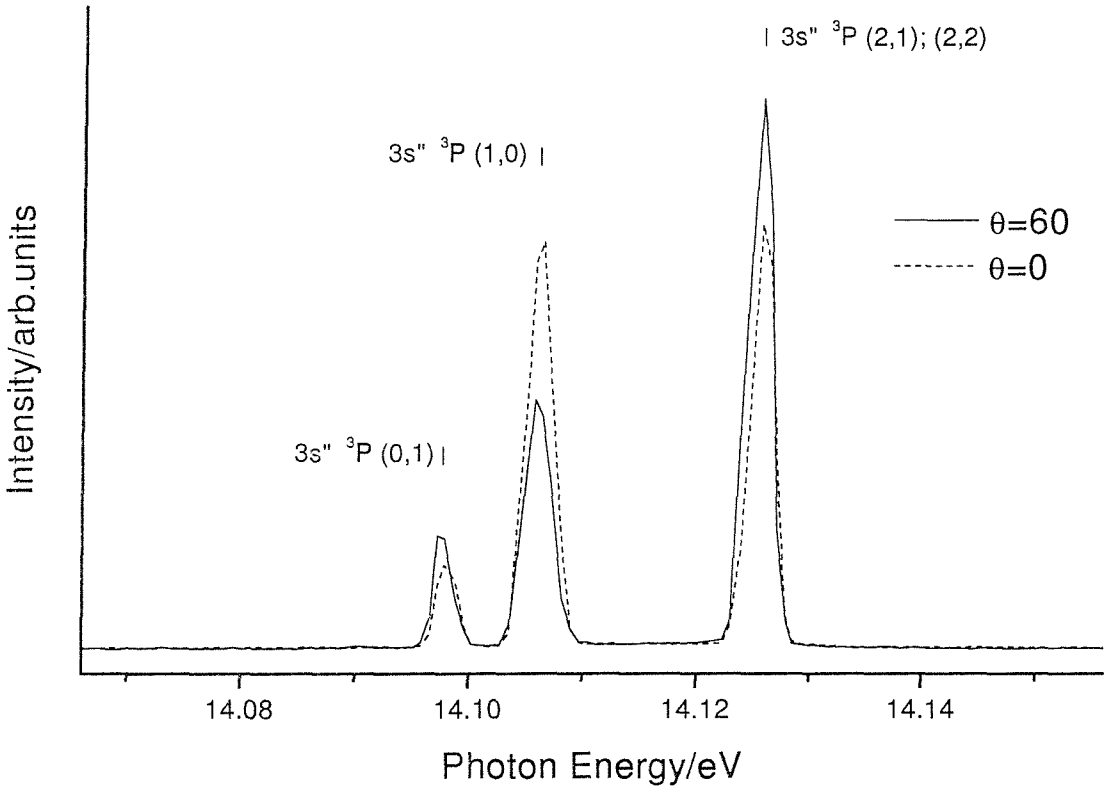

Figure 7.5: CIS spectra recorded for the $O^+(^4S) \leftarrow O^* \leftarrow O(^3P)$ process in the 14.08-14.14 eV photon energy region, at two angles of detection (θ=0°and 60°) with respect to the horizontal direction of polarization of the photon source. Transitions are labelled at (J",J') ; transitions from J"= 0, 1 and 2 from the initial $O(^3P)$state are clearly observed.

production of a ^3P continuum with an $O^+(^4S)$ ionic state (the continuum $O^+(^4S)$ plus a p free electron is parity forbidden from these O^* states). However, as has been pointed out previously [18,20], autoionization becomes allowed if a coupling scheme which is intermediate between the L-S and j-j limits is more appropriate. Then, for example, the $3s''^3P_{1,2}$ state can interact with nearby $^3S_1$, $^5S_2$ and $^3D_{1,2}$ states allowing the J'=1 and J'=2 levels of the O^* excited state to autoionize to ^3S, ^5S and ^3D continua with an $O^+(^4S)$ ionic core , hence satisfying the parity selection rule. Similarly, in intermediate coupling, the nominal $O^+(^4S_{3/2})$ ionic ground state acquires a small amount of $^2P_{3/2}$ character which, when combined with s and d free electron character, provides an allowed autoionization route from the $3s''^3P$ O^* state. These mechanisms also apply to the nd'^3P states and the $2s2p^5$ ^3P O^* state, although it is noted that in the latter case an extra important factor is that this state interacts strongly with the $3d'^3P$ state, which itself relies on a departure from L-S coupling for its autoionization strength.

Above the second ionization energy (16.94 eV), all the observed O^* states are allowed in an L-S scheme for both the resonance step and the autoionization step. For example, the $4s''^3P$ state is produced by an allowed transition from the ground ^3P state and autoionization to $O^+(^2D)$ plus a d free electron is allowed. Similarly, an O^* nd''^3D state can be produced from $O(^3P)$ by an allowed transition and can autoionize to $O+(^2D)$ and an s or d free electron.

At each photon energy, the relative photoionization cross-sections can be evaluated by taking the intensity measurements made at θ=0°and θ=60°, and calculating the relative integrated cross-section and angular distribution parameter,β [25]. This has been carried out to give the spectrum shown in Figure 7.6, where comparison has been made with a spectrum obtained by photoionization mass spectrometry (PIMS) [17]. In this PIMS work, an effusive beam of O atoms was produced and relative photoionization cross-sections were measured in the photon energy region 13.5 to 19.1 eV using a mass spectrometer to detect O^+ production. The nature of the experiment meant that no state selective measurements were made to determine the state (or states) that O^+ is produced in, at a particular photon energy. Comparison of Figures 7.6(a) and 7.6(b) shows that $O^+(^4S)\leftarrow O(^3P)$ is the ionization route in the photon energy region 13.6 to 16.9 eV (as expected, as it is the only available channel) and $O^+(^2D)\leftarrow O(^3P)$ is the main ionization route in the photon energy region 16.9-19.0 eV. This means that ionization of an O^* state occurs mainly to the nearest available ionic state. Also, comparison of the relative band intensities in Figures 7.6(a) and 7.6(b) shows good overall agreement. In particular, for the spectrum recorded in this work,

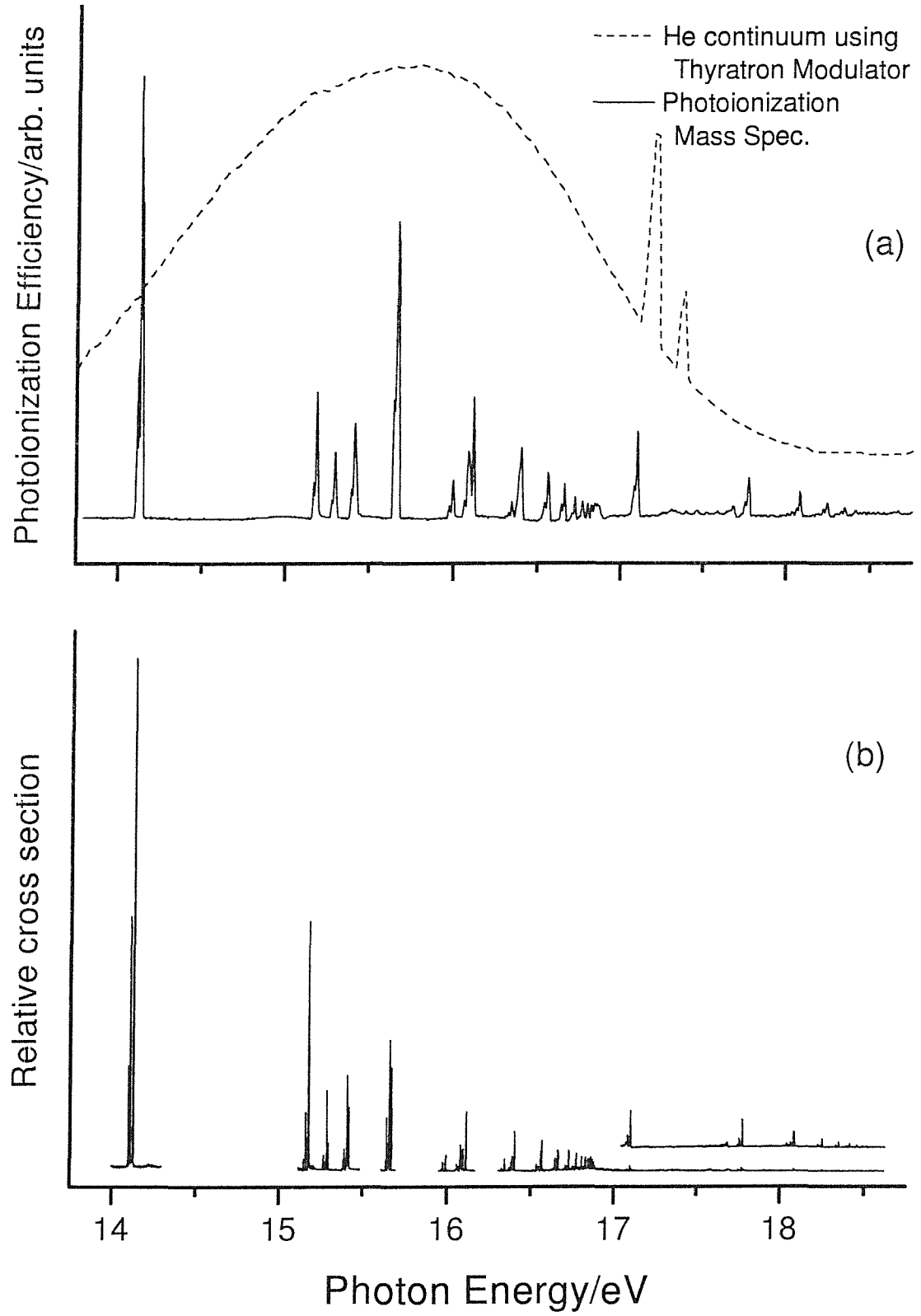

Figure 7.6: Comparison of a CIS relative photoionization cross-section plot, derived for θ=54°44′ in this work(Figure 7.6(b)),with a PIMS $O^+ \leftarrow O^* \leftarrow O(^3P)$ spectrum obtained in reference [17] (Figure 7.6(a)) (see text for further details).

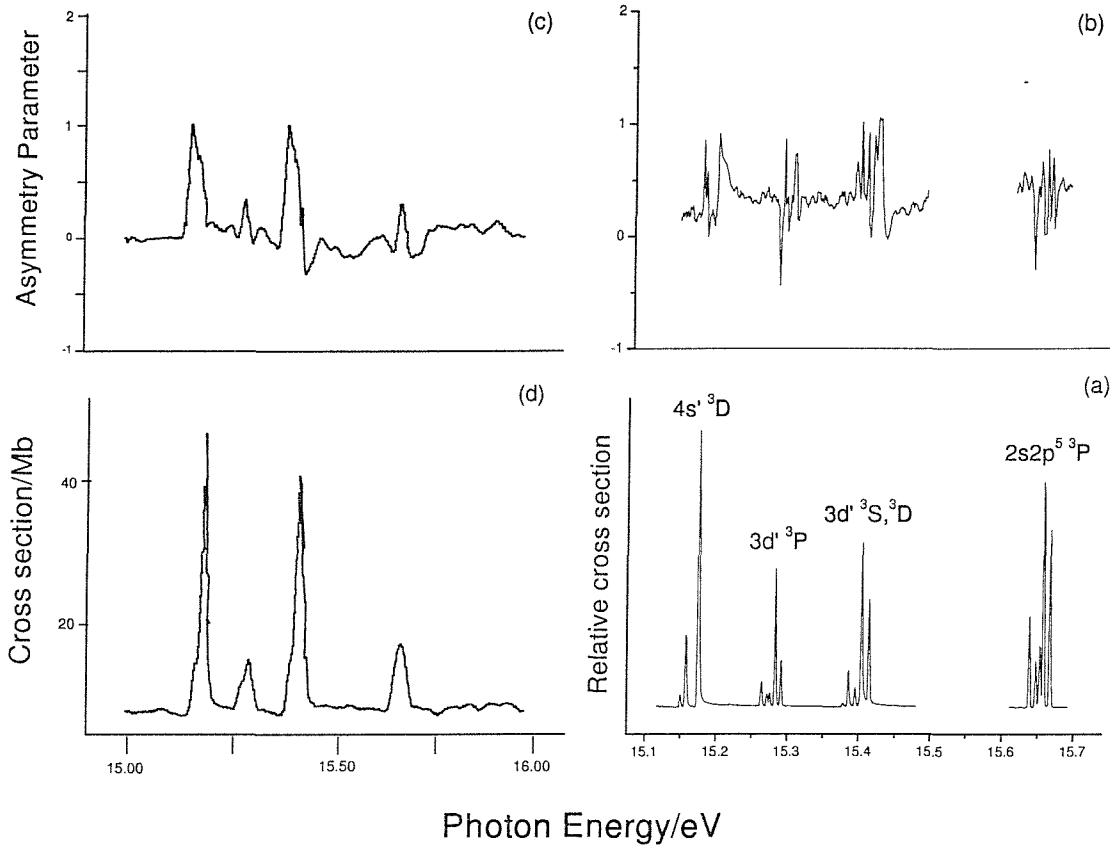

Figure 7.7: Comparison of relative photoionization cross-section plots and derived asymmetry parameter (β) plots in the photon energy range 15.1-15.7 eV obtained in this work (Figures 7.7a and 7.7b) with that of van der Meulen *et al.* [16] (Figures 7.7d and 7.7c). The resolution in the CIS plots of this work is 3 meV compared to the resolution in the CIS plots of ref. [16] of 15 meV.

the intensities of the bands in the 14.0-14.2 eV region relative to the intensity of bands at higher photon energy show good agreement to those of the PIMS study [17]. The bands in the 14.0-14.2 eV photon energy region, and other bands associated with ^{3}P excited states, were weaker in an angle resolved PES study of van der Meulen *et al.* [16]. The explanation put forward in reference [16] to account for these weak ^{3}P features was that in the PIMS study [17] traces of oxygen were present in the helium discharge photon source and these led to production of O* ^{3}P states in the discharge which decay by photon emission and these photons then enhance population of O* states in the photoionization region [26, 27]. However, this appears not to be valid given the good agreement of the relative intensities of this present work, the relative intensities measured in earlier work at Daresbury (see Figure 7.2(b)) and that of the PIMS study [17], and bearing in mind that the oxygen partial pressure in the synchrotron beamline used in this work was extremely low.

Comparison of the relative photoionization cross-section and angular distribution parameter, β, as a function of photon energy derived from this work, with that obtained in the earlier work of van der Meulen *et al.* [16] in a lower resolution study at the Wisconsin synchrotron, has been made over the full photon energy range studied. Examples of this comparison are shown in Figure 7.7. On comparison of the two β-parameter plots in Figure 7.7, it can be seen that off-resonance the values of the asymmetry parameter, β, evaluated in this work agree with those of van der Meulen *et al.* [16], within experimental error. The higher resolution obtained with the ELETTRA synchrotron makes comparison of the β-plots obtained in this work in resonance regions with the results obtained by van der Meulen *et al.* [16] in these regions difficult.

A more meaningful comparison of cross-sections can be made if the resolution in the relative photoionization cross-section plot is reduced from 3 meV to 15 meV (FWHM values), the estimated CIS resolution of the work of Van der Meulen *et al.* [16]. This has been done and the results are shown in Figure 7.8. As can be seen in this figure, the agreement between the two cross-section plots is poor with moderate agreement being obtained in the central photon energy region (15.1-15.8 eV) but poor agreement being obtained in the lower (14.0-14.5 eV) and higher (15.9-16.6 eV) regions. It has already been noted that the relative intensities measured here show much better agreement with the relative intensities measured in a PIMS study [17] (see Figure 7.8), and with the relative intensities obtained in a lower resolution study at Daresbury in the present work; therefore the present results are considered more reliable than those of Van der Meulen *et al.* [16].

Recently, Tayal [11] presented the first detailed theoretical calculations of the asymmetry parameters for photoionization of atomic oxygen across autoionization resonances. β-values were calculated for the $O^+(^4S,^2D,^2P)\leftarrow O(^3P)$ ionizations from threshold to 50eV photon energy using the R-matrix method with extensive configuration interaction being used to describe the ^3P initial state and the final $^3S,^3P$ and ^3D continuum states. As already noted (see section 7.3), between the ^4S and ^2D thresholds, the ^3S and ^3D Rydberg states are allowed to autoionize, whereas autoionization of the ^3P states is forbidden in an L-S coupling scheme. j-j interaction is required to enable these ^3P excited states between the first and second threshold to autoionize. As this is not included in the work of Tayal [11], the β-values calculated in reference [11] are expected to be in only semi-quantitative agreement with experiment (particularly for ^3P resonances between the first and second thresholds). Comparisons of the computed [11] and experimental β-values for the $O^+(^4S)\leftarrow O(^3P)$ and $O^+(^2D)\leftarrow O(^3P)$ ionizations in

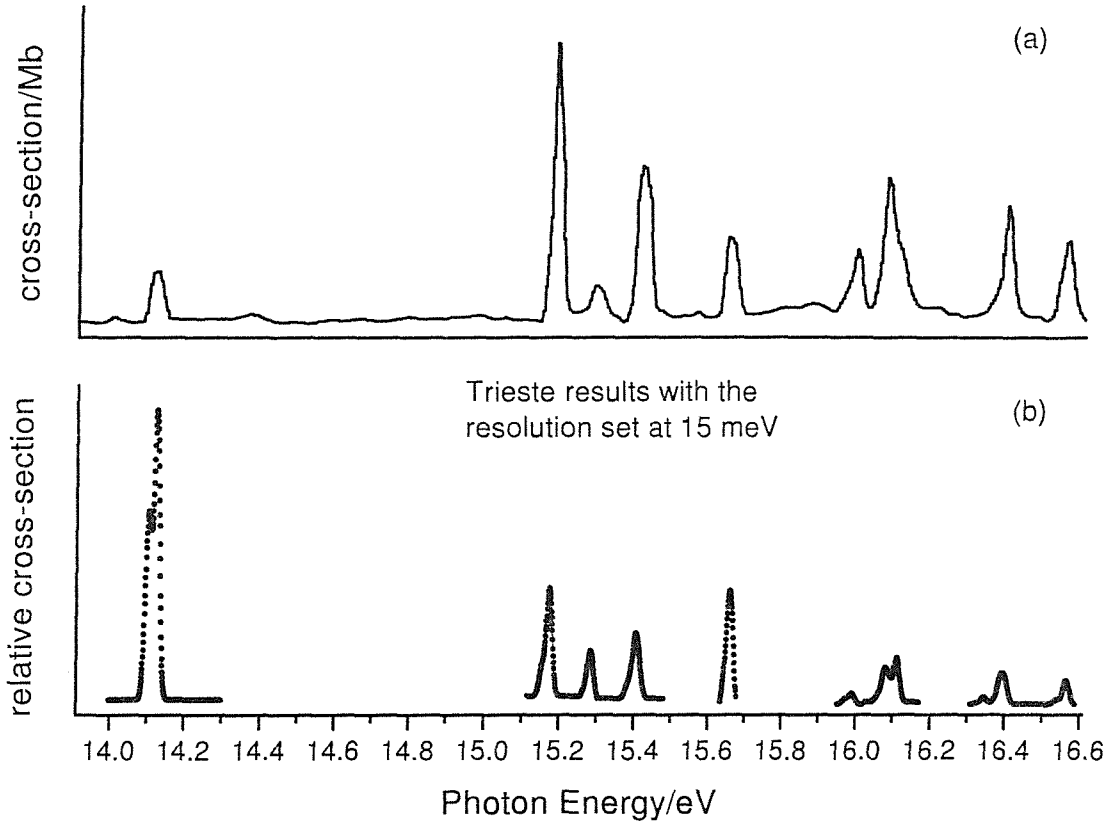

Figure 7.8: Comparison of the relative photoionization cross-section as a function of photon energy obtained in this work (with a resolution, FWHM, reduced from 3 to 15 meV, Figure 7.8(b)), with the corresponding plot obtained by van der Meulen *et al.* [16] (Figure 7.8(a)).

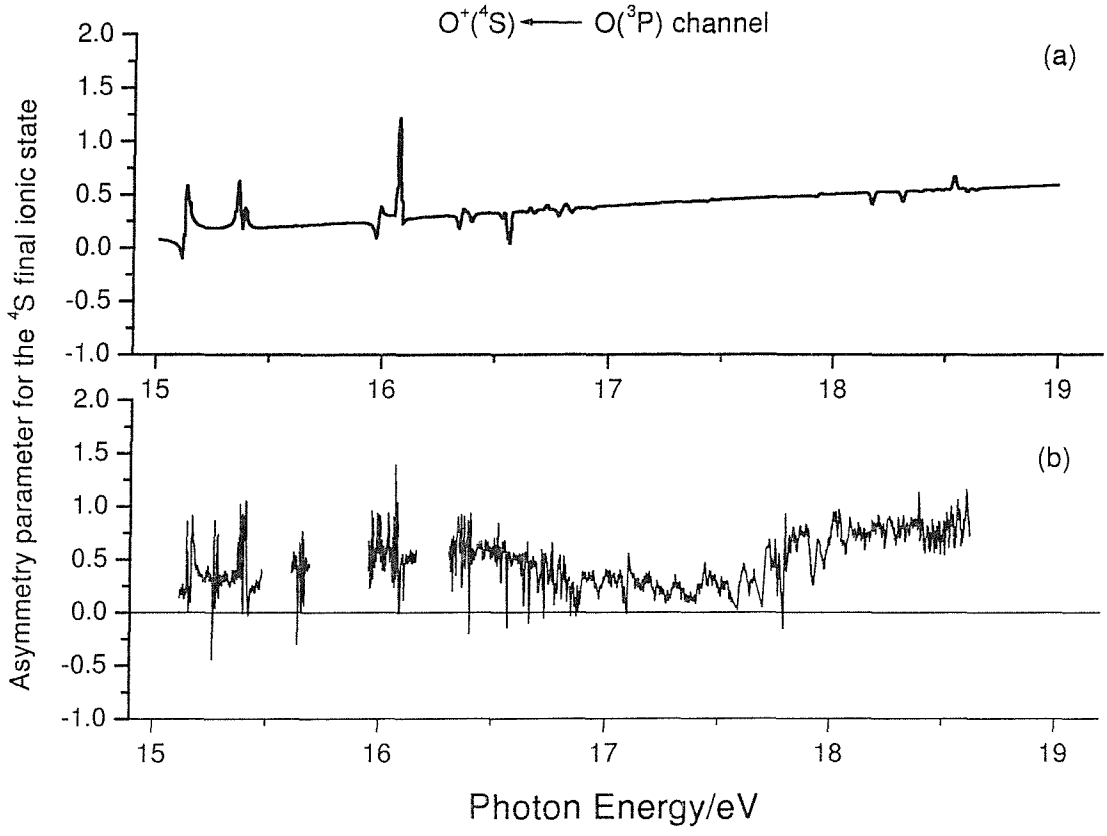

Figure 7.9: Comparison of plots of the asymmetry parameter as a function of photon energy for the $O^+(^4S) \leftarrow O^* \leftarrow O(^3P)$ ionization in the photon energy region 15.0-19.0 eV; (a) from the calculations of Tayal [11], and (b) derived from the measurements of this work.

the photon energy regions 15.0-18.5 and 17.0-18.6 eV respectively are shown in Figures 7.9 and 7.10 respectively.

Figure 7.9 shows reasonable agreement between Tayal's calculations and the experimental results of this work, except for the ^3P resonances which occur below the second ionization threshold *e.g.* the bands at *ca.* 15.28 and *ca.* 15.66 eV, where large changes in β are observed experimentally but no change in β relative to the off-resonance background is seen in the calculations. This is clearly because these ^3P states derive their autoionization intensities from departure from the L-S coupling scheme, and this is not included in the calculations of reference [11]. Figure 7.10 shows poorer agreement between the experimental β-plot and the calculations of Tayal [11], possibly due in part to the poorer quality of the experimental data in the photon energy region 17.0-18.6 eV ,for the $O^+(^2D) \leftarrow O(^3P)$ ionization, as well as neglect of j-j coupling in the calculations [11].

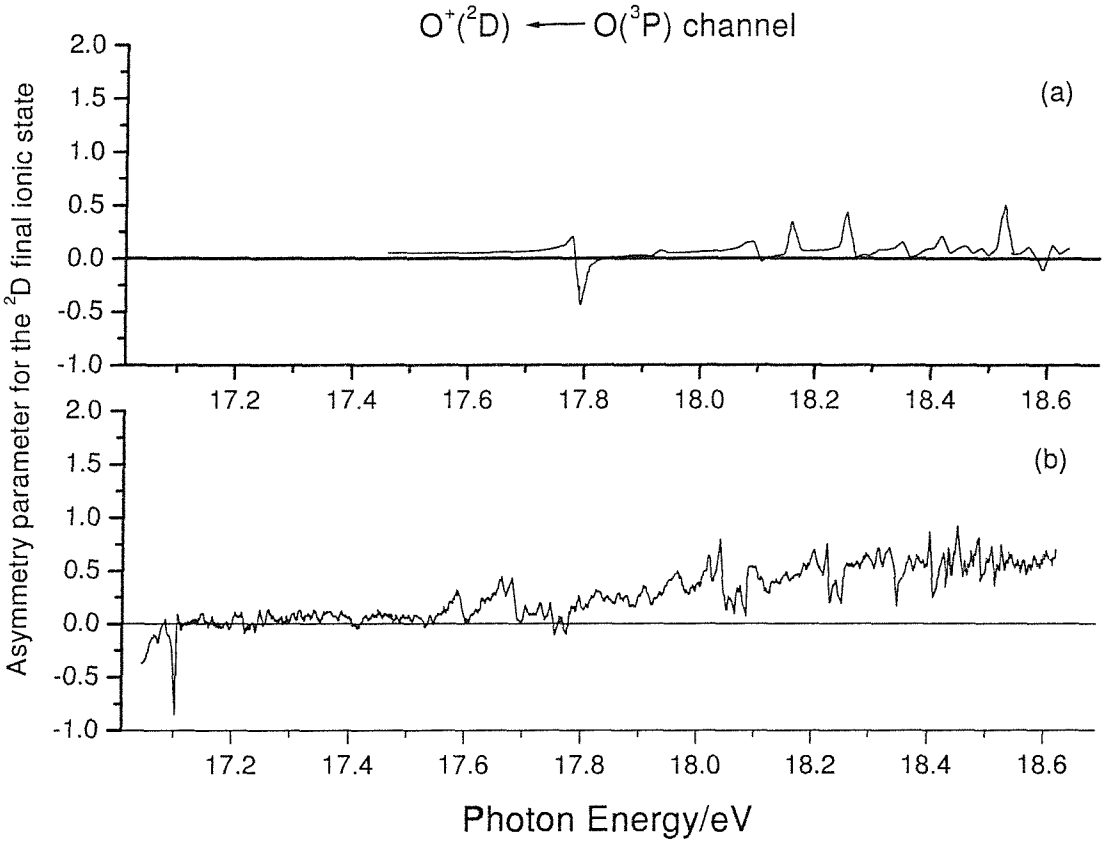

Figure 7.10: Comparison of plots of the asymmetry parameter as a function of photon energy for the $O^+(^2D) \leftarrow O^* \leftarrow O(^3P)$ ionization in the photon energy region 17.2-18.6 eV; (a) from the calculations of Tayal [11], and (b) derived from the measurements of this work.

7.4 Conclusions

The work in this chapter has demonstrated the feasibility of performing angle resolved PES and CIS measurements on reactive species on beamline 4.2R at the ELETTRA synchrotron source at Trieste, by taking oxygen atoms as an example. The relative photoionization cross-sections and angular distribution parameters for the $O^+(^4S)\leftarrow O(^3P)$ and $O^+(^2D)\leftarrow O(^3P)$ ionizations have been measured from threshold (13.6 eV) to 19.0 eV, at the highest resolution yet reported. The results obtained have been compared with recent experimental measurements and calculations. Relative photoionization cross-sections are found to be in error in some recent experimental studies and the need for including intermediate coupling (*i.e.* intermediate between the L-S and j-j limits) in calculations of photoionization cross-sections and angular distribution parameters of atomic oxygen is emphasized.

Following the success of the work described in this chapter, the Southampton PES group plans further studies of atoms and small molecular radicals (*e.g.* S, OH, SH and CF) with the methods described, using the ELETTRA photon source.

Bibliography

[1] A. A. Dias L. Beeching, J. M. Dyke, A. Morris, S. Stranges, J. B. West, N. Zema, and L. Zuin, Mol. Phys , accepted 2002.

[2] L. A. Hall and H. E. Hinteregger, J. Geophys. Res. **75**, 6959 (1970).

[3] K. Takayanagi and Y. Itikawa, Space Science Reviews **11**, 380 (1970).

[4] R. C. Whitten and I. G. Popoff, *Fundamentals of Aeronomy* (Wiley, New York, 1971).

[5] N. Jonathan, D. J. Smith, and K. J. Ross, J. Chem. Phys.**53**, 3758 (1970).

[6] N. Jonathan, A.Morris, D. J. Smith, and K. J. Ross, Chemical Physics Letters**7**, 497 (1970).

[7] J. A. R. Samson and V. E. Petrovsky, Phys. Rev. A **9**, 2449 (1974).

[8] J. A. R. Samson and W. H. Hancock, Phys. Letts. A **61**, 380 (1977).

[9] J. L. Dehmer and P. M. Dehmer, J. Chem. Phys. **67**, 1782 (1977).

[10] A. F. Starace, S. T. Manson, and D. J. Kennedy, Phys. Rev. A **9**, 2453 (1974).

[11] S.S.Tayal, J. Phys. B **34**, 2215 (2001).

[12] M. I. A. Hussein, D. M. P. Holland, K. Codling, P. R. Woodruff, and E. Ishiguro, J. Phys. B **18**, 2827 (1985).

[13] J.A.R.Samson and P.N.Pareek, Phys. Rev. A **31**, 1470 (1985).

[14] W. J. van der Meer, P. van der Meulen, M. Volmer, and C . A. de Lange, Chem. Phys. **126**, 385 (1988).

[15] G. Prumper, B. Obst, W. Benten, B. Zimmerman, P. Zimmerman, and U. Becker, J. Phys. B **32**, 4101 (1999).

[16] P. van der Meulen, M. O. Krause, and C. A. de Lange, Phys. Rev. A **43**, 5977 (1991).

[17] P. M. Dehmer, J. Berkowitz, and W. A. Chupka, J. Chem. Phys. **59**, 5777 (1973).

[18] P. M. Dehmer, W. L. Luken, and W. A. Chupka, J. Chem. Phys.**67**, 195 (1977).

[19] R. E. Huffman, J. C. Larrabee, and Y Tanaka, J. Chem. Phys. **46**, 2213 (1967).

[20] P. M. Dehmer and W. A. Chupka, J. Chem. Phys. **62**, 4525 (1975).

[21] D. Desiderio, S. DiFonzo, B. Diviacco, W. Jark, J. Krempasky, R. Krempaska, F. Lama, M. Luce, H. C. Mertins, M. Piacentini, T. Prosperi, S. Rinaldi, F. Schefers, F. Schmolla, G. Soulle, L. Stichauer, S. Turchini, R. P. Walker, and N. Zema, Synchrotron Radiation News **12**, 34 (1999).

[22] A. Derossi, F. Lama, M. Piacentini, T. Prosperi, and N. Zema, Rev. Sci. Instrum. **66**, 1718 (1995).

[23] J. B. West and G. V. Marr, Atomic and Nuclear Data Tables **18**, 497 (1976).

[24] C. E. Moore, *Atomic Energy Levels*, Vol. 1 of *Circular of the national bureau of standards 467* (US Govt. Printing Office, Washington, DC, 1952).

[25] C. N. Yang, Phys. Rev. **74**, 764 (1984).

[26] D. M. de Leeuw and C. A. de Lange, Phys. Rev. **54**, 123 (1980).

[27] J. A. R Samson and V. E. Petrovsky, J. Elec. Spec. Rel. Phen. **3**, 461 (1974).

Chapter 8

PES of the Hydroxyl radical, $OH(X^2\Pi)$

8.1 Introduction

This chapter gives a brief overview of the continuing studies of the hydroxyl radical in the Southampton PES group.

The hydroxyl radical (OH) is of interest as it plays key roles in the chemistry of the Earth's atmosphere [1, 2], combustion processes [3, 4] and the interstellar medium [5, 6]. The low-lying electronic states of the neutral molecule have been extensively studied by experiment [7–14] and theory [15–17]. The UV absorption spectrum at wavelengths shorter than 1200 Å is poorly resolved [13] and resonant states above the first ionization energy have only been observed by photoionization mass spectrometry (PIMS). [18, 19]

The ground state electronic configuration of OH is

$$1\sigma^2 2\sigma^2 3\sigma^2 1\pi^3, X^2\Pi,$$

where each 1π molecular orbital consists of an O $2p_\pi$ atomic orbital and is thus non-bonding in character, and the 3σ orbital is a bonding orbital consisting of H$1s$ and O$2p_\sigma$ contributions. The $(1\pi)^{-1}$ ionization produces the $X^3\Sigma^-$, $a^1\Delta$, and $b^1\Sigma^+$ states of OH^+, while the $(3\sigma)^{-1}$ ionization gives rise to the $A^3\Pi$ and $c^1\Pi$ ionic states. [20, 21]. The HeI (21.22 eV) photoelectron spectrum of OH shows three bands associated with the $(1\pi)^{-1}$ ionization [21], with adiabatic ionization energies of 13.01, 15.17, and 16.61 eV. For the $(3\sigma)^{-1}$ ionization, only the $OH^+(A^3\Pi)\leftarrow OH(X^2\Pi)$ band was observed because of the poor transmission of the spectrometer above 18.0 eV. [21]

A UV emission spectroscopic study of OH^+ by Merer *et al.* [22] gave accurate spectroscopic constants for the $X^3\Sigma^-$, $A^3\Pi$, and $b^1\Sigma^+$ ionic states. The $c^1\Pi$ state

of OH^+ has been observed by laser photofragmentation spectroscopy [23],leading to a derived AIE for the $OH^+(c^1\Pi)\leftarrow OH(X^2\Pi)$ ionization of 18.30 eV [24].

The lowest-lying states of OH have been extensively studied by theoretical methods [16, 17, 25]. The position and spectroscopic properties of neutral states near or above the first ionization threshold (*i.e.* Rydberg states) are less well known [15, 25, 26]. Potential curves for the first five electronic states of OH^+ have been calculated by the multireference double excitation configuration interaction (MRDCI, see section 4.7.4) method [24] and molecular constants derived from the computed potential curves are in good agreement with available experimental values and those derived from other calculations [27, 28].

Excited states of OH which autoionize to OH^+ states have been observed by PIMS [18, 19]. Three Rydberg series have been identified in the photon energy range 13.0-18.2 eV converging to the $a^1\Delta$, the $b^1\Sigma^+$ and $A^3\Pi$ ionic limits.

The Southampton PES group has previously carried out an investigation into the photoelectron spectroscopy of OH and OD radicals [26] using synchrotron radiation (see Chapter 3) at the SRS (Daresbury, see section 5.2). Rydberg states converging to the $a^1\Delta$ and $A^3\Pi$ states were observed in the constant ionic state spectra of both OH and OD. These were confidently assigned with the aid of FCF calculations (see section 4.7.3) and by comparson with previous work, as autoionizations via Rydberg states. The two observed Rydberg series were assigned as excitations to $a^1\Delta, nd$ states, in the photon energy range 13.0-15.2 eV, and as excitations to $A^3\Pi, nd$ states in the photon energy range 14.8-17 eV [26].

To evaluate the viability of further synchrotron studies on small radicals using the third generation synchrotron source at Elettra (see section 5.2.3), a selection of the measurements previously made at Daresbury [26] were repeated. The two Rydberg series observed previously were briefly re-investigated, to try to take advantage of the increased flux and improved narrow bandwidth available at Elettra.

8.2 Experimental

The synchrotron spectrometer used was as described in section 5.3, with BL4.2 at Elettra (see section 5.2.3 [29]) as a photon source. Experiments could be performed either of the conventional PES type, in which photoelectron spectra are recorded at fixed photon energy, or of the CIS type in which the intensity of a particular photoelectron feature is monitored as a function of photon energy.

OH radicals were produced by the rapid reaction of atomic hydrogen with nitrogen dioxide, as described in section 5.3.7 and shown below.

$$H_2 \xrightarrow[discharge]{\mu-wave} H + H$$

$$H + NO_2 \xrightarrow[atom-molecule]{fast} OH + NO$$

Hydrogen atoms were produced by passing a flowing mixture of helium and hydrogen through a microwave discharge (2.45 GHz) in a phosphoric acid coated, dog-leg, glass inlet tube (12 mm inner diameter, see section 5.3.7). NO_2 was introduced into the H_2/H/He mixture, about 3 cm above the photon beam, through an inner inlet tube, 1 mm internal diameter (see Figure 5.8). The reaction conditions were optimized for the maximum production of OH, under conditions of little or no observable NO_2 signals, by monitoring the signals of the first bands of NO, OH, and NO_2 in photoelectron spectra recorded at 21.22 eV photon energy. Photoelectron spectra were calibrated using the known ionization energies of NO and H_2O [26, 30].

HeI photoelectron spectra were recorded initially to optimize the yield of OH. CIS spectra were then recorded for the $OH^+(X^3\Sigma^+,\ v^+ = 0) \leftarrow OH(X^2\Pi, v'' = 0)$ vibrational component, in the photon energy range 13.1-14.8 eV, and the $OH^+(a^1\Delta,\ v^+ = 0) \leftarrow OH(X^2\Pi, v'' = 0)$ vibrational component, in the photon energy range 15.5-16.8 eV, where plenty of structure is expected to be observed.

8.3 Results and discussion

Figure 8.1 shows the HeI (21.22 eV) photoelectron spectrum recorded for the H+NO_2 reaction with the H_2/He discharge on and off. As can be seen from Figure 8.1, there is almost complete reaction of the NO_2 in the discharge-on spectrum. The spectra obtained are in good agreement with those recorded previously by Katsumata and Lloyd [20] and those previously recorded by the Southampton PES group [26].

Figure 8.1 clearly shows the first two photoelectron bands of OH at 13.01 and 15.17 eV AIE corresponding to the ionizations $OH^+(X^3\Sigma^-, v^+ = 0, 1) \leftarrow OH(X^2\Pi, v'' = 0)$ and $OH^+(a^1\Delta^-, v^+ = 0) \leftarrow OH(X^2\Pi, v'' = 0)$, respectively. Bands associated with H_2, H, NO, and OH were observed in the discharge-on spectrum, along with signals arising from H_2O, O, and O_2 produced by secondary reactions.

In this brief study the most intense vibrational components for the first band $[OH^+(X^3\Sigma^-, v^+ = 0) \leftarrow OH(X^2\Pi, v'' = 0)]$ and the second band $[OH^+(a^1\Delta^-, v^+ = 0) \leftarrow OH(X^2\Pi, v'' = 0)]$ of OH were selected for CIS studies.

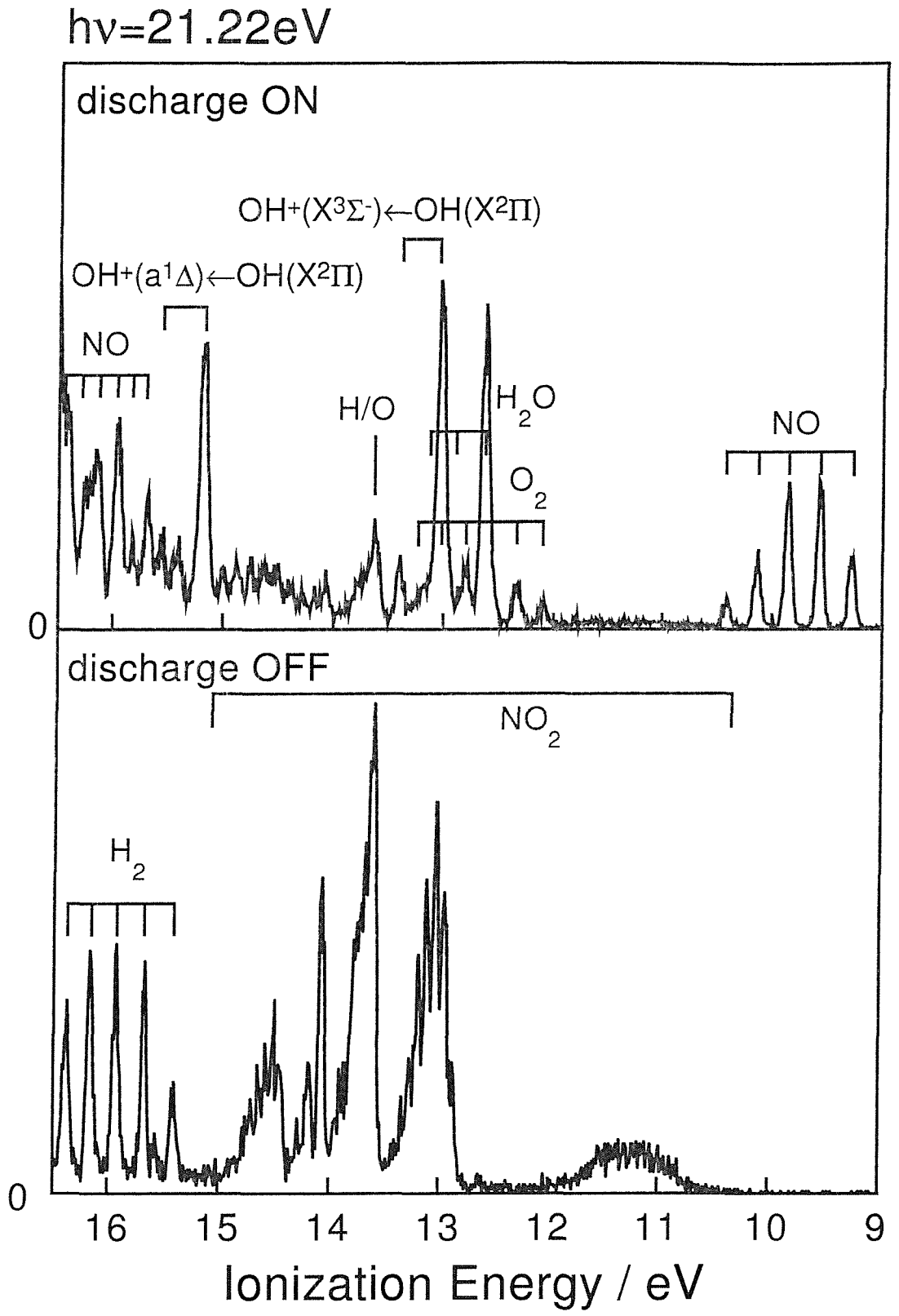

Figure 8.1: HeI Photoelectron spectra recorded for the reaction mixture H_2/He+NO_2 with the microwave discharge on and off.

8.3.1 CIS of $OH^+(X^3\Sigma^+, v^+ = 0)$, h$\nu$=13.1-14.8 eV

The CIS spectrum was recorded for the $OH^+(X^3\Sigma^+, v^+ = 0) \leftarrow OH(X^2\Pi, v'' = 0)$ ionization, in the photon energy range 13.1-14.8 eV, and this was compared with spectra previously recorded at the SRS (Daresbury). The CIS spectra recorded at the two different synchrotron sources are shown in Figure 8.2. The new spectrum (Figure 8.2a) shows good agreement with the previously recorded spectrum (Figure 8.2b, [26]); however, it is immediately evident that the new spectrum is of much higher resolution. The previously assigned Rydberg series for autoionization via the $OH^*(a^1\Delta, nd)$ intermediate state is shown in Figure 8.2 [19, 26]. Figure 8.2a shows much rotational structure in each of the vibrational components of the excited state and this is demonstrated in Figure 8.3, which expands the photon energy range 13.5-13.6 eV. Figure 8.3a shows the previously recorded photoionization mass spectrometric (PIMS) spectrum recorded by Cutler *et al.* [19] with features with linewidths of ~2 meV. Figure 8.3b shows the newly obtained CIS spectra for the $OH^+(X^3\Sigma^-, v^+ = 0) \leftarrow OH(X^2\Pi, v'' = 0)$ ionization. The PIMS spectra shows that all the rotationally resolved features in this region can be assigned to autoionizaion via the $OH^*(a^1\Delta, 3d)$ Rydberg state.

The rotational structure shown in Figure 8.3 has not yet been assigned. The spin-orbit splitting in the $^2\Pi$ state (139.1 cm^{-1}, 0.017 eV) [31] means that the $^2\Pi_{1/2}$ will be 139.1 cm^{-1} above the $^2\Pi_{3/2}$ state with a relative population of 0.51 at 300°K.

From the method used to make OH, ionization will occur from both spin-orbit components with a Boltzmann population of the rotational levels at ≈300°K. In the CIS experiments, $OH^+(X^3\Sigma^-, v^+ = 0)$ is detected (irrespective of the ionic rotational level produced) and the structure shown in Figure 8.3 must arise from $OH^*(a^1\Delta, 3d, v'' = 0, J') \leftarrow OH(X^2\Pi_{1/2,3/2}, v'' = 0, J'')$ transitions. Attempts will be made in future in the Southampton PES group to simulate this structure using one-photon rotational line strengths.

Also, a $^1\Delta 3d$ Rydberg state is expected to give $^1\Delta 3d\sigma$, $^1\Delta 3d\pi$ and $^1\Delta 3d\delta$ components in $C_{\infty v}$ symmetry. These give rise to the following states:

$$a^1\Delta 3d\sigma \longmapsto {}^2\Delta$$
$$a^1\Delta 3d\pi \longmapsto {}^2\Pi, {}^2\Phi$$
$$a^1\Delta 3d\delta \longmapsto {}^2\Sigma, {}^2\Gamma$$

Using the $\Delta\Lambda = 0, \pm 1$ one photon selection rule, only the $OH^* \leftarrow OH$ $^2\Delta \leftarrow {}^2\Pi$, $^2\Pi \leftarrow {}^2\Pi$ and $^2\Sigma \leftarrow {}^2\Pi$ transitions are allowed.

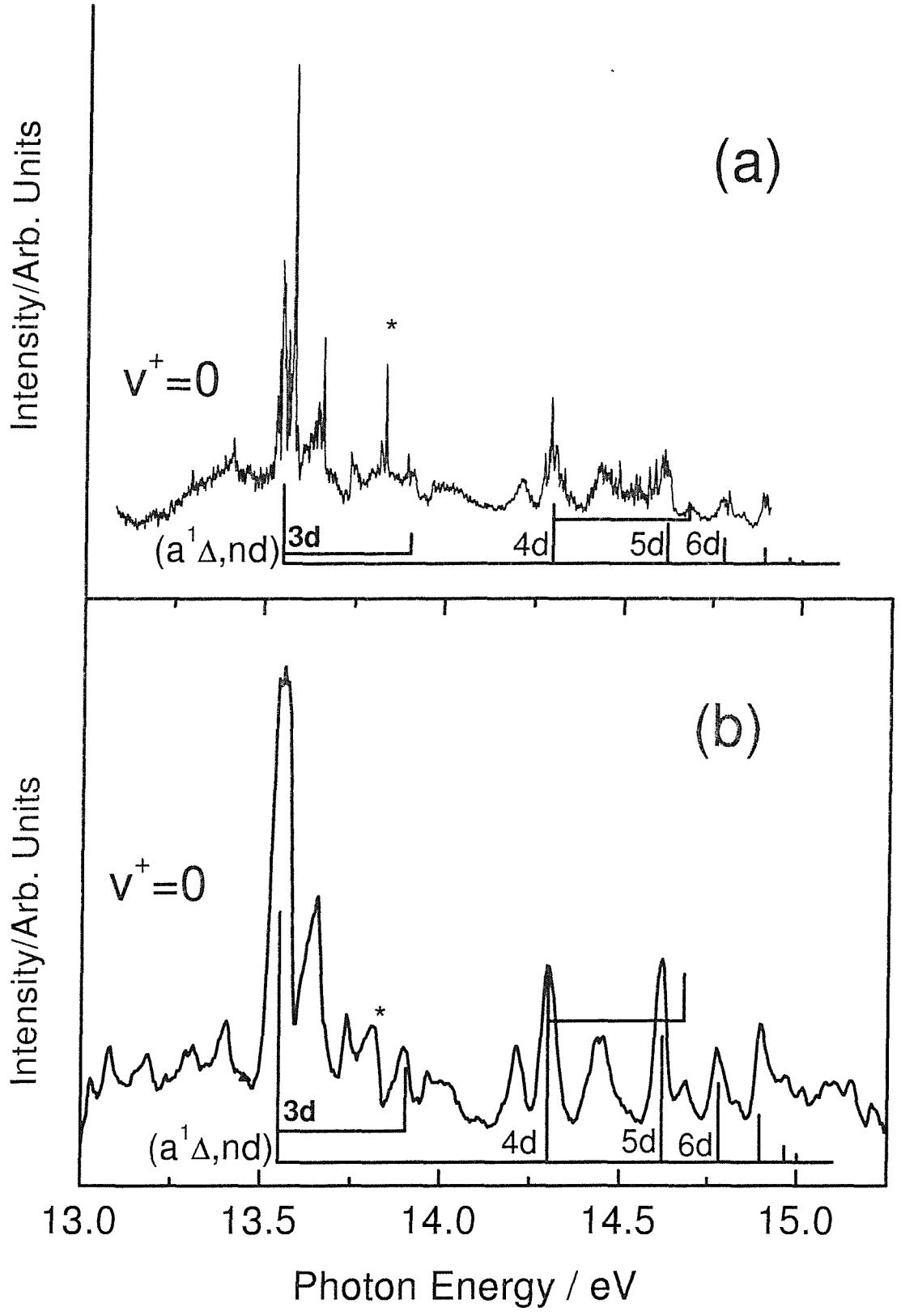

Figure 8.2: CIS spectra for the $OH^+(X^3\Sigma^+, v^+ = 0) \leftarrow OH(X^2\Pi, v''=0)$ ionization, in the photon energy range 13.1-14.8 eV; (a)recorded at Elettra (Trieste, Italy).(b)recorded at the SRS (Daresbury). The asterisks (*) mark the position of an NO resonance.

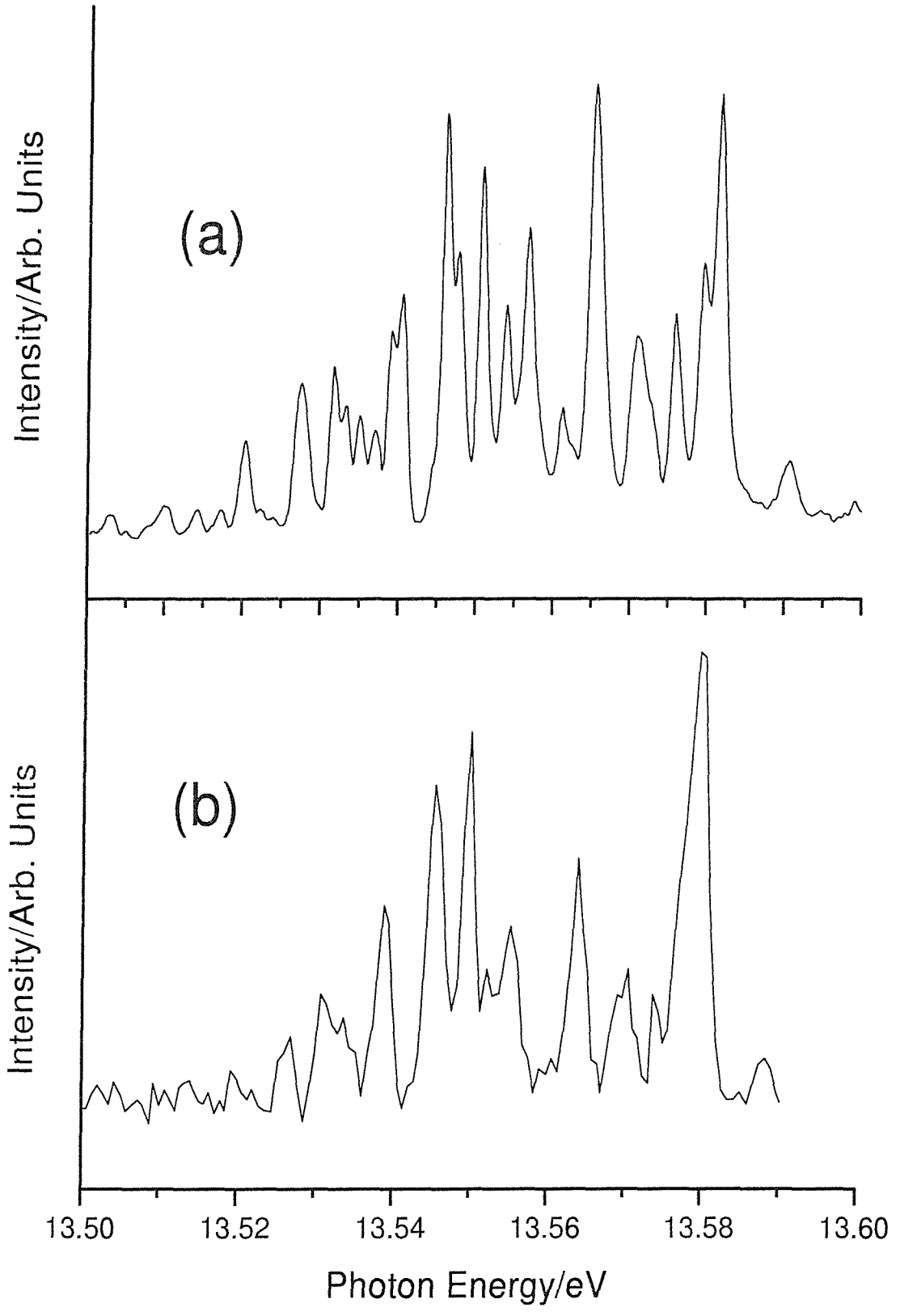

Figure 8.3: Spectra of OH in the photon energy range 13.5-13.6 eV. (a)PIMS spectrum recorded by Cutler [19].(b)CIS spectra for the $OH^+(X^3\Sigma^+, v^+ = 0) \leftarrow OH(X^2\Pi, v''=0)$ ionization.

8.3.2 CIS of $OH^+(a^1\Delta, v^+ = 0)$, hν=15.5-16.8 eV

The CIS spectrum was recorded for the $OH^+(a^1\Delta, v^+ = 0) \leftarrow OH(X^2\Pi)$ ionization, in the photon energy range 15.5-16.8 eV, and this was compared with spectra previously recorded at the SRS (Daresbury). The CIS spectra recorded at the two different synchrotron sources are shown in Figure 8.4. As previously seen for the $OH^+(X^3\Sigma^+, v^+ = 0) \leftarrow OH(X^2\Pi)$ ionization, a great improvement in resolution is observed and most of the features observed can be matched to the $OH^*(a^3\Pi, nd)$ series that has been previously assigned [19, 26]. The example shown in Figure 8.4 unfortunately has poor signal to noise ratio (due to limited synchrotron time), but this could be greatly improved if the experiment was repeated.

8.4 Conclusion

The work in this chapter is presented to demonstrate the feasibility of synchrotron studies on short-lived radicals. The increased photon flux and improvement in spectral resolution available at the third generation source at Elettra, with the synchrotron spectrometer (described in section 5.3) makes the study of short-lived molecules possible with PES, CIS and angle-resolved measurements.

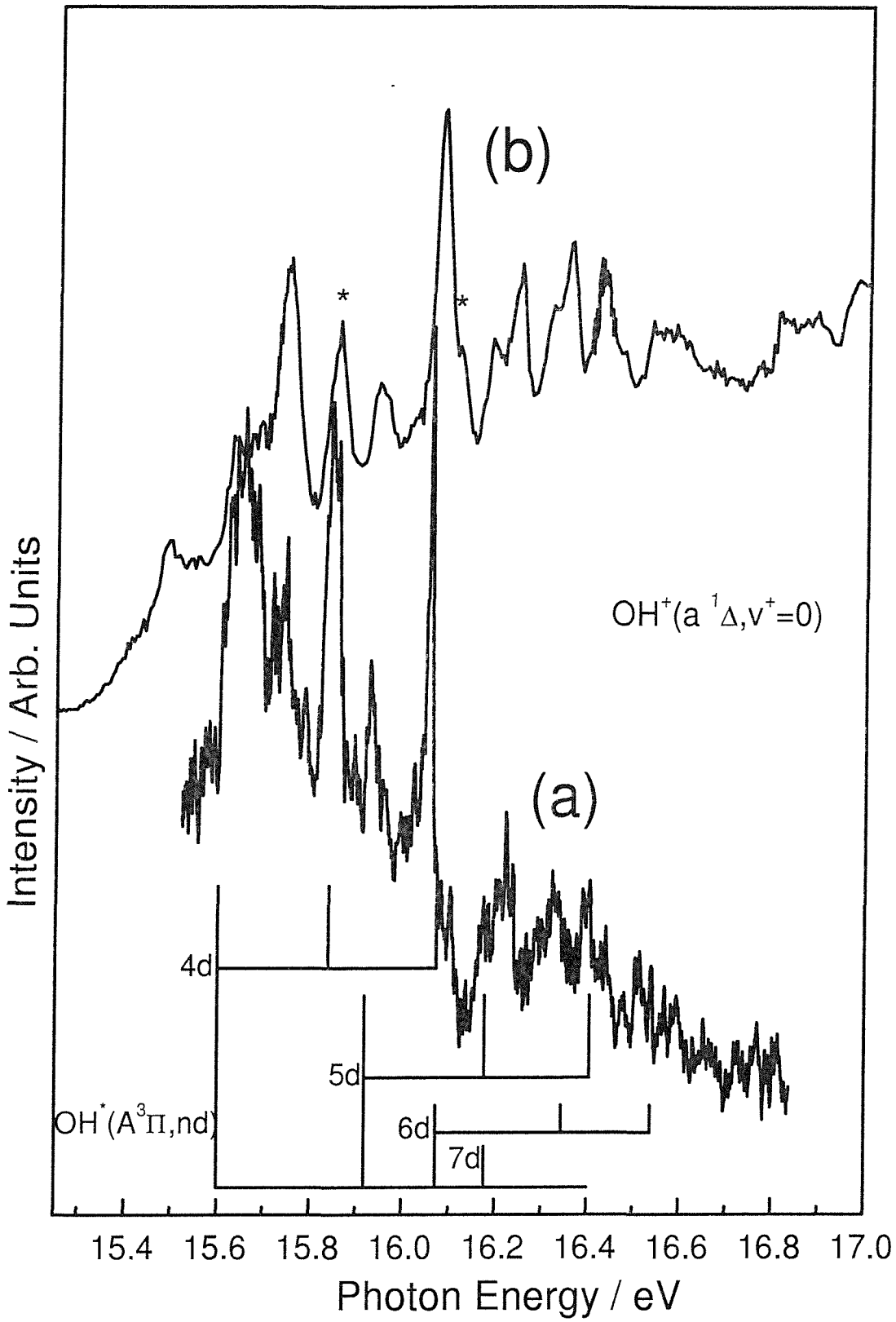

Figure 8.4: CIS spectra for the $OH^+(a^1\Delta^+,\ v^+ = 0)\leftarrow OH(X^2\Pi,v"=0)$ ionization, in the photon energy range 15.5-16.8 eV; (a)recorded at Elettra (Trieste, Italy).(b)recorded at the SRS (Daresbury).The asterisks (*) mark the position of NO resonances.

Bibliography

[1] R. P. Wayne, *Chemistry of Atmospheres* (Clarendon Press, Oxford, 1991).

[2] F. J. Comes, Angew. Chem. Int. Ed. **33**, 1816 (1994).

[3] D. J. Hucknall, *Chemistry of Hydrocarbon Combustion Reactions* (Chapman Hall, London, 1985).

[4] G. J. Mintoff and C. F. H. Tipper, *Chemistry of Combustion Reactions* (Butterworths, London, 1962).

[5] A. Dalgarno and J. H. Black, Rep. Prog. Phys. **39**, 573 (1976).

[6] W. D. Watson, Rev. Mod. Phys **48**, 513 (1976).

[7] J. B. Nee and L. C. Lee, J. Chem. Phys. **81**, 31 (1984).

[8] R. J. Cody, C. Maralejo, and J. E. Allen, J. Chem. Phys. **95**, 2491 (1991).

[9] M. Collard, P. Kerwin, and A. Hodgson, Chem. Phys. Lett. **179**, 422 (1991).

[10] E. de Beer, M. P. Koopmans, C. A. de Lange, Y. Wang, and W. A. Chupka, J. Chem. Phys. **94**, 7634 (1991).

[11] E. de Beer, C. A. de Lange, J. A. Stephens, Y. Wang, and V. McKoy, J. Chem. Phys. **95**, 714 (1991).

[12] C. A. de Lange, in *High Resolution Laser Photoionization and Photoelectron Studies*, edited by I. Powis, T. Baer, , and C. Y. Ng (Wiley, Chichester, YEAR).

[13] J. C. Viney, J. Mol. Spectrosc. **83**, 465 (1980).

[14] A. E. Douglas, Can. J. Phys. **52**, 318 (1984).

[15] E. F. van Dishoeck and A. Dalgarno, J. Chem. Phys. **79**, 873 (1983).

[16] E. F. van Dishoeck, S. R. Langhoff, and A. Dalgarno, J. Chem. Phys. **78**, 4552 (1983).

[17] A. V. Nemukhin and B. L. Grigorenko, Chem. Phys. Lett. **276**, 171 (1997).

[18] P. M. Dehmer, Chem. Phys. Lett. **110**, 79 (1984).

[19] J. N. Cutler, Z. X. He, and J. A. R. Samson, J. Phys. B **28**, 4577 (1995).

[20] S. Katsumata and D. R. Lloyd, Chem. Phys. Lett. **45**, 519 (1977).

[21] H. van Lonkhuyzen and C. A. de Lange, Mol. Phys. **51**, 551 (1984).

[22] A. J. Merer, D. N. Malm, R. W. Martin, M. Horani, and J. Rostas, Can. J. Phys. **53**, 251 (1975).

[23] D. J. Rodgers and P. J. Sarre, Chem. Phys. Lett. **143**, 235 (1988).

[24] M. Hirst and M. F. Guest, Mol. Phys. **49**, 1461 (1983).

[25] I. Easson and M. H. L. Pryce, Can. J. Phys. **51**, 518 (1973).

[26] J. D. Barr, A. De Fanis, J. M. Dyke, S. D. Gamblin, N. Hooper, A. Morris, S. Stranges, J. B. West, and T. G. Wright, J. Chem. Phys. **110**, 345 (1999).

[27] R. P. Saxon and B. Liu, J. Chem. Phys. **85**, 2099 (1986).

[28] R. de Vivie, C. M. Marion, and S. D. Peyerimhoff, Chem. Phys. **112**, 349 (1987).

[29] J. M. Dyke, S. D. Gamblin, A. Morris, T. G. Wright, A. E. Wright, and J. B. West, J. Electron Spect. Relat. Phenom. **97**, 5 (1998).

[30] D. W. Turner, *Molecular Photoelectron Spectroscopy* (Wiley-Interscience, London, UK, 1971).

[31] K. P. Huber and G. Herzberg, *Molecular Spectra and Molecular Structure IV: Constants of Diatomic Molecules* (van Nostrand Reinhold Co., New York, 1979).

Chapter 9

Study of the electronic structure of the actinide tetrabromides $ThBr_4$ and UBr_4

9.1 Introduction

The uranium and thorium tetrahalides play important roles in nuclear fuel enrichment and reprocessing [1] and they have been studied in some detail both in the solid state and the gas phase. Uranium tetrafluoride is of particular importance in the nuclear industry as it acts as a precursor for both uranium metal and UF_6 required for isotope enrichment processes. UF_4 is usually prepared from UO_2 , extracted from uranium ore, by reaction with HF at 850°K in a fluidized-bed reactor. It is then directly fluorinated to produce UF_6 for isotope separation. Similarly, thorium tetrafluoride is a key intermediate for the reprocessing and recovery of thorium metal. [1]

The investigation of the electronic structure of the uranium and thorium tetrahalides provides a good opportunity to study the role of metal 5f electrons in chemical bonding [2–6]. The gas-phase HeI photoelectron spectra of UF_4, ThF_4, UCl_4, and $ThCl_4$ have been recorded previously [2]. The spectra were first interpreted using nonrelativistic multiple-scattering SCF-Xα calculations [2] and later reinterpreted using relativistic Hartree-Fock-Slater (HFS) density functional calculations (see section 4.5) [7]. For each tetrafluoride or tetrachloride, the results are consistent with an effective tetrahedral geometry with no evidence of any Jahn-Teller distortion away from tetrahedral symmetry. In the uranium tetrahalides, a distortion from tetrahedral symmetry is possible because of the open-shell degenerate ground state and gas-phase electron diffraction studies indicated a structure of C_{2v} symmetry, with equal metal-halogen bond lengths [8]. Recently

a density functional study of the ground states of the thorium tetrahalides has also provided estimates of equilibrium bond lengths and harmonic vibrational frequencies of ThX_4 (where X=F, Cl, Br, and I) [9]. These thorium tetrahalides were all found to have tetrahedral minimum energy geometries in their ground states.

In summary, although reasonably detailed experimental studies have been undertaken to probe the electronic structure of the uranium and thorium tetrafluorides and tetrachlorides, relatively little work has been undertaken on the corresponding tetrabromides, UBr_4 and $ThBr_4$.

Electron-impact high temperature mass spectrometric studies of the uranium and thorium halides [10–12] have measured the appearance energy of $ThBr_4^+$ from $ThBr_4$ as 10.4±0.3 eV [10] and UBr_4^+ from UBr_4 as 9.6±0.3 eV [11]. These represent the only available values for the first ionization energies of these molecules.

The aim of work described in this chapter was to record HeI photoelectron spectra of $ThBr_4$ and UBr_4 in the vapor phase using the high temperature photoelectron spectrometer which uses radio frequency induction heating to vaporize a solid sample (see section 5.4) [13–15]. It was proposed to compare the photoelectron spectra obtained for $ThBr_4$ and UBr_4 with those previously recorded for UF_4, ThF_4, UCl_4, and $ThCl_4$. Relativistic density functional calculations of vertical ionization energies (VIEs) were also performed for all six MX_4 tetrahalides (where M=Th, U; X=F, Cl, and Br). Comparison with experimental VIEs should allow ionic state assignment to be achieved for the tetrabromides and trends in ionization energies and ionic state spin-orbit splittings in the metal tetrahalides deduced as the halide ligand gets heavier. Supporting matrix isolation experiments were also carried out under very similar vaporization conditions in order to confirm the composition of the vapor and obtain infrared spectra of the MBr_4 species.

9.2 Experimental

9.2.1 Sample preparation

$ThBr_4$ was commercially available as an anhydrous solid (Pfaltz and Bauer, 99.5%). It was used as received, as the small impurities would have so low partial pressure in the spectrometer as to be negligible. Samples were kept in a desiccator prior to use and loaded into a furnace under nitrogen prior to transfer to the photoelectron spectrometer. This reduced, but did not eliminate, hydration

Crystal parameter	Values from single crystal diffraction pattern[a]	Reference parameters [18]
Space group	C2/m	C2/m
a	11.01	11.04(2)
b	8.77	8.76(2)
c	7.06	7.04(1)
α	90.00	90.00
β	94.24	94.05(8)
γ	90.00	90.00

a. Single crystal data were obtained using the Nonius COLLECT software, incorporationg the DENZO Package [19, 20].

Table 9.1: Comparison of the values used to reproduce the X-ray diffraction pattern obtained from a UBr_4 single crystal prepared in this work, with those reported in the literature [18].

of the sample.

UBr_4 was prepared from UO_2 (Strem Chemicals) using an existing preparative route [16]. This involved passing bromine in dry nitrogen over a heated UO_2/C mixture at 1300°K. The product, which was collected downstream of the solid UO_2/C mixture in a long reaction tube, was initially identified as UBr_4 by its appearance as a tan coloured powder [17] which distinguished it from the main likely impurity, UO_2Br_2, which is a brick-red colour.

9.2.2 X-ray Diffraction

A small sample of the product was sealed in a Lindemann capillary and examined by X-ray diffraction using a Nonius Kappa CCD diffractometer with Mo $K\alpha$ radiation (λ = 0.71069Å). This diffractometer forms part of the National X-ray Crystallographic Service, based at Southampton. A good powder pattern was obtained from a single one degree image, but this also showed single crystal reflections. Following recording of a further ten one degree images, it proved possible to index all observed reflections, as one set, to give a cell analogous to that previously reported for UBr_4 [18] (see Table 9.1). The powder lines were all compatible with this cell, indicating a homogeneous sample.

9.2.3 Matrix isolation

The general features of the matrix isolation equipment used for this work have been described previously [21]. Matrix isolation infrared studies on UBr_4 and

$ThBr_4$ involved vaporization of the samples in the temperature range 720-800°K and subsequent co-condensation with argon onto a cesium iodide window cooled to ≈12°K. The bromide samples were contained in silica holders and extensively degassed at ≈600°K in order to remove traces of HBr, arising from hydrolysis. Final purification was by sublimation immediately prior to co-condensation with argon. Pure samples of solid UBr_4 were yellow-brown in color, while those of $ThBr_4$ were white. Deposition times were typically 1-2 h and the argon matrix was estimated to be at least 1000-fold in excess relative to the metal tetrabromide in the final matrix used for spectroscopic study. Infrared spectra were recorded over the range 4000-180 cm^{-1} using a PE983 infrared spectrometer, supported by standard data processing facilities.

9.2.4 Photoelectron spectroscopy

In the photoelectron experiments, the actinide tetrabromide molecules, UBr_4 and $ThBr_4$, were produced in the gas phase by vaporizing a solid sample from an inductively heated graphite furnace using the high temperature spectrometer described in section 5.4 [13–15]. $ThBr_4$ and UBr_4 are known to vaporize congruently [10, 12]. The temperature range over which vaporization occurred, and over which photoelectron spectra were recorded with reasonable signal-to-noise ratios, was 870-1000°K for $ThBr_4$ and 820-970°K for UBr_4 as estimated from measurements made with a chromel-alumel (K-type) thermocouple attached to the furnace. For both tetrabromides, it was found necessary to bake the sample on the photoelectron spectrometer, initially at 550°K for 1 h to remove residual water and hydrogen bromide. Any MO_2Br_2 (M=Th or U) that may have been present as a minor impurity in the MBr_4 samples would have decomposed (to less volatile MO_2 and MBr_4) at the temperatures at which photoelectron spectra were obtained [1, 17, 22].

In a typical photoelectron experiment, a solid MBr_4 sample was loaded into a graphite furnace in a glove bag under dry nitrogen. This was then transferred as quickly as possible to the high temperature photoelectron spectrometer, which was immediately evacuated to minimize exposure of the samples to air. Both $ThBr_4$ and UBr_4 hydrolyze in air with UBr_4 appearing to hydrolyze more rapidly.

The typical resolution of the spectrometer under the conditions at which HeI ($h\nu$=21.22 eV) photoelectron spectra were recorded was 25-35 meV full width at half maximum (FWHM), as measured for the $(3p)^{-1}$ HeI ionization of argon. Spectra were calibrated using argon, methyl iodide, nitrogen, carbon monoxide, and hydrogen bromide. The transmission of the spectrometer, which varies lin-

early with pass energy [23], was checked regularly using oxygen. Under conditions at which the MBr_4 spectra were recorded, it was found to be acceptable, as the fifth band of oxygen could be observed with reasonable intensity relative to the other four oxygen bands. Hence, the relative band intensities in the MBr_4 spectra presented in this work are not unduly affected by loss of intensity at lower kinetic energy.

9.3 Computational details

Relativistic density functional theory (DFT) calculations (see section 4.5) of vertical ionization energies were carried out for the actinide tetrahalides MX_4 (M=U, Th; X=F, Cl, Br) to facilitate a complete valence ionic state assignment of their ultraviolet photoelectron spectra. Calculations for the actinide halides ThF_4, $ThCl_4$, $ThBr_4$, UF_4, UCl_4, and UBr_4 were carried out using the Amsterdam Density Functional (ADF) program [24] on the superscalar supercomputer, Columbus, at the Rutherford Appleton Laboratories [25]. The $ThBr_4$ and UBr_4 results presented here assumed a tetrahedral geometry with metal-bromine bond lengths being taken from gas-phase electron diffraction studies [8] (2.73 Å for $ThBr_4$ and 2.69 Å for UBr_4). For both uranium and thorium tetrabromide, a relativistic frozen core was used, due to the large number of electrons. Calculations were carried out using two different metal cores.

1. Frozen up to the 6p level.

2. Frozen up to the 5d level.

This allowed the effect of having the metal 6p orbitals frozen or unfrozen on the computed VIEs to be investigated. For the bromine atoms, the 4s and 4p orbitals were in the valence region in these calculations, while the lower-lying orbitals were in the frozen core. Including the Br 3d orbitals in the valence region (unfreezing them) was found to have negligible effect on computed VIEs. Therefore, with the metal 6s and 6p orbitals not frozen, the valence space contained the metal 6s, 6p, 7s, and 5f orbitals and the bromine 4s and 4p orbitals. A triple zeta plus polarization (TZ+P) Slater-type basis set was used (see section 4.3). Also, the gradient-corrected BLYP functional, which includes the uniform electron gas exchange, the Becke 88 correction to exchange [26] and the Lee-Yang-Parr correlation functional [27] was utilized (see section 4.5). Relativistic effects are taken into account using a relativistic frozen core and a perturbation treatment in the valence region [28, 29]. This method has been shown to give reliable

minimum energy geometries and ionization energies for compounds containing heavy elements [30–32].

The splitting of irreducible representations into double point groups as used in the relativistic DFT calculations is given in Table 9.2.

Non-relativistic T_d group	Relativistic T_d double group
t_2	$u_{3/2}$
	$e_{5/2}$
t_1	$u_{3/2}$
	$e_{1/2}$
e	$u_{3/2}$
a_1	$e_{1/2}$

Table 9.2: Splitting of the T_d point group

In order to calculate VIEs, the transition state method was used as described in section 4.6. This involved half an electron being removed from each orbital, in turn, and the negative of the orbital energy of the resulting partially filled orbital, obtained from a converged calculation, being equated to the VIE. These VIEs were then compared with the experimentally measured VIEs. The transition state method has been shown to give results which are equivalent to ΔSCF calculations [33, 34] and this was confirmed by performing transition state and ΔSCF calculations on VIEs on $ThBr_4$.

9.4 Results and discussion

9.4.1 Matrix isolation studies

Figure 9.1 shows the argon matrix infrared spectra obtained from samples of UBr_4 and $ThBr_4$ in the wavenumber region 300-200 cm^{-1}. One band is observed for each tetrabromide, and this feature is assigned in each case to the T_2 stretching mode of the T_d monomer. The only other absorptions present in these spectra were bands arising from traces of adventitious water at ≈3700 and 1600 cm^{-1}, and a number of sharp, weak features in the region 2300-2600 cm^{-1}, which may be assigned to HBr and its oligomers. These latter features appeared at considerably lower vaporization temperatures than the metal tetrabromide absorptions, and their positions corresponded very closely to the absorptions previously reported for HBr in argon over a range of concentrations [35, 36]. It is particularly

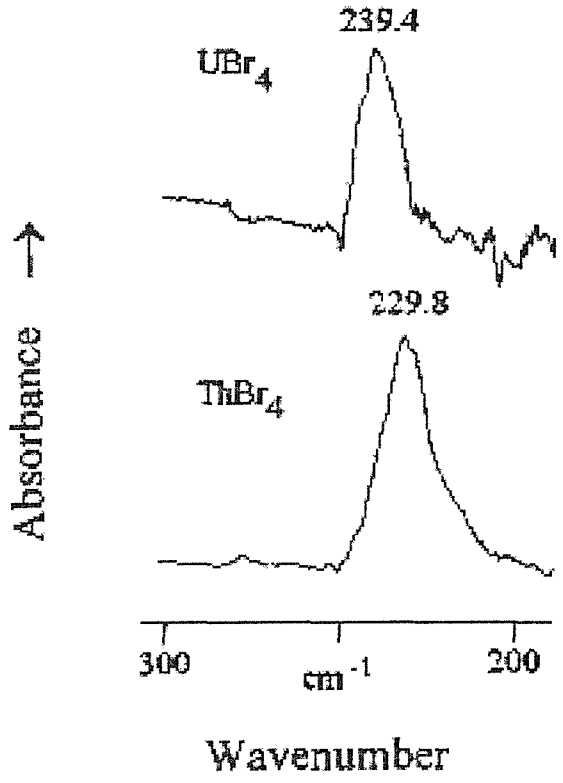

Figure 9.1: Infrared spectra of the 200-300 cm^{-1} spectral region obtained for UBr_4 and $ThBr_4$ isolated in argon matrices at 12°K.

significant that no absorptions were observed in the U-O (or Th-O) stretching region (typically 700-1000 cm^{-1}) indicating that under the vaporization conditions used, no uranium (or thorium) oxybromides were produced.

Previous studies on UBr_4 have assumed T_d symmetry in the gas-phase [8,37, 38]. In an experimental gas-phase infrared study, a single infrared-active band has been reported at 233±3 cm^{-1}, and assigned as the T_2 stretch [38]. This value is in very satisfactory agreement with the results obtained in this present work (239±2 cm^{-1}, see Figure 9.1), when one considers that the gas phase band contour would be expected to include an appreciable contribution from a hot band (slightly decreasing the wavenumber of the apparent centre of the observed peak).

There appears to be no published infrared spectral data for molecular $ThBr_4$, but the experimental value of 230±2 cm^{-1} for the T_2 stretching mode observed here compares very favorably with the recommended value of 227 cm^{-1} obtained from density functional calculations with a B3LYP functional [9].

There are no other infrared active stretching modes predicted for T_d UBr_4 and $ThBr_4$ and the infrared active T_2 bends are anticipated to lie at ~45 cm^{-1} [8,9],

which is well below the lower limit of the infrared spectrometer used. There is no evidence from these results of any significant distortion from T_d symmetry, and indeed, it can be shown that if a static C_{3v} distortion of more than $\sim 5^\circ$ in bond angle were present in these tetrabromides, the effect would be to split the observed "T_2" stretching modes by ~ 8 cm^{-1}, which would be clearly visible in the matrix infrared spectra.

These matrix isolation infrared measurements therefore provide support for the purity of the tetrabromide effusive beams used in these studies, and for the T_d symmetry of molecular UBr_4 and $ThBr_4$. They also provide the first experimental measurement of the T_2 stretching mode in $ThBr_4$.

9.4.2 Photoelectron spectra

If the actinide tetrabromides, UBr_4 and $ThBr_4$, have tetrahedral geometries then the transformation properties of the metal 7s, 6p, and 6d orbitals and the halogen 4s and 4p orbitals can be readily determined. Also, metal 5f orbitals in T_d symmetry transform as a_1, t_1, and t_2. One way of understanding the valence energy level ordering as well as the character of each valence level in these MBr_4 molecules is to compute the valence energy levels of the Br_4 group, at the geometry it has in the MBr_4 neutral molecule, and study the effect of the introduction of the central metal M. This has been done for $ThBr_4$ and UBr_4. The eigenvalues obtained from non-relativistic ADF density functional calculations have been plotted for M, Br_4 , and MBr_4 (for M=Th and U) in Figures 9.2 and 9.3.

The following order of the Br 4p symmetry orbitals was obtained for the Br_4 unit;

$$3t_2 < 1e < 1t_1 < 3a_1 < 4t_2.$$

These symmetry orbitals interact with the orbitals of the central atom, i.e., $6p(t_2)$, $5f(a_1+t_1+t_2)$, $6d(e+t_2)$, and $7s(a_1)$ and the order changes to;

$$3a_1 < 3t_2 < 1e < 1t_1 < 4t_2.$$

In $ThBr_4$, these are the outermost occupied five levels. Mulliken analysis of the occupied levels in $ThBr_4$ shows that the next deepest levels, the $2t_2$ and $2a_1$ levels, are essentially ligand 4s symmetry combinations with the $2t_2$ level having some metal $6p(t_2)$ character. The next lowest level, the $1t_2$ level, is almost completely composed of Th $6p(t_2)$ orbitals. UBr_4 has two more electrons than $ThBr_4$ and these go into the $5t_2$ level which has metal 5f and 6d character.

The experimental HeI photoelectron spectra of UBr_4 and $ThBr_4$ are shown in Figures 9.4 and 9.5. The 10.0-13.5 eV ionization energy regions of these spectra

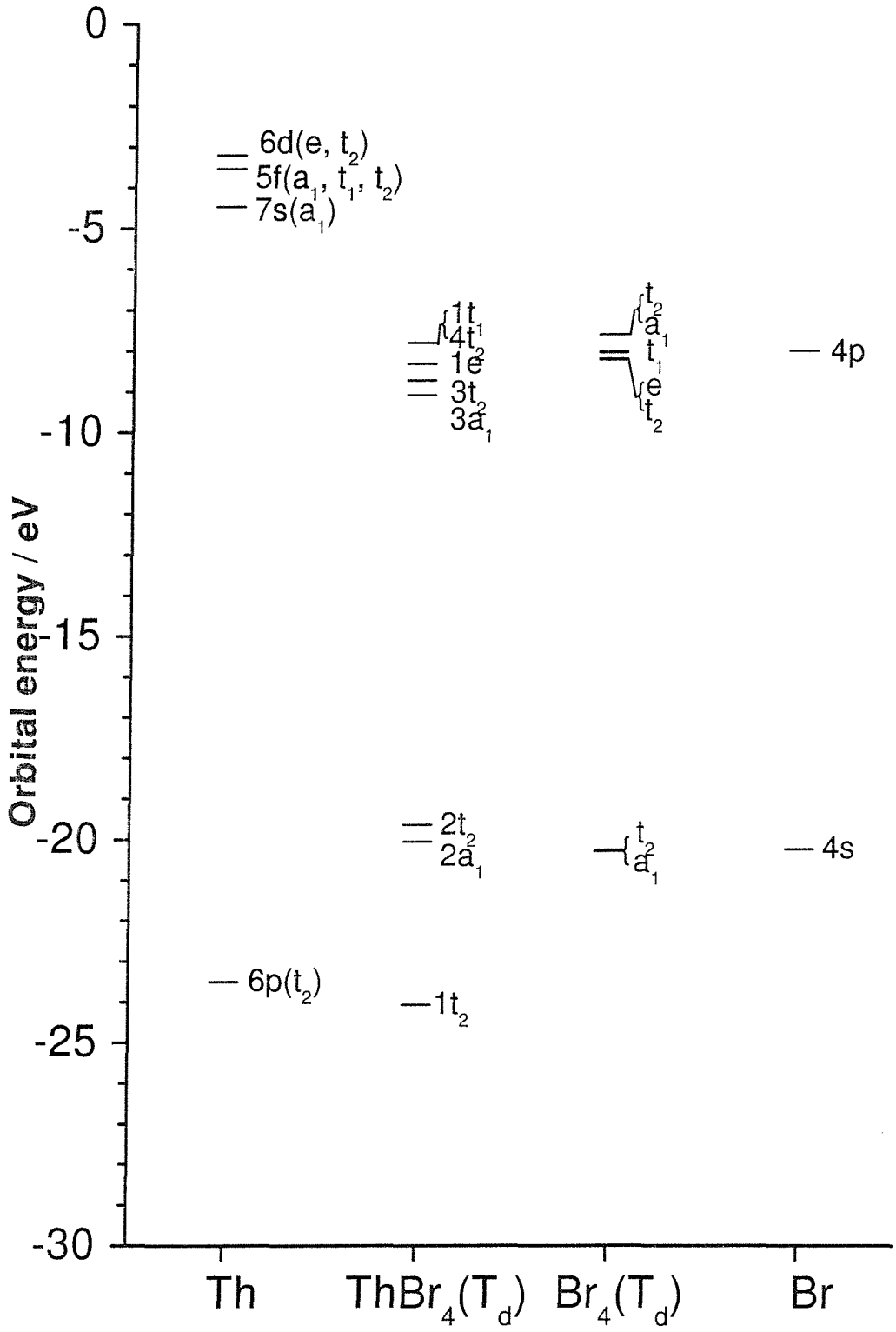

Figure 9.2: Computed orbital energies for Th, Br, Br_4, and $ThBr_4$ obtained from non-relativistic density functional calculations. The $1a_1$ molecular orbital in the $ThBr_4$ is essentially a metal 6s orbital and is too low in energy to be shown in this figure.

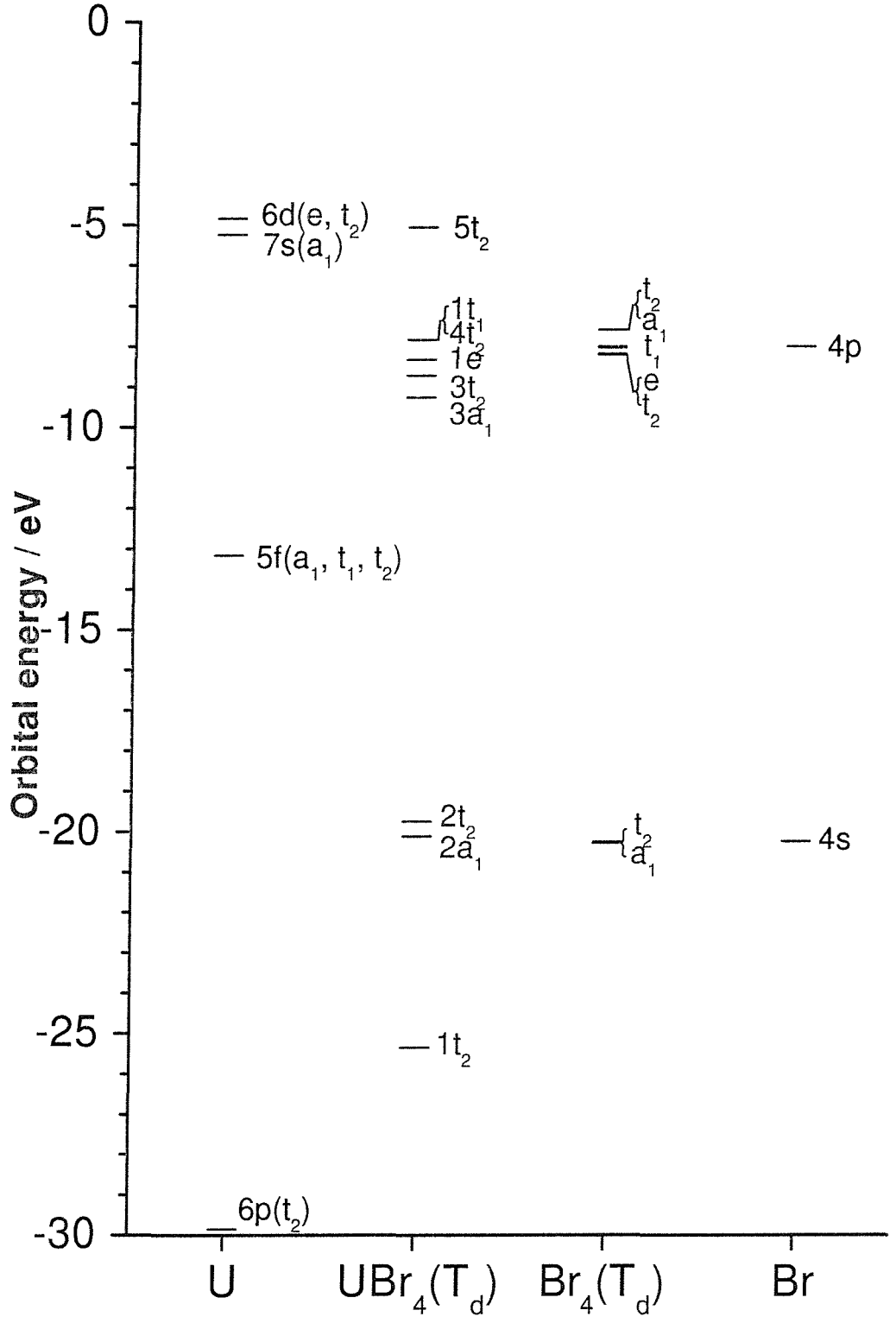

Figure 9.3: Computed orbital energies for U, Br, Br_4, and UBr_4 obtained from non-relativistic density functional calculations. The $1a_1$ molecular orbital in the UBr_4 is essentially a metal 6s orbital and is too low in energy to be shown in this figure.

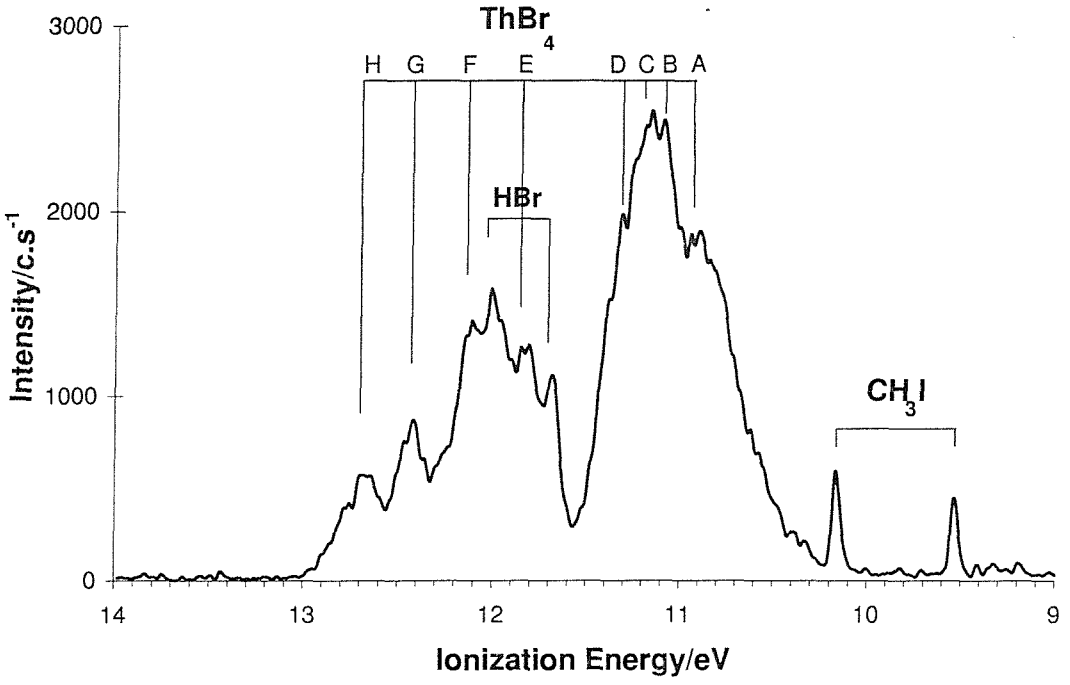

Figure 9.4: HeI photoelectron spectrum obtained for $ThBr_4$.

exhibit a remarkable similarity and each spectrum shows eight reproducible band maxima, labelled A-H in Figures 9.4 and 9.5. UBr_4 shows an extra band which is not present in the $ThBr_4$ spectrum. This has a vertical ionization energy (VIE) of 9.65±0.02 eV and an adiabatic ionization energy (AIE) (band onset) of 9.35±0.10 eV. These values compare with the only previously determined value for the first AIE of UBr_4, from electron impact mass spectrometry, of 9.6±0.3 eV [11]. The corresponding values in $ThBr_4$, the band maximum and band onset of band A in Figure 9.4, are 10.92±0.02 eV and 10.28±0.05 eV, which compare with the earlier value, from electron impact mass spectrometry of 10.4±0.3 eV [10]. Scans in the higher ionization energy region 13.5-21.0 eV showed no bands that could be attributed to these tetrabromides, although it was noted that the bands in the 10.0-13.5eV region were lower in intensity than the corresponding bands observed for the tetrafluorides and tetrachlorides, and hence any weak metal tetrabromide bands in the 13.5-21.0 eV region would be difficult to detect.

Tables 9.3 and 9.3 show the computed VIEs for $ThBr_4$ and UBr_4 with the metal orbitals (a) frozen up to the 6p level (the M6p core in Tables 9.3 and 9.4) and (b) frozen up to the 5d level (the M5d core in Tables 9.3 and 9.4). As can be seen, the computed VIEs are all slightly too low. This is attributed to;

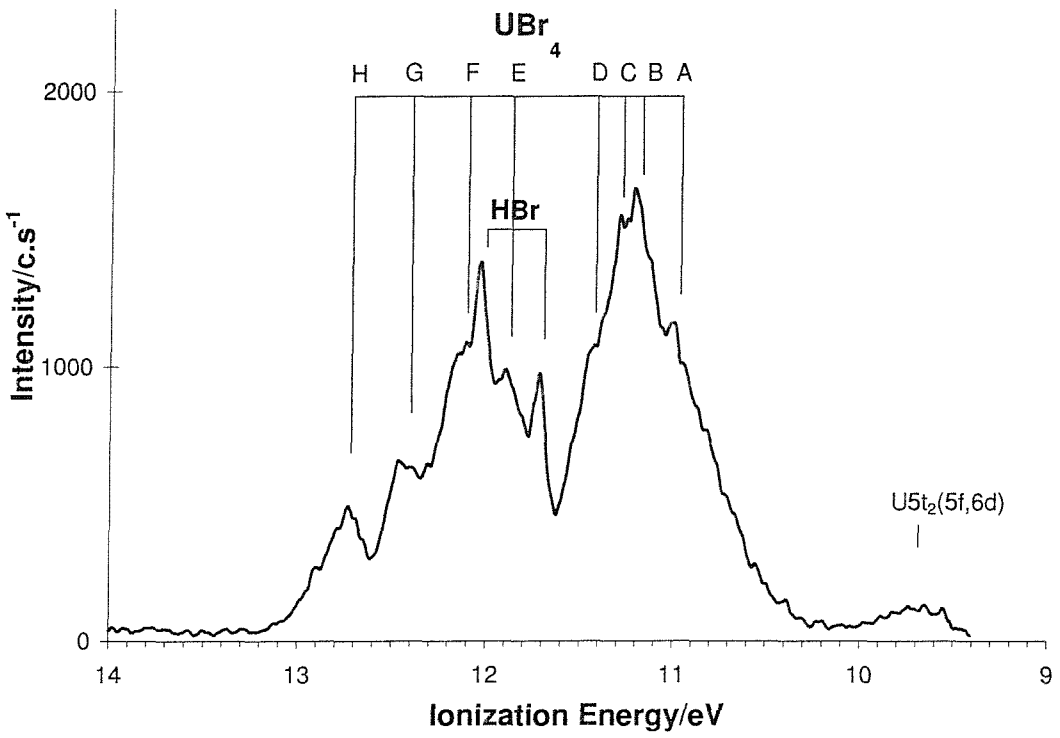

Figure 9.5: HeI photoelectron spectrum obtained for UBr_4.

(a) the use of a relatively small basis set,

(b) the use of a frozen core, and

(c) the use of the transition-state method which neglects some electron correlation energy change on ionization, although the gradient corrected functional includes some electron correlation in each state involved in the ionization process.

In order to compare computed and experimental VIEs, for both tetrabromides the computed VIE of band A [the first $(4t_2)^{-1}$ VIE] was shifted to match the experimental VIE of band A, and this shift was then applied to all computed VIEs. This shift was 0.10 eV for $ThBr_4$ and 0.08 eV for UBr_4. The spread in the computed VIEs, both with and without the metal 6p orbitals in the valence region, for bands A-H (1.60 and 1.58 eV for $ThBr_4$, 1.73 and 1.70 eV for UBr_4) compares very favorably with the experimental spread (1.75 eV for $ThBr_4$ and 1.70 eV for UBr_4) for both metal tetrabromides (see Tables 9.3 and 9.4).

The assignment of the bands shown in Figures 9.4 and 9.5 relies on the computed VIEs of $ThBr_4$ and UBr_4 shown in Tables 9.3 and 9.4 and the assignment achieved previously for the UV photoelectron spectra of the uranium and thorium

Orbital				Th.5d core		
Non-relativistic	Relativistic	Th.6p core	Th.5d core	Shifted values	Experiment	Assignment
$4t_2$	$6u_{3/2}$	10.83	10.82	10.92	10.92	A
$4t_2$	$4e_{5/2}$	10.86	11.08	11.18	11.23	C
$1t_1$	$5u_{3/2}$	11.02	11.00	11.10	11.12	B
$1t_1$	$4e_{1/2}$	11.19	11.16	11.26	11.33	D
1e	$4u_{3/2}$	11.60	11.56	11.65	11.85	E
$3t_2$	$3u_{3/2}$	12.01	11.93	12.02	12.11	F
$3t_2$	$3e_{5/2}$	12.23	12.23	12.32	12.40	G
$3a_1$	$3e_{1/2}$	12.43	12.40	12.50	12.67	H
$2t_2$	$2u_{3/2}$	23.35	22.84	22.94	(a)	...
$2t_2$	$2e_{5/2}$	23.37	23.39	23.49		
$2a_1$	$2e_{1/2}$	23.59	23.56	23.66		
$1t_2$	$1u_{3/2}$		26.33	26.43		
$1t_2$	$1e_{5/2}$		32.67	32.77	...	
$1a_1$	$1e_{1/2}$		49.87	49.97		

(a) Bands outside the photon energy range used.

Table 9.3: Comparison of experimental and computed VIEs (in eV) of $ThBr_4$, with band assignments.

tetrafluorides and tetrachlorides [7], which is also based on VIEs computed with relativistic density functional calculations.

It is well established that the spin-orbit splitting of the outermost occupied t_2 level in ThF_4 and $ThCl_4$ (the $4t_2$) level, is responsible for the first two bands in their UV photoelectron spectra. This arises because the $4t_2$ level contains a small amount of thorium 6p character. Th 6p orbital (and the $1t_2$ level of $ThBr_4$, which is mainly Th 6p in character) shows a large spin-orbit splitting, of ~6.3 eV, and the small metal 6p contribution to the $4t_2$ level is responsible for the observed splitting of this level. Similar values are also obtained for this splitting in the other uranium and thorium tetrahalides. For ThF_4, $ThCl_4$, and $ThBr_4$, the experimental spin-orbit splitting of the outermost t_2 level stays approximately constant at 0.35±0.06 eV with values of 0.41, 0.35, and 0.31 eV being measured. Table 9.3 confirms the origin of this splitting as it is only reproduced when the metal 6p orbitals are not frozen and included in the valence space.

The $1t_1$ level is almost completely halogen in character, and the computed spin-orbit splittings in ThF_4, $ThCl_4$, and $ThBr_4$ are 0.03, 0.05, and 0.16 eV repectively. This splitting is only resolved in the photoelectron spectra of $ThBr_4$ and UBr_4 and these components are assigned to bands B and D. Although the

Orbital				U.5d core		
Non-relativistic	Relativistic	U.6p core	U.5d core	Shifted values	Experiment	Assignment
$5t_2$	$7u_{3/2}$	9.46	9.30	9.37	9.65	U(5f,6d)
$4t_2$	$6u_{3/2}$	10.88	10.91	10.99	10.99	A
$4t_2$	$4e_{5/2}$	10.88	11.17	11.25	11.28	C
$1t_1$	$5u_{3/2}$	11.10	11.09	11.16	11.18	B
$1t_1$	$4e_{1/2}$	11.30	11.27	11.34	11.42	D
1e	$4u_{3/2}$	11.64	11.61	11.68	11.88	E
$3t_2$	$3u_{3/2}$	12.03	11.99	12.06	12.12	F
$3t_2$	$3e_{5/2}$	12.24	12.28	12.35	12.42	G
$3a_1$	$3e_{1/2}$	12.61	12.61	12.68	12.69	H
$2t_2$	$2u_{3/2}$	23.41	23.08	23.16	(a)	...
$2t_2$	$2e_{5/2}$	23.42	23.51	23.58		
$2a_1$	$2e_{1/2}$	23.69	23.67	23.74		
$1t_2$	$1u_{3/2}$		27.17	27.25		
$1t_2$	$1e_{5/2}$		34.48	34.56	...	
$1a_1$	$1e_{1/2}$		54.74	54.81		

(a) Bands outside the photon energy range used.

Table 9.4: Comparison of experimental and computed VIEs (in eV) of UBr_4, with band assignments.

$4t_2$ level is split into $u_{3/2}$ and $e_{5/2}$ levels with the $u_{3/2}$ level lying lower (expected degeneracy ratio 2:1) and the $1t_1$ level is split into $u_{3/2}$ and $e_{1/2}$ levels with the $u_{3/2}$ level lying lower (expected degeneracy ratio 2:1), the bands A, B, C, and D in the experimental UBr_4 and $ThBr_4$ spectra are not sufficiently well resolved to estimate the A:C relative intensity (the $4t_2$ components) and the B:D relative intensity (the $1t_1$ components). The 1e level is $u_{3/2}$ relativistically and ionization from this level is assigned to band E in $ThBr_4$ (and UBr_4). The $(3t_2)^{-1}$ ionization is expected to give two components $u_{3/2}$ and $e_{5/2}$, degeneracy ratio 2:1. Bands F and G in Figures 9.4 and 9.5 are assigned to these ionizations and support for this assignment is provided by the fact that the intensity ratio of these bands is approximately 2:1. This splitting is not resolved in the ThF_4 and $ThCl_4$ spectra (or the UF_4 and UCl_4 spectra). The computed separations of the $u_{3/2}$ and $e_{5/2}$ components in ThF_4, $ThCl_4$, and $ThBr_4$ are 0.08, 0.10, and 0.30 eV respectively, consistent with a large halogen p and a small metal 6p contribution to this level. The measured splitting of bands F and G in the UBr_4 and $ThBr_4$ spectra are 0.30 and 0.29 eV, consistent with the computed splittings of 0.29 and 0.30 eV obtained from calculations with the metal 6p orbitals in the valence region. These

computed splittings reduce slightly, to 0.21 and 0.22 eV, on putting the metal 6p orbitals in the core. Band H is assigned to ionization from the $3a_1$ orbital, which is $3e_{1/2}$ relativistically.

A comparison of the assignment of the ThF_4, $ThCl_4$, and $ThBr_4$ spectra, and the UF_4, UCl_4, and UBr_4 spectra are presented in Figures 9.6 and 9.7. Apart from the extra band seen in the uranium tetrahalide spectra at low ionization energy, which arises in each case from ionization from the outermost $5t_2(7u_{3/2})$ level, the assignments of the uranium and thorium spectra are remarkably similar. The splitting of the ionic states that arise from the $(4t_2)^{-1}$ ionization in ThF_4, $ThCl_4$, and $ThBr_4$ (0.41, 0.35, and 0.31 eV) and in UF_4, UCl_4, and UBr_4 (0.30, 0.36, 0.29 eV) are approximately constant, consistent with it being associated with a spin-orbit splitting arising from a metal 6p contribution to the $4t_2$ level. In contrast, the $1t_1$ and $3t_2$ levels have spin-orbit splittings which are expected, from the computed VIEs, to increase on going along the series MF_4, MCl_4, MBr_4 (with M=Th or U) consistent with these levels being halogen np in origin. This is consistent with the spectra, as these splittings are only resolved in the tetrabromides. If the $1t_1$ level in each tetrahalide is composed solely of halogen np valence orbitals, then neglecting off-diagonal spin-orbit interactions, the $^2T_1(u_{3/2}\text{-}e_{1/2})$ splitting is just $-3/4\zeta$, where ζ is the spin-orbit coupling constant for the free halogen ion [39, 40]. The negative sign implies that the splitting is inverted with the $u_{3/2}$ component lying lower than the $e_{1/2}$ component, consistent with Hund's third rule as the t_1^5 shell in the tetrahalide ion is more than half full. ζ values can be readily evaluated for F^+, Cl^+, and Br^+ from atomic tables as 0.04, 0.08, and 0.32 eV giving calculated $1t_1$ spin-orbit splittings in the uranium and thorium tetrafluorides, tetrachlorides and tetrabromides of 0.03, 0.06, and 0.24 eV. The only observed $1t_1$ splittings occur for $ThBr_4$ and UBr_4 with values of 0.21 and 0.24 eV being measured, in good agreement with the value of 0.24 eV obtained from this simple model. The $1t_1$ splittings in the tetrafluorides and tetrachlorides are unresolved experimentally and are therefore expected to be <0.10 eV. The $1t_1$ splittings computed for ThF_4, $ThCl_4$, and $ThBr_4$ by relativistic density functional calculations are 0.03, 0.06, and 0.16 eV in good agreement with the above values derived from atomic halogen ion splittings. The $3t_2$ levels show splittings of 0.29 and 0.30 eV in $ThBr_4$ and UBr_4 which are slightly greater than the corresponding splittings in the $1t_1$ levels. The $3t_2$ splittings are unresolved in the tetrafluorides and tetrachlorides. The simple atomic spin-orbit model cannot be so readily applied to the t_2 ionic states, as the t_2 molecular orbitals contain a larger number of contributions, notably halogen ns, halogen np

σ, halogen np π, metal 6d, metal 5f, and metal 6p orbitals [39–41]. The density functional computed values of the $3t_2$ spin-orbit splitting for ThF_4, $ThCl_4$, and $ThBr_4$ are, however, 0.02, 0.10, and 0.30 eV. These values are very similar to the splittings computed by relativistic density functional calculations for the $1t_1$ levels, consistent with the $3t_2$ levels also being composed of mainly halogen np valence orbitals. However, the computed $3t_2$ values are slightly larger and this is probably due to a small metal 6p contribution to these levels. It is particularly notable that when the metal 6p level is included in the core, the computed $3t_2$ spin-orbit splitting reduces to the spin-orbit splitting of the $1t_1$ level (from 0.29 to 0.22 eV in $ThBr_4$).

9.5 Conclusion

The photoelectron and infrared matrix isolation results obtained in this work are consistent with effective tetrahedral geometries for UBr_4 and $ThBr_4$. The photoelectron spectrum of $ThBr_4$ exhibits eight bands which arise from ionization of the five outermost orbitals derived from the Br 4p symmetry combinations in a Br_4 tetrahedral unit, with three of the bands split by spin-orbit interaction. The UBr_4 spectrum is very similar but it also exhibits a weak band at lower ionization energy arising from ionization of a $5t_2$ orbital, which is unfilled in $ThBr_4$ and has two electrons in it in UBr_4. The origin of the observed spin-orbit splittings can be understood on the basis of this combined experimental and theoretical study. Improved calculations of ionization energies of the uranium and thorium tetrahalides that give better agreement with experimental values would be valuable.

The final conclusion is that the photoelectron spectra of the actinide tetrahalides have been successfully interpreted and fully assigned with the aid of relativistic density functional calculations, including the observed spin-orbit splittings.

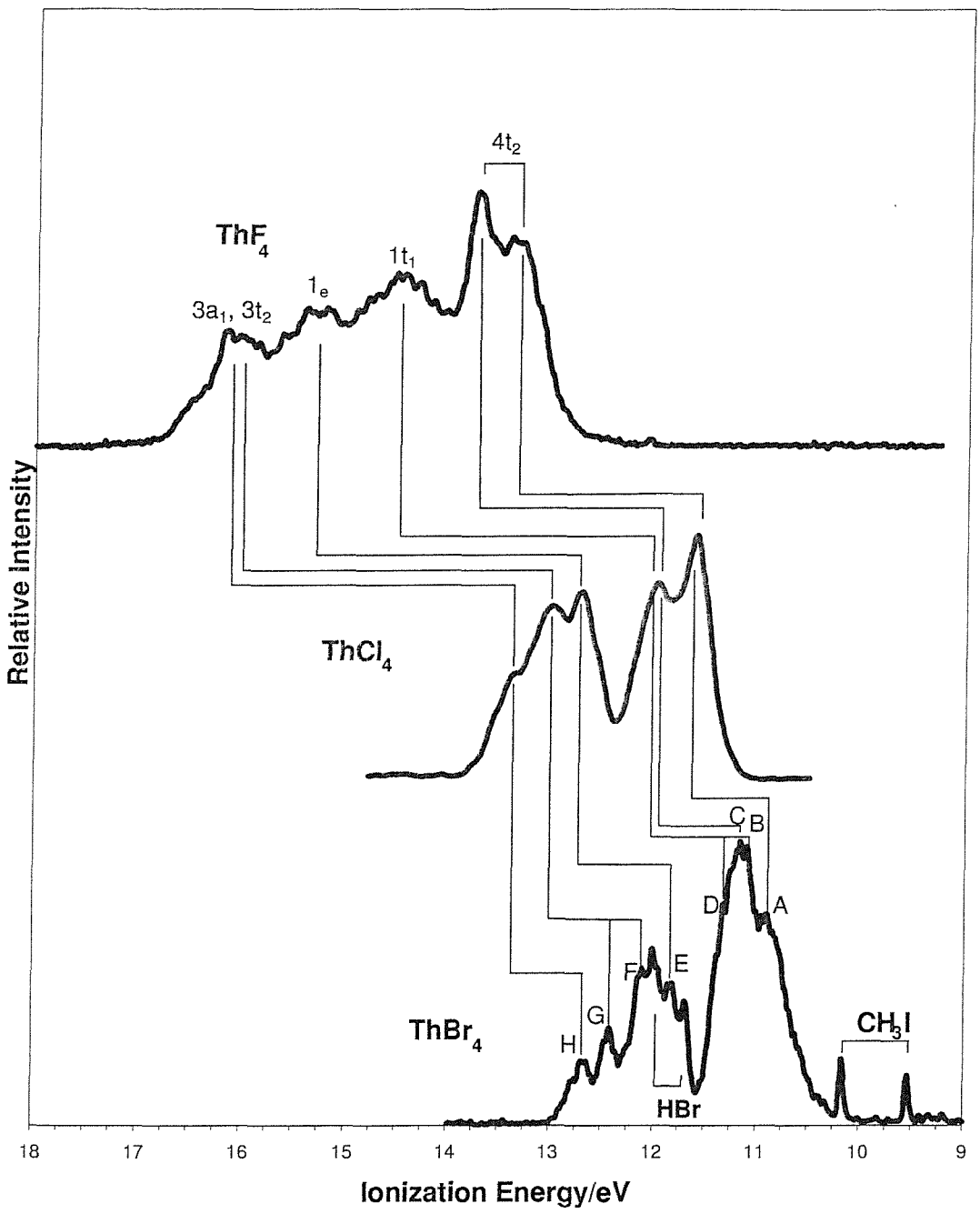

Figure 9.6: Comparison of the HeI photoelectron spectra of ThF_4, $ThCl_4$, and $ThBr_4$, and correlation of the ionic state assignment of the bands.

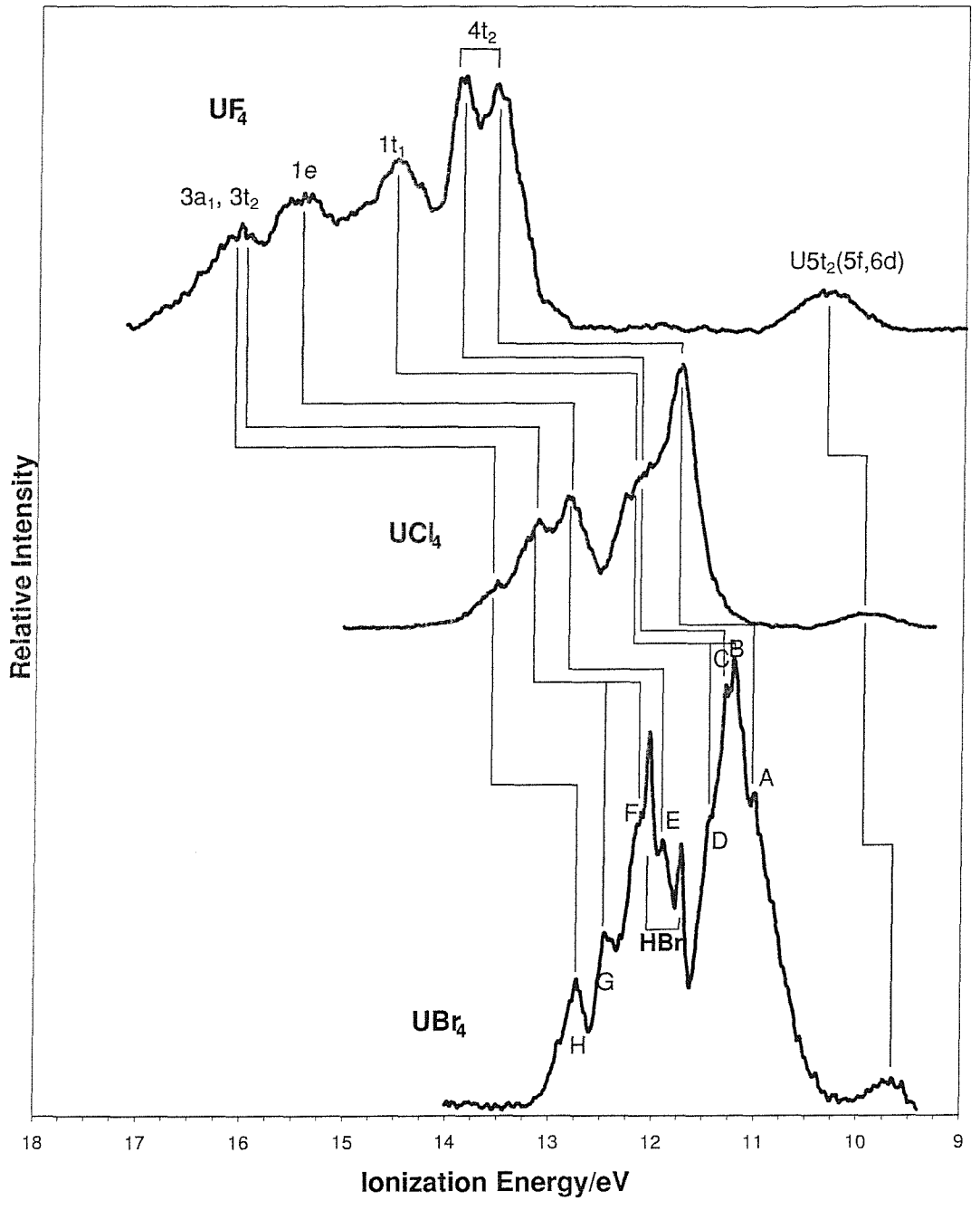

Figure 9.7: Comparison of the HeI photoelectron spectra of UF_4, UCl_4, and UBr_4, and correlation of the ionic state assignment of the bands.

Bibliography

[1] J. J. Katz, G. T. Seaborg, and T. R. Morss, *The Chemistry of the Actinide Elements*, 2nd ed. (Chapman and Hall, London, 1986), Vol. 1.

[2] J. M. Dyke, N. K. Fayad, A. Morris, and I. R. Trickle, J. Chem. Phys. **72**, 3822 (1980).

[3] E. Thibaut, J. P. Boutique, J. J. Verbist, J. C. Levet, and H. Noel, J. Am. Chem. Soc. **104**, 5266 (1982).

[4] G. C. Allen, S. Hubert, and E. Simoni, J. Chem. Soc., Faraday Trans. **91**, 2767 (1995).

[5] G. C. Allen and J. W. Tyler, J. Chem. Soc., Faraday Trans. **83**, 1355 (1987).

[6] J. M. Dyke, G. D. Josland, A. Morris, P. M. Tucker, and J. W. Tyler, J. Chem. Soc., Faraday Trans. **77**, 1273 (1981).

[7] P. M. Boerrigter, J. G. Snijders, and J. M. Dyke, J. Elect. Spec. Relat. Phenom.**46**, 43 (1988).

[8] R. J. M. Konings and D. L. Hildenbrand, J. Alloys Compd. **271**, 583 (1998).

[9] L. Gagliardi, C. K. Skylaris, A. Willetts, J. M. Dyke, and V. Barone, Phys. Chem. Chem. Phys. **2**, 3111 (2000).

[10] D. L. Hildenbrand and K. H. Lau, J. Chem. Phys **93**, 5983 (1990).

[11] K. H. Lau and D. L. Hildenbrand, J. Chem. Phys **86**, 2949 (1987).

[12] D. L. Hildenbrand, K. H. Lau, and R. D. Brittain, J. Chem. Phys **94**, 8270 (1991).

[13] D. Bulgin, J. M. Dyke, F. Goodfellow, N. Jonathan, E. P. F. Lee, and A.Morris, J. Electron Spect. Relat. Phenom. **12**, 67 (1977).

[14] J. M. Dyke, A. Morris, G. D. Josland, M. P. Hastings, and P. D. Francis, High Temperature Science **22**, 95 (1986).

[15] J. M. Dyke, N. Jonathan, and A. Morris, in *Electron Spectroscopy*, edited by C. R. Brundle and A. D. Baker (Academic Press, New York, 1979), Vol. 3, p. 189.

[16] G. Brauer, *Handbook of Preparative Inorganic Chemistry*, 2nd ed. (Academic, London, 1986), Vol. 2.

[17] J. J. Katz and E. Rabinowitz, *The Chemistry of Uranium*, Vol. VII of *National Nuclear Energy Series* (McGraw Hill, New York, 1951).

[18] J. C. Taylor and P. W. Wilson, Acta Crystallogr., Sect. B: Struct. Crystallogr. Cryst. Chem. **30**, 2664 (1974).

[19] R. Hooft, Nonius COLLECT Software, 1998, nonius, Delft, The Netherlands.

[20] Z. Otwinowski and W. Minor, Methods Enzymol **276**, 307 (1997).

[21] J. S. Ogden and R. S. Wyatt, J. Chem. Soc. Dalton Trans. **4**, 859 (1987).

[22] D. Brown, *Halides of the Lanthanides* (Wiley, New York, 1968).

[23] J. L. Gardner and J. A. R. Samson, J. Elect. Spec. Relat. Phenom. **8**, 469 (1976).

[24] E. J. Baerends, Theoretical Chemistry Department of the Vrije Universiteit, Amsterdam, http://chem.few.vu.nl/afdelingen/TC/index-en.html.

[25] Rutherford Appleton Laboratory, Chilton, Didcot Oxon OX11, OQZ, UK, http://www.rl.ac.uk.

[26] A. D. Becke, Phys. Rev. **38**, 3098 (1988).

[27] C. Lee, W. Yang, and R. G. Parr, Phys. Rev. B **37**, 785 (1988).

[28] J. G. Snijders and E. J. Baerends, Mol. Phys. **36**, 1789 (1978).

[29] J. G. Snijders, E. J. Baerends, and P. Ros, Mol. Phys. **38**, 1909 (1978).

[30] T. Zeigler, J. G. Snijders, and E. J. Baerends, J. Chem. Phys. **74**, 1271 (1981).

[31] E. J. Baerends, J. G. Snijders, C. A. de Lange, and G. Jonkers, in *Local Density Approximations in Quantum Chemistry and Solid State Physics*, edited by J. P. Dahl and J. Avery (Plenum, New York, 1984), p. 515.

[32] J. G. Snijders and E. J. Baerends, in *Electron Distributions and the Chemical Bond*, edited by M. B. Hall and P. Coppens (Plenum, New York, 1982), p. 111.

[33] N. H. F. Beebe, Chemical Physics Letters **19**, 290 (1973).

[34] J. M. Dyke, N. Jonathan, and A. Morris, in *Electron Spectroscopy*, edited by G. R. Brundle and A. D. Baker (Academic Press, New York, 1979), Vol. 3, p. 189.

[35] M. T. Bowers and W. H. Flygare, J. Chem. Phys. **44**, 1389 (1966).

[36] A. J. Barnes, H. E. Hallam, and G. F. Scrimshaw, Trans. Faraday Soc. **65**, 3150 (1969).

[37] V. I. Bazhanov Y. S. Ezhov, S. A. Komarov, V. G. Sevastyanov, and F. Yuldashev, Vysokochist. Veshchestva **5**, 197 (1989).

[38] V. M. Kovba and I. V. Chikh, Zh. Strukt. Khim. **24**, 172 (1983).

[39] J. C. Green, M. L. H. Green, P. J. Joachim, A. F. Orchard, and D. W. Turner, Philos. Trans. R. Soc. London **268**, 111 (1970).

[40] B. D. Bird and P. Day, J. Chem. Phys. **49**, 392 (1968).

[41] R. N. Dixon and R. P. Tuckett, Chem. Phys. Lett **140**, 553 (1987).

Chapter 10

Study of the thermal decomposition of azide compounds

10.1 Introduction

The work described in this chapter is part of an on-going collaboration between the Southampton PES group and colleagues at the Universidade Nova de Lisboa. This work forms the basis of a recently submitted paper [1].

The intrinsic instability of organic azides makes their properties difficult to measure and experimental work has to be carried out with care. Nevertheless, the study of the mechanisms of their decomposition is of considerable interest both from a fundamental viewpoint and because azides play important roles in heterocycle synthesis [2–4], biological and pharmaceutical processes [5–7], the preparation of semiconductor materials [8, 9] and as high energy density materials used in solid propellants [10, 11]. It is generally believed that the initial stage in the thermal decomposition of an organic azide such as R_2CHN_3 is the release of molecular nitrogen and the formation of a nitrene (R_2CHN). Experimentally there have been no observations of nitrene intermediates from gas-phase decompositions, although the UV photoelectron spectrum of CH_3N has recently been reported by Dianxun and coworkers [12, 13]. In Dianxun's work, CH_3N was produced by passing CH_3N_3 mixed with NO through a heated plug of molecular sieve positioned 1-2 cm above the photon source of the spectrometer. CH_3N photoelectron spectra were observed at a molecular sieve temperature of 420°K. It is clear from the conditions used that CH_3N was not produced in this work from a gas-phase decomposition but from decomposition of methyl azide on the surface of the molecular sieve in the presence of NO [12, 13].

The thermal decompositions of a number of alkyl azides have been studied several years earlier in the gas-phase by Bock and Dammel [14–17] using UV photoelectron spectroscopy. The conclusion from this work is that, for the azides studied, N_2 evolution is accompanied by a 1,2 hydrogen shift to form an imine ($R_2C{=}NH$), which can undergo further decomposition to produce simple hydrocarbons, HCN and H_2.

The work presented here is part of a series of studies [18,19] on organic azides performed in order to investigate the mechanisms of their thermal decomposition. In these two previous studies [18, 19], the thermal decomposition of azidoacetic acid and azidoacetone were investigated using ultraviolet photoelectron spectroscopy and matrix isolation infrared spectroscopy. In the case of azidoacetic acid [18], the results were shown to be consistent with a single decomposition pathway involving the ejection of N_2 and the simultaneous formation of methanimine (CH_2NH) and CO_2. At higher temperatures HCN was produced. These results were supported by later *ab initio* and DFT calculations [20] which showed that decomposition occurs via a concerted reaction which proceeds via a five membered transition state leading to the products (N_2, CH_2NH, and CO_2). The decomposition of azidoacetone was found to be more complicated [19], producing not only the products expected from the analogous pathway (N_2, CH_2NH, HCN and ketene, CH_2CO) but also significant yields of CO and acetaldehyde were observed. It was suggested that alternative radical pathways might be responsible for the observed distribution of products.

This present paper describes related studies on the pyrolysis of 2-azidoethanol and 2-azidoethylacetate using the techniques of real-time ultraviolet photoelectron spectroscopy and matrix isolation infrared spectroscopy, supported by *ab initio* molecular orbital calculations. The main aim is to investigate the mechanism of thermal decomposition of these azides through the observation of the reactants, intermediates and products, at different pyrolysis temperatures. Also included in this study is the measurement of other spectroscopic properties for both parent azides.

10.2 Experimental

10.2.1 Sample Preparation

Samples of 2-azidoethanol and 2-azidoethylacetate were prepared as follows:-

2-azidoethanol

2-azidoethanol was prepared from 2-bromoethanol (95%, Aldrich) and sodium azide (99%, Aldrich), mixed in a molar ratio of 1:2.5. Solid sodium azide (2.05 g) was added slowly to a vigorously stirred solution of 2-bromoethanol (2.62 g) in distilled water at 273°K (10 ml). The solution was then allowed to warm to room temperature and was stirred for 4 hrs. More solid sodium azide was then added (1.05 g) and stirring was continued overnight at 355°K. The solution was then cooled, and the azidoethanol extracted with diethyl ether (3×10 ml), after which the combined ether layers were dried (over $MgSO_4$) and filtered. The filtrate was concentrated by vacuum distillation, first at room temperature and then finally at 378°K to yield a colourless oil.

2-azidoethylacetate

In a very similar preparative procedure to that described above, 2-azidoethylacetate was prepared from the reaction of ethyl bromoacetate (98%, Aldrich) with sodium azide (99%, Aldrich) mixed in the molar ratio of 1:2.5. To a vigorously stirred solution of ethyl bromoacetate (1.51 g) in acetone (10 ml) at 273°K was slowly added a solution of sodium azide (1.47 g) in water (10 ml). The mixture was allowed to warm to room temperature and then heated overnight at 335°K. The resulting solution was extracted with dichloromethane (3×10 ml). The combined organic layers were washed first with 10% aqueous sodium bicarbonate solution, and then with water, and dried over magnesium sulphate and filtered. The filtered solution was concentrated by vacuum distillation and the residue distilled at 388°K to yield a colourless oil.

The samples prepared as above were characterised by a variety of spectroscopic methods as described in the following sections. Care was taken to minimize the effect of possible explosions at all stages in the preparation and handling of the azide samples, but no untoward occurrences were experienced during this work.

10.2.2 Matrix Isolation Studies

Matrix isolation infrared studies on these azides followed a very similar pattern to those described in our recent studies on the pyrolysis of azidoacetic acid and azidoacetone [18, 19]. The inlet and pyrolysis parts of the apparatus were identical, as were the low temperature Displex and infrared (IR) spectrometers. Spectra of each parent azide and its decomposition products were obtained in ni-

trogen matrices, and supporting experiments were also carried out on H_2CO/N_2, CH_3NH_2/N_2, C_2H_4/N_2, C_2H_6/N_2 and CH_4/N_2 mixtures to aid spectral identification. Deposition times were typically 30-60 mins at a particular superheater temperature, and any changes occurring during this period were monitored by spectral subtraction. Matrix ratios were estimated to be well in excess of 1000:1.

10.2.3 Photoelectron Spectroscopy

All photoelectron spectra recorded in this work were obtained using HeI (21.22eV) radiation. The spectrometers used were very similar, and have been previously described [21, 22](see section 5.4). For each azide, photoelectron spectra of the parent compound and its decomposition products were obtained by passing the azide vapour through a heated furnace positioned inside the ionization chamber of the spectrometer, a short distance above the photon source.

The vapour pressures of the parent materials ($N_3CH_2CH_2OH$ and $N_3CH_2COOCH_2CH_3$) were sufficient at room temperature to allow photoelectron spectra to be obtained with good signal-to-noise ratios by direct pumping on a liquid sample held in a small flask, through a needle valve outside the spectrometer ionization chamber, rather than having to vaporize the samples from within the ionization chamber of the spectrometer as was necessary for the less volatile azidoacetic acid [18]. The operating resolution of each spectrometer (typically 35meV FWHM as measured for the argon $(3p)^{-1}$ signal obtained with HeI radiation) was found to be unaffected when the heating system was in operation.

Photoelectron spectra were recorded in real-time as the furnace temperature was changed. For each azide, the onset of decomposition was marked by the appearance of photoelectron bands associated with molecular nitrogen. Spectral calibration was achieved by reference to known ionization energies of methyl iodide added to the chamber, and traces of nitrogen and water [23, 24].

The photoelectron spectrum was also recorded for the precursor, $BrCH_2CH_2OH$, used in the preparation of the 2-azidoethanol, and it was in good agreement with that reported previously [25, 26]. The first and second bands of the 2-azidoethanol, at vertical ionization energies of (9.90±0.01) and (11.01±0.01) eV respectively, were the most intense and photoelectron spectra recorded for $N_3CH_2CH_2OH$ showed no evidence of $BrCH_2CH_2OH$. Similarly, the photoelectron spectrum was recorded for the precursor, $BrCH_2COOCH_2CH_3$, used in the preparation of $N_3CH_2COOCH_2CH_3$, and the photoelectron spectrum of the 2-azidoethylacetate showed no evidence of bands associated with bromoethylacetate.

The pyrolysis system used for the azidoethanol experiments consisted of a resistively heated furnace which was made of molybdenum wire wrapped around an inner glass tube connected to a power supply via tungsten feed-throughs. The operating temperature of the furnace in the heated section was measured by a chromel-alumel thermocouple, and the maximum operating temperature recorded was 825°K.

The pyrolysis experiments carried out for the 2-azidoethylacetate were performed using the radiofrequency (r.f.) induction heating system on the high temperature spectrometer (see section 5.4.5). This could achieve much higher temperatures (up to 2500°K) than the resistively heated system used for azidoethanol. It consisted of a tantalum cylinder (the r.f. susceptor) positioned inside the r.f. heating coils a few centimetres above the photon source. The sample vapour was then passed through an alumina tube which was positioned in the centre of the tantalum susceptor. As in the 2-azidoethanol experiments, photoelectron spectra were recorded as a function of heater temperature.

10.3 Results and discussion

10.3.1 Characterisation of $N_3CH_2CH_2OH$

2-Azidoethanol was characterised in the vapour phase by mass spectrometry, UV photoelectron spectroscopy and also in the liquid phase by ^1H NMR, ^{13}C NMR, Raman and infrared spectroscopy.

The 70 eV electron impact mass spectrum showed a parent peak at 87 (10%), together with two intense fragments at 28 (40%, N_2^+ or NCH_2^+) and 31 (100%, CH_2OH^+) amu. Weaker signals were also observed at 45 (5%, $CH_2CH_2OH^+$), 43 (5%, N_3H^+), 29 (15%, COH^+) and 27 (5%, NCH^+) amu. No signals were seen that could be attributed to unreacted $BrCH_2CH_2OH$ and the mass spectrum was in good agreement with that reported previously [27].

Two signals were observed in the 300 MHz ^1H NMR spectrum of 2-azidoethanol in $CDCl_3$ solution. These were at 3.41 and 3.77 ppm relative to TMS with integrated relative intensities of 0.4:0.6 respectively. After expansion it could be seen that both peaks were triplets but the band at 3.77 ppm had a much more intense central band; this was due to the -OH proton appearing at exactly the same chemical shift as one of the $-CH_2$ groups of protons. Two signals were also observed in the ^{13}C NMR spectrum at 53.7 and 61.5 ppm with integrated relative intensities of 1:1. H-C correlation was also carried out and good correlation was found between the two sets of peaks. The H-C correlation

indicated that the proton signal at 3.77 ppm (^{1}H NMR) and the carbon signal at 61.5 ppm (^{13}C NMR) were from the same group (-CH_2OH); also that the proton signal at 3.41 ppm (^{1}H NMR) and the carbon signal at 53.7 ppm (^{13}C NMR) were from the other group (N_3-CH_2-).

The most intense absorption band in the liquid infrared spectrum was found at 2123 cm^{-1}, which was assigned to the N_3 group. Other prominent bands were present at 3442 cm^{-1} (OH stretch), 2988 and 2928 cm^{-1} (CH stretch), 1296 cm^{-1} and 1066 cm^{-1}. The infrared bands in a nitrogen matrix were in general shifted only slightly from the liquid phase values, and their positions and relative intensities are shown in Figure 10.1 and in Table 10.1. The only significant differences between the liquid and matrix infrared spectra were in the position of the O-H stretching band, which was significantly higher (3623 cm^{-1}) for the isolated molecule, and in the multiplet structure observed for the N_3 absorption at ca. 2120 cm^{-1}. This band is quite broad in the liquid spectrum, and the resolution of at least two components in this band in the matrix spectrum perhaps reveals the existence of more than one conformer.

The liquid Raman spectrum exhibited counterparts to all the above bands except for the OH stretch.

The HeI photoelectron spectrum of 2-azidoethanol is shown in Figure 10.2(a). Assignment of this spectrum is achieved with reference to *ab initio* molecular orbital calculations carried out as part of this study. The computed minimum energy geometry of $N_3CH_2CH_2OH$ was obtained at the MP2/6-31G** level using the Gaussian 94 code [37]. The geometrical parameters listed in Table 10.2 from the MP2/6-31G** calculations correspond to a stationary point on the potential energy surface with all real vibrational frequencies. This was found to be the lowest energy conformer.

The highest occupied molecular orbital in the ground state (orbital 23) is weakly antibonding between the terminal nitrogen atoms of the N_3 group, non-bonding between the adjacent nitrogen atoms, and weakly antibonding in the C-N direction. Orbital 22 is π-bonding in the terminal N-N bond, weakly antibonding between the other N-N group, and weakly C-N antibonding. Orbital 21 consists of a π(C-O) bonding orbital and orbital 20 is bonding between the two carbon atoms and C-O antibonding.

Table 10.3 compares the experimental vertical ionization energies (VIEs) with VIEs obtained from application of Koopmans' theorem to the SCF/6-31G** molecular orbital energies obtained at the MP2/6-31G** computed minimum energy geometry (Table 10.2). The values computed were, as expected, higher

N_2 Matrix (letter in Figures 1 and 3)[a]	Previous Studies	Assignment
3623, 2977, 2958, 2930, 2888, 2137/2105 ,1282, 1074		$N_3CH_2CH_2OH$
2116, 1753, 1373, 1351, 1293, 1199, 1034		$N_3CH_2COOCH_2CH_3$
2139(F)	2139	CO [28,29]
2347(O), 662(S)	2347, 662	CO_2 [30]
3032(B), 2919(C), 1637, 1450, 1352(H), 1127(I), 1065(J)	3033, 2920, 1637, 1450, 1353, 1128, 1065	CH_2NH [31]
3287(A), 747/727	3287, 747/737	HCN [31,32]
2864(D), 2800(E),1738(G), 1497, 1245, 1169	2865, 2800, 1740, 499, 1244, 1167	H_2CO [33,34]
3106(M), 3077, 2988 (N), 1888(P), 1437(Q), 947(R)	3107, 3077, 2989, 1889, 1438, 947	C_2H4 [35]
1306	1306 (most intense)	CH_4 [36]
2967, 2885, 1263,970(K), 816(L)		unassigned features appearing on pyrolysis

a. Wavenumber accuracy ± 1 cm^{-1}

Table 10.1: Significant IR bands (cm^{-1}) observed in matrix isolation studies on the pyrolysis of 2-Azidoethanol and 2-Azidoethylacetate

Bond	Length/ Å	Angle	Value / °
C_1-C_2	1.5134	C_1-C_2-N_3	106.94
C_1-O_4	1.4221	C_2-C_1-O_4	105.73
C_2-N_3	1.4781	H_9-O_4-C_1	107.81
O_4-H_9	0.9635	C_2-N_3-H_{10}	115.39
N_3-N_{10}	1.2449	C_1-C_2-$H_{7/8}$	109.58
N_{10}-N_{11}	1.1633	C_2-C_1-$H_{5/6}$	109.32
C_1-$H_{5/6}$	1.094	N_3-N_{10}-N_11	180
C_2-$H_{7/8}$	1.092		

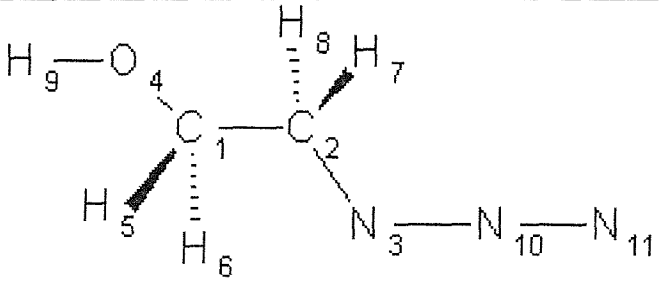

Table 10.2: Computed structural parameters of azidoethanol at the MP2/6-31G** level showing the atom numbering.

than the experimental values but scaling by a factor of 0.92 [38,39] afforded much better agreement with the experimental VIEs. This result was similar to the azidoacetic acid [18] and azidoacetone cases [19] where a factor of 0.9 was used. Also included in Table 10.3 are the first two adiabatic ionization energies (AIEs) and VIEs for 2-azidoethanol calculated by the ΔSCF method, using the optimized geometries of the cation obtained at the MP2/6-31G** level. These show good agreement with experimental values.

10.3.2 Thermal Decomposition Experiments: IR Matrix Isolation Spectroscopy

Figure 10.1(a) shows a typical nitrogen matrix infrared spectrum obtained from a sample of $N_3CH_2CH_2OH$ deposited from the vapour phase without superheating. The absorptions denoted by the asterisk (*) indicate the most intense infrared absorptions of matrix isolated H_2O, and arise from traces of water in the system. The most intense parent absorption consists essentially of a doublet at 2137/2105 cm^{-1}, one component of which exhibits weaker shoulders. These absorptions are assigned to the N_3 unit, and the complex appearance is attributed to different conformers trapped in the matrix. Our previous study on azidoacetone [19] also showed a multiplet structure in this spectral region. Other prominent features were noted at 1282 and 1074 cm^{-1}, which are in similar positions to those found

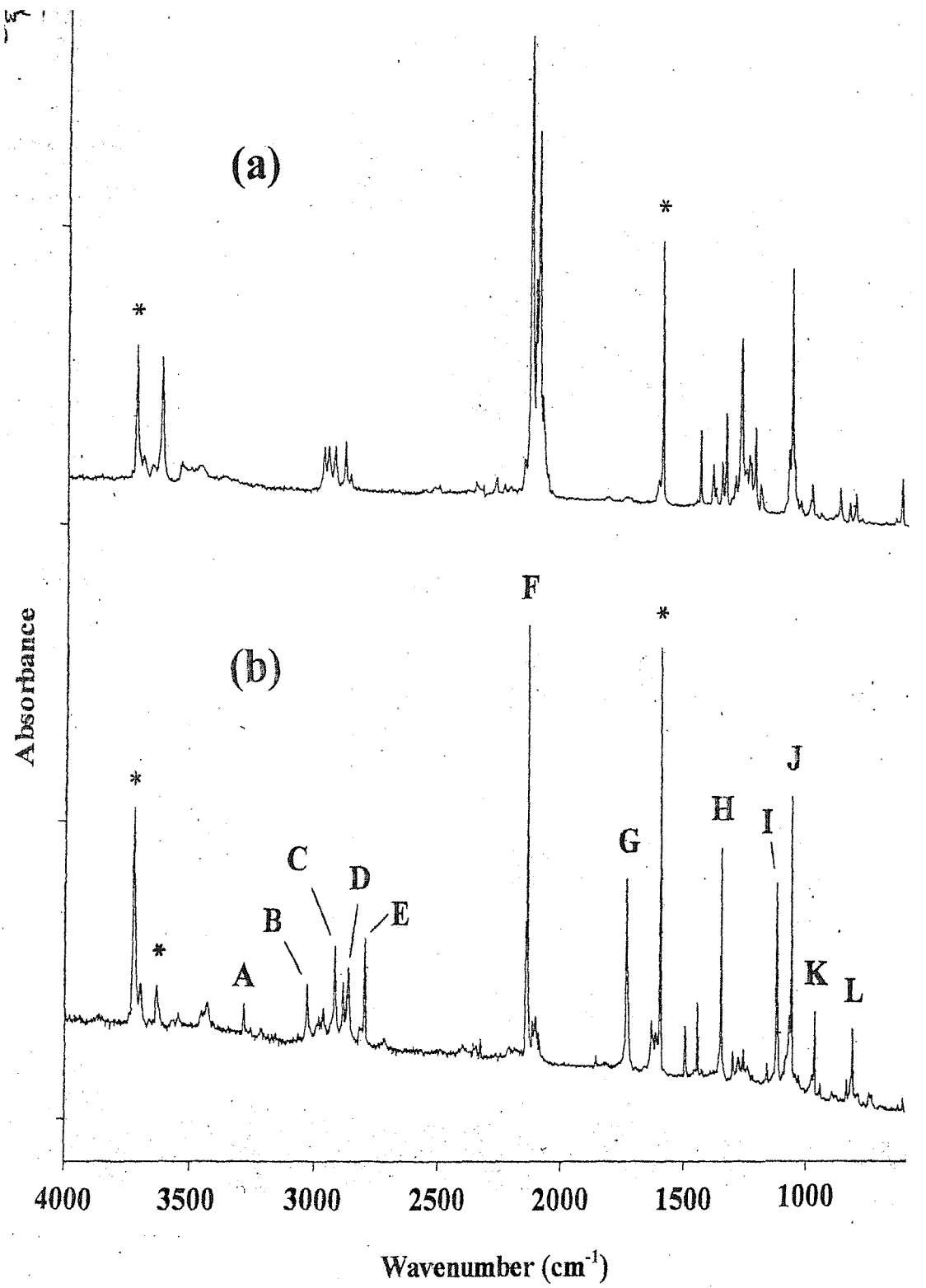

Figure 10.1: Nitrogen matrix infrared bands observed during pyrolysis studies on 2-azidoethanol. Absorptions denoted by an asterisk are assigned to H_2O. Band identification is shown in Table 10.1. (a) Spectrum with no superheating (parent 2-azidoethanol sublimed at room temperature) (b) Spectrum obtained after passage through superheater at 845°K

Mol. Orbital	Band No.	Exptl. VIE(eV)	KT VIE(eV)	KT Value ×0.92	ΔSCF values MP2/6-31G** AIE (eV)	VIE (eV)
23	1	9.9	10.18	9.37	9.94	9.99
22	2	11.01	11.93	10.98	10.64	11.3
21	3	11.47	12.38	11.38		
20	4	12.64	13.8	12.7		
19	5	14.06	15.23	14.01		
18	6	15.03	15.67	14.42		
17			17.82	16.39		
16			17.86	16.43		
15	7	17.42	18.26	16.8		

Table 10.3: Comparison of experimental and computed vertical ionization energies (VIEs) of 2-Azidoethanol

in the neat liquid, and a relatively high OH stretch at 3623 cm^{-1} which owes its position to the absence of hydrogen bonding.

Pyrolysis experiments were carried out in the range ca. 375-875°K, and even at the lowest temperatures, there was evidence for some decomposition, with the generation of new products. However, traces of the parent azide could still be detected up to 775°K.

Figure 10.1(b) shows the spectrum obtained at a superheater temperature of 845°K. An intense feature is still present close to the original N_3 doublet at 2137/2105 cm^{-1}, but closer examination shows that this now appears as a sharp feature at 2139 cm^{-1} with a shoulder at 2146 cm^{-1}. This new band (labelled F) is assigned to CO. Apart from a weak residual N_2 feature near 2100 cm^{-1}, all other bands corresponding to parent absorptions are clearly absent, having been replaced by numerous new features. However, despite the complexity of these matrix infrared spectra, many of these new features can be assigned from previous studies [18, 19], based on a consideration of expected reaction products. The results are summarised in Table 10.1.

CH_2NH is unequivocally identified by at least five characteristic peaks: B, C, H, I, and J, whilst band A indicates the formation of HCN. A fourth prominent pyrolysis product is identified as H_2CO (bands D, E and G) by comparison both with previously published work, and also as a result of supporting matrix infrared experiments. The identification of these four products accounts for most of the new features produced on pyrolysis, but six additional weak features were routinely observed at 2967, 2885, 1306, 1263, 970 and 816 cm^{-1}, the assignment of which was unknown. In an attempt to establish their identity, supporting matrix

infrared experiments were carried out on CH_3NH_2, CH_4, C_2H_4 and C_2H_6 isolated separately in nitrogen matrices, with the aim of obtaining a suitable match for at least two frequencies for each compound. In practice, only the most intense feature of CH_4 gave a positive match for the frequency at 1306 cm^{-1}.

10.3.3 Thermal Decomposition Experiments: Photoelectron Spectroscopy

The HeI photoelectron spectrum obtained for azidoethanol is shown in Figure 10.2(a), and the photoelectron spectrum obtained upon partial pyrolysis is shown in Figure 10.2(b). The temperature of the furnace under these conditions was approximately 513°K(240°C) as estimated from chromel-alumel (Type K) thermocouple measurements. The HeI photoelectron spectrum recorded for complete pyrolysis is shown in Figure 10.2(c), recorded at a furnace temperature of approximately 653°K(380°C).

Signals arising from N_2, CO and HCN are clearly observed on pyrolysis (Figures 10.2(b) and 10.2(c)). In addition, pyrolysis also produced four further features:- a broad band with a VIE of 10.65 eV which is associated with the vibrationally resolved band at 12.66 eV (VIE), and a sharp feature at 10.90 eV (VIE) which is associated with the vibrationally resolved band at 15.84 eV (VIE). These can be attributed to the first two bands of CH_2NH and the first two bands of CH_2O respectively by comparison with known spectra of methanimine [17, 40] and formaldehyde [23].

No spectral features were observed which indicated the possible formation of an imine intermediate ($HN{=}CHCH_2OH$, 1st VIE computed at the ΔSCF QCISD/6-31G** level for the X^1A' state is 9.96 eV) or a nitrene intermediate (NCH_2CH_2OH, 1st VIE computed at the ΔSCF QCISD/6-31G** level for the X^3A'' state is 10.59 eV). Also, it is significant that the bands assigned to N_2, H_2CO, CH_2NH, CO and HCN appear together on pyrolysis and show the same temperature profiles. No spectral features were observed associated with CH_4, indicating that if it is produced it is a very minor product.

10.3.4 Characterisation of $N_3CH_2COOCH_2CH_3$

2-Azidoethylacetate was characterised in the vapour phase by mass spectrometry, ultraviolet photoelectron spectroscopy and also in the liquid phase by ^1H NMR, ^{13}C NMR, Raman and infrared spectroscopy.

The 70 eV electron impact mass spectrum showed an intense parent peak at 129 amu (100%) together with the following fragments:- 73 (20%, $CO_2CH_2CH_3^+$),

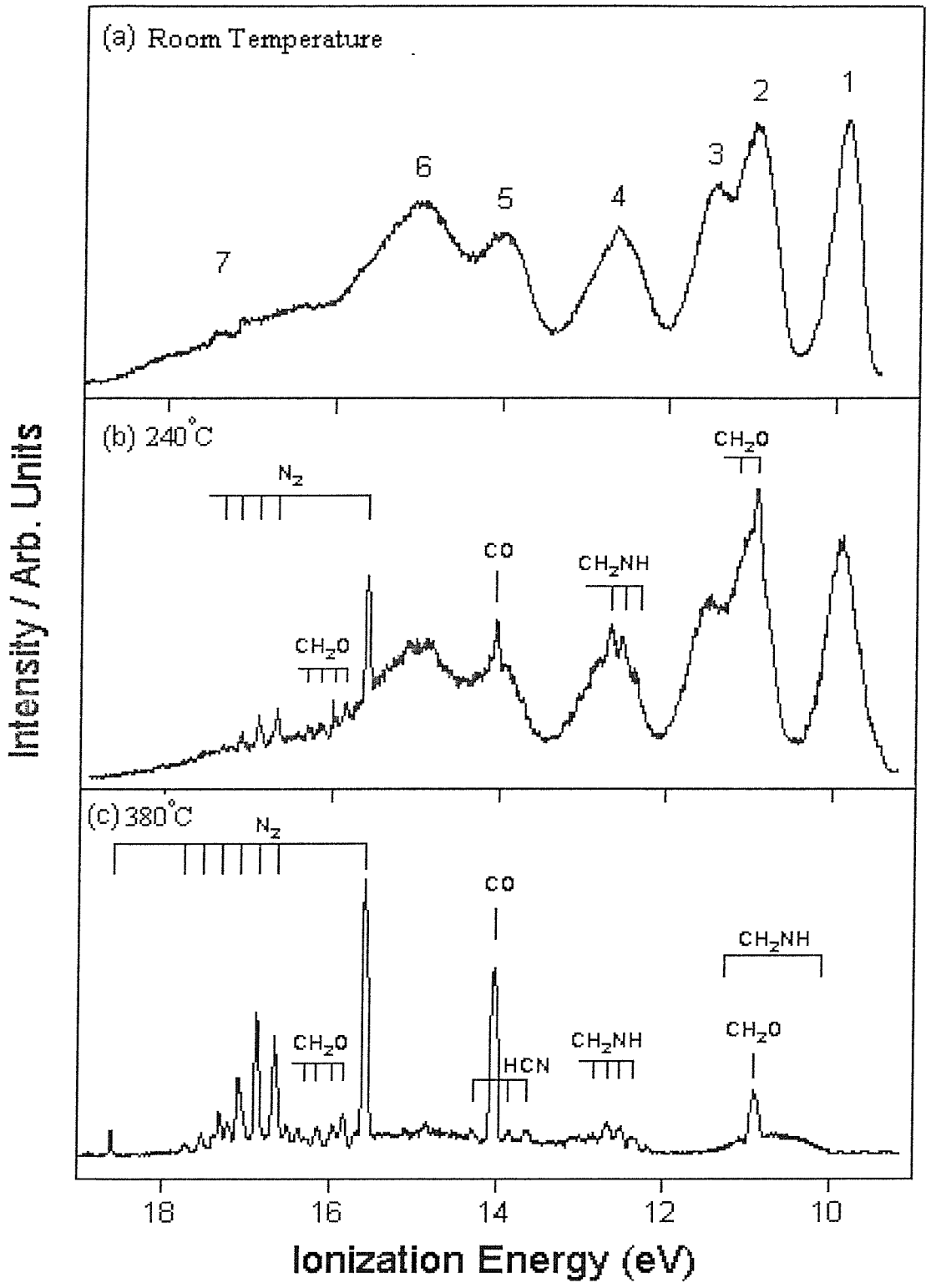

Figure 10.2: HeI photoelectron spectrum recorded for 2-azidoethanol at different stages of pyrolysis. (a) The photoelectron spectrum of the parent 2-azidoethanol. The numbered bands are listed in Table 10.3. (b) The photoelectron spectrum obtained on pyrolysis of 2-azidoethanol at a temperature of 513°K(240°C). (c) The photoelectron spectrum obtained for complete pyrolysis of 2-azidoethanol at 653°K(380°C).

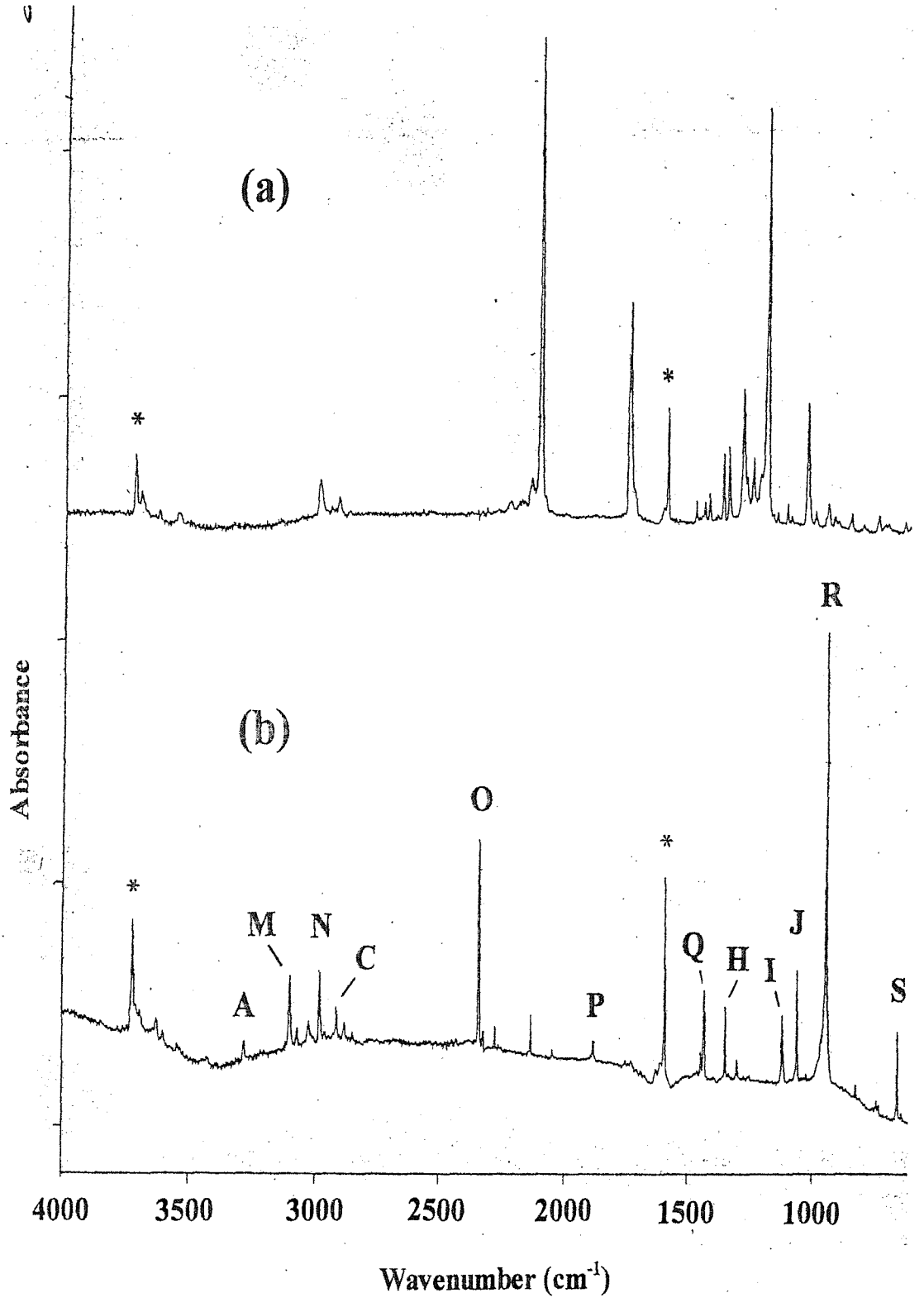

Figure 10.3: Nitrogen matrix infrared bands observed during pyrolysis studies on 2-Azidoethylacetate. Absorptions denoted by an asterisk are assigned to H_2O. Band identification is shown in Table 10.1. (a) Spectrum with no superheating (parent ester sublimed at room temperature). (b) Spectrum obtained after passage through superheater at ~773°K(~500°C).

56 (55%, $N_3CH_2^+$), 45 (25%, $OCH_2CH_3^+$), 42 (20%, N_3^+) and 29 amu (45%, $CH_2CH_3^+$). No signals were seen that could be attributed to the unreacted precursor $BrCH_2COOCH_2CH_3$.

In the 400 MHz ^1H NMR spectrum of 2-azidoethylacetate in $CDCl_3$, three signals were observed at 4.25, 3.86 and 1.30 ppm with integrated relative intensities of 2:2:3 respectively. These three signals were assigned as follows: - The signal at 4.25ppm was a quartet corresponding to the two protons on the CH_2 in the $-OCH_2CH_3$ group, the signal at 3.86 ppm was a singlet corresponding to the N_3CH_2- group and the signal at 1.30 ppm corresponds to the protons on the terminal methyl group. In the ^{13}C NMR of the 2-azidoethylacetate four strong signals were observed at 14.20, 50.44, 61.96 and 168.4ppm. Good ^1H-^{13}C correlation was found between the two sets of NMR signals, indicating that the signal at 14.20 ppm corresponds to the terminal methyl group, the signal at 50.44 ppm corresponds to the N_3CH_2- group, the signal at 61.96 ppm corresponds to the CH_2 in the $-OCH_2CH_3$ group. The final signal at 168.4 ppm is due to the carbon in the carbonyl group.

In the liquid phase infrared spectrum, intense absorptions were observed at 1749, 2110, 2935 and 2993 cm^{-1}. These were assigned to the C=O stretch, the N_3 group and the C-H stretches (2935 and 2993 cm^{-1}) respectively. The liquid Raman spectra exhibited counterparts to each of these bands observed in the infrared spectrum. The infrared spectrum recorded in a nitrogen matrix is shown in Figure 10.3(a) and the main absorptions are summarised in Table 10.1.

The HeI photoelectron spectrum of 2-azidoethylacetate is shown in Figure 10.4(a). As in the azidoethanol case, assignment of the spectrum is made by use of *ab initio* molecular orbital calculations with the Gaussian 94 code [37]. The minimum energy structure at the MP2/6-31G** level is shown in Table 10.4. This was the lowest energy conformer. The highest occupied molecular orbital (orbital 34) is antibonding between the terminal nitrogens on the N_3 group. Orbital 33 is delocalised over the $N_3CH_2CO_2$- grouping and is antibonding between each pair of bonded atoms. Orbital 32 has a major contribution from the lone pair on the oxygen on the C-O group and a minor bonding contribution from the C-N group. Orbital 31 is localized on the two oxygens and is mainly O2p antibonding in character.

The experimental VIEs have been compared with VIEs obtained from application of Koopmans' theorem to the SCF/6-31G** molecular orbital energies obtained at the MP2/6-31G** computed minimum energy geometry (see Tables 10.4 and 10.5). The Koopmans' theorem values are, as expected, higher than

Bond	Length/ Å	Angle	Value/ °
C_1-C_2	1.5127	C_1-C_2-O_3	110.7
C_2-O_3	1.4544	C_2-O_3-C_4	115.05
O_3-C_4	1.3498	O_3-C_4-C_5	109.7
C_4-C_5	1.5202	C_4-C_5-N_6	112.56
N_6-C_5	1.4609	C_5-N_6-N_7	115.49
N_7-N_6	1.2493	N_6-N_7-N_8	171.07
N_8-N_7	1.1616	O_{16}-C_4-O_3	125.68
C-H	~1.09	C-C-H	~110
C_4=O_16	1.2173		

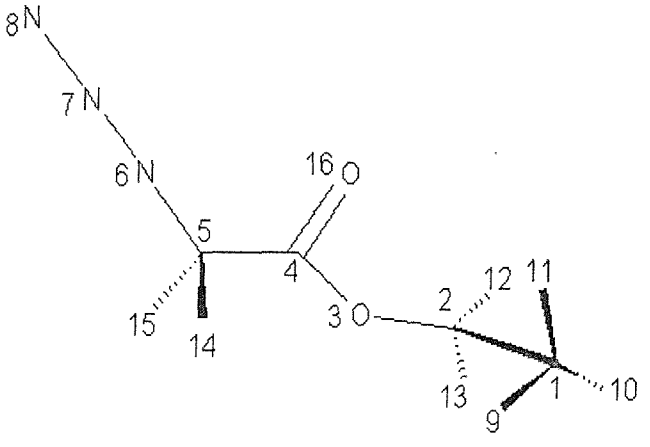

Table 10.4: Computed structural parameters of 2-azidoethyl acetate at the MP2/6-31G** level showing the atom numbering

the experimental values, but scaling by 0.92 gives much better agreement with experiment, as in the azidoethanol case. Also included in Table 10.5 is the first AIE and VIE computed by the ΔSCF method, using optimised geometries of the cationic states obtained at the MP2/6-31G** level. The ΔSCF first VIE shows good agreement with the experimental value.

10.3.5 Thermal Decomposition Experiments: IR Matrix Isolation Spectroscopy

Figure 10.3(a) shows a typical nitrogen matrix infrared spectrum obtained from a sample of $N_3CH_2COOCH_2CH_3$ deposited from the vapour phase without superheating. The absorptions arising from matrix isolated H_2O are again denoted by an asterisk (*), and the intense N_3 mode in the parent azide now lies at 2116 cm^{-1}. Other prominent features are to be found at 1753 and 1199 cm^{-1}, and are in similar positions to those found in the neat liquid. A list of the more significant bands is given in Table 10.1 .

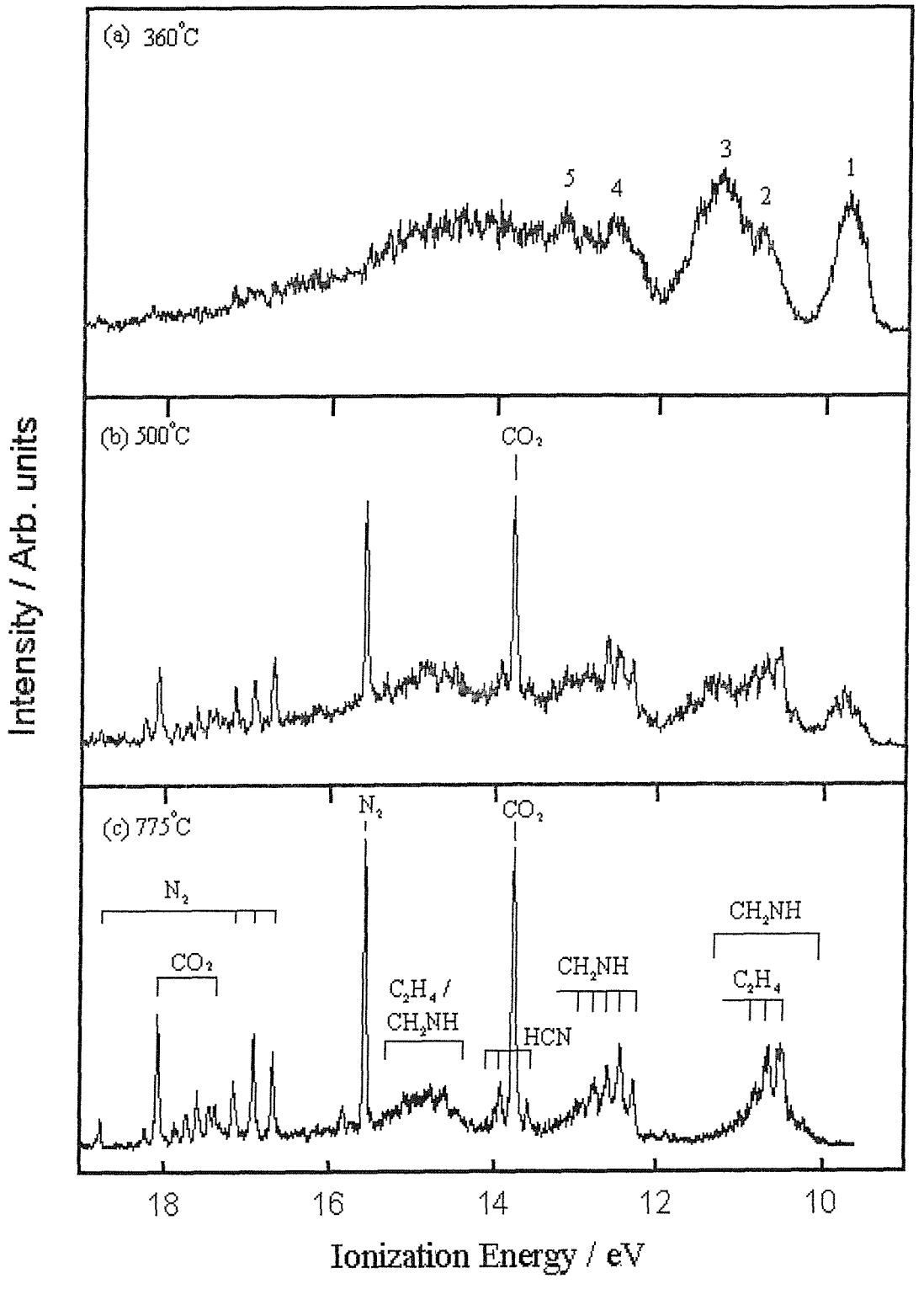

Figure 10.4: HeI photoelectron spectrum recorded for 2-azidoethylacetate at different stages of pyrolysis. (a) The photoelectron spectrum of the parent 2-azidoethylacetate. The numbered bands are listed in Table 10.5 (b) The photoelectron spectrum obtained on pyrolysis of 2-azidoethylacetate at a temperature of 773°K (500°C). (c) The photoelectron spectrum obtained for complete pyrolysis of 2-azidoethylacetate at 1048°K (775°C).

Mol. Orbital	Band No.	Exptl. VIE(eV)	KT VIE(eV)	KT Value ×0.92	ΔSCF values MP2/6-31G** AIE (eV)	VIE (eV)
34	1	9.74	10.27	9.45	9.76	9.94
33	2	10.82	11.87	10.93		
32	3	11.33	12.68	11.66		
31	4	12.6	12.82	11.8		
30	5	13.2	13.77	12.66		
29			14.57	13.41		
28			14.71	13.53		
27			15.6	14.35		
26			16.09	14.8		
25			16.71	15.38		
24			17.91	16.47		

Table 10.5: Comparison of experimental and computed vertical ionization energies (VIEs) of 2-azidoethylacetate

Pyrolysis experiments were carried out in the range ca. 373-823°K, and Figure 10.3(b) shows the spectrum obtained at a superheater temperature of ca. 773°K (500°C). At this temperature, all the parent absorptions are effectively absent, but several of the new features which have appeared can be assigned from previous studies.

Both CH_2NH (bands C, H, I and J) and HCN (band A) are again present, and the very intense new band labelled R is identified as being due to C_2H_4 by comparison with previously published work (Table 10.1). Closer inspection reveals that a further four bands (M, N, P and Q) may also be assigned to C_2H_4. CO_2 is unequivocally identified by bands O and S, leaving only very weak features unidentified.

10.3.6 Thermal Decomposition Experiments: Photoelectron Spectroscopy

The HeI photoelectron spectrum obtained for 2-azidoethylacetate is shown in Figure 10.4(a). The photoelectron spectra obtained on partial and complete pyrolysis are shown in Figures 10.4(b) and 10.4(c) recorded at furnace temperatures of 773°K (500°C) and 1048°K (775°C) respectively. The bands associated with the parent azide decrease, as expected, as the furnace temperature increases and bands associated with C_2H_4, CH_2NH, HCN, CO_2 and N_2 appear. The temperature profiles of these product bands are the same (within experimental error), all reaching a maximum intensity at the same furnace temperature. No pho-

toelectron bands associated with an imine intermediate ($HNCHCOOCH_2CH_3$, X^1A', 1st VIE computed at the ΔSCF MP2/6-31G** level 10.57 eV) or a nitrene intermediate ($NCH_2COOCH_2CH_3$, X^3A'', 1st VIE computed at the ΔSCF MP2/6-31G** level, 10.03 eV) were observed in these pyrolysis experiments.

10.3.7 Mechanisms of Gas-Phase Decomposition

In order to present mechanisms for the gas-phase thermal decomposition of 2-azidoethanol and 2-azidoethylacetate which are consistent with the experimental photoelectron and matrix infrared spectroscopic evidence, it is valuable to make a comparison with the earlier results obtained for 2-azidoacetic acid and 2-azidoacetone where concerted and stepwise mechanisms respectively were put forward to explain the decomposition.

In the case of azidoacetic acid, CO_2, CH_2NH and N_2 were observed at the same time on pyrolysis, with HCN being produced from CH_2NH at higher temperatures. The results are consistent with a concerted mechanism which can be written as:-

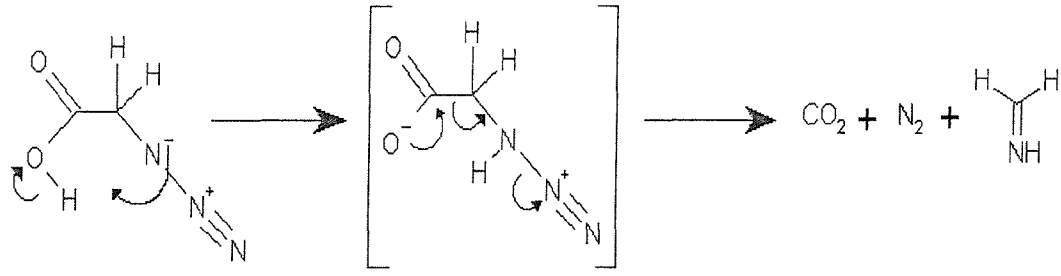

This mechanism is consistent with results of DFT and ab initio molecular orbital calculations performed by Cordeiro *et al.* [20] on the stepwise and concerted dissociation processes of 2-azidoacetic acid.

The results obtained in this work for 2-azidoethylacetate are also consistent with such a concerted mechanism, which can be written as:-

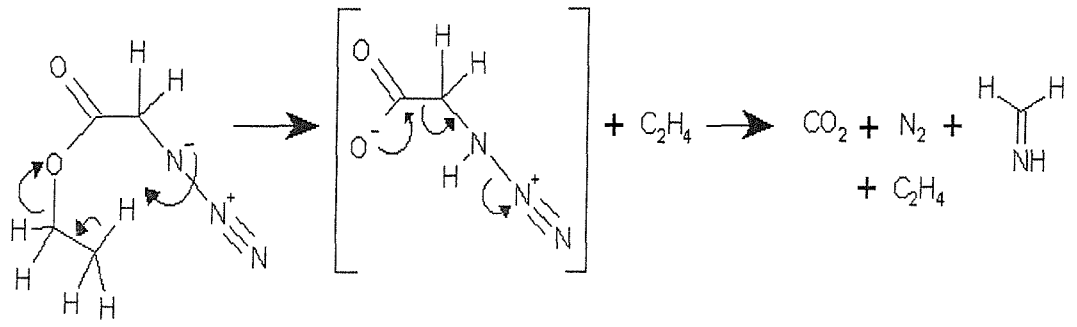

This mechanism would explain the production of C_2H_4, CO_2, CH_2NH and N_2 at the same temperatures (as is observed) with HCN being produced by subsequent pyrolysis of CH_2NH. However, the temperatures used for the ethylazidoacetate pyrolyses were greater than those used for the azidoacetic pyrolysis and are probably sufficient to lead to some decomposition of CH_2NH to HCN in the heated flow tube. Hence, it is felt that the results obtained for ethylazidoacetate are consistent with a concerted mechanism with C_2H_4, CO_2, CH_2NH and N_2 being the major products.

In the case of the azidoacetone, the simultaneous production of CH_2NH, H_2CO, HCN, CO, N_2 and CH_3CHO meant that although a concerted mechanism of the type:-

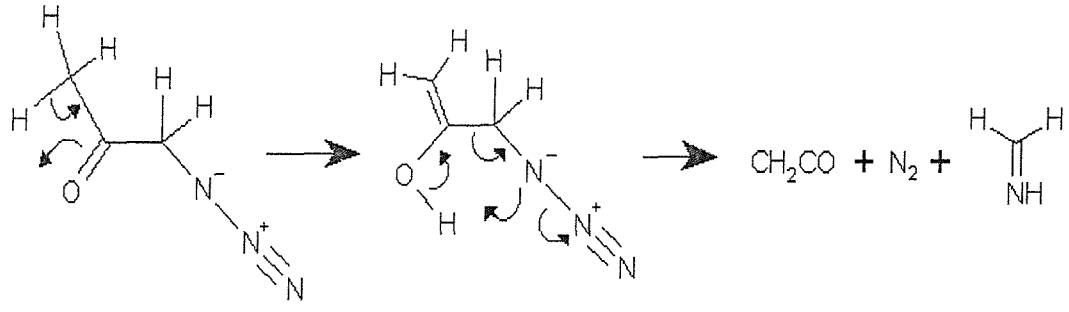

which gives rise to $H_2C{=}C{=}O$, CH_2NH, N_2 and HCN is possible, a stepwise pathway, possibly involving radicals, had to be invoked to explain production of CH_3CHO and CO simultaneously with the other products, *e.g.*

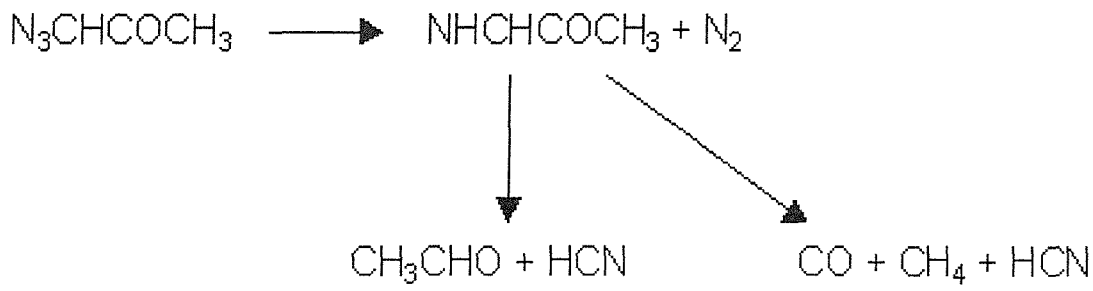

For 2-azidoethanol, it was expected that N_2, H_2CO and CH_2NH would be observed on pyrolysis from the following reaction:-

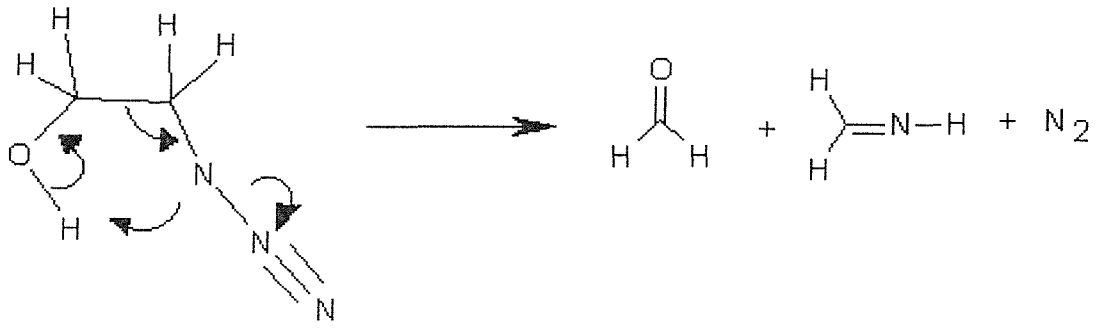

The observation of CO and HCN at the same time as N_2, H_2CNH and H_2CO was not anticipated if the above mechanism was taking place. The experimental evidence provided by PES and matrix isolation infrared experiments showed that CO, N_2, H_2CO, CH_2NH and HCN are observed at the same time. Therefore, the following stepwise mechanism is put forward to explain the decomposition:-

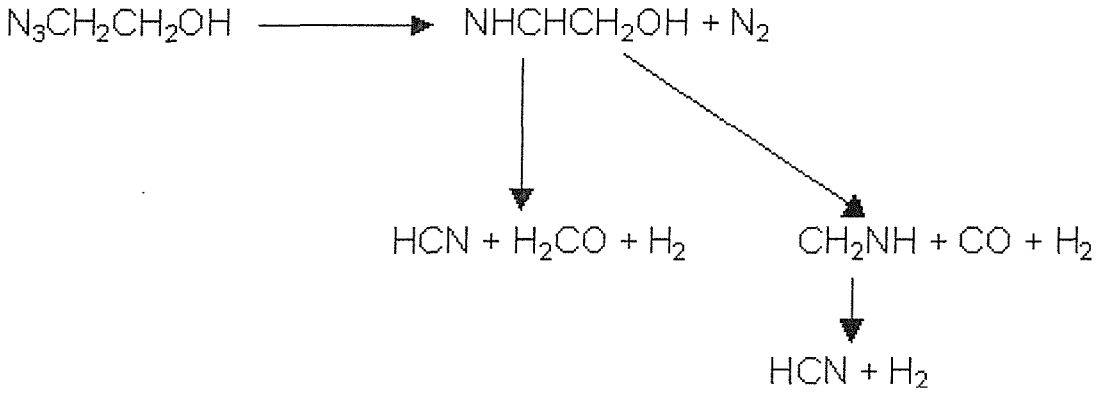

This is very similar to the stepwise mechanism put forward for the decomposition of azidoacetone and, as in the azidoacetone case, it is also possible that this multistep process proceeds via a radical mechanism.

10.4 Conclusions

The results of this study of 2-azidoethanol and 2-azidoethylacetate as well as the results from earlier studies on the thermal decomposition of 2-azidoacetic acid and 2-azidoacetone mean that two main mechanisms of decomposition of organic azides of the type considered are beginning to emerge. 2-Azidoacetic acid and 2-azidoethylacetate decompose via a concerted process through a cyclic transition state to give the products, whereas 2-azidoethanol and 2-azidoacetone decompose via a step-wise mechanism through an imine intermediate which is not detected experimentally, probably because it is short-lived, being produced from thermal decomposition with excess energy.

Bibliography

[1] N. Hooper, L. J. Beeching, J. M. Dyke, A. Morris, J. S. Ogden, A. A. Dias, M. L. Costa, M. T. Barros, M. H. Cabral, and A. M. C. Moutinho, J. Phys. Chem. (Submitted) (2002).

[2] S. Patai, *The Chemistry of the Azide Group* (Interscience, New York, 1971).

[3] E. F. V. Scriven and K. Turnbull, Chem. Rev. **88**, 298 (1988).

[4] V. Vantinh and W. Stadlbauer, J. Heterocycl. Chem. **33**, 1025 (1996).

[5] R. Maurus, R. Bogumil, N. T. Nguyen, A. G. Mauk, and G. Brayer, Biochem. J. **332**, 67 (1998).

[6] G. B. Schuster and M. S. Platz, Adv. Photochem. **17**, 69 (1992).

[7] Y. Matsumara, T. Shiozawa, H. Matsushita, and Y. Terao, Biol. Pharm. Bull. **18**, 1805 (1995).

[8] C. Tindall and J. Hemminger, Surface Science **330**, 67 (1995).

[9] A. S. Bridges, R. Greef, N. B. H. Jonathan, A. Morris, and G. Parker, Surf. Rev. Lett. **1**, 573 (1994).

[10] N. J. Kubota, Propul. Power **11**, 67 (1995).

[11] Y. L. Liu, G. H. Hsuie, and Y. S. Chiu, J. Appl. Polymer Sci. **58**, 579 (1995).

[12] W. Jing, S. Zheng, Z. Xinjiang, Y. Xiaojun, G. Maofa, and W. Dianxun, Angew. Chem. Int. Ed. Engl. **40**, 3055 (2001).

[13] W. Dianxun, Private Communication.

[14] H. Bock and R. Dammel, Angew. Chem. Int. Ed. Engl. **26**, 504 (1987).

[15] R. Dammel, Ph.D. thesis, University of Frankfurt,, Germany, 1985.

[16] H. Bock, R. Dammel, and S. J. Aygen, J. A. C. S. **110**, 5261 (1983).

[17] H. Bock, R. Dammel, and L. Horner, Chem. Ber. **114**, 220 (1981).

[18] J. M. Dyke, A. P. Groves, A. Morris, J. S. Ogden, A. A. Dias, A. M. S. Oliveira, M. L. Costa, M. T. Barros, M. H. Cabral, and A. M. C. Moutinho, J. A. C. S. **119**, 6883 (1997).

[19] J. M. Dyke, A. P. Groves, A. Morris, J. S. Ogden, M. I. Catarinoand, A. A. Dias, A. M. S. Oliveira, M. L. Costa, M. T. Barros, M. H. Cabral, and A. M. C. Moutinho, J. Phys. Chem. A. **103**, 8239 (1999).

[20] M. N. D. S. Cordeiro, A. A. Dias. M. L. Costa, and J. A. N. F. Gomes, J. Phys. Chem. A. **105**, 3140 (2001).

[21] J. M. Dyke, N. Jonathan, and A. Morris, in *Electron Spectroscopy*, edited by C. R. Brundle and A. D. Baker (Academic Press, New York, 1979), Vol. 3, p. 189.

[22] J. M. Dyke, A. Morris, G. D. Josland, M. P. Hastings, and P. D. Francis, High Temperature Science **22**, 95 (1986).

[23] D. W. Turner, *Molecular Photoelectron Spectroscopy* (Wiley-Interscience, London, UK, 1971).

[24] J. H. D. Eland, *Photoelectron Spectroscopy* (Butterworths, London, UK, 1974).

[25] A. D. Baker, D. Betteridge, N. R .Kemp, and R. E. Kirby, Anal. Chem. **43**, 375 (1971,).

[26] A. D. Baker, D. Betteridge, N. R .Kemp, and R. E. Kirby, Phys. Letts. **103A**, 424 (1984).

[27] A. M. Olivera, M. T. Barros, A. M. Martins, M. A. R. Cabral, A. A. Dias, M. L. Costa, M. H. Cabral, A. M. C. Moutinho, and K. R. Jennings, Rapid Comm. Mass Spectrom. **13**, 559 (1999).

[28] J. S. Ogden, unpublished observation (unpublished).

[29] H. Dubost and L. Abouaf-Marguin, Chem. Phys. Letts. **17**, 269 (1972).

[30] L. Fredin, B. Nelander, and G. J. Ribbegard, J. Mol. Spec. **53**, 410 (1974).

[31] M. E. Jacox and D. E. Milligan, J. Mol. Spec. **56**, 333 (1975).

[32] C. M. King and E. R. Nixon, J. Chem. Phys. **48**, 1685 (1968).

[33] C. B. Moore and G. C. Pimentel, J. Chem. Phys. **38**, 2816 (1963).

[34] H. Khoshkoo and E. R. Nixon, Spectrochemica Acta. **29A**, 603 (1973).

[35] H. Frei, L. Fredin, and G. C. Pimentel, J. Chem. Phys. **74**, 397 (1981).

[36] B. Nelander, J. Chem. Phys. **82**, 5340 (1985).

[37] M. J. Frisch, Æ. Frisch, and J. B. Foresman, *Gaussian 94 User's Reference* (Gaussian Inc., Pittsburgh, PA15106 U. S. A., 1994).

[38] H. Basch, M. B. Robin, N. A. Kuebler, C. Baker, and D. W. Turner, J. Chem. Phys. **51**, 52 (1969).

[39] M. B. Robin, C. R. Brundle, N. A. Kuebler, G. B. Ellison, and K. B. Wiberg, J. Chem. Phys. **57**, 1758 (1972).

[40] J. B. and G. D. Willett, J. C. S. Faraday Trans II **71**, 1799 (1975).

Chapter 11

Simulation of the HeI Photoelectron Spectrum of F_2O

11.1 Introduction

The HeI photoelectron spectrum of F_2O was first reported by Cornford *et al.* in 1971 [1]. The observed bands were assigned with the aid of results of INDO and CNDO/2 semi-empirical calculations, and previous *ab initio* calculations (see reference [1] for details). A year later, Brundle *et al.* [2] reported a very similar HeI PE spectrum of F_2O, perhaps with slightly better resolution. *Ab initio* calculations were performed, and both the Koopmans' Theorem (KT) and the ΔSCF method were utilized to assign the observed spectrum. The assignments of the first four PE bands from these two studies are essentially identical, giving the order of the lowest four states of F_2O^+ as $^2B_1$, $^2A_1$, $^2B_2$ and $^2A_2$. These cationic states were assigned to four distinct PE bands observed in the HeI PE spectra, with measured vertical ionization energies (VIEs) of 13.25, 16.10, 16.44 and 18.50 eV respectively ([2], see also Table 11.1). However, Brundle *et al.* [2] also suggested an alternative assignment. Since the ionization leading to the $^2A_2$ state corresponds to an electron being removed from the nonbonding, F-localized, a_2 molecular orbital, this band is expected to be sharp. In view of this consideration, the $^2A_2$ ionic state might be more appropriately assigned to the relatively sharp third PE band at 16.44 eV, rather than the broad and relatively weak band at a significantly higher VIE of 18.50 eV. Thus, the $^2A_1$, $^2B_2$ and the $^2A_2$ states of F_2O^+ would be assigned to the observed overlapping second and third PE bands with measured VIEs of 16.10 and 16.44 eV respectively. With this alternative assignment, the precise positions of the lowest $^2A_1$, $^2B_2$ and the $^2A_2$ states of F_2O^+ are unclear, as three states are now assigned to two observed bands with no resolved vibrational structure.

Since the publication of these two HeI PE studies on F_2O [1, 2], numerous theoretical studies, which calculated the ionization energies (IEs) of the low-lying states of F_2O^+ by various methods, have appeared in the literature. Some of the computed VIEs reported for the lowest four cationic states [1–9] are summarized in Table 11.1 (see footnote a). From Table 11.1, it is clear that the assignment of the $^2B_1$ state of F_2O^+ to the first observed PE band is reasonably certain. However, based on available calculations, the order of the next three cationic states is far from unambiguous. Regarding the alternative assignment of the position of the $^2A_2$ state mentioned by Brundle *et al.* [2], some calculated vertical ionization energies (VIEs) (*e.g.* those obtained by the ROCI+Q, LDA-rTS and pGW2 methods; see Table 11.1) clearly support it, but for the others, there is no clear preference between the original [1, 2] and the alternative assignment [2]. The computed value obtained from the highest level of calculation prior to the present study is that obtained by Valenta *et al.* [3] from an MRDCI study. Their VIE value of 17.41 eV for the $^2A_2$ state can be considered to favour the original assignment of the $^2A_2$ state to the broad band at 18.50 eV.

In view of the above considerations, it is the purpose this chapter to provide more reliable assignments for the observed PE spectra of F_2O and to supply more precise positions of the low-lying states of F_2O^+ by presenting the results of high-level *ab initio* calculations (see Chapter 4) and spectral simulations. The work described here may also be found in a recently published paper [10]. For the $^2A_2$ state, the two proposed assignments would have their respective experimental VIEs differing by over 2 eV. It is expected that current near state-of-the-art quantum chemical calculations should give IEs, with uncertainties of less than 0.2 eV, and hence should be able to determine which of the two proposed assignments of the $^2A_2$ state is more reliable. In addition, the HeI PE spectrum of F_2O has been recoreded again with the intention of obtaining a better resolved spectrum than previously reported, in order to resolve vibrational structure, which was unresolved previously in the second and third bands. With a higher quality experimental spectrum and the assistance of spectral simulations, it was hoped that the assignments and the positions of the four lowest-lying cationic states of F_2O^+ could be firmly established.

Recently, the Southampton PES group have reported related investigations on the HeI PE spectra of Cl_2O [11] and ClO_2 [12] by *ab initio* calculations and spectral simulation. For Cl_2O, which is valence isoelectronic with F_2O, the first four observed PE bands are well resolved with vibrational structure [13], and their assignments have been firmly established to be due to ionization to the lowest

Method[a]	$^2B_1$	2^B_2	$^2A_1$	$^2A_2$	Ref.	First author/Year
INDO[b]	14.3	16.7	15.8	18.1	1	Cornford/1971
DSCF/DZ[c]	13.5	16.9	16.3	18.3	2	Brundle/1972
MRDCI/DZP+bp[d]	13.43	16.17	16.36	17.41	3	Valenta/1980
ROCI+Q[e]/DZP	13.18	16.01	16.59	16.62	4	Langhoff/1981
RSPT-KT[f]/DZ-STO	13.29	16.54	16.33	16.69	5	Chong/1974
GF[g]	13.06	16.46	16.37	16.95	6	Von Niessen/1979
RSPT-KT[h]/DZP	13.14	16.78	16.75	17.14[i]	7	Langhoff/1982
LDA-rTS[j]/ANO	13.3	16.1	16.48	16.23	8	Duffy/1993
pGW2[k]	13.39	16.27	16.61	16.54	9	Hu/1997
Observed[m]	13.26	16.47	16.17	18.68	1	Cornford/1971
Observed[l]	13.25	16.44	16.1	18.5	2	Brundle/1972

a. The highest level of calculation from the respective reference.

b. For earlier calculations, see reference 1 and references therein.

c. Whether the irreducible representation b_1 or b_2 in the C_{2V} point group corresponds to being symmetrical with respect to the molecular plane, depends on the choice of the axes system. Brundle et al. employed an axes system, which differs from others. Here, the convention that b2 corresponds to being symmetrical with respect to the molecular plane is used.

d. sp bond functions (exponent=1.0) at the centre of mass of the two OF bond were included in the basis set.

e. RO refers to relaxed orbitals, which mean that the molecular orbitals of the ground state of the cation (instead of those of the neutral molecule) were employed as the many particle basis set in the CI calculation. Q refers to the Davidson correction for quadruple excitations.

f. Third order Rayleigh-Schrodinger perturbation corrections to Koopmans' Theorem (KT).

g. Green Function calculation.

h. As footnote f; $\Delta(E^{GA})$ values (see original work for details).

i. A best estimated VIE for the $^2A_2$ state was given to be 16.6 eV.

j. Restricted transition state method employing the deMon density functional program; an observed VIE value of 16.32 eV was given to the $^2B_2$ state in this work, which was quoted to be from the original work of Cornford *et al.* [1], but we are unable to trace the origin of this value.

k. Parametrized second order Green Function (pG) times screened interaction (W2) approximation (see original work for details). It is noted that in this work, the assignments given for the observed VIEs from Cornford *et al.* [1] are not the same as those in the original paper. Some typing errors in Table 2 of this paper of Hu *et al.* [9] are suspected. See also footnote j for the observed VIE value of the $^2B_2$ state given in this work.

l. Assignments based on KT from previous ab initio and their own semi-empirical calculations.

m. Assignments based on KT and ΔSCF results; an alternative assignment of the $^2A_2$ state to the relatively sharp peak at 16.44 eV was given, because of the nonbonding character of the $1a_2$ molecular orbital; see text.

Table 11.1: The vertical ionization energies (VIEs in eV) to the first four cationic states of F_2O^+ from F_2O ($\tilde{X}^1A_1$) from previous calculations.

$^2B_1$, $^2B_2$, $^2A_1$ and $^2A_2$ cationic states respectively. Comparing the assignments of the observed bands in the PE spectra of Cl_2O with those of F_2O (original assignments [1, 2]), the following points should be noted. Firstly, the order of the second and third cationic states is reversed. Secondly, the fourth PE band, assigned to ionization to the $^2A_2$ state of Cl_2O^+ has a very strong 0,0,0 - 0,0,0 vibrational component, while the third PE band assigned to ionization to the $^2A_1$ state is broad and relatively weak. In addition, the third (ionization to the $^2A_1$ ionic state) and fourth (ionization to the $^2A_2$ ionic state) bands are close to, and overlapping with, each other.

For ClO_2, the second PE band is a heavily overlapping band [14], with contributions from ionization to five cationic states. Nevertheless, with the aid of spectral simulations, which employ the recently developed anharmonic Franck-Condon (FC) code [12], most of the observed vibrational structure of this band could be adequately accounted for, and a reasonably reliable order of the five cationic states involved was proposed. In the present study on the He I PE spectrum of F_2O, an approach similar to the above two investigations [11, 12] has been employed.

The equilibrium structure of neutral F_2O has been determined by microwave spectroscopy [15, 16]; the OF bond distance is 1.4053 Å, and the bond angle is 103.07°. The harmonic and anharmonic force fields of F_2O have received considerable attention [17–21]. Since F_2O is in the test set of molecules, whose heats of formation were calculated by the composite method, G2 [22], many calibration studies [23, 24] on new theoretical methods, such as RI-MP2 [25], G3 [26] and some new density functionals [27–33] have included F_2O. However, the cation, F_2O^+, has received significantly less attention.

11.2 Theoretical Considerations and Computational Details

The theoretical methods outlined here, are described in Chapter 4. For more detailed analysis of the computational methods used, it is recommended that the original cited papers should be consulted.

11.2.1 *Ab initio* Calculations

Initially, geometry optimization (see section 4.7.1) and harmonic vibrational frequency calculations (see section 4.7.2) were carried out on the ground state of neutral F_2O and the four lowest-lying states of F_2O^+. The CASSCF, B3LYP, MP2

and QCISD methods were used with various standard basis sets. The Gaussian98 suite of programs [34] was employed for these calculations. In order to obtain more reliable geometries, RCCSD(T)/cc-pVTZ and/or RCCSD(T)/cc-pVQZ geometry optimization calculations were carried out, using the MOLPRO [35, 36] suite of programs. For relative energies, adiabatic ionization energies (AIEs) and/or VIEs were evaluated up to the RCCSD(T)/cc-pV5Z//RCCSD(T)/cc-pVQZ level and also were obtained by various extrapolation to the complete basis set (CBS) limit techniques [37–40]. In addition, CASSCF/MRCI/cc-pVQZ//RCCSD(T)/cc-pVQZ calculations were also carried out using MOLPRO [36, 41] to assess the effect of multi-reference character on the computed IEs. The optimized geometrical parameters, computed force constants and AIEs obtained at their respective highest levels of calculation were then employed in the subsequent Franck-Condon factor (FCF) calculations, which are based on the harmonic oscillator model and include the Duschinsky effect [42,43]. For reasons, which will be discussed in the Results and Discussion section, the anharmonic FC code was also employed for spectral simulation [12]. The asymmetric stretching mode, ν_3, has not been considered in the anharmonic FCF calculations, because harmonic FCF calculations gave negligible intensities for excitation of this vibrational mode upon ionization to all four lowest cationic states. For the ground state neutral and the four lowest ionic states, energy scans are performed to obtain the potential energy functions (PEFs), equilibrium geometrical parameters and fundamental frequencies of the symmetric stretch and bending modes (see section 11.2.2).

11.2.2 Determination of Potential Energy Surfaces

The potential energy functions (PEFs, see section 4.7.2) employed in the vibrational Schrödinger equation for the variational calculation of the vibrational wavefunctions (see next subsection) are determined by fitting the polynomial (given in equation 11.1) to RCCSD(T) single energy points.

$$\begin{aligned} V &= \sum_{ij} C_{ij}(S_1)^i(S_2)^j + V_{eqm}, \\ \text{where } S_1 &= (\Delta r_1 + \Delta r_2)\sqrt{2}, \\ S_2 &= \Delta\theta + \alpha\Delta\theta^2 + \beta\Delta\theta^3, \end{aligned} \tag{11.1}$$

$\Delta r_{1,2}$ and $\Delta\theta$ are the changes in FO bond lengths and the bond angle respectively ($\Delta r_1 = \Delta r_2$ for a symmetric stretch in a C_{2v}) molecule). S_1 is a function of the

changes in bond length and S_2 is the pure bending co-ordinate suggested by Carter and Handy [44]. The parameters α and β are related as previously given in equation 4.41, a condition which is imposed to ensure that the resulting PEF takes a value of zero when the molecule is linear. The non-linear least square fit procedure, NL2SOL [45] was employed to obtain the C_{ij}'s, V_{eqm}, r_{eqm}, θ_{eqm} and α values from the computed single point energies.

In all the PEFs, all terms up to the fourth order and also C_{05} and C_{06} were included. For the ground states of F_2O and F_2O^+, as the vibrational structure observed in the HeI PE spectrum is essentially due to the symmetric stretching mode, the fifth and sixth order terms for stretching, C_{50} and C_{60}, were included as well. The numbers of single point energies evaluated were 26 for the ground states of F_2O and F_2O^+, 29 for the $^2B_2$ ionic state and 24 for the $^2A_1$ and $^2A_2$ ionic states. From the harmonic spectral simulation, the bending mode progression of the $^2B_2$ state is rather long, so more points are used along the bending mode of the $^2B_2$ state. A higher level of theory, RCCSD(T)/ aug-cc-pVQZ, was employed to determine the PEFs of the neutral and cationic ground states, so that a more reliable cationic geometry can be deduced using the Iterative Franck-Condon Analysis (IFCA) procedure (see sections 4.7.3 and 11.2.3). The energy scans of the neutral and cationic ground states covered the range, -0.21 Å$\leq \Delta r \leq$+0.35 Å and -30°$\leq \Delta\theta \leq$+30°. For the $^2B_2$, $^2A_1$ and $^2A_2$ cationic states, the RCCSD(T)/aug-cc-pVTZ level of calculation was used. The energy scans of these cationic states covered the range, -0.14 Å$\leq \Delta r \leq$+0.21 Å and -30°$\leq \Delta\theta \leq$+30°.

11.2.3 Anharmonic FC Code (AN-FCF) and Spectral Simulation

The variational calculation of the anharmonic vibrational wavefunctions and the anharmonic FCF method have been reported previously [12]. A brief description and some technical details specific to the present study are given below, using some of the methods outlined in section 4.7.

Variational Calculation of Anharmonic Vibrational Wavefunctions

The anharmonic vibrational wavefunctions are expressed as described in equation 4.42 (see section 4.7.2). The anharmonicities of the vibrational motions are included in the formalism used via the anharmonic PEFs and the anharmonic vibrational wavefunctions defined in equation 4.42. The Hamiltonian matrix elements, $< n|H|m >$, are evaluated using the Gauss-Hermite quadrature along

each normal mode. Since the *ab initio* PEFs described above are not expressed in normal coordinates, each quadrature grid point is transformed to the coordinate system of the PEF. For neutral F_2O, vibrational levels with quantum numbers up to 10 were considered in the variational calculations, with a constraint of $v_1 + v_2 \leq 10$. This was shown to be more than sufficient from a series of calculations including different numbers of vibrational levels. Similarly, for calculations involved the F_2O^+ electronic states, vibrational levels with quantum numbers of up to 25 were included, with a constraint of $v_1 + v_2 \leq 25$. Thus, a total of 66 harmonic basis functions for the neutral $F_2O(\tilde{X}^1A_1)$ and a totel of 351 harmonic basis functions for the cationic states have been used in the variational calculations to obtain the anharmonic vibrational wavefunctions as given by equation 4.42. FCF calculations (see next subsection) employing vibrational wavefunctions obtained with larger harmonic basis sets for the ground neutral state and ground cationic state were also carried out to test the sensitivity of calculated FCFs and simulated PE bands to the selected basis sets. These calculations show that larger basis sets than the ones mentioned above do not alter the quality of the calculated FCFs or the spectral simulation to any significant extent.

Anharmonic FCF Calculation, IFCA Procedure and Spectral Simulation

The anharmonic FCF is expressed as described in equation 4.44, where the anharmonic wavefunctions are expressed as linear combinations of harmonic functions in normal coordinates. The overlap integral can be evaluated readily using the methods outlined in section 4.7.3.

With the equilibrium geometry of the ground state of F_2O available experimentally [15, 16], the Iterative Franck-Condon Analysis (IFCA) procedure can be applied to derive the geometry of the cationic states, as in previous studies [11, 12, 46, 47]. In the IFCA procedure, the geometry of the neutral molecule is fixed at the available experimental geometry, while the cationic state geometrical parameters are adjusted systematically (initially from the predicted *ab initio* geometry changes), until the simulated spectrum matches the experimental one. The IFCA procedure can be carried out with both the harmonic and anharmonic FCF method. In the latter case, during the IFCA procedure, the shape of the *ab initio* PEFs of the two electronic states involved are kept unchanged [12]. The IFCA procedure was applied to the first PE band, where well resolved vibrational structure was observed. Experimentally derived geometrical parameters of the $\tilde{X}^2B_1$ state were thus obtained for the first time (see section 11.4). For the sec-

ond and third bands, the observed vibrational structure is poorly resolved and the AIE positions of the three cationic states involved are uncertain from the observed spectrum. Consequently, the IFCA procedure was only applied to the ionization leading to the $^2A_2$ state (the fourth ionic state) in order to obtain a qualitative match between the observed and simulated spectra (see section 11.4).

Gaussian functions with the appropriate full-width-half-maximum (FWHM), and relative intensities as given by the computed FCFs were used to simulate the vibronic peaks in the HeI PE spectrum. For the bands corresponding to ionization to the $^2B_2$, $^2A_1$ and $^2A_2$ ionic states, their individual simulated band areas were assumed to be the same. This was thought to be a good approximation as the molecular orbitals associated with these ionizations are composed of O2p and F2p atomic orbitals which are expected to have very similar cross-sections at the HeI photon energy [48]. For the first PE band of F_2O, the experimental AIE was used in the simulation. For the three excited cationic states considered in this work, the RCCSD(T)/cc-pV5Z//RCCSD(T)/cc-pVQZ AIEs were employed initially. Subsequently, some small adjustments in band positions were made in order to obtain a reasonable match between the observed and simulated spectra. The details of these adjustments are discussed in the section 11.4.

11.3 Experimental

11.3.1 Synthesis of F_2O

The preparation of oxygen difluoride was based on the original procedures described by Ruff and Menzel [49], and Lebeau and Damiens [50]. In a typical synthesis, helium gas containing 5% F_2 was bubbled through a solution of 0.5 M NaOH at atmospheric pressure. The resultant gases were then allowed to pass firstly through a U-tube at ca. 200°K to remove H_2O, and then through a spiral trap at 77°K, before finally emerging via a bubbler containing aqueous KI solution. Pyrex vessels and tubing fitted with PTFE taps and joints proved to be quite satisfactory at the low partial pressures of F_2 and F_2O used in the system. The He/F_2 flow rate was held at ca. 20 ml/min, and after ca 3-4 hrs, small quantities of liquid F_2O could be observed in the spiral trap. At this temperature (77°K), F_2O has a finite vapor pressure (ca. 1 mbar), and also has the capacity to dissolve O_2, which is formed as a bi-product in the F_2/NaOH reaction. The final purification step, which involves the removal of dissolved O_2 under reduced pressure, therefore results in significant loss of F_2O. However, after this purification step, F_2O was the only volatile material remaining at 77°K, and it was

therefore admitted to the spectrometer inlet system directly from the 77°K trap. This procedure resulted in HeI PE spectra, which showed effectively no impurities other than the normal background trace amounts of N_2. Sample purity was also checked by matrix isolation infrared spectroscopy, and no other products were detected.

11.3.2 The Photoelectron Spectrometer

The high temperature photoelectron spectrometer was used for the study of F_2O, as described in detail in section 5.4. The high temperature furnace assembly was removed and replaced with a blank flange as is was not required due to the sufficiently high vapour pressure of F_2Oat 77°K trap. F_2O was kept in a glass bulb and admitted into the spectrometer via a simple 12 mm bore inlet tube. Low partial pressures of O_2 and N_2 were introduced into the ionization chamber as calibrants for the first, and the second and third bands of F_2O respectively.

Methods	$\tilde{X}^1A_1$	$\tilde{X}^2B_1$	$^2B_2$	$^2A_1$	$^2A_2$
MP2/cc-pVTZ	1.398/103.15	1.2715/107.99	1.3714/79.92	1.3177/121.25	1.5096/104.93
B3LYP/cc-pVTZ	1.4036/103.97	1.3186/108.01	1.4280/84.96	1.3777/118.71	1.4462/98.48
QCISD/cc-pVTZ	1.3945/103.15	1.3178/107.29	1.4200/83.48	1.3794/119.17	[a]
CCSD(T)/cc-pVTZ	1.4056/103.04	1.3238/107.43	1.4416/82.71	1.3660/118.89	1.4681/98.54
CCSD(T)/cc-pVQZ			1.4383/82.46	1.3613/118.88	1.4644/98.20
CCSD(T)/aug-cc-pVTZ[b]			1.4437/82.28	1.3689/118.57	1.4698/97.94
CCSD(T)/aug-cc-pVQZ[b]	1.4056/103.04	1.3190/107.28			
CASSCF(7,6)/6-311+G(2d)					1.5098/94.70
CASSCF(7, 6)/cc-pVTZ					1.5023/95.08
CCSD(T)/cc-pVTZ[c]	1.4056/103.09				
CCSD(T)/cc-pVQZ[c]	1.4036/103.10				
IFCA[d]		1.331/107.3			
IFCA[e]		1.323/107.3			1.460/95.0
Experimental values[f]	1.4053/103.07				

a. QCISD excessive iterations in the numerical second derivative calculations.
b. The optimized geometrical parameters were from energy scans and PEF fittings.
c. Reference [20].
d. The IFCA geometry from the **harmonic** IFCA procedure.
e. The IFCA geometry from the **anharmonic** IFCA procedure; these are the recommended values in this work.
f. References [15] and [16]; these are equilibrium values.

Table 11.2: The minimum-energy geometrical parameters (bond length in Å/bond angle in degrees), obtained in this work, for the neutral ($\tilde{X}^1A_1$) and the four lowest-lying cationic states ($\tilde{X}^2B_1$, $^2B_2$, $^2A_1$, $^2A_2$) of F_2O.

Methods	$\tilde{X}^1A_1$	$\tilde{X}^2B_1$	$^2B_2$	$^2A_1$	$^2A_2$
MP2/cc-pVTZ	985.5/485.5/ 917	1499.2/663.3 /1346.9	1760.8/707.6 /1353.7	1109.3/485.7 /1811.4	946.9/323.8 /251.1i
B3LYP/cc-pVTZ	1018.7/480.1/ 893.8	1125.0/570.0 /993.5	1029.5/445.0 /538.9	821.9/429.7/ 385.1	959.2/424.6 /723.3i
QCISD/cc-pVTZ	1007.5/494.0/ 951	1146.3/573.8 /1059.0	1089.5/479.6/ 484.3	799.0/427.3 /6495	
CASSCF(7,6)/6-311+G(2d)					769.2/366.0/ 575.9
CASSCF(7,6)/cc-pVTZ					794.6/372.1/ 573.9
RCCSD(T)/aug-cc-pVTZ[a]			957.3/454.6/–	862.1/414.9/–	879.2/378.9
RCCSD(T)/aug-cc-pVQZ[a]	952.4/466.9/–	1068.3/556.7/–			
CCSD(T)/cc-pVTZ[b]	951/471/865				
CCSD(T)/cc-pVQZ[b]	955/474/868				
Experimental (fundamental)	924.1504[c]/ 460.56[d]/828.69[e]	1032[f];1010[g]; 1000[h]/–/–	–/440h/–		900h/480h/–
Experimental (harmonic)[i]	941.6/467.5/ 849.5				

a. Fundamental frequencies from the *ab initio* scans in this work.
b. Reference [20]. c. Reference [51]. d. Reference [52]. e. Reference [53]. f. Reference [1]. g. Reference [2].
h. This work (±20, ±30 and ±50 cm^{-1} for the $^2B_1$, $^2B_2$ and $^2A_2$ states respectively).
i. Reference [19]; estimated from fundamentals and MP2/TZ2PF $\omega_e x_e$ (from reference [18]).

Table 11.3: The computed harmonic vibrational frequencies {$\omega_1(a_1$ symmetric stretch) / $\omega_2(a_1$ symmetric bending) / $\omega_3(b_2$ asymmetric stretch) in cm-1}, obtained in this work, for the neutral ($\tilde{X}^1A_1$) and the four lowest energy cationic states ($\tilde{X}^2B_1$, $^2B_2$, $^2A_1$, $^2A_2$) of F_2O.

11.4 Results and Discussion

11.4.1 *Ab initio* Calculations: Minimum-energy Geometries and Vibrational Frequencies

The minimum-energy geometries, computed harmonic vibrational frequencies and IEs obtained in this work for $F_2O(\tilde{X}^1A_1)$ and the low-lying states of F_2O^+ are summarized in Tables 11.2 to 11.4, respectively, and compared with experimental values where available. From Table 11.2, it can be seen that the calculated geometrical parameters of neutral $F_2O(\tilde{X}^1A_1)$ readily converge to the available experimental values as the level of calculation improves. At the highest level, CCSD(T)/aug-cc-pVQZ, the calculated geometrical parameters are very close to the experimental values.

For the cationic states considered here ($\tilde{X}^2B_1$, $^2B_2$, $^2A_1$, $^2A_2$), no experimentally derived geometries were available prior to the present study. From Table 11.2, it seems clear that, for all the cationic states considered, the optimized geometrical parameters are rather sensitive to the levels of calculations used in obtaining them. This is particularly true for the $^2A_2$ state and this will be further discussed later in this section. A higher level of calculation is clearly required to obtain reliable geometrical parameters for the cationic states than the neutral ground state. A similar conclusion can be drawn from Table 11.3 for the computed vibrational frequencies. In particular, the MP2 level is inadequate for all the cationic states studied, giving both geometrical parameters and harmonic vibrational frequencies significantly different from those obtained from higher levels of calculation. In contrast, the B3LYP results are in closer agreement with the QCISD and/or RCCSD(T) results. For the $^2A_2$ ionic state, CASSCF calculations were carried out to obtain the minimum-energy geometry and harmonic vibrational frequencies, because QCISD geometry optimization on this state faced excessive QCISD iteration problems; in addition, both MP2 and B3LYP frequency calculations yielded an imaginary frequency for the B_2 asymmetric stretching mode. The CASSCF calculations on the $^2A_2$ state considered seven electrons in six active orbitals. The second CI root was requested in order to obtain the $^2A_2$ ionic state (a similar approach was employed in a previous study of the $^2A_2$ state of Cl_2O^+ [11]). With both the 6-311+G(2d) and cc-pVTZ basis sets, the CASSCF calculations gave all real frequencies at their respective optimized geometries. The most reliable computed geometrical parameters and fundamental vibrational frequencies of the symmetric stretch and bending modes were, however, obtained from calculations from the scans/PEFs at the highest

Methods	$\tilde{X}^2B_1$	$^2B_2$	$^2A_1$	$^2A_2$
Experimental values	13.13 / 13.26a	– / 16.47a	– / 16.17a	– / 18.68a
	13.11 / 13.25b	–/ 16.44b	15.74 / 16.10b	17.9 / 18.50b
	13.109/13.233c	15.83/16.11d		16.44/16.44e
MP2/cc-pVTZ	13.42 / –	16.28 / –	16.84 / –	16.42 / –
QCISD/cc-pVTZ	12.84 / –	15.76 / –	15.99 / –	
RCCSD/aug-cc-pVQZ //QCISD/cc-pVTZ	– / 13.40	– / 16.28	– / 16.74	
RCCSD(T)/cc-pVTZ	12.93 / –	15.72 / –	16.19 / –	16.46 / –
RCCSD(T)/cc-pVQZ	13.07 / –	15.78 / –	16.36 / –	16.63 / –
RCCSD(T)/cc-pV5Z// RCCSD(T)/cc-pVQZ	13.13/–	15.85 / –	16.43 / –	16.71 / –
MRCI+D/cc-pVQZ// RCCSD(T)/cc-pVQZ	12.87/13.07	15.59 /15.97	15.99 /16.18	16.26 /16.41
Extrapol. VTZ/VQZf	13.17/–	15.89/–	16.48/–	16.76/–
VQZ/V5Zf	13.20/–	15.91/–	16.51/–	16.78/–
Extrapol. VDZ/VTZg	13.11/–	15.86/–	16.41/–	16.72/–
Extrapol. VDZ-V5Zh	13.19/–	15.79/–	16.48/–	16.75/–
VTZ-V5Zh	13.18/–	15.90/–	16.48/–	16.76/–
Extrapol. VDZ-V5Zi	13.20/–	15.90/–	16.49/–	16.75/–
Spectral simulationj		15.71/ 16.11	16.17/16.40	16.44/ 16.53

a. Reference [1]. b. Reference [2]. c. This work (±0.010 eV); see text.
d. This work (± 0.02 eV); the AIE value given here is the position of the first identifiable peak (see text).
e. This work (± 0.02 eV); see text.
f Two point extrapolation [37]:$E_{lim} = \frac{x^\alpha}{x^\alpha-(X-1)^\alpha}E_x - \frac{(x-1)^\alpha}{x^\alpha-(X-1)^\alpha}E_{X-1}$; data from the RCCSD(T)/cc-pVTZ (i.e. VTZ) and RCCSD(T)/cc-pVQZ (i.e. VQZ) calculations etc. (similar for the rest in the Table).
g. Two point extrapolation (VDZ and VTZ data; see Reference [38]:
$E_{lim} = \frac{3^\alpha}{3^\alpha-2^\alpha}E_3^{HF} - \frac{2^\alpha}{3^\alpha-2^\alpha}E_3^{HF} + \frac{3^\beta}{3^\beta-2^\beta}E_3^{cor} - \frac{2^\beta}{3^\beta-2^\beta}E_2^{cor}$
h. Energies fitted to [39]: $E_{SCF}(X) = E_{SCF} + Be^{-ax}$ and
$E_{corr}(X) = E_{corr} + B'X^{-3}$.
i. Energies fitted to [40]: $E(X) = E_{lim} + F(X)$, where $F(X) = Be^{-ax}$.
j. See text.

Table 11.4: The observed and calculated adiabatic and vertical ionization energies (AIE / VIE in eV) to the four lowest energy cationic states ($\tilde{X}^2B_1$, $^2B_2$, $^2A_1$, $^2A_2$) in the HeI PE spectrum of F_2O

Method	$^2B_2$	$^2A_1$	$^2A_2$
RCCSD(T)/cc-pVTZ	2.79	3.26	3.53
RCCSD(T)/cc-pVQZ	2.71	3.29	3.56
RCCSD(T)/cc-pV5Z// RCCSD(T)/cc-pVQZ	2.72	3.3	3.58
MRCI+D/cc-pVQZ// RCCSD(T)/cc-pVQZ	2.72	3.12	3.39
Extrapol. VTZ/VQZ[a]	2.72	3.31	3.59
VQZ/V5Z[a]	2.71	3.31	3.58
Extrapol. VDZ/VTZ[b]	2.75	3.3	3.61
Extrapol. VDZ-V5Z[c]	2.6	3.29	3.57
VTZ-V5Z[c]	2.72	3.3	3.58
Extrapol. VDZ-V5Z[d]	2.67	3.29	3.55

a. See footnote f of Table 11.4. b. See footnote g of Table 11.4. c. See footnote h of Table 11.4. d. See footnote i of Table 11.4.

Table 11.5: The computed relative electronic energies, T_e (in eV), obtained in this work, of the low-lying cationic states of F_2O^+ (with respect to the $\tilde{X}^2B_1$ state).

levels {RCCSD(T)/aug-cc-pVTZ and/or RCCSD(T)/aug-cc-pVQZ}.

11.4.2 *ab initio* Calculations: Computed Ionization Energies

The computed ionization energies of $F_2O$are given in Table 11.4. Firstly, the first AIE [for the $F_2O^+(\tilde{X}^2B_1) \leftarrow F_2O(\tilde{X}^1A_1)$] is considered, as reliable experimental values are available. All the computed values obtained in this work agree with the experimental values (including the most reliable experimental value obtained from the present work, 13.11 eV) to within 0.3 eV. If only the RCCSD(T) values are considered, the agreement is within 0.2 eV. At the highest level of calculation RCCSD(T)/cc-pV5Z, the computed AIE value agrees with the most reliable experimental value to $\leq$0.02 eV. The difference between the RCCSD(T)/cc-pVQZ and RCCSD(T)/cc-pV5Z levels is only 0.06 eV, suggesting near exhaustion of basis set effects. The complete basis set (CBS) limit values obtained from various extrapolation techniques (see Table 11.4 and footnotes f, g, h and i) agree with each other to within 0.03 eV, and agree with the most reliable experimental value to less than 0.1 eV. All these comparisons support the expectation mentioned in the Introduction that near state-of-the-art quantum chemical calculations on relative energies are reliable to within 0.2 eV.

For the order of the low-lying cationic states and the position of the $^2A_2$ ionic state, a clearer picture is obtained, if the T_e's (the relative electronic energy of the excited cationic state with respect to the ground cationic state), rather than the AIEs, are considered. From Table 11.5, the consistency in the computed T_e values of the low-lying states of F_2O^+ obtained at various levels of calculation is remarkably high. Therefore, it can be concluded that the reliability of these values is beyond any reasonable doubt. The order of the low-lying states of F_2O^+ is conclusively $^2B_1$, $^2B_2$, 2A1 and $^2A_2$, which is the same as for Cl_2O^+ (see references [11, 13]), but different from the original assignments of Cornford *et al.* [1] and Brundle *et al.* [2] in the early PE studies. From the present systematic theoretical investigation on the computed IEs, it can be concluded that it would be very unlikely for this order to be changed with any further improvement in the level of calculation.

Regarding the position of the $^2A_2$ state, it can be seen from the RCCSD(T) calculations in Table 11.5 that the range of the computed T_e values is from 3.4 to 3.6 eV. Combining the experimental AIE of the first band with the computed T_e values, the AIE values to the $^2A_2$ state range from 16.5 to 16.7 eV. In addition, the differences between the computed T_e values of the $^2A_1$ and $^2A_2$ states obtained at various levels of calculation (Table 11.5) are remarkably consistent. Excluding the extrapolated CBS values, obtained using the two-point formula of reference [38] (which give a separation of 0.31 eV), the average computed AIE/T_e separation between the $^2A_1$ and $^2A_2$ state is 0.27 ± 0.02 eV. The CASSCF/MRCI separation is 0.27 eV, in excellent agreement with RCCSD(T) values and most of the CBS values. Based on all these highly consistent computed results, it can be concluded that the $^2A_1$ and $^2A_2$ states should be very close, with a separation of $\leq$0.3 eV. This conclusion clearly favours the alternative photoelectron assignment suggested by Brundle *et al.* [2], that the ionization leading to the $^2A_2$ state has to be assigned together with the ionizations leading to the $^2B_2$ and $^2A_1$ states in the second and third PE bands of F_2O. However, the detailed assignments of these two observed bands and the precise AIE/VIE positions of the three cationic states, which contribute to these two experimental PE bands, could not be deduced unambiguously from the observed spectrum without the aid of spectral simulations, which will be discussed later. It is just noted that the ΔSCF AIE values obtained with the different basis sets used in this work have also been examined. It is found that the large differences in the computed correlation energies between the neutral ground state and the cationic $^2A_2$ state have caused the correlated AIEs to have significantly lower values than the corresponding ΔSCF

values. Higher computed IE values from previous calculations for the $^2A_2$ state of F_2O^+ (see Table 11.1, [2–4]) are almost certainly due to a lack of inclusion of sufficient electron correlation in the calculations.

11.4.3 The Fitted PEFs and the Anharmonic Vibrational Wavefunctions

The C_{ij}, α, r_e and θ_e values obtained from the fitting are given in Table 11.6 for all the electronic states studied. The root mean square (RMS) deviations in the fits are smaller than 11 cm^{-1} in all the PEFs reported here. For the $\tilde{X}^1A_1$ state of neutral F_2O, the anharmonic force field at the CCSD(T) level (quadratic force field from CCSD(T)/cc-pVQZ, cubic and quartic force fields from CCSD(T)/cc-pVTZ calculations) have been reported by Breidung *et al.* [20]. Variational calculation of vibrational wavefunctions was also performed employing the best PEF from reference [20]. A basis size limit of $v_1, v_2 \leq 10$ and a further constraint of $v_1 + v_2 \leq 10$ was imposed, when only the two symmetric vibrational modes were considered. When all three vibrational modes are considered, a basis limit of $v_1, v_2, v_3 \leq 10$ with a constraint of $v_1 + v_2 + v_3 \leq 10$ was imposed. The computed vibrational energies thus obtained are compared with those obtained using the PEF of the present study for the neutral ground state of F_2O, and this comparison is shown in Table 11.7. The agreement among the computed vibrational energies (and with available experimental values) is generally very good. The effect of including the asymmetric mode, ν_3, in the variational calculation on the computed vibrational energies of the two symmetric modes (ν_1 and ν_2) seems small. The present PEF for the ground state of F_2O may be considered to be of a slightly higher quality than those reported by Breidung *et al.* [20], as the basis set used here (aug-cc-pVQZ), which includes diffuse valence and polarization functions, is of higher quality than those (cc-pVTZ and cc-pVQZ) used in reference [20].

It should be noted that for the neutral ground state of F_2O, significant mixing of harmonic basis functions of the stretching and bending modes occurs in the computed anharmonic vibrational levels. This is expected, as the $2\nu_2$ and ν_1 levels have close vibrational energies ($2\nu_2 \approx \nu_1$) particularly for the $^1A_1$ state of neutral F_2O. The labels given in Table 11.7 are based on the computed largest coefficients of the harmonic basis function in the respective anharmonic vibrational wavefunctions. However, for highly excited vibrational levels, mixing could become so strong that their labels cannot be determined unambiguously. Nevertheless, for all the cationic states considered here, mixing between the symmetric stretching and bending mode is negligible.

$C_{ij}{}^a$	$\tilde{X}^1A_1{}^b$	$\tilde{X}^2B_1{}^b$	$^2B_2{}^c$	$^2A_1{}^c$	$^2A_2{}^c$
20	0.5722	0.7628	0.5545	0.6165	0.4712
11	0.063	0.1005	0.2042	0.1081	0.0436
02	0.1683	0.2	0.1927	0.0996	0.125
30	-0.929	-1.365	-0.885	-1.06	-0.731
21	-0.245	-0.365	-0.537	-0.222	-0.176
12	-0.457	-0.543	-0.758	-0.265	-0.392
03	0.0405	0.0614	-0.16	-0.022	0.0191
40	0.8944	1.457	0.751	0.9484	0.5865
31	0.4298	0.5556	0.7623	0.2837	0.3495
22	0.5696	0.6467	0.8996	0.3399	0.548
13	0.0328	0.0008	0.2398	0.1019	0.067
04	0.1922	0.2293	0.2822	0.1012	0.1717
50	-0.766	-1.253			
05	0.2009	0.3029	1.012	0.0455	0.1584
60	0.4288	0.6481			
06	0.1404	0.2155	1.1904	0.0474	0.1013
r_e	1.4052	1.3185	1.4441	1.3686	1.469
θ_e	1.7975	1.8714	1.4345	2.0699	1.7099
α	0.0703	0.0706	0.1868	-0.119	0.1047
V_e	-274.4	-274	-273.8	-273.8	-273.8

a. See text for the definitions of C_{ij}, r_e, θ_e, α and V_e.
b. Employing RCCSD(T)/aug-cc-pVQZ energy points (see text).
c. Employing RCCSD(T)/aug-cc-pVTZ energy points (see text).

Table 11.6: The calculated anharmonic potential energy functions (PEFs) obtained in this work (in units of Hartree $Å^{-m}$ rad^{-n} for m stretching and n bending coordinates) for the neutral ground state ($\tilde{X}^1A_1$) and the cationic states ($\tilde{X}^2B_1$, $^2B_2$, $^2A_1$, $^2A_2$) of F_2O

v_1 v_2 v_3 [a]	Obs[b]	Calc[c]	Breidung *et al.*[d]	Breidung *et al.*[e]
0 1 0	460.56	464.1	461.7	465.1
0 2 0	916.04	924.7	928.1	925.9
1 0 0	928.07	943.2	943.9	937.6
1 1 0		1382.7	1388.5	1384.4
0 3 0		1406.8	1408.4	1403.1
0 4 0		1838.1	1846.6	1840.1
1 2 0		1864.7	1868.9	1859.5
2 0 0		1878.4	1880.2	1871.2
0 5 0		2291.4	2302.7	2294.5
1 3 0		2320.6	2327.5	2317.6
2 1 0		2342.4	2345.4	2337.6

a. The vibrational quantum numbers, v_1, v_2 and v_3, correspond to the symmetric stretching, bending and asymmetric stretching modes, respectively.
b. References [51–53].
c. Employing the RCCSD(T)/aug-cc-pVQZ PEF of this work; see text for details.
d. Employing the "best" PEF of reference [20] with the asymmetric mode ignored in the basis set (see text).
e. Employing the "best" PEF of reference [20] (see text).

Table 11.7: The observed and calculated vibrational term values (with respect to the ground vibrational state in cm^{-1}) of $\tilde{X}^1A_1$ state of F_2O.

The computed fundamental frequencies obtained from the PEFs of this work are given in Table 11.3. In general, they are in closer agreement with available experimental values than the computed harmonic frequencies, as expected.

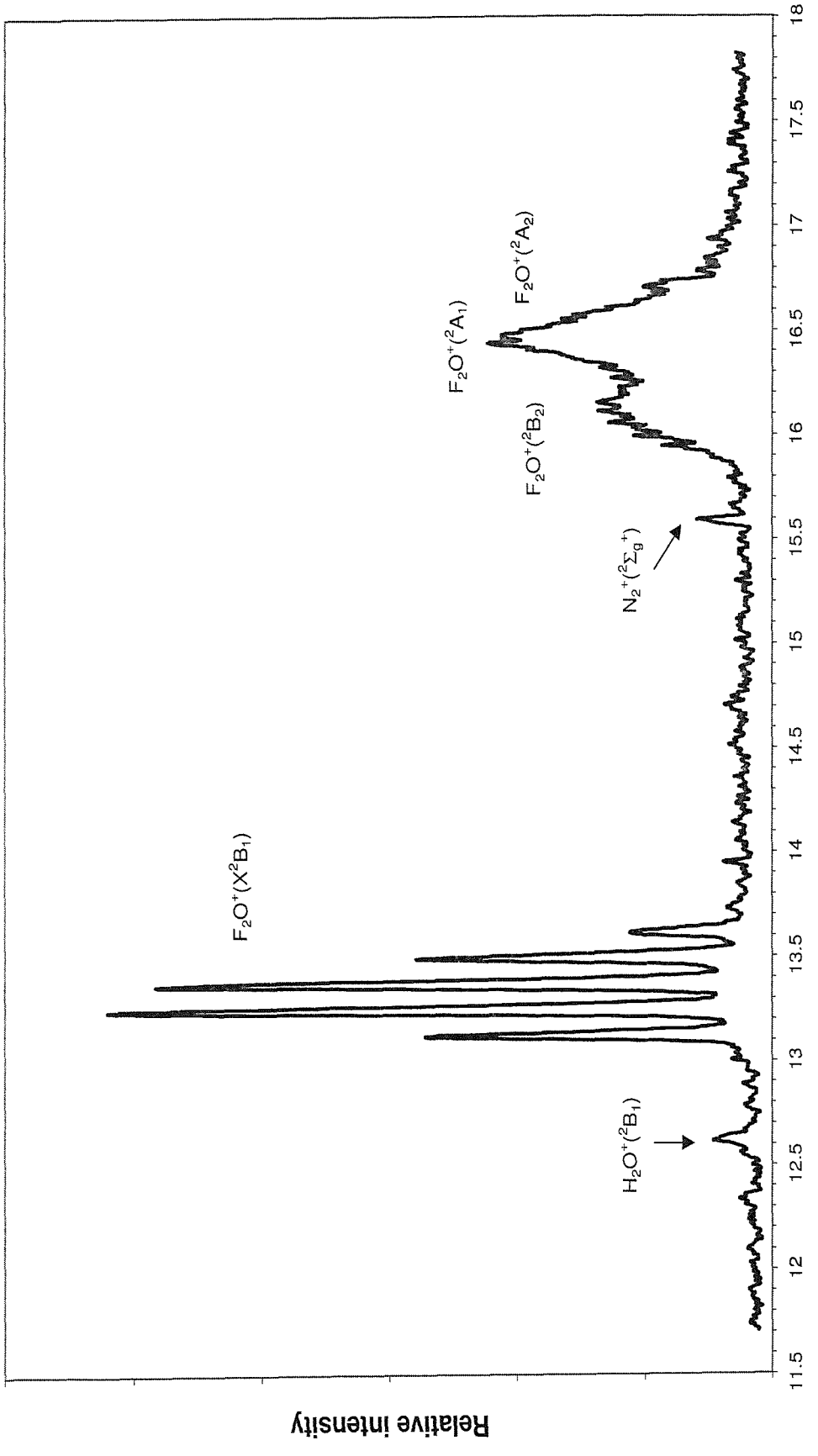

Figure 11.1: The HeI photoelectron spectrum of F_2O, obtained in this work.

11.4.4 Spectral simulation: First photoelectron band, $F_2O^+(\tilde{X}^2B_1) \leftarrow F_2O(\tilde{X}^1A_1)$

The photoelectron spectrum of $F_2O$is shown in Figure 11.1; all of the bands in the HeI region are shown (with their final ionic state assignments). Greater detail for the bands of interest is given in subsequent figures.

The observed first band in the HeI PE spectrum of F_2O from the present study and its simulations employing the anharmonic and harmonic FCF methods are shown in Figure 11.2(a), (b) and (c) respectively. The measured AIE/VIE and vibrational spacings of this band are given in Tables 11.4 and 11.3 respectively. They are in excellent agreement with previously reported experimental values, but with smaller uncertainties, as the present spectrum is of higher quality. The "hot band" associated with the first PE band is clearly observed. The observed vibrational components, which belong to the symmetric stretching progression of the cation, are resolved to the baseline. It is clear that excitation of the bending mode is not involved.

From spectral simulation, a temperature of 300°K is sufficient to produce a simulated "hot band" in the symmetric stretching mode of the neutral (assuming a Boltzmann distribution of vibrational levels in the initial state), which matches well with that in the observed spectrum. Therefore, all the simulations performed in this work have assumed an initial state Boltzmann distribution at 300 K. The simulated spectra shown were obtained after applying the IFCA procedure. The corresponding IFCA ionic state geometrical parameters are given in Table 11.2. From Figure 11.2, it is clear that the simulated spectrum with harmonic FCFs gives a symmetric stretching progression which is too long when compared with the observed spectrum. Nevertheless, it is pleasing that the simulated spectrum with anharmonic FCFs matches the observed spectrum almost exactly.

The IFCA geometrical parameters obtained from the anharmonic simulation for the cationic ground state are R(FO) = 1.323 ± 0.002 Åand ∠FOF = 107.3 ± 0.2°. The uncertainties in the geometrical parameters take into account not only the change in FCFs with bond angle and bond length (compared to experiment) but also factors such as the approximations and assumptions involved in the theoretical model and experimental limitations from the observed spectra (e.g. the non-observance of the bending mode in the first PE band). Further details of how the uncertainties were obtained are given in reference [54]. It is noted here that with the harmonic simulation, despite various attempts, it was not possible to obtain a good match across the whole stretching progression of the PE band. The IFCA geometry given in Table 11.2 with the harmonic method

was obtained mainly by matching the relative intensities of the most intense components in the low IE region, and assuming that the relative intensities of the bending mode components are negligibly small. It seems clear that the harmonic oscillator model is inadequate for the ionization to the $\tilde{X}^2B_1$ state. The anharmonic simulation is more convincing and the IFCA ionic state geometry derived from these simulations is the most reliable.

11.4.5 Spectral Simulation of the overlapped bands in the region 15.8-17.0 eV

Before the simulated spectra for the ionizations leading to the $^2B_2$, $^2A_1$ and $^2A_2$ cationic states are discussed (Figures 11.3, 11.4 and 11.5), the HeI PE spectrum obtained in the present study deserves some attention. The second and third bands in the HeI PE spectrum of F_2O obtained in the present investigation are shown in Figure 11.6 (top spectrum). Partially resolved vibrational structure is clearly observed on the low IE side of the second band, and the high IE side of the third band. For the former, a single vibrational progression with a number of components can be identified {labeled (a) in Figure 11.6}. The first observable component has a measured IE of 15.83 eV and at least five components are observed. However, the vibrational structure becomes diffuse in a region beyond the maximum of the second band (a VIE of 16.11 eV). For the vibrational structure of the third band, two vibrational progressions can be identified {labelled (b) and (c) in Figure 11.6}. The AIE and VIE positions of this band appear to be coincide at the band maximum of 16.44 eV. The measured vibrational spacings in the second and third bands are reported here for the first time, with their values given in Table 11.3. These values are in reasonably good agreement with the computed vibrational frequencies of the $^2B_2$ and $^2A_2$ ionic states respectively (see Table 11.3). In addition, between the two band maxima, some poorly resolved vibrational structure can be seen, though reliable vibrational spacings could not be obtained. The measured IE positions of the onset of the second band and the band maxima of the second and third bands are in good agreement with previously reported values (though the assignments are different) and are given in Table 11.4.

The simulated spectra for ionizations to the $^2B_2$, $^2A_1$ and $^2A_2$ states are shown individually in Figures 11.3, 11.4 and 11.5 respectively, with bar diagrams showing the computed FCFs. It can be seen that the simulated spectra employing the harmonic and anharmonic FC models for ionizations to the $^2A_1$ and $^2A_2$ ionic states are almost identical (Figures 11.3 and 11.4). However, for the ionization to

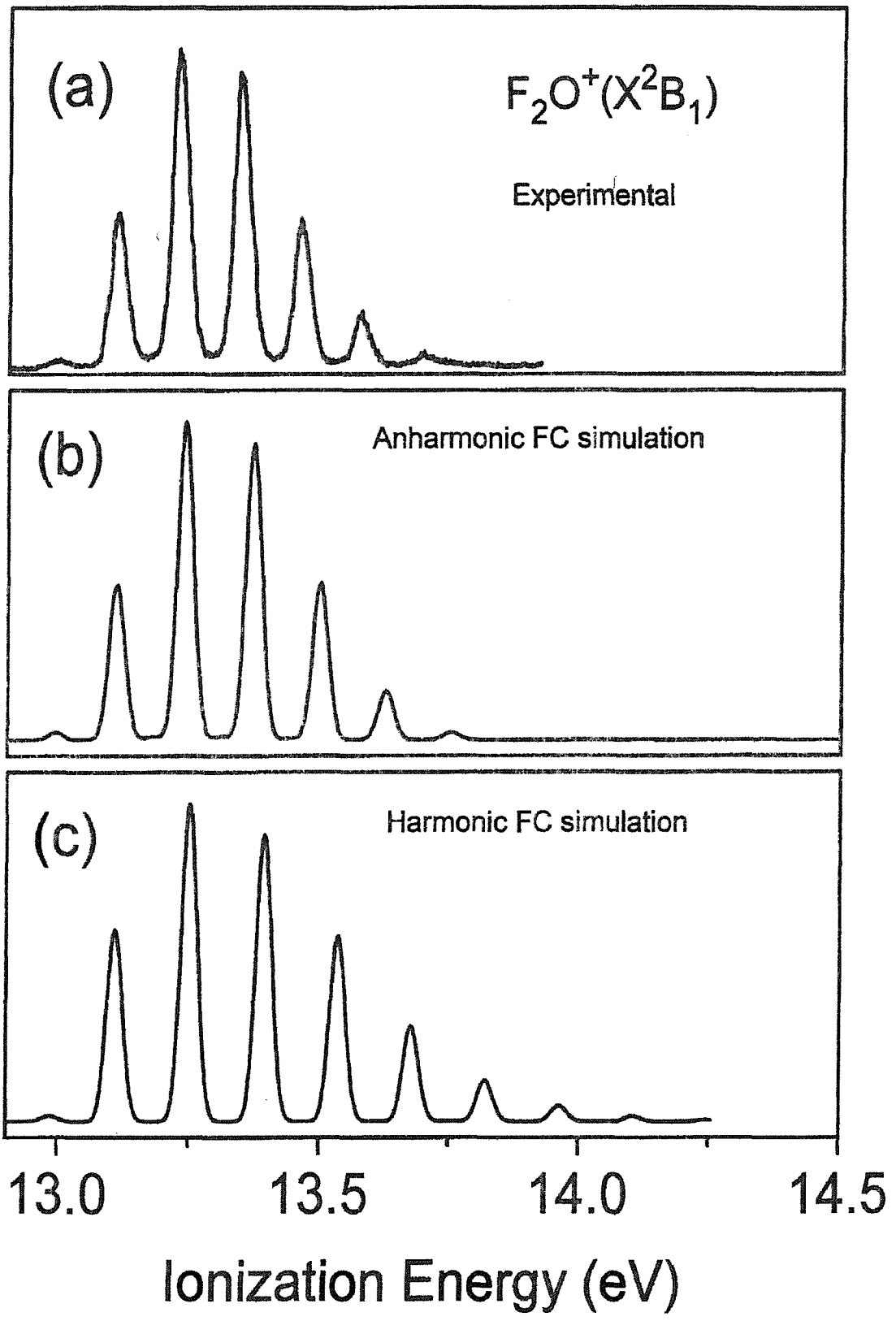

Figure 11.2: The first band in the HeI photoelectron spectrum of F_2O: (a) observed (from this work), (b) simulated (with a FWHM of 35 meV) employing anharmonic FCFs (c) simulated with harmonic FCFs (see text).

the $^2B_2$ state, the harmonic simulation has a significantly longer progression than the anharmonic one. From here onwards, only the anharmonic simulations would be considered, as they should be more reliable. For the $F_2O^+(^2A_2)\leftarrow F_2O(\tilde{X}^1A_1)$ ionization, an IFCA simulated spectrum is also shown in Figure 11.5(c) and this will be discussed below. Regarding the comparison between the simulated and observed spectra, ionization to all three states, namely the $^2B_2$, $^2A_1$ and $^2A_2$ states, have to be considered together, as they overlap to form the observed second and third PE bands. Figure 11.6(c) shows the simulated composite spectrum, based on the highest levels of calculations {i.e. combining Figures 11.3(b), 11.4(b) and 11.5(b)}. Comparing this "purely" theoretical simulation with the observed spectrum, it seems clear that the observed second and third bands are mainly due to ionization leading to the $^2B_2$ and $^2A_2$ states respectively, and the ionization to the $^2A_1$ state would be in between the second and third bands. These assignments are similar to those in the HeI PE spectrum of Cl_2O [11, 13]. Figure 11.6(b) shows the simulation that matches best with the experimental spectrum with the following empirical adjustments. The simulated band maximum of ionization to the $^2B_2$ state is set to align with the band maximum of the observed second band (16.11 eV). The AIE position of ionization to the $^2A_2$ simulation is set to the band maximum of the observed third PE band (16.44 eV). The highly consistent computed AIE/T_e separation of 0.27 eV (see previous subsection 11.4.2) between the $^2A_1$ and $^2A_2$ states is employed in the simulation for setting the position of the $^2A_1$ state. The IFCA procedure was carried out only for the ionization leading to the $^2A_2$ state. The IFCA geometrical parameters of R(OF) = 1.460 Å and $\angle$FOF = 95.0° for the $^2A_2$ state were found to give the simulation which matched best with the experimental envelope.

The following points should be noted regarding the simulation which matches best for the second and third bands. Firstly, the IFCA procedure has been carried out on neither the $^2B_2$ nor $^2A_1$ ionizations, because their AIE positions cannot be identified unambiguously from the observed spectrum. (There is, thus, no way to lock the simulated spectrum to the observed one.) If the IFCA procedure were to be carried out on these envelopes (as even the best *ab initio* geometry is likely to differ from the true one), the simulated band maximum (i.e. the VIE position) and the position of the first observable vibrational component would change. These changes may help to obtain a better match with the observed spectrum without adjusting the AIE and/or VIE positions, as described above. Nevertheless, it is felt that slight adjustments on the computed AIE and/or VIE values involve less arbitrariness than carrying out the IFCA procedure on bands associ-

ated with ionizations to the $^2B_2$ and $^2A_1$ states, where the vibrational structure is only partially resolved ($^2B_2$ band) or not resolved ($^2A_1$).

Secondly, regarding carrying out the IFCA procedure on the $F_2O^+(^2A_2)\leftarrow F_2O(\tilde{X}^1A_1)$ ionization, it was found that employing the geometry obtained from the highest level of calculations (RCCSD(T)/cc-pVQZ), the simulated spectrum could not give a reasonable match with the observed spectrum (the third band). With the RCCSD(T)/cc-pVQZ geometry for the $^2A_2$ ionic state, the bending mode is very weak and hence the stretching progression should be well resolved {Figure 11.5(b)}. However, the vibrational structure observed on the high IE side of the third band could not be well resolved {Figure 11.6(a)}. This is despite the fact that the resolution (FWHM), as judged from other resolved features observed elsewhere in the spectrum (e.g. argon), is better than 30 meV. Clearly the bending mode must have been invoked in the ionization process in order to produce the observed vibrational structure. From Table 11.2, it is clear that the magnitudes of the computed geometrical parameters for the $^2A_2$ ionic state are very sensitive to the level of calculations, as mentioned above briefly. The computed bond lengths range from *ca.* 1.44 to 1.51 Å and the bond angles, from 94.70 to 104.9°. The IFCA geometrical parameters used for the $^2A_2$ state to produce the best match with the observed third PE band are within the ranges of the computed ones. It seems that the RCCSD(T) bond length and CASSCF bond angle give the best combination. The IFCA geometrical parameters for $F_2O^+(^2A_2)$ are recommended as R(OF)=1.460±0.050 Åand ∠(FOF)=95.0±0.5°.

11.5 Conclusions

The HeI PE spectrum of F_2O has been recorded with a better resolution than previously reported. New vibrational structure associated with the second and third PE bands has been observed for the first time. The order and positions of the lowest four states of F_2O^+ have been studied by near state-of-the-art *ab initio* calculations. Anharmonic PEFs for $F_2O(\tilde{X}^1A_1)$and the four lowest cationic states have been obtained at the CCSD(T)/aug-cc-pVQZ or RCCSD(T)/aug-cc-pVTZ level of theory. Spectral simulations based on both the harmonic and anharmonic oscillator models were carried out to assist assignment of the observed PE spectrum. The order of the first four states of F_2O^+ has been firmly established as $^2B_1$, $^2B_2$, $^2A_1$ and $^2A_2$, which is the same as that in the valence isoelectronic Cl_2O^+.

The IFCA procedure was carried out on the $F_2O^+(\tilde{X}^2B_1)\leftarrow F_2O(\tilde{X}^1A_1)$

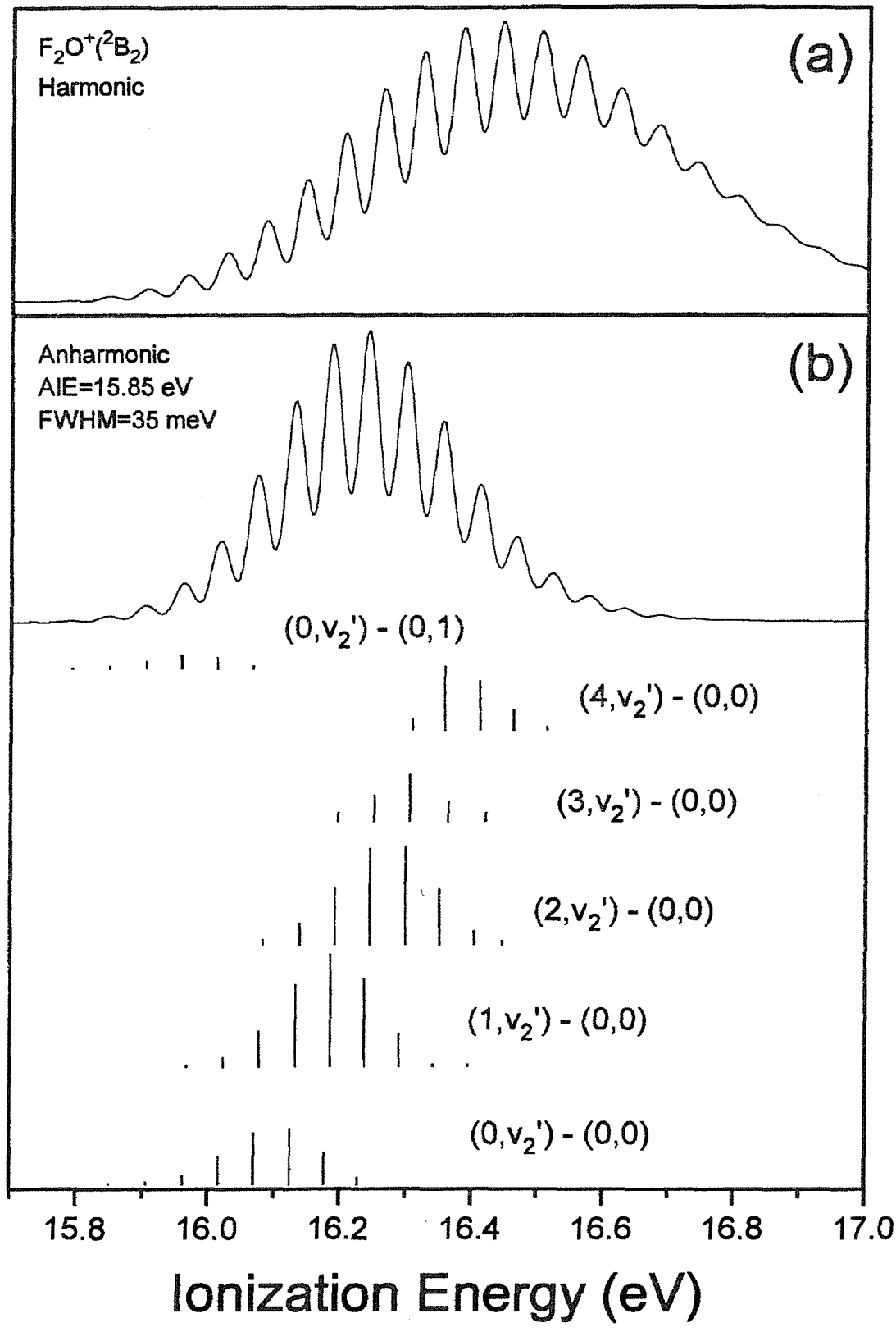

Figure 11.3: The simulated spectra (with a FWHM of 35 meV) of the $F_2O^+(^2B_2) \leftarrow F_2O(\tilde{X}^1A_1)$ionization, obtained using (a) harmonic and (b) anharmonic FCFs (bar diagrams showing the computed FCFs in the symmetric stretching and bending modes).

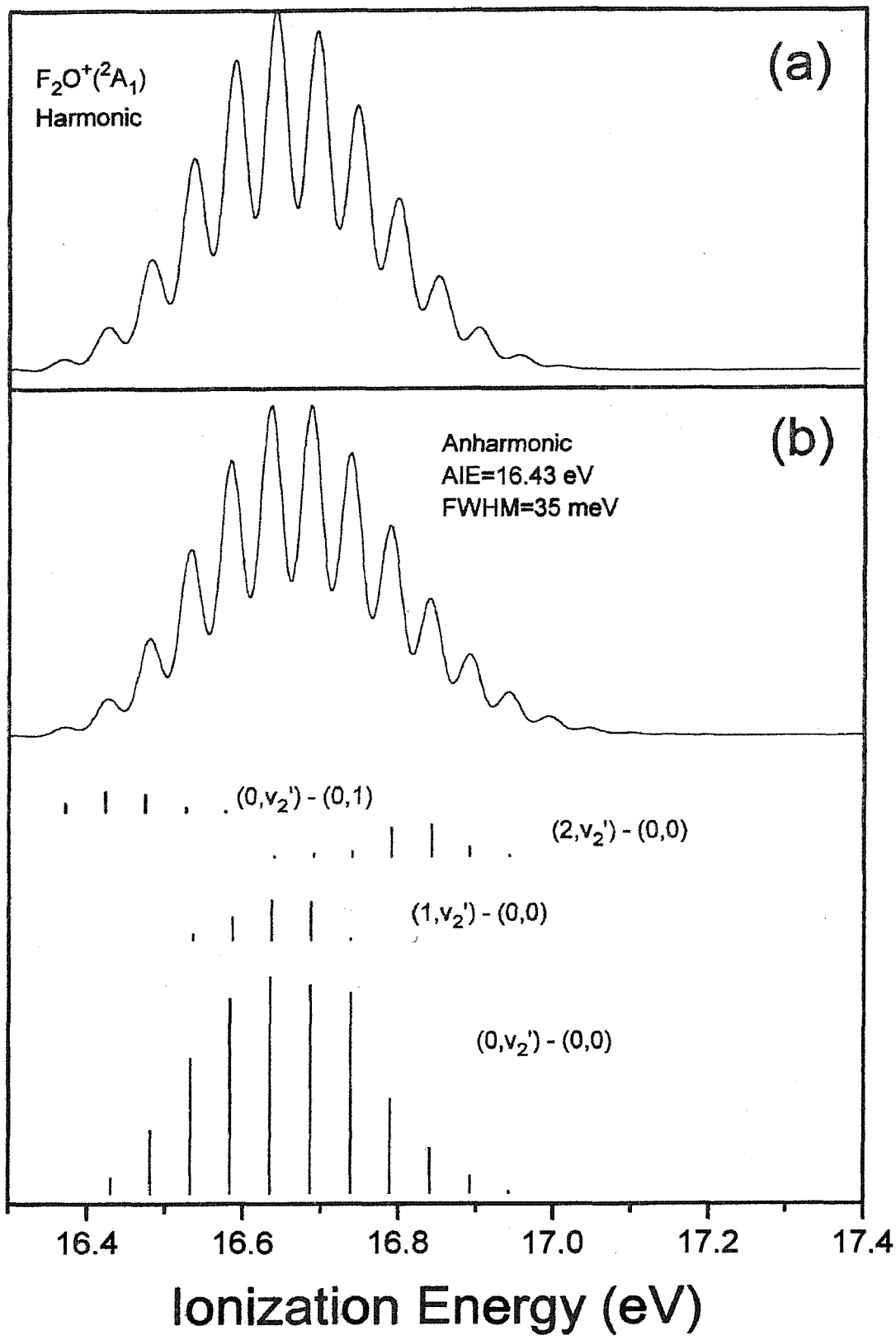

Figure 11.4: The simulated spectra (with a FWHM of 35 meV) of the $F_2O^+(^2A_1) \leftarrow F_2O(\tilde{X}^1A_1)$ ionization, obtained using (a) harmonic and (b) anharmonic FCFs (bar diagrams showing the computed FCFs in the symmetric stretching and bending modes).

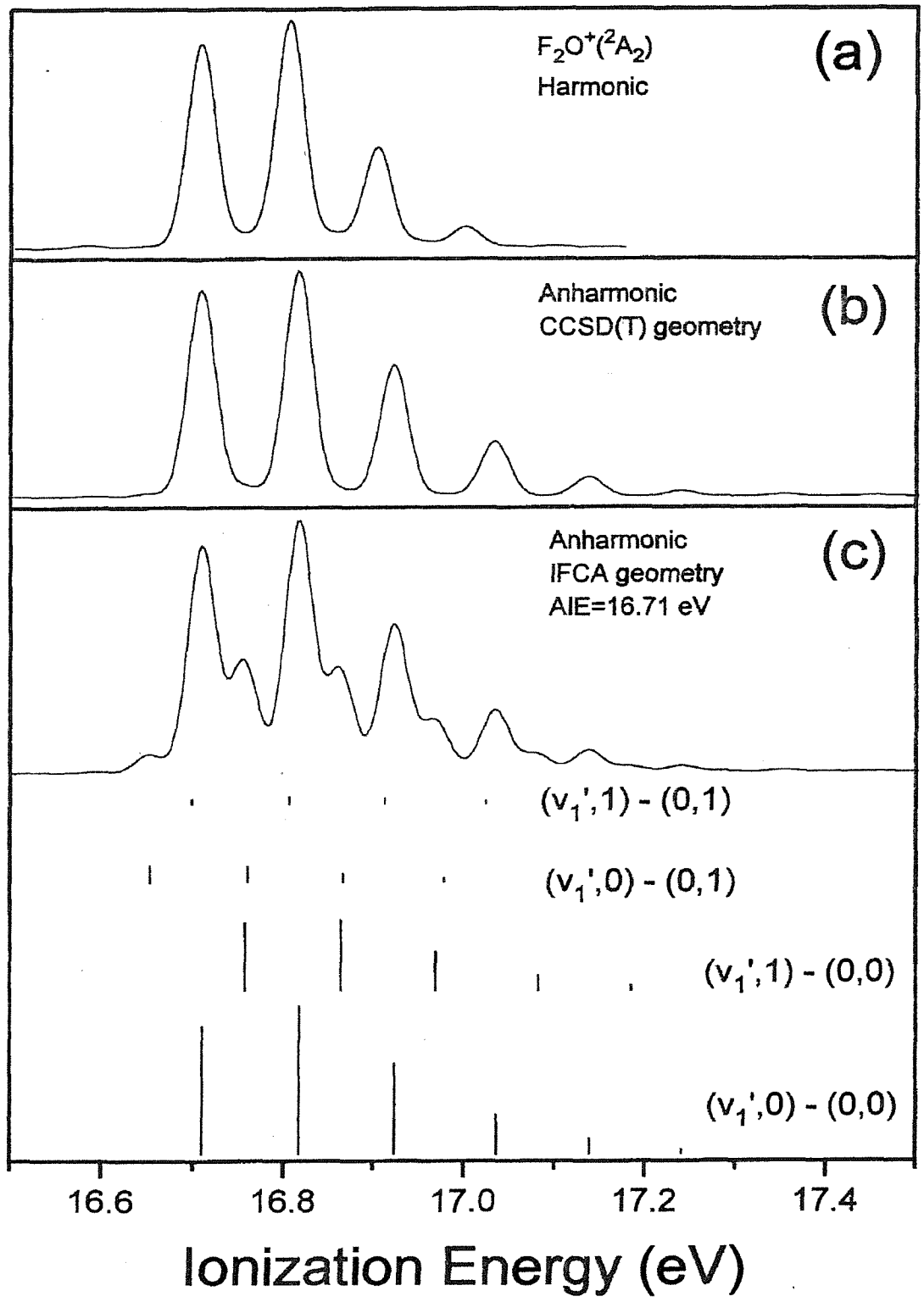

Figure 11.5: The simulated spectra (with a FWHM of 35 meV) of the $F_2O^+(^2A_2) \leftarrow F_2O(\tilde{X}^1A_1)$ ionization, obtained using (a) harmonic FCFs, (b) anharmonic FCFs with the RCCSD(T)/cc-pVQZ geometrical parameters of the $^2A_2$ ionic state and (c) anharmonic FCFs with the IFCA geometry of R(OF) =1.460 Å and FOF = 95.0° the $^2A_2$ ionic state(bar diagrams showing the computed FCFs in the symmetric stretch and bending modes; see text).

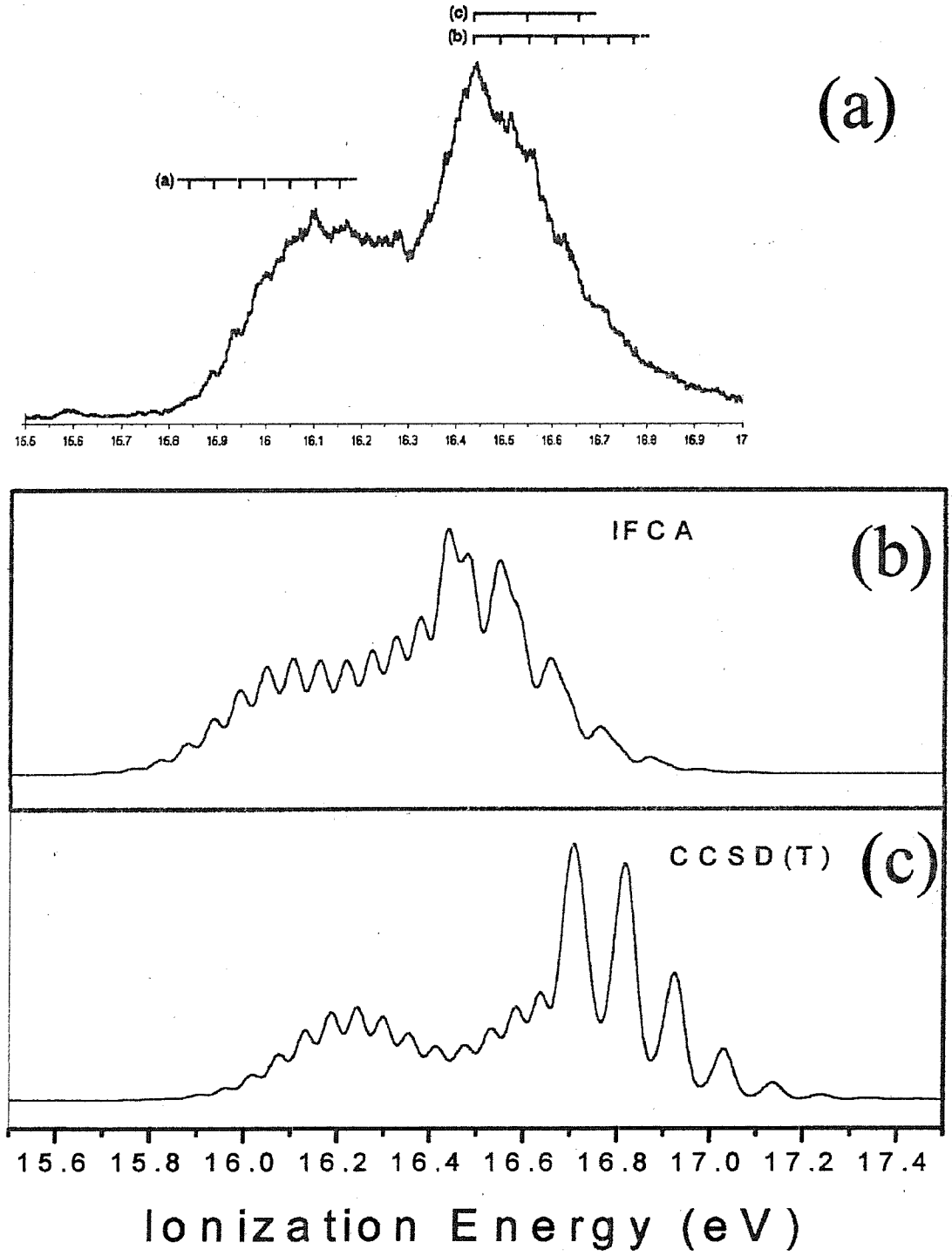

Figure 11.6: The second and third bands in the HeI photoelectron spectrum of F_2O: (top) experimental spectrum from this work {(a), (b) and (c) are labels of the three vibrational progressions identified from the experimental spectrum (see text for details)}; (middle) simulated spectrum employing anharmonic FCFs with some empirical adjustments of band positions and the IFCA geometry of the $^2A_2$ ionic state {Figure 11.5(c); see text for details}; (bottom) simulated spectrum employing anharmonic FCFs with RCCSD(T)/cc-pV5Z//RCCSD(T)/cc-pVQZ AIEs and RCCSD(T)/cc-pVQZ geometrical parameters {i.e. combining Figures 2(b), 3(b) and 4(b)}.

and $F_2O^+(^2A_2)\leftarrow F_2O(\tilde{X}^1A_1)$ PE bands. Experimentally derived geometrical parameters were obtained for the two associated cationic states for the first time. For the $^2B_1$ state, the IFCA geometry of R(FO)=1.323±0.002 Å and ∠FOF=107.2±0.2°, obtained within the anharmonic model, should be highly reliable. For the $^2A_2$, state, however, the IFCA geometry {R(OF)=1.460±0.50 Å and ∠(FOF)=95.0±0.5°} is less reliable, because of the poorly resolved vibrational structure observed in the experimental spectrum. Nevertheless, in view of the wide range of the computed geometrical parameters obtained for the $^2A_2$ state as discussed (see also Table 11.2), the present IFCA geometry should be currently the most reliable. In this connection, the computed RCCSD(T) bond lengths for the $^2A_2$ ionic state are reasonably close to the IFCA value, but the RCCSD(T) bond angles are slightly too large. The computed CASSCF bond angles seem to be superior.

The second and third PE bands in the HeI PE spectrum of F_2O, which correspond to three one-electron ionizations, are heavily overlapping with each other and the vibrational structure is only partially resolved. Nevertheless, based on the simulation, which matches best with the experimental spectrum, the following conclusions can be made. The observed onset of the second band corresponds to the (0,0,2)←(0,0,0) position of the ionization leading to the $^2B_2$ state. Both "hot bands" and the adiabatic position are too weak to be identified from the observed spectrum. Nevertheless, the AIE position for ionization to the $^2B_2$ state can be deduced from the comparison between the simulated and observed spectra to be 15.71 eV. Similarly, the observed VIE component of the second band is mainly due to contributions from the (1,5,0)←(0,0,0) and (2,3,0)←(0,0,0) vibrational components.

For the third PE band, although the observed AIE and VIE appear to coincide at 16.44 eV {Figure 11.6(a)}, spectral simulation suggests otherwise {see Figure 11.5}. The contribution from the ionization leading to the $^2A_1$ state causes the adiabatic component of the $^2A_2$ ionization to appear stronger than it actually is. The VIE component of the $^2A_2$ band is the (1,0,0)←(0,0,0) vibrational component at 16.54 eV. The observed diffuse vibrational features on the low and high IE side of the maximum of the third PE band are very likely due to overlap with the vibrational structure associated with the $^2A_1$ ionization. From the observed spectrum alone, it is impossible to derive any information on the AIE and/or VIE positions of ionization to the $^2A_1$ ionic state. Nevertheless, from the highly consistent computed AIEs/T_e values, and the excellent match between the simulated and observed spectra, the AIE and VIE positions to the $^2A_1$ state should

be close to the values of 16.17 and 16.40 eV, respectively, as obtained from spectral simulation. Once again, the combination of high-level *ab initio* calculations with spectral simulation has been demonstrated as a powerful tool for extracting valuable information from a complex PE spectrum.

Bibliography

[1] A. B. Cornford, D. C. Frost, F. G. Herring, and C. A. McDowell, J. Chem. Phys. **55**, 2820 (1971).

[2] C. R. Brundle, M. B. Robin, N. A. Kuebler, and H. Basch, Journal of the American Chemical Society **94**, 1451 (1972).

[3] K. E. Valenta, K. Vasudevan, and F. Grein, J. Chem. Phys. **72**, 2148 (1980).

[4] S. R. Langhoff and D. P. Chong, Chem. Phys. **55**, 355 (1981).

[5] D. P. Chong, F. G. Herring, and D. McWilliam, J. Chem. Phys. **61**, 958 (1974).

[6] W. V. Niessen, J. Elect. Spec. Relat. Phenom. **17**, 197 (1979).

[7] S. R. Langhoff and D. P. Chong, Chemical Physics Letters **86**, 487 (1982).

[8] P. Duffy and D. P. Chong, Org. Mass Spectrom. **28**, 321 (1993).

[9] C.-H. Hu and D. P. Chong, J. Elect. Spec. Relat. Phenom. **85**, 39 (1997).

[10] D. C. Wang, F. T. Chau, D. K. W. Mok, E. P. F. Lee, L. Beeching, J. S. Ogden, and J. M. Dyke, Journal of Chemical Physics **114**, 10682 (2001).

[11] D.-C. Wang, E. P. F. Lee, F.-T. Chau. D. K. M. MoK, and J. M. Dyke, J. Phys. Chem. A **104**, 4936 (2000).

[12] D. K. W. Mok, E. P. F. Lee, F.-T. Chau, D.-C. Wang, and J. M. Dyke, J. Chem. Phys. **113**, 5791 (2000).

[13] F. Motte-Tollet, J. Delwiche, J. Heinesch, M.-J. Hubin-franskin, J. M. Gingell, N. C. Jones, N. J. Mason, and G. Marston, Chemical Physics Letters **284**, 452 (1998).

[14] R. Flesch, E. Ruhl, K. Hottmann, and H. Baumgartel, J. Chem. Phys. **109**, 400 (1998).

[15] L. Pierce, N. DiCianni, , and R. Jackson, J. Chem. Phys. **38**, 730 (1963).

[16] Y. Morino and S. Saito, J. Mol. Spectrosc **19**, 435 (1966).

[17] T. J. Lee, J. E. Rice, and C. E. Dateo, Mol. Phys. **89**, 1359 (1996).

[18] W. Thiel, G. Scuseria, H. F. Schaefer, III, and W. D. Allen, J. Chem. Phys. **89**, 4965 (1988).

[19] S. Dressler and W. Thiel, Chem. Phys. Lett **273**, 71 (1997).

[20] J. Breidung, W. Thiel, J. Gauss, and J. F. Stanton, J. Chem. Phys **110**, 3687 (1999).

[21] T. Saarinen, E. Kauppi, and L. Halonen, J. Mol. Spectrosc. **142**, 175 (1990).

[22] L. A. Curtiss, K. Raghavachari, G. W. Trucks, and J. A. Pople, J. Chem. Phys. **94**, 7221 (1991).

[23] G. A. Petersson, D. K. Malick, W. G. Wilson, J.W. Ocliterski, J. A. Montgomery, Jr., and M. J. Frisch, J. Chem. Phys **109**, 10570 (1998).

[24] M. Kieninger, M. Segovia, and O. N. Ventura, Chemical Physics Letters **287**, 597 (1998).

[25] D. E. Bernholdt and R. J. Harrison, J. Chem. Phys. **109**, 1593 (1998).

[26] L. A. Curtiss, K. Raghavachari, P. C. Redfern, V. Rassolov, and J. A. Pople, J. Chem. Phys. **109**, 7764 (1998).

[27] F. Abu-Awwad and P. Politzer, J. Comput. Chem. **21**, 227 (2000).

[28] P. Politzer and F. Abu-Awwad, Mol. Phys. **95**, 681 (1998).

[29] H. L. Schmider and A. D. Becke, J. Chem. Phys. **108**, 9624 (1998).

[30] T. V. Voorhis and G. E. Scuseria, J. Chem. Phys. **109**, 400 (1998).

[31] S. A. Kafafi and E.-S. R. H. El-Gharkawy, J. Phys. Chem. **102**, 3202 (1998).

[32] S. A. Kafafi, J. Phys. Chem. **102**, 10404 (1998).

[33] M. W. Wong, Chem. Phys. Lett. **356**, 391 (1996).

[34] M. J. Frisch, G. W. Trucks, H. B. Schlegel, G. E. Scuseria, M. A. Robb, J. R. Cheeseman, V. G. Zakrzewski, J. A. Montgomery, R. E. Stratmann, J. C. Burant, S. Dapprich, J. M. Millam, A. D. Daniels, K. N. Kudin, M. C. Strain, O. Farkas, J. Tomasi, V. Barone, M. Cossi, R. Cammi, B. Mennucci, C. Pomelli, C. Adamo, S. Cliffoird, J. Ochterski, G. A. Petersson, P. Y. Ayala, Q. Cui, K. Morokuma, D. K. Malick, A. D. Rabuck, K. Raghavachari, J. B. Foresman, J. Cioslowski, J. V. Ortiz, B. B. Stefanov, G. Liu, A. Liashenko, P.

Piskorz, I. Komaromi, R. Gomperts, R. L. Martin, D. J. Fox, T. Keith, M. A. Al-Laham, C. Y. Peng, A. Nanayakkara, C. Gonzalez, M. Challacombem, P. M. W. Gill, B. G. Johnson, W. Chen, M. W. Wong, J. L. Andres, M. Head-Gordon, E. S. Replogle, and J. A. Pople., GAUSSIAN98, gaussian, Inc., Pittsburgh PA.

[35] P. J. Knowles, C. Hampel, and H.-J. Werner, J.Chem.Phys. **99**, 5219 (1993).

[36] R. D. Amos, A. Bernhardsson, A. Berning, P. Celani, D. L. Cooper, M. J. O. Deegan, A. J. Dobbyn, F. Eckert, C. Hampel, G. Hetzer, P. J. Knowles, T. Korona, R. Lindh, A. W. Lloyd, S. J. McNicholas, F. R. Manby, W. Meyer, M. E. Mura, A. Nicklass, P. Palmieri, R. Pitzer, G. Rauhut, M. Schütz, U. Schumann, H. Stoll, A. J. Stone, R. Tarroni, T. Thorsteinsson, and H.-J. Werner, MOLPRO, a package of ab initio programs designed by H.-J. Werner and P. J. Knowles, version 2002.1, 2002.

[37] A. Halkier, T. Helgaker, W. Klopper, P. Jorgensen, and A. G. Csaszar, Chem. Phys. Lett. **310**, 385 (1999).

[38] D. G. Truhlar, Chem. Phys. Lett. **294**, 45 (1998).

[39] A. Halkier, T. Helgaker, P. Jorgensen, W. Klopper, H. Koch, J. Olsen, and A. K. Wilson, Chem. Phys. Lett. **286**, 243 (1998).

[40] A. Halkier, T. Helgaker, P. Jorgensen, W. Klopper, H. Koch, J. Olsen, and A. K. Wilson, J. Chem. Phys. **108**, 154 (1998).

[41] H.-J. Werner and P. J. Knowles, J. Chem. Phys. **89**, 5803 (1988).

[42] P. Chen, in *Photoelectron spectroscopy of reactive intermediates*, edited by C. Y. Ng, T. Baer, and I. Powis (Wiley, New York, 1994), pp. 371–425.

[43] F.-T. Chau, J. M. Dyke, E. P. F. Lee, , and D.-C. Wang, J. Elect. Spec. Relat. Phenom.**97**, 33 (1998).

[44] S. Carter and N. C. Handy, J. Chem. Phys. **87**, 4294 (1987).

[45] J. E. Dennis, Jnr, D. M. Gay, and R. E. Walsh, ACM Transactions on Mathematical Software **7**, 348 (1981).

[46] F.-T. Chau, D.-C. Wang, E. P. F. Lee, J. M. Dyke, and D. K. W. Mok, J. Phys. Chem. A **103**, 4925 (1999).

[47] E. P. F. Lee, D.-C. Wang, and F.-T. Chau, J. Phys. Chem. **100**, 19795 (1996).

[48] J. J. Yeh and I. Lindau, Atomic Data and Nuclear Data Tables **32**, 1 (1985).

[49] O. Ruff and W. Menzel, Z. Anorg. Allg. Chem. **190**, 257 (1930).

[50] P. Lebeau and A. Damiens, Compt. Rend. Hebd. Seances Acad. Sci. **188**, 1253 (1938).

[51] G. Taubmann, H. Jones, and H. D. Rudolph, J. Mol. Spectrosc. **120**, 90 (1986).

[52] H. Burger and G. Schippel, J. Chem. Phys. **121**, 238 (1987).

[53] G. Taubmann, Z. Naturforsch **42a**, 87 (1987).

[54] D. K. W. Mok, E. P. F. Lee, F.-T. Chau, and J. M. Dyke, J. Comput. Chem. **22**, 1896 (2001).

Chapter 12

Conclusions and further work

12.1 Introduction

The scope of the work presented in this thesis is broad. The aim of the work was to use photoelectron spectroscopy, allied with electronic structure calculations, to understand the electronic structure, photoionization dynamics, and pyrolysis of a number of compounds. This work covers spectroscopic studies of atmospherically important species ($O_2(a^1\Delta_g)$, O atoms, OH and F_2O), heavy metal compounds ($ThBr_4$ and UBr_4), and two organic azides ($N_3CH_2CH_2OH$ and $N_3CH_2CO_2Et$). An overview of what has been achieved, suggestions for further studies, and possible improvements for the spectrometers used are given in the following sections of this chapter.

12.2 Advancement of the PE spectrometers

The basic designs of the high-temperature spectrometer and the synchrotron spectrometer enables them to study short-lived atoms and molecules, but their performance could be readily enhanced to produce extra spectral information, by increasing the efficiency of electron collection, improving the resolution or utilizing the ions produced from photoionization.

12.2.1 Multichannel detector

At present both instruments utilize a single channel electron multiplier as a detector. It is proposed to replace the single channel detector with a position-sensitive, multichannel device [1]. This will increase the rate of acquisition of spectra by at least an order of magnitude. This would be especially advantageous for the synchrotron spectrometer, as synchrotron time is limited in availability. The use of

chemically aggressive species can rapidly contaminate the spectrometer, decreasing its performance. Hence, spectra of reactive intermediates must be acquired as quickly as possible, while achieving acceptable signal-to-noise ratios.

12.2.2 Threshold spectroscopy

The resolution of a UV photoelectron spectrometer is routinely ≈30 meV and, at best, ≈20 meV. This is only adequate to resolve vibrational structure in most molecules, and often gives rise to difficulties in assignment when several bands are overlapped. For example, the interpretation of the photoelectron spectrum of F_2O would have been simplified if spectra could be recorded at higher resolution (see Chapter 11). This is also a common problem in studying radicals as they are often produced in an experiment at small relative partial pressures with other gases. This can lead to weak bands of the radical of interest being overlapped with a stronger band of a reagent or product.

A large improvement in resolution (3 meV) and sensitivity can be achieved in PES if threshold techniques are employed. Threshold photoelectron spectroscopy (TPES) is complementary to conventional PES as threshold techniques are more sensitive to indirect processes (*e.g.* autoionization). TPES requires a continuously tunable photon source (*e.g.* a synchrotron) and the photoelectron yield of nominally zero kinetic energy electrons is recorded as a function of photon energy [2, 3]. Photoelectrons are collected over a solid angle of 4π (using the penetrating field technique [3]), which greatly increases sensitivity, but means total loss of any angular information. The work of King, Yencha *et al.* has demonstrated the usefulness of TPES with synchrotron radiation for a number of small molecules including HF [4], ICl [5], BF_3 [6], HCl and DCl [7]. An alternative to the penetrating field technique is pulsed field ionization (PFI). In PFI a field is applied to the ionization region shortly after the sample has been illuminated with UV radiation. This applied field causes field ionization of long-lived Rydberg states, producing low kinetic energy electrons which are subsequently detected [3]. This requires the timing of the detection system of the spectrometer to be coupled with the temporal structure of the photon source. For example it is possible to collect threshold electrons during the dark gap of a synchrotron radiation source [3].

12.2.3 Coincidence Studies

A common problem when studying the photoelectron spectra of short-lived intermediates is that of overlapping photoelectron bands produced by different species

present in the ionization region, *e.g.* the photoelectron spectrum recorded for the production of OH shown in Figure 8.1. If the electrons and the ions produced in a photoionization event can be correlated, then the signal attributed to each species present in the mixture may be separated and the overlapping band problem is avoided.

Photoelectron-photoion-coincidence (PEPICO) has been widely used in laser spectroscopy [8] and similar experiments can be performed in UV-PES. If PFI (see section 12.2.2) is employed along with a time-of-flight ion and electron detection system, coupled to a time-structured light source, then photoelectrons and photoions may be measured in coincidence (PFI-PEPICO) [3, 9]. Although sub-meV resolution is possible, it should be noted that ionizations are only observed with the PFI technique where there is a resonance with a Rydberg state. Several examples of PFI-PEPICO measurements using synchrotron radiation have proved successful [9–11]. It should be possible to perform ion-electron coincidence measurements of reactive intermediates in a UV photoelectron spectroscopy experiment using a synchrotron as a radiation source.

12.3 Photoelectron spectroscopy of short-lived species using synchrotron radiation

In this work, synchrotron radiation was successfully used for angle-resolved studies of $O_2(a^1\Delta_g)$(see Chapter 6). CIS spectra taken at two angles enabled the assignment of Rydberg series to autoionizing resonances and enabled the calculation of the asymmetry parameter (β) a function of incident photon energy [12]. This study established the viability of angle-resolved studies of short-lived species using synchrotron radiation with the spectrometer used.

Photoelectron spectroscopy of O atoms (see Chapter 7) and OH (see Chapter 8) using a third generation synchrotron source (Elettra) have shown that the increased photon flux and improved spectral resolution can be used to obtain CIS spectra of short-lived species that contain much more information than was previously possible with a second generation source [13]. For OH rotational resolution of the bands corresponding to transitions to Rydberg states was observed in the CIS spectra and the spectra obtained compared favourably with earlier UV absorption and PIMS sudies. Similarly the work on O atoms demonstrated the advantages of the use of the third generation synchrotron source.

The studies of $O_2(a^1\Delta_g)$ [12], O atoms and OH radicals have shown that with the high photon flux, high degree of polarization and good spectral resolution,

photoelectron spectroscopy can be used to obtain information on photoionization dynamics, asymmetry parameters as a function of photon energy, and highly excited Rydberg states.

The success of the studies made on short-lived species means that these methods can be confidently applied to other short-lived species. In the future it is planned to complete studies on OH and undertake analogous studies on CF, SH, S and N. There also exists the possibility of studying metal vapours (*e.g.* Pb) in this way.

CF and other group(IV) monohalides (*e.g.* CCl, SiF, and SiCl) are of interest because they are present in plasmas used to etch or modify semiconductor devices (e.g. microchip manufacture) [14]. The CF radical has been subject to a recent PES study by the Southampton PES group [15].

Sulfur (S) and the mercapto radical (SH) are of spectroscopic interest. This is because of the high cosmic abundance of the sulphur molecule, with many sulfur containing species being detected in interstellar space [16]. SH also plays an important role in the UV photochemistry of sulfur-containing compounds present in the atmosphere. S and SH were previously studied in Southampton by conventional UV-PES [17] and have more recently been studied spectroscopically by higher resolution laser techniques by Milan, Buma and De Lange [18–20]. By studying S and SH with angle-resolved CIS spectroscopy, comparison can be made with the results obtained for O and OH.

It is also planned to carry out CIS and angular distribution measurements on the first PES band of N atoms at ELETTRA during the next period of beam time. This work will extend the angle-resolved study of atomic nitrogen by Schaphorst *et al.* [21].

12.4 The electronic structure of heavy metal compounds

In this work UBr_4 and $ThBr_4$ were studied with HeI photoelectron spectroscopy (see Chapter 9). The aim was to investigate the electronic structure of these molecules by comparing the ionization energies obtained from UV photoelectron spectra with ionization energies calculated using relativistic density functional theory [22].

The results obtained were consistent with the equilibrium geometries of UBr_4 and $ThBr_4$ being tetrahedral, and a complete ionic state assignment was achieved for all the bands observed in their HeI photoelectron spectra, including spin-orbit

splittings, with the aid of DFT calculations that included relativistic affects.

The excellent agreement between theory and experiment for these heavy metal compounds should encourage the theoretical (DFT) and experimental investigations of further compounds containing heavy atoms [22]. DFT has proven to be a valuable tool to study molecules for which *ab initio* calculations cannot be carried out with enough accuracy to give chemically meaningful results or for which *ab initio* calculations would be too computationally demanding.

In the near future, in the Southampton PES group, it is intended to attempt to record the UV photoelectron spectra of actinide tetraiodide compounds and compare the vertical ionization energies with values computed by relativistic DFT calculations. Larger spin-orbit spittings are expected for the tetraiodides compared with the tetrabromides due to the incorporation of the heavier halide. However, studying such air-sensitive and hygroscopic compounds will present extra experimental difficulties.

12.5 The pyrolysis of azide compounds

The pyrolysis studies of 2-azidoethanol and 2-azidoethylacetate (see Chapter 10) helped elucidate the main mechanisms of thermal decomposition of these organic azides. 2-Azidoacetic acid and 2-azidoethylacetate decompose via a concerted process through a cyclic transition state, whereas 2-azidoethanol and 2-azidoacetone decompose via a step-wise mechanism through an imine intermediate [23].

It was shown that monitoring the progress of a reaction using photoelectron spectroscopy , combined with results obtained on the pyrolysis products by matrix isolation IR spectroscopy, can clarify the possible routes of decomposition of organic compounds.

12.6 Simulation of the HeI Photoelectron Spectrum of F_2O

In the study of F_2O (see Chapter 11), the HeI PE spectrum of F_2O has been recorded with better resolution than previously reported. Extra vibrational structure has been observed for the first time. The order and positions of the lowest four states of F_2O^+ have been calculated by near state-of-the-art *ab initio* methods. The order of the first four states of F_2O^+ has been firmly established as $^2B_1$, $^2B_2$, $^2A_1$ and $^2A_2$ [24].

Reliable experimentally derived geometrical parameters were obtained for the $F_2O^+(\tilde{X}^2B_1)$ and $F_2O^+(^2A_2)$ states for the first time using the iterative Franck-Condon analysis (IFCA) procedure, whereby simulated envelopes are compared with experimental envelopes.

Vibrational analysis of the second and third, heavily overlapped PE bands in the HeI PE spectrum of F_2O was achieved based on a Fanck-Condon simulation, which matched most accuratley with the experimental spectrum. The AIE position for ionization to the $^2B_2$ ionic state was deduced from the comparison between the simulated and observed spectra to be 15.71 eV

For the third PE band, the observed AIE was found to be at 16.44 eV. Spectral simulation suggested that, although the adiabatic component of this band appeared to be the strongest, the VIE component of the third band is the (1,0,0)←(0,0,0) vibrational component at 16.54 eV.

From the highly consistent computed AIEs/T_e values, and the excellent match between the simulated and observed spectra, the AIE and VIE positions to the $^2A_1$ state should be close to the values of 16.17 and 16.40 eV respectively.

High-level *ab initio* calculations with spectral simulations using state-of-the-art anharmonic potential energy functions have enabled a better understanding of the complex PE spectrum of F_2O [24]. It is hoped that similar methods will be used to study the electronic structures and derive ionic state equilibrium geometries of other atmospherically important small molecules.

Bibliography

[1] J. V. Hatfield, P. J. Hicks, D. G. Lomas, and J. Comer, Rev. Sci. Instrum. **63**, 792 (1992).

[2] G. C. King, M. Zubek, P. M. Rutter, and F. H. Read, J. Phys. E: Sci. Instrum. **20**, 440 (1987).

[3] G. C. King, A. J. Yencha, M. Cristina, and A. Lopes, J. Elect. Spec. Relat. Phenom. **114**, 33 (2001).

[4] A. J. Yencha, A. Lopes, M. A. MacDonald, and G. C. King, Chemical Physics Letters **310**, 433 (1999).

[5] A. J. Yencha, M. Cristina, A. Lopes, and G. C. King, Chemical Physics Letters **325**, 559 (2000).

[6] A. J. Yencha, M. Cristina, A. Lopes, and G. C. King, Chemical Physics Letters **279**, 55 (2002).

[7] A. J. Yencha, A. J. Cormack, R. J. Donovan, A. Hopkirk, and G. C. King, Chem. Phys. **238**, 109 (1998).

[8] J. B. West, in *Vacuum ultraviolet photoionization and photodissociation of moleculs ions and clusters*, edited by C. Y. Ng (World Scientific, London, 1991), Chap. 5, p. 259.

[9] G. K. Jarvis, K. M. Weitzel, M. Malow, T. Baer, Y. Song, and C. Y. Ng, Rev. Sci. Instrum. **70**, 3892 (1999).

[10] T. Baer, Y. Song, J. Liu, W. Chen, and C. Y. Ng, Far. Disc. **115**, 137 (2000).

[11] G. K. Jarvis, K. J. Boyle, C. A. Mayhew, and R. P. Tuckett, J. Phys. Chem. A **102**, 3219 (1998).

[12] L. Beeching, A. De Fanis, J. M. Dyke, S. D. Gamblin, N. H. Hooper, A. Morris, and J. B. West, J. Chem. Phys. **112**, 1707 (2000).

[13] J. D. Barr, A. De Fanis, J. M. Dyke, S. D. Gamblin, N. Hooper, A. Morris, S. Stranges, J. B. West, and T. G. Wright, J. Chem. Phys. **110**, 345 (1999).

[14] K. T. Faber and K. J. Malley, *Semi-Conductors and Semi-Metals* (Academic Press, Boston, MA, 1992), Vol. 37.

[15] J. M. Dyke, N. Hooper, and A. Morris, J. Elec. Spec. Rel. Phen. **119**, 49 (2001).

[16] K. Sinha, Proc. Astron. Soc. Austr. 9, 32 **9**, 32 (1991).

[17] S. J. Dunlavey, J. M. Dyke, N. K. Fayad, N. Jonathan, and A. Morris, Mol. Phys. **44**, 265 (1979).

[18] J. B. Milan, W. J. Buma, and C. A. de Lange, J. Chem. Phys. **104**, 521 (1996).

[19] J. B. Milan, W. J. Buma, and C. A. de Lange, J. Chem. Phys. **105**, 6688 (1996).

[20] J. B. Milan, W. J. Buma, C. A. de Lange, K. Wang, and V. McKoy, J. Chem. Phys. **107**, 2782 (1997).

[21] S. J. Schaphorst, S. B. Whitfield, H. P. Saha, C. D. Caldwell, and Yoshiro Azuma, Phys. Rev. A **47**, 3007 (1993).

[22] L. J. Beeching, J. M. Dyke, A. Morris, and J. S. Ogden, Journal of Chemical Physics **114**, 9832 (2001).

[23] N. Hooper, L. J. Beeching, J. M. Dyke, A. Morris, J. S. Ogden, A. A. Dias, M. L. Costa, M. T. Barros, M. H. Cabral, and A. M. C. Moutinho, J. Phys. Chem. (Submitted) (2002).

[24] D. C. Wang, F. T. Chau, D. K. W. Mok, E. P. F. Lee, L. Beeching, J. S. Ogden, and J. M. Dyke, Journal of Chemical Physics **114**, 10682 (2001).

Appendix A

Parts of the results presented in this thesis have been published in the following papers :

- Angle resolved photoelectron spectroscopy of $O_2(a^1\Delta_g)$ with synchrotron radiation.
  L Beeching, A De Fanis, JM Dyke, SD Gamblin, N Hooper, A Morris and JB West, J. Chem. Phys., **112**, 1707-1712 (2000).

- The $\tilde{X}^2B_1$,$^2B_2$, $^2A_1$, and $^2A_2$ states of oxygen difluoride cation (F_2O^+): High-level *ab initio* calculations and simulation of the ultraviolet photoelectron spectrum of F_2O.
  De-Chao Wang, Foo-Tim Chau, Daniel Kam-Wah Mok, and Edmond P. F. Lee, Levi Beeching, J. Steven Ogden and John M. Dyke. J. Chem. Phys., **114**, 10682-10694 (2001)

- Study of the electronic structure of the actinide tetrabromides $ThBr_4$and UBr_4using ultraviolet photoelectron spectroscopy and density functional calculations
  L. J. Beeching, J. M. Dyke, A. Morris and J. S. Ogden. J. Chem. Phys.**114**, 9832-9839 (2001)

- Photoelectron spectroscopy of reactive intermediates using synchrotron radiation.
  J. D. Barr, L. Beeching, A. De-Fanis, J. M. Dyke, S. D. Gamblin, N. Hooper, A. Morris, S. Stranges , J. B. West , A. E. Wright and T. G. Wright. J. Elect. Spec. Relat. Phenom.**108** (2000) 4761

Further manuscripts, containing the results on the studies of OH (see Chapter 8) and azide pyrolysis (see Chapter 10) are in preparation.